# Thermoelectric Transport Properties of Novel Nanoscaled Materials via Homemade and Commercial Apparatus Measurements

Author: Kevin C. Lukas

Persistent link: http://hdl.handle.net/2345/2971

This work is posted on eScholarship@BC,
Boston College University Libraries.

---

Boston College Electronic Thesis or Dissertation, 2013

Copyright is held by the author, with all rights reserved, unless otherwise noted.

Boston College

The Graduate School of Arts and Sciences

Department of Physics

# THERMOELECTRIC TRANSPORT PROPERTIES OF NOVEL NANOSCALED MATERIALS VIA HOMEMADE AND COMMERCIAL APPARATUS MEASUREMENTS

a dissertation

by

Kevin C. Lukas

submitted in partial fulfillment of the requirements

for the degree of

**Doctor of Philosophy**

May 2013

© copyright by **Kevin Charles Lukas** 2012

# Abstract

**Title:** THERMOELECTRIC TRANSPORT PROPERTIES OF NOVEL NANOSCALED MATERIALS VIA HOMEMADE AND COMMERCIAL APPARATUS MEASUREMENTS

**Author:** Kevin C. Lukas

**Advisor:** Dr. C.P. Opeil, S.J.
**Committee Members:** Dr. M.S. Dresselhaus, Dr. M.J. Graf, and Dr. Z.F. Ren

Thermoelectric (TE) materials are of broad interest for alternate energy applications, specifically waste heat applications, as well as solid-state refrigeration. The efficiency of TE materials can be improved through either the enhancement of the Seebeck coefficient and electrical conductivity, or through the reduction of the thermal conductivity, $\kappa$, specifically the lattice portion of thermal conductivity, $\kappa_{latt}$. Nanostructuring has been proven to reduce $\kappa_{latt}$ and therefore increase efficiency. The inability to accurately model the lattice and electronic contributions to $\kappa$ makes optimizing the reduction of $\kappa_{latt}$ difficult[1]. This work demonstrates that the lattice and electronic contributions to $\kappa$ in nanostructured materials can be directly measured experimentally by separating the contributions using magnetic field[2]. We use this technique along with other characterization techniques to determine the effects of doping Ce, Sm, and Ho into $Bi_{88}Sb_{12}$[3]. Along with enhancing the efficiency of the material, TE devices must be thermally stable in the temperature range of operation. Therefore we also study the effects of temperature cycling, annealing, oxidation, and diffusion barriers[4] on TE devices. These studies are accomplished through both homemade[5] and commercially available measurement equipment.

[1] M. Zebarjadi, J. Yang, K. C. Lukas, B. Kozinsky, B. Yu, M.S.Dresselhaus, C. Opeil, Z. Ren, G. Chen, *J. App. Phys*., 2012, 112, 044305.

[2] K.C. Lukas, W.S. Liu, G. Joshi, M. Zebarjadi, C. P. Opeil, G. Chen, M.S. Dresselhaus, Z.F. Ren, *Phys. Rev. B*, 2012, 85, 205410.

[3] K.C. Lukas, G. Joshi, K. Modic, C.P. Opeil, Z.F. Ren, *J. of Mat. Sci*., 2012, 45, 15.

[4] K.C. Lukas, W.S. Liu, Z.F. Ren, C.P. Opeil, *J. App. Phys*., 2012, 112, 054509.

[5] K.C. Lukas, W.S. Liu, Q. Jie, Z.F. Ren, C.P. Opeil, *Rev. Sci. Inst*. 2012, 83, 115114.

## Dedication

To Kimberly Ann and my family.

# Quotations

Live as if you were to die tomorrow. Learn as if you were to live forever.

(Mahatma Gandhi)

**in·ten·si·ty** [in-**ten**-si-tee]

*noun, plural* **in·ten·si·ties**

1. Disposition to dominate.

(Coach Reiser)

# Acknowledgements

A thesis is not the sole work of one individual, and therefore I would like to take this opportunity to express my gratitude to all those who helped me throughout this process. I first want to thank my advisor Fr. Cyril P. Opeil, S.J. for allowing me the freedom to break most of the things we salvaged from the dumpster and even some that were purchased. Also for his guidance, encouragement, and assistance throughout this research work and during my tenure here at Boston College.

I also wish to express my sincere thanks to my dissertation committee members, Prof. Michael Graf and Prof. Zhifeng Ren from Boston College as well as Prof. Millie S. Dresselhaus from MIT who have provided continuous support and valuable suggestions throughout this work.

I would like to express my thanks to Prof. Gang Chen, Dr. Mona Zebarjadi, and Mr. Sangyeop Lee from MIT for their collaborative efforts to theoretically understand the experimental data. Their fruitful suggestions have been extremely helpful. I would like to extend acknowledgement to my colleagues Mr. Mani Pokharel, Dr. Weishu Liu, Dr. Huaizho Zhao, Dr. Qian Zhang, Dr. Qing Jie, Dr. Dezhi Wang, Dr. Xiao Yan, and Dr. Bo Yu for their assistance with sample preparation along with discussion and creating the ideal collaborative research environment.

To all my friends and classmates especially Mr. Steve Disseler, Mr. Fan Ye, and Mr. Yi Zhan for their dining companionship, soccer skills, and endless assistance over the course of my stead. And to anyone who went, goes, or will go to wings on Monday nights at five, that they may always keep the universe in order with fifteen wings and a

PBR.

Finally I would like to express sincere thanks to my family and friends for their support throughout this process, especially my wife and best friend Kimberly Ann without whom none of this would have been possible.

Kevin Charles Lukas

# Table of Contents

# List of Figures and Tables

Chapter 1



Chapter 2

# Chapter 1: Introduction and Thermoelectric Theory

## 1.1 Introduction

In 1823 T. J. Seebeck discovered that a voltage was generated when a temperature gradient was established across two dissimilar metals [1]. Shortly after Peltier found that by running a current through the dissimilar metals, heat was liberated at the junction and if the direction of the current was reversed, heat was absorbed [2]. Thermoelectric generators as well as thermoelectric refrigerators available today grew out of these two discoveries. Both the generators as well as the refrigerators have the benefits of no moving parts and therefore are less likely to mechanically fail. This is important when reliability is of upmost importance, even above efficiency, as is the case in deep space satellite missions which utilize a radioactive element as a heat source to generate the electricity required to power the electronics [3].

Given the present concern over the changing climate of the planet as well as dependence on foreign oil, thermoelectrics have emerged as a potential source of clean alternate energy. When generating electricity, the majority of energy is lost as heat; if this waste heat could be harnessed through the use of thermoelectric generators, then all processes for generating electricity would become more efficient. In order for thermoelectric generators to become a viable commercial option, their efficiency must be increased. The efficiency of a thermoelectric generator can be increased by enhancing the electrical and thermal transport properties of the material. The interrelation of the different electrical and thermal transport properties makes increasing the thermoelectric

efficiency quite difficult. In order to increase efficiency, we must have a greater understanding of the mechanisms which lead to the optimization of thermoelectric transport properties.

Besides having a high efficiency, the thermoelectric device must also have mechanical, thermal, and electrical properties that are stable over an extended period of time as well as during temperature cycling. A device is not commercially viable if it cannot be turned on and off several times or run for several hours or even days; thermal stability is quite important in device fabrication.

In this thesis I describe steps that we have taken in order to better understand thermal transport, thermal stability, as well as the effects of doping impurities into different thermoelectric materials. The remainder of this chapter briefly describes the theory of thermoelectricity. Chapter 2 describes a high temperature (300-700 K) experimental setup that has been designed, constructed, and benchmarked to measure arbitrarily shaped samples as well as thermal stability. Chapter 3 gives details of a commercially available Physical Properties Measurement System (PPMS) from Quantum Design, as well as how it was used to experimentally separate components of the thermal conductivity. The last two chapters describe how the commercial and home built equipment were used to investigate the effects of impurity doping in both a bismuth telluride and bismuth antimony system.

Due to the amount of data taken during each of these studies, the chapters contain the minimum amount of figures and tables required to accurately demonstrate understanding. Several pertinent figures are included as appendices which are mentioned throughout the chapters. Along with the work presented in this thesis, several other

studies have been performed on both thermoelectric and non-thermoelectric materials using the described experimental equipment. Several publications have come out of these collaborative measurements. All publications are included in Appendix D.

## 1.2 Thermoelectric Theory

### 1.2.1 Introduction

In this chapter, basic thermoelectric (TE) principles and concepts will be discussed. Only concepts that are pertinent to this thesis will be introduced and summarized, with no extensive theoretical derivations. Expressions for electronic and thermal transport will be given, and there will be a brief review of TE devices.

#### 1.2.1.1 Seebeck Effect

The Seebeck effect was a phenomenological discovery in 1823 by Thomas Seebeck [1]. He found that when two dissimilar metals are placed electrically in contact and a temperature gradient, $\Delta T$, is established in the circuit a voltage, $V$, is produced. The voltage is given by the expression [4],

$$V = S_{ab}\Delta T \qquad 1.1$$

where $S_{ab}$ is the relative Seebeck coefficient which is given by the difference between the

absolute Seebeck coefficients $S_a$ and $S_b$ of the individual materials a and b by [4],

$$S_{ab} = S_b - S_a \qquad 1.2$$

Figure 1.1 shows a schematic of the Seebeck effect described by Equations 1.1 and 1.2 where a is defined as positive with respect to b if electrons flow from a to b at the cold junction [4].

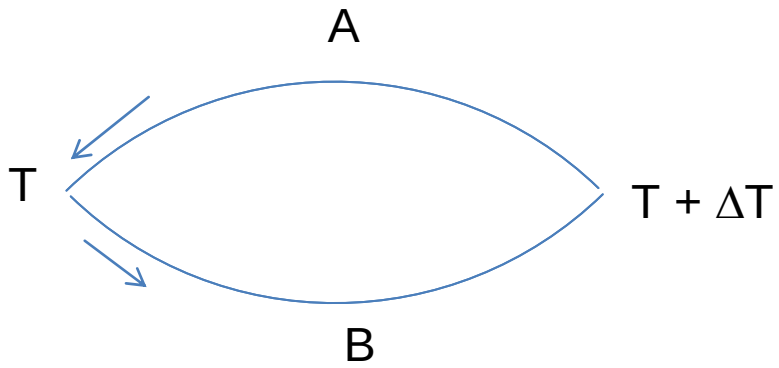


Figure 1.1: Closed thermoelectric loop connecting two dissimilar metals A and B. A temperature gradient in the circuit induces the carriers to move [4].

1.2.1.2 Peltier Effect

Jean-Charles Peltier found in 1834 that when a current ($I$) is run through a junction of two dissimilar metals, heat ($Q$) is either liberated or absorbed depending on the direction of current [2]. For his efforts the phenomena is dubbed the Peltier Effect. The amount of heat liberated or absorbed is given by [5],

$$Q = \Pi_{ab} I \qquad 1.3$$

Where $\Pi_{ab}$ is the relative Peltier coefficient which is equal to the difference between the absolute Peltier coefficients $\Pi_a$ and $\Pi_b$ given by [5],

$$\Pi_{ab} = \Pi_b - \Pi_a \qquad 1.4$$

Figure 1.2 shows a schematic of the Peltier Effect in the same circuit as shown in Figure 1.1. In this diagram heat is absorbed at the hotter junction and liberated at the colder junction.

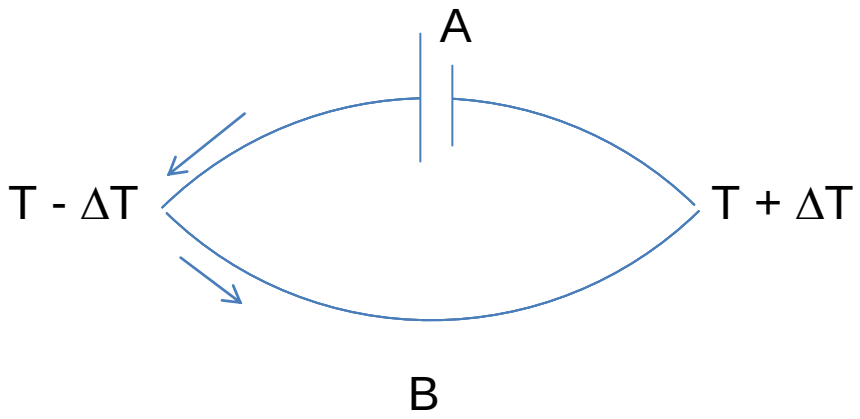


Figure 1.2: Closed thermoelectric loop connecting two dissimilar metals A and B. Current flowing through the loop causes heat to be liberated at one junction and absorbed at the other [4].

1.2.1.3 Thomson Effect

The Thomson effect manifests itself in a single current carrying material in the presence of a temperature gradient. The Thomson coefficient is defined as the rate of heating per unit length that is produced when a current passes through a single conductor that resides in a temperature gradient [6]. The Thomson coefficient ($\beta$) is given by,

$$\beta = \frac{dq/dx}{IdT/dx} \qquad 1.5$$

where dq/dx is the rate of heating or cooling per unit length and dT/dx is the temperature gradient.

1.2.1.4 Kelvin Relations

The thermoelectric effects described above are related to each other by the Kelvin relations, named after Lord Kelvin who derived their relations theoretically. The relations are given by the following expressions [7],

$$\Pi = ST \qquad 1.6$$

$$\beta = T\frac{dS}{dT} \qquad 1.7$$

1.3 Thermoelectric Transport Properties

1.3.1 Electrical Conductivity

The conduction of charge carriers, electrons or holes, in a material are given by the general expression,

$$\sigma = ne\mu \tag{1.8}$$

where $\mu$ is the mobility of the charge carrier, $e$ is the electronic charge, and $n$ is the carrier concentration. When the number of carriers becomes large, the carriers can no longer be treated as non-interacting particles and Fermi–Dirac statistics must be used. The electrical conductivity in the degenerate limit for a single parabolic band is given by [8],

$$\sigma = 2(\frac{2\pi m^* k_B T}{h^2})^{3/2} e\mu \frac{F_{r+1/2}(\xi)}{(s+1/2)!} \tag{1.9}$$

where n can be defined as [8],

$$n = 4\pi(\frac{2m^* k_B T}{h^2})^{3/2} F_{1/2}(\xi) \tag{1.10}$$

where $m^*$ is the effective mass of the carrier, $k_B$ is Boltzmann's constant, $T$ is the absolute temperature, $h$ is Planck's constant, $F_n(\xi)$ is the Fermi integral, $r$ is the scattering parameter, and $\xi$ is the reduced Fermi energy given by,

$$\xi = \frac{E_F}{k_B T} \tag{1.11}$$

where $E_F$ is the Fermi energy.

In semiconductors, there are two contributions to the electrical transport, one from electrons and one from holes. The expression for conduction in the two band model is given by [8],

$$\sigma = \sigma_e + \sigma_h = n_e e\mu_e + n_h e\mu_h \qquad 1.12$$

It can be seen that the total conductivity is the simple sum of the conductivities of holes $\sigma_h$ and electrons $\sigma_e$, which themselves are composed of the individual carrier concentrations and mobilities.

### 1.3.2 Seebeck Coefficient

The electrical conductivity and the Seebeck coefficient can be equated through Mott's formula [8],

$$S = -\frac{\pi^2 k_B^2 T}{3e}\left[\frac{d\ln(\sigma)}{dE}\right]_{E=E_F} \qquad 1.13$$

or in terms of the carrier concentration and mobility as [8],

$$S = -\frac{\pi^2 k_B^2 T}{3e}\left[\frac{1}{n}\frac{dn(E)}{dE} + \frac{1}{\mu}\frac{d\mu(E)}{dE}\right]_{E=E_F} \qquad 1.14$$

From Equations 1.13 and 1.14 it is evident that $S$ and $\sigma$ are inversely proportional and the carrier concentration predominantly dictates carrier transport and optimization between the two transport coefficients.

The Seebeck coefficient in the degenerate limit for a single parabolic band can be expressed as [8],

$$S = \pm \frac{k_B}{e} \frac{(r+5/2)F_{r+3/2}(\xi)}{(r+3/2)F_{r+1/2}(\xi)} - \xi \qquad 1.15$$

Just as in the electrical conductivity a two band model is required for semiconductors, however unlike $\sigma$ the Seebeck coefficient is not the simple sum of the contributions from the two carriers but is given by [8],

$$S = \frac{(S_e\sigma_e + S_h\sigma_h)}{(\sigma_e + \sigma_h)} \qquad 1.16$$

### 1.3.3 Thermal Conductivity

The conduction of heat in solids is the sum of two contributions, that of the lattice and that of the carriers. Therefore the total thermal conductivity ($\kappa_{total}$) is given as the sum of the two components by [9],

$$\kappa_{total} = \kappa_{carrier} + \kappa_{lattice} \qquad 1.17$$

where $\kappa_{carrier}$ is the contribution to the thermal conductivity due to the charge carriers and $\kappa_{lattice}$ is the contribution due to the lattice. For metals $\kappa_{total}$ is dominated by the carrier component of the thermal conductivity, while in semiconductors and insulators $\kappa_{total}$ is dominated by $\kappa_{lattice}$. The carrier contribution to the total thermal conductivity can be expressed in terms of the Lorenz number ($L$) by [9],

$$\kappa_{carrier} = L\sigma T \tag{1.18}$$

For metals it is common practice to use a constant value for $L$ of $2.45 \times 10^{-8}$ $V^2/K^2$ which is valid for the free electron model in the Sommerfeld approximation [10-11]. This value is close to actual values for many metals as determined experimentally by Wiedemann and Franz where $\kappa_{carrier}$ is approximately equal to $\kappa_{total}$ [10]. However for most materials, especially good thermoelectrics, the free electron approximation is not valid. In degenerate materials, the Lorenz number for the single parabolic band approximation is given by [8],

$$S = \left(\frac{k_B}{e}\right)^2 \left( \frac{(r+7/2)F_{r+5/2}(\xi)}{(r+3/2)F_{r+1/2}(\xi)} - \left[ \frac{k_B}{e} \frac{(r+5/2)F_{r+3/2}(\xi)}{(r+3/2)F_{r+1/2}(\xi)} \right]^2 \right) \tag{1.19}$$

For semiconductors the thermal conductivity is again the sum of the carrier and lattice contributions, however $\kappa_{carrier}$ now has contributions from two types of carriers and is given by [9],

$$\kappa_{carrier} = \kappa_e + \kappa_h + \frac{(\sigma_e \sigma_h)}{(\sigma_e + \sigma_h)}(S_e - S_h)^2 T \qquad 1.20$$

where $\kappa_e$ and $\kappa_h$ are the contributions to thermal conductivity from electrons and holes, respectively. The third term in Equation 1.20 is referred to as the bipolar contribution which manifests itself at temperatures near or exceeding the energy of the band gap ($E_g$). At these temperatures electrons have a much higher probability of jumping from the valence band to the conduction band thereby creating electron-hole pairs which propagate along and upon recombination, or annihilation of the electron-hole pair, energy is released in the form of a phonon.

The lattice contribution to the thermal conductivity can be quantized in the form of phonons and using classical kinetic theory is given by [12,13],

$$\kappa_{lattice} = \frac{C_v v_s l}{3} \qquad 1.21$$

where $C_v$ is the specific heat, $v_s$ the average velocity of sound, and $l$ is the mean free path of the phonons.

### 1.3.4 Scattering Mechanisms

The scattering of charge carriers and phonons is imperative in the study of transport properties. The scattering mechanisms for charge carriers manifest themselves in the carrier mobility which as shown in the previous section impacts both the Seebeck coefficient as well as the electrical conductivity. Scattering of carriers can also have an impact on the carrier component of the thermal conductivity. The carriers can be individual electrons, holes, or both. The carriers can scatter off each other as in electron-electron scattering. Carriers can also scatter off phonons, impurities, boundaries, or defects. The more time that passes in between scattering collisions the longer the scattering time and therefore the mean free path, and the higher the mobility.

The scattering of phonons has an impact on the lattice portion of the thermal conductivity. Peierls was the first to introduce the concept of phonons as quantized vibrational wave packets that can interact with each other in two ways, normal processes (N-processes) in which momentum is conserved or Umklapp processes (U-processes) in which momentum is not conserved, though momentum for the system is conserved if translation of the whole system is taken into account [8]. Umklapp processes dominate at higher temperature where phonon-phonon interactions are responsible for the suppression of thermal conductivity [8]. Still of importance, especially at lower temperatures, are phonon-carrier, phonon-defect, and phonon-boundary scattering.

The time a carrier or phonon travels before it is scattered can be given by a time $\tau$ and the individual scattering times are typically summed using Matthiessen's rule where [8],

$$\frac{1}{\tau} = \frac{1}{\tau_1} + \frac{1}{\tau_2} + .... + \frac{1}{\tau_i} \qquad 1.22$$

## 1.4 Thermoelectric Devices

### 1.4.1 Applications

It was quickly realized that the combined effects described in the previous sections could be used to create a heat engine or, by running the heat engine in reverse, a refrigerator. Utilizing the Seebeck effect, a temperature gradient can create an electrical output. A model of a thermoelectric generator is shown in Figure 1.3. Thermoelectrics have the potential to be quite useful as waste heat recovery systems, especially when one considers that the majority of energy created is lost as heat in any type of fuel based electrical power generator. For this reason the U.S. Department of Energy as well as several automobile companies have invested millions of dollars into research on thermoelectric materials [5]. Presently thermoelectric generators are available but only in niche applications, the most well known being for deep space missions [3,5]. The mechanical stability and long lifetime due to lack of movable parts makes the radio – isotope thermoelectric generator (RTG) ideal for satellite missions where solar power cannot be harnessed [3,5]. Figure 1.3 (left) shows how the Peltier effect can be used for thermoelectric cooling applications. Presently there are several commercially available TE cooling devices that are used in electronics, lasers, and even small household refrigerators [14].

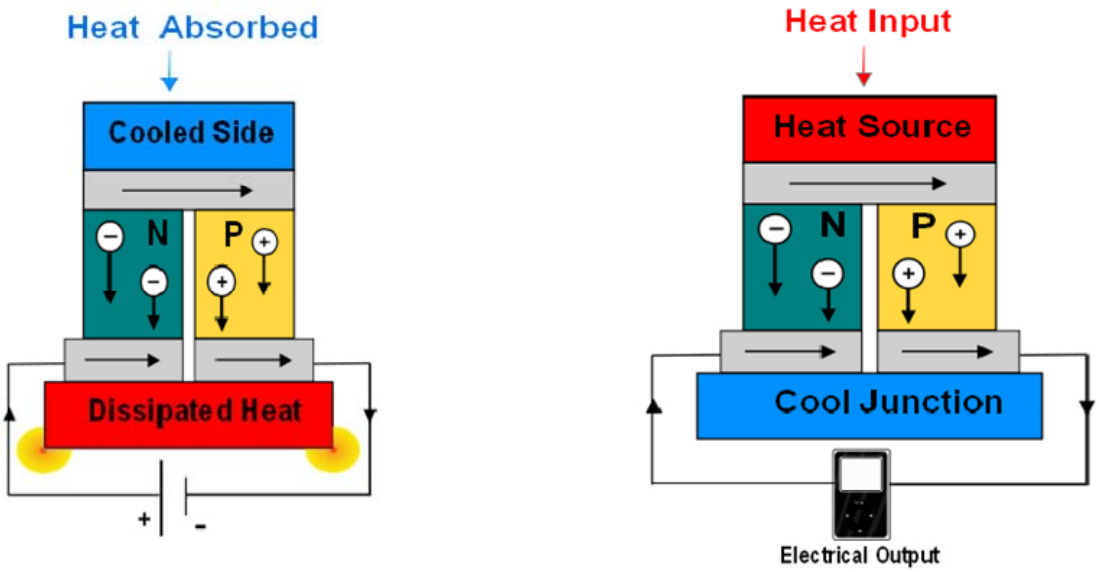


Figure 1.3: The image on the left is a diagram of a thermoelectric circuit used for cooling while the diagram on the right is for power generation.

### 1.4.2 Performance

The efficiency of a TE generator or refrigerator is presently too low to be commercially competitive with other forms of power generation or refrigeration. The efficiency of the TE generator ($\eta$) shown in Figure 1.3 is given by the expression [8],

$$\eta = \frac{\frac{\Delta T}{T_h}\left(\sqrt{1+ZT}-1\right)}{\sqrt{1+ZT}+\frac{T_c}{T_h}} \qquad 1.23$$

where $T$ is the average temperature, $T_c$ and $T_h$ are the temperatures of the cold and hot reservoirs, respectively, and $Z$ is the figure of merit defined in section 1.4.2.1. Figure 1.4 plots $\eta$ as a function of $ZT$ for several different temperature gradients. From the plot we

see that as $ZT$ increases so does the efficiency. The efficiency also increases as the temperature gradient increases, the lowest line having a $\Delta T$ of 150 degrees while the top most line has a $\Delta T$ of 600 degrees. Therefore for any TE generator it is ideal to have the highest value possible for $ZT$ while establishing as large a temperature gradient as possible.

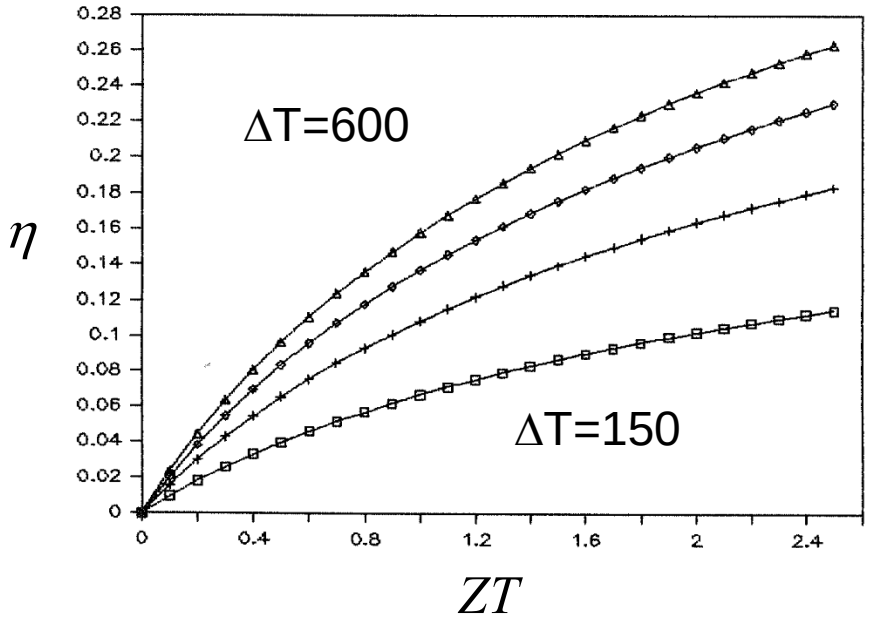


Figure 1.4: The efficiency of a thermoelectric generator plotted against $ZT$. As $ZT$ increases, so does the efficiency. Efficiency also increases as $\Delta T$ increases [8].

The efficiency of a refrigerator is given by the coefficient of performance (COP, $\phi$) which can also be expressed as a function of $ZT$ and is given as [8],

$$\phi = \frac{T_c}{T_h - T_c} \frac{(\sqrt{1+ZT} - \frac{T_h}{T_c})}{\sqrt{1+ZT}+1} \qquad 1.24$$

It is again apparent that $\phi$ depends on $ZT$. A plot of $\phi$ versus $ZT$ is given in Figure 1.5 for

an arbitrary temperature difference.

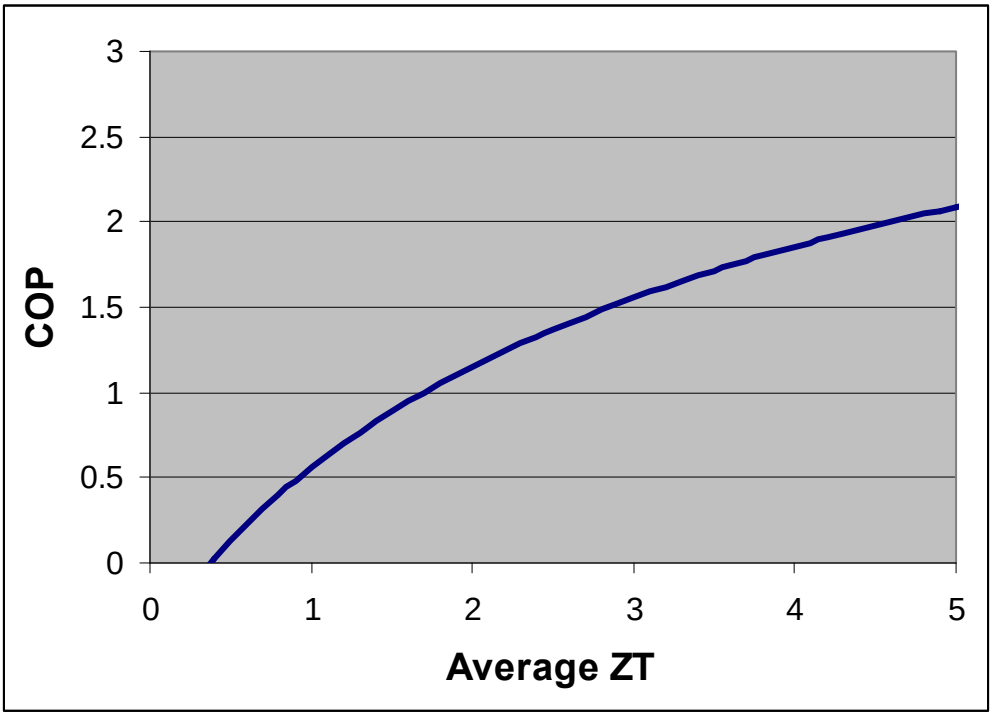


Figure 1.5: The coefficient of performance is plotted against $ZT$ for a thermoelectric refrigerator. It is seen that as $ZT$ increases so does $\phi$.

1.4.2.1 Figure of Merit

It becomes immediately apparent that the efficiency of TE generators or coolers is dependent on the parameter $ZT$. $ZT$ is a materials parameter defined as [15],

$$ZT = \left( \frac{S^2 \sigma}{\kappa} \right) T \qquad 1.25$$

where $S$ is the Seebeck coefficient, $\sigma$ the electrical conductivity, $\kappa$ the thermal conductivity, and $T$ the absolute temperature where the numerator $S^2\sigma$ is referred to as the power factor (PF). Recalling the inverse relationship between the Seebeck coefficient and electrical conductivity presented in section 1.3.2 we can easily see there will be an optimal point at which the PF will be maximized. Rewriting $S$ and $\sigma$ in terms of the

carrier concentration the maximum value for the power factor is in the range of carrier concentration which is typical for semimetals or narrow band gap semiconductors as described by Snyder, *et. al* and shown in Figure 1.6 for PbTe [16].

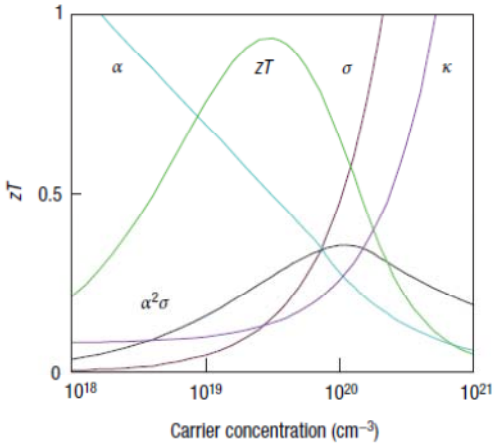


Figure 1.6: Plot taken from Ref. 16 demonstrating the interrelation between the transport properties of *ZT* [16].

### 1.4.3 Device Requirements

Several requirements must be met in order for a material to become commercially competitive, which is the ultimate goal for optimizing the materials. As mentioned in the previous section, materials must have a high value for *ZT*. *ZT* is material dependent and there are several well known materials that show the best known thermoelectric properties depending on the temperature range. Figure 1.7 shows several of the best TE materials. The search continues for materials that exhibit even higher values of *ZT*, however even in the well established materials, further improvements can be made. Several recent attempts to enhance *ZT* include lowering the dimensionality of the material to either enhance the density of states near the Fermi level [17-19], or decrease $\kappa$ by increasing the number of interfaces by grain boundary scattering [20]. Doping is another

common technique to improve the properties of TE materials [21].

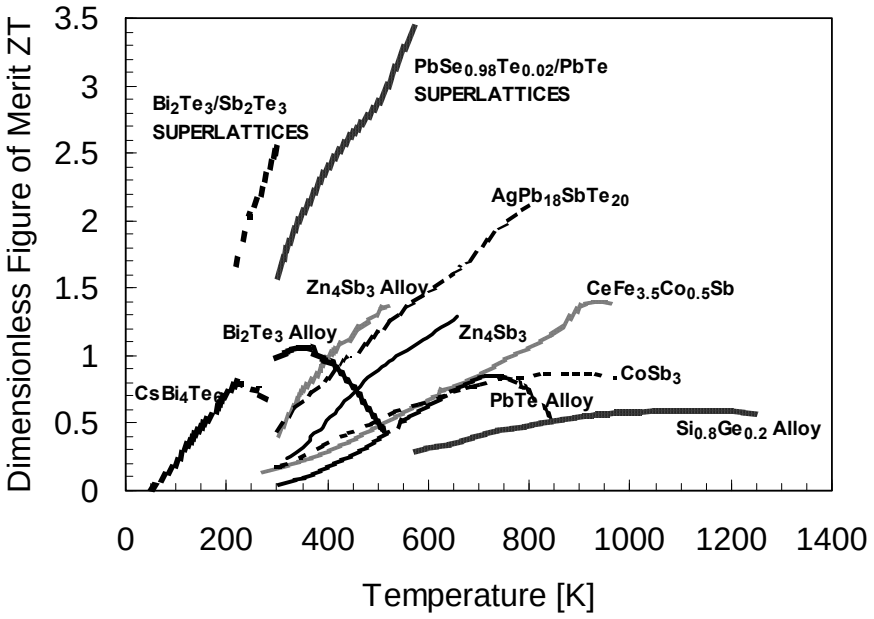


Figure 1.7: Plot of *ZT* with temperature for a variety of different materials [8].

Besides having a high *ZT*, materials must also have properties that are stable in their typical temperature range of operation. It does not matter how high *ZT* is if the material cannot function at that temperature for minimal time. Therefore it is just as important to study the mechanical and electrical stability properties of TE materials, as it is ultimately the intention to use these devices for extended periods of time. The main objective of this dissertation is to study the effects on the electrical transport properties, thermal transport properties, and thermal stability of doped nanostructured TE materials. This is done by utilizing a newly constructed experimental setup described in Chapter 2 along with a commercially available system in which new methodologies were developed to extract further information with regards to the thermal conductivity (Chapter 3).

## 1.5 References

1. T. J. Seebeck, Magnetic polarization of metals and minerals, Berlin, 265, (1822).
2. J. C. Peltier, Ann. Chim. LV1 371 1834.
3. D. M. Rowe, Proc. VIIIth Int. Conf. Thermoelectric Energy Conversion Nancy, France 133 (1989).
4. D. D. Pollock Thermocouples: Theory and Properties(CRC Press, Boston, 1991**)**.
5. D. M. Rowe (Ed.) CRC Handbook of Thermoelectrics (CRC Press, Boca Raton, 1995).
6. A. F. Ioffe Semiconductor Thermoelements and Thermoelectric Cooling (Infosearch, London, 1957**)**.
7. H. J. Goldsmid Introduction to Thermoelectricity (Springer, New York, 1964).
8. D. M. Rowe, Thermoelectrics Handbook: Macro to Nano (Taylor & Francis, New York, 2006).
9. G. S. Nolas, J. Sharp, and H. J. Goldsmid, Thermoelectrics: Basic Principles and New Materials Developments (Springer, 2001).
10. N. E. Ashcroft and N. D. Mermin, Solid State Physics (Saunders College Publishing, New York, 1976).
11. A. Sommerfeld Z. Phys. **47**, 1 (1928).
12. C. Kittel Introduction to Solid State Physics (Wiley, 1996).
13. T. M. Tritt (Ed.) Thermal conductivity (Kluwer Academic/Plenium Publishers, New York, 2003).

14. H. J. Goldsmid Thermoelectric Refrigeration (Plenum Press, New York, 1964).

15. T. M. Tritt (Ed.) Semiconductors and Semimetals Vol. 69-71(Academic Press, San Diego, CA, 2001).

16. G. J. Snyder and S. Toberer Nature materials **7**, 105 (2008).

17. M. S. Dresselhaus, G. Chen, M. Y. Tang, R. G. Yang, H. Lee, D. Z. Wang, Z. F. Ren, J. P. Fleurial, and P. Gogna Adv. Mater. **19**, 1 (2007).

18. L. D. Hicks and M.S. Dresselhaus, Physical Review B **47**, 12727 (1993).

19. L.D. Hicks and M.S. Dresselhaus, Physical Review B **47**, 16631 (1993).

20. B. Poudel, Q. Hao, Y. Ma, Y. Lan, A. Minnich, B. Yu, X. Yan, D. Z. Wang, A. Muto, D. Vashaee, X. Chen, J. Liu, M. S. Dresselhaus, G. Chen, and Z. F. Ren Science **320**, 634 (2008).

21. J. P. Heremans, V. Jovovic, E. S. Toberer, A. Saramat, K. Kurosaki, A. Charoenphakdee, S. Yamanaka, G. J. Snyder Science **321**, 554 (2008).

# Chapter 2: Power Factor Measurements at High Temperature

## 2.1. Introduction

This chapter describes in detail the construction of an apparatus for the measurement of the thermoelectric power factor. The system described below makes two separate independent measurements of the Seebeck coefficient and electrical resistivity. The section discussing the electrical resistivity has been published in *Review of Scientific Instruments* and can be found in Appendix D. The construction of each independent measurement setup is described in detail followed by a comparison of data with a commercially available system for a variety of thermoelectric samples. It is necessary to compare several samples with commercially available systems due to the fact that there are no high temperature thermoelectric standards. It is true that there are metals available such as constantan or nickel for benchmarking, however these metals have a value for the thermopower that is an order of magnitude lower and a thermal conductivity at least an order of magnitude higher than the best TE materials currently available. Though thermoelectrics have been around for nearly two centuries, there is still no standard technique or standard reference material for measuring the Seebeck coefficient at higher temperatures. Therefore it is imperative that any homemade system be benchmarked against other systems that are commonly used for the same measurements from 300 – 700 K.

## 2.2.Electrical Resistivity Measurement

### 2.2.1. Construction

The resistivity measurements are set up, Figure 2.1, in a helium backfilled vacuum chamber (I). Samples, especially at high temperature must be measured in an oxygen free environment to prevent oxidation effects, unless studying oxidation is the purpose of the measurement. Since the chamber must create an isolated environment, Viton o-rings are used to seal the chamber. The o-rings have a maximum operating temperature which when exceeded cause the o-rings to fail. In order to maintain an optimal operating temperature, a coolant plate (J) is used to dissipate excess heat. The coolant plate is kept at roughly 14 $^{o}$C via a closed loop water coolant system. This has proven to be enough cooling power to keep the o-rings under their maximum operating temperature, 100 $^{o}$C, while the inside of the chamber reaches temperatures in excess of 550 $^{o}$C. The chamber is evacuated with a mechanical pump down to pressures of 10 Pa. The chamber is then back filled with He gas, typically ambient pressure (100 kPa) because it was determined that the cartridge heaters (B), which supply the heat, function better when in the presence of an exchange gas as opposed to in vacuum. Feed-throughs for electrical leads for current, voltage, heater power, and thermocouple inputs were mechanically fabricated. A sketch of the setup is shown in Figure 2.1. Nickel wire (3 mil) (H) is spark welded to each sample and then mechanically connected (D) to copper wire leads which in turn are mechanically connected to the vacuum chamber feed-throughs leading out of the chamber where the instrumentation for data acquisition are attached. Ni wire is used because it does not diffuse into the sample as readily as Cu, Au, or Ag which is of concern at high temperature. Temperature is read using 24 gage K-type thermocouple wire from Omega which is mechanically attached to the heating block with

a screw; the 24 gage wire should be thick enough to negate any effects of "green rot" on the positive element which is a problem in oxygen depleted environments, but thin enough to still have a relatively quick response time with respect to the sample [5]. Mechanical connections are used at higher temperatures because solder or other electrically conducting epoxies are more difficult to use due to their lower operating temperatures. Heat is provided by a 120 V, 400 W cartridge heater (B) from Omega with a length of 3" and a 3/8" diameter. The cartridge heater is placed into a 1 x 1 x 3 inch stainless steel (SS) block (A) with a hole size slightly larger than the diameter of the cartridge heater.

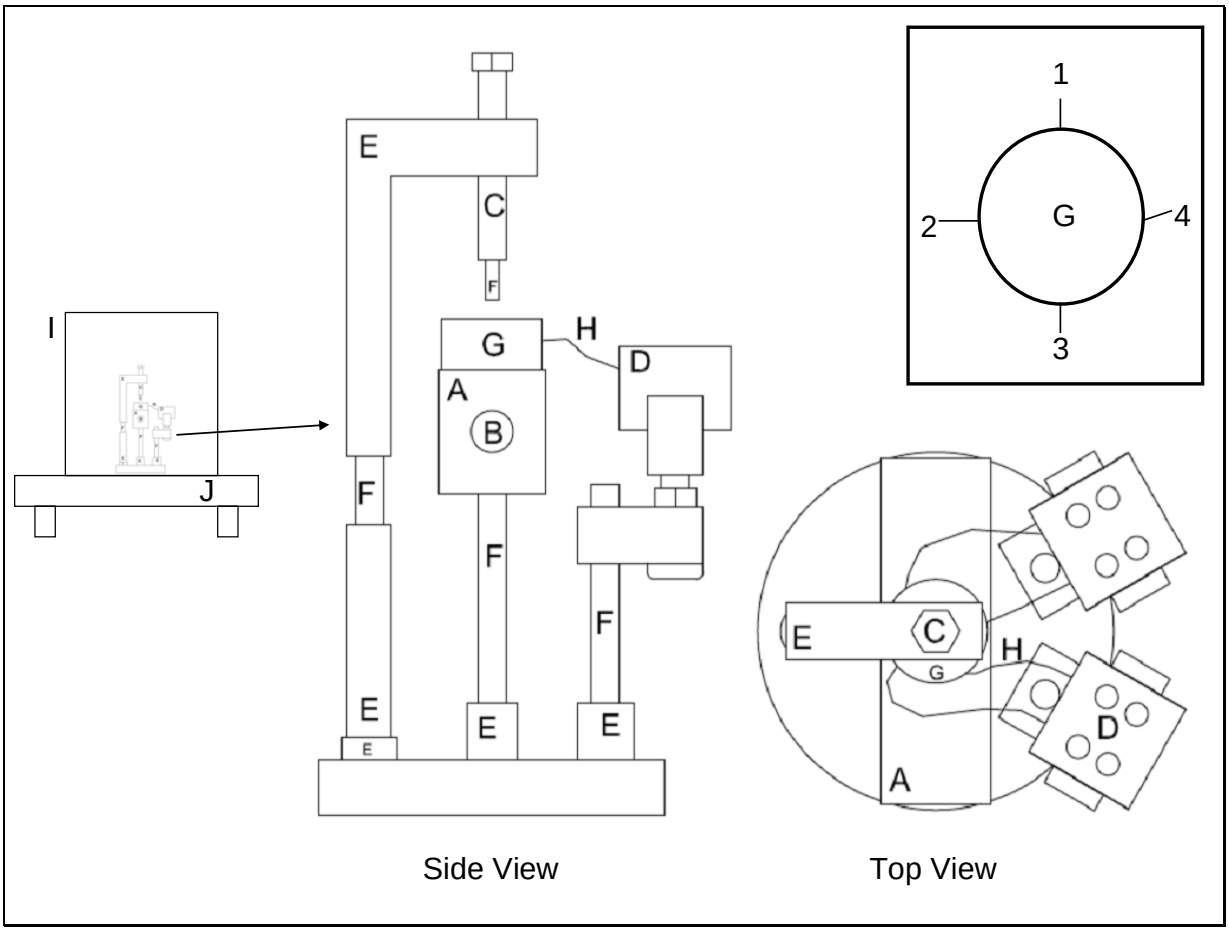


Figure 2.1: Diagram of experimental setup for in situ resistivity measurements. Alumina

rods, ¼", (F) are connected to SS pieces (E) machined with hole sizes a fraction larger than the alumina rods. The inset shows the wiring configuration for a sample being measured using the Van der Pauw technique.

In an ambient environment the cartridge heater resting in the SS block can typically reach 700 $^{o}$C. In vacuum this temperature is much more difficult to reach, and it was found that placing oxygen-free high conductivity (OFHC) Cu shim stock inside the hole of the SS block creates greater surface contact area so that the SS block can remove the heat away from the cartridge heater, allowing the heater to reach higher temperatures without electrically shorting. Another necessity was to backfill the chamber with an exchange gas, which can also transfer heat from the heater to the SS block. Combining these two effects allows the temperature to easily be raised to 550 $^{o}$C, and if necessary can reach up to 600 $^{o}$C. The sample (G) sits on top of a 0.1 mm thick layer of mica which is on top the of the SS block providing electrical insulation but the mica is also thin enough where it can be assumed that the sample temperature is the same as that of the heating block. To ensure the sample is thermally connected to the heating block, it is mechanically pressed down onto the block from above with a thin, 1/16" diameter, alumina rod (F) in a tungsten screw (C), which applies enough force to ensure good thermal contact but not enough to fracture the sample. The rod is thin and of low thermal conductivity which means heat flow out of the sample through the rod should be negligible.

The temperature is read and controlled by a PXR 4 (PID) temperature controller from Fuji Electric to which both the heater and K-type thermocouple are connected. The PXR 4 allows the rate at which the temperature is increased or decreased to be accurately controlled. Temperature is simultaneously read using a NI 9211 data acquisition system

from National Instruments. The resistance is read using the 370 AC Resistance Bridge from LakeShore which uses an alternating current (AC) of 13.7 Hz. A LabVIEW program records the temperature (NI 9211), resistance (LS 370), time, and allows the user to set the frequency at which data is recorded. Unless otherwise noted, data is recorded roughly once every second.

Resistivity measurements can be made either using a four-point probe method on a bar shaped sample, or the Van der Pauw (VDP) technique [6]. The use of four probes negates any concerns about contact resistance [7-8]. The current used is AC with a frequency of 13.7 Hz which is sufficient to negate any voltage build up due to the Peltier and Seebeck effects [7]. The Peltier effect is due to the fact that when current flows from the current wire to the sample and out of the other current wire, heat is liberated at one junction and absorbed at the other due to the Peltier effect. This in turn will create a temperature gradient, which will give rise to a voltage due to the Seebeck effect. When a direct current (DC) is used one must take this into consideration and switch the direction of the current to average out the excess voltage. However, the Peltier effect takes a finite amount of time to manifest itself which is usually on the order of 1 second [8]. So when an AC current is used, there is no concern of an excess voltage caused by thermoelectric effects.

For a bar shaped sample the resistivity is obtained from $\rho=RA/L$ where $R$ is the resistance, $A$ is the cross sectional area, and $L$ is the voltage lead separation. The placement of voltage leads always satisfies the ratio $2w < L_s - L$ where $w$ is the thickness of the sample, $L_s$ is the length of the sample and $L$ is the voltage lead separation which ensures uniformity of the electric field, or one dimensional current flow, at the voltage

leads [7].

The Van der Pauw technique can be used to measure a sample of any arbitrary shape as long as the sample is flat and is singly connected, meaning it does not contain any holes [6,9]. The resistivity is given by the expression [6,9-10]

$$\rho = \frac{t\pi}{\ln(2)} \frac{\left(R_{12,34} + R_{23,41}\right)}{2} F \qquad (2.1)$$

where $R_{12,34}$ is defined as the current flowing between points 1 and 2 while the voltage is read between points 3 and 4 (inset Figure 1), $R_{23,41}$ has the current between points 2 and 3 with voltage read between 1 and 4, $t$ is the thickness of the sample, and $F$ is a correction factor that is a function of the ratio $R_r = R_{1234}/R_{2341}$ which can be solved graphically and is given by [10]

$$\frac{R_r - 1}{R_r + 1} = \frac{F}{\ln(2)} \operatorname{arccosh}\left(\frac{\exp[\ln(2)/F]}{2}\right) \qquad (2.2)$$

Because thermoelectric materials have no widely accepted standard at high temperature (NIST only recently developed a low temperature standard [11]), it is imperative to accurately understand and account for any sources of error in the measurement so that data can be more accurately understood and communicated among research groups. The error bars for bar shaped samples from the propagation of independent errors are given by [12]

$$\frac{\sigma(\rho)}{\rho} = \sqrt{\left(\frac{\sigma(R)}{R}\right)^2 + \left(\frac{\sigma(L)}{L}\right)^2 + \left(\frac{\sigma(A)}{A}\right)^2} \qquad (2.3)$$

The error bars displayed for the Van der Pauw method are given by

$$\frac{\sigma_{VdP}(\rho)}{\rho} = \sqrt{\left(\frac{\sigma_{VdP}(R)}{R}\right)^2 + \left(\frac{\sigma(t)}{t}\right)^2} \qquad (2.4)$$

where

$$\sigma_{VdP}(R) = \sqrt{\sigma(R_{12,34})^2 + \sigma(R_{23,41})^2} \qquad (2.5)$$

The resistance values at each temperature are binned every one degree which gives the value of $\sigma(R)$ in Equation 2.3 from [12]

$$\sigma(R)_{st.dev.} = \sqrt{\frac{1}{N-1}\sum_{i=1}^{N}(R_i - \overline{R})^2} \qquad (2.6)$$

where $\overline{R}$ is the average resistance and $N$ is the total number of measurements taken. It should be noted that Equation 2.1 is written under the assumption that the size of the contact points are infinitesimal and the contacts are made directly on the edge of the specimen. In reality the wire will always have some finite thickness and it is not possible to place the wire exactly on the edge of the sample, leading to additional error. This error

is very difficult to quantify but should not be too large as long as care is taken in wire placement [13]. Therefore it is not taken into account in the expression for the error given in Equation 2.4, but should always be kept in mind.

### 2.2.2. Results and Benchmarking

Figures 2.2 and 2.3 show resistivity data while the temperature is increased in two different modes, discrete and continuous, for constantan and Ni respectively. Constantan is measured at discrete temperatures for a period of time on a bar shaped sample of dimensions 2 x 2 x 14 $mm^3$. The resistance values at each temperature are binned which gives the value of $\sigma(R)$ in Equation 2.3. It can be seen that the data measured by the constructed setup matches within 1% of the data taken by the ZEM-3 (ULVAC) on the standard constantan bar provided by ULVAC. The Ni data in Figure 2.3 is measured on a flat square shaped sample of dimensions 16 x 16 x 2 $mm^3$ using the Van der Pauw technique. The temperature was increased continuously from 20-550 $^oC$ at a rate of 1 $^oC$/min to measure $R_{12,34}$. The sample was then cooled and wires reconfigured to measure $R_{23,41}$. The sample was again measured while the temperature was increased at 1 $^oC$/min. Resistance values were binned every degree to obtain the standard deviation. Though no error bars are expressed for the literature data, the agreement is within our experimental uncertainty up to temperatures of 375 $^oC$. The deviation at higher temperatures never exceeds 6%, but is in very good agreement. And the fact that it is not exact is not unexpected as it has been noted that the resistivity of Ni is very dependent on the sample purity [14]. The ferromagnetic transition temperature [15], which should not be as dependent on sample purity as the absolute resistivity value, is in very good agreement

with the literature. The transition takes place at 355.5 $^{o}$C according to the literature [15], while the measurement here gives a transition temperature of 354 $^{o}$C which is well within the industrial error of 0.75% given for K-type thermocouples by Omega Engineering Inc.

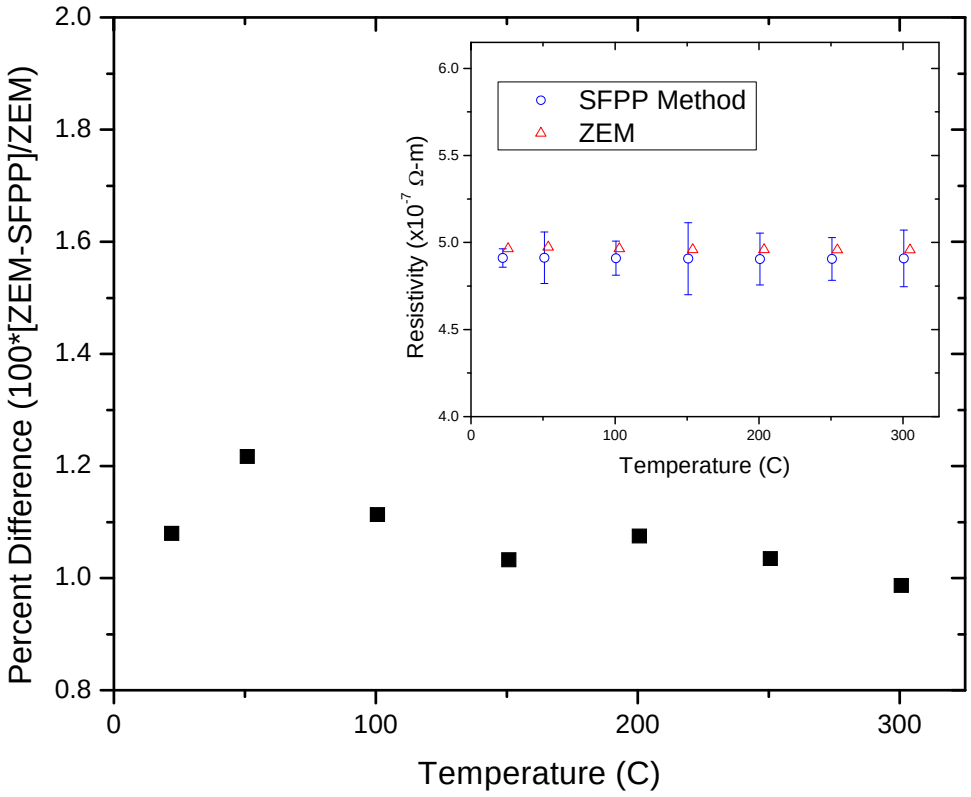


Figure 2.2: The percent error is plotted with data obtained from measurements made on the same standard bar shaped sample using a standard four point probe (SFPP) technique in the setup shown in Figure 2.1 as well as the commercially available ZEM-3. The inset shows resistivity of constantan plotted versus temperature along with uncertainty calculated from Equation 2.3 demonstrating agreement between both systems with the standard.

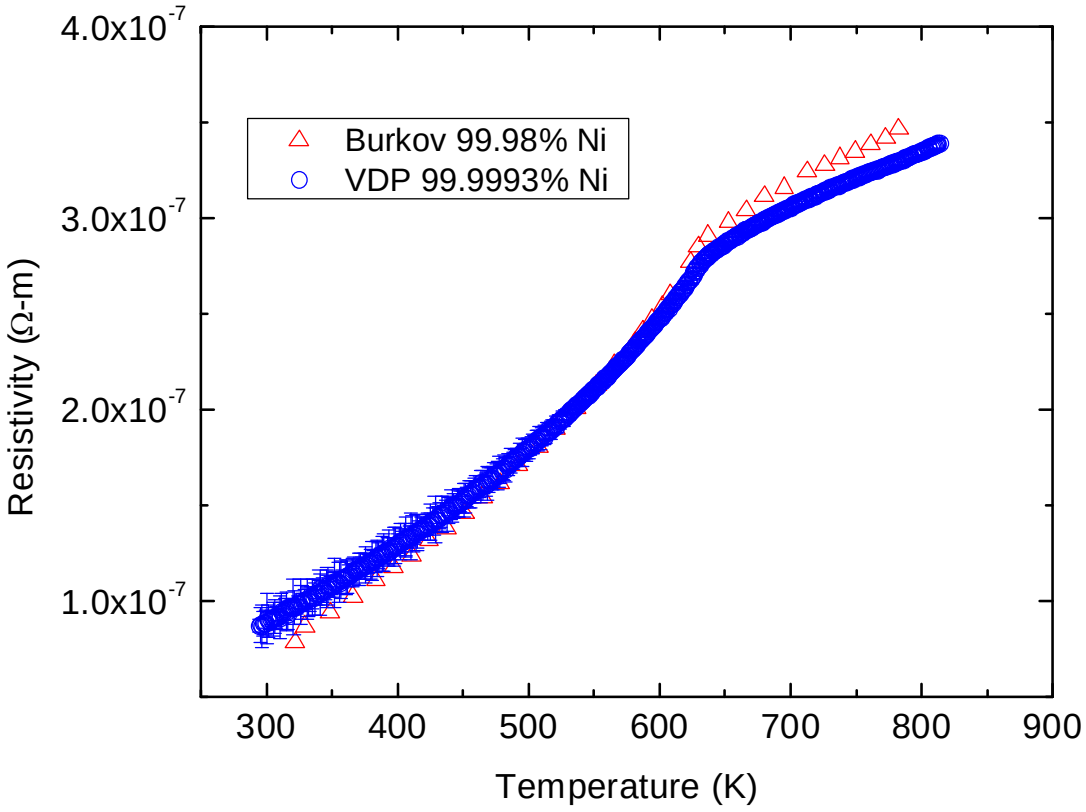


Figure 2.3: Resistivity of nickel is plotted against temperature. Measurements were made using the Van der Pauw technique on a sample of 99.9993% purity from AJA International, Inc. Values obtained from ref. [13] for Ni of 99.98% purity are shown for comparison.

Several other thermoelectric samples were run in order to validate the accuracy of the machine. These data are not included here but are presented in Appendix A, however the results are summarized. For bar shaped samples where the same exact bar was measured in both the above setup as well as the ZEM-3, disagreement never exceeds 3% which is within the experimental uncertainty of the above system. The difference for Van der Pauw measurements never exceeds 9%, however if the ZEM is given an uncertainty of 3%, which is commonly used, there is again agreement within experimental error. There are several possible reasons for a greater disagreement in Van der Pauw

measurements, but there are two that are most probable. The first is the fact that the resistivity is being compared between two different samples. One is a thin disk used for Van der Pauw measurements, while the other is a bar that is not cut from the same exact disk used for VP measurements; the ZEM can only measure bar shaped samples, and there can be slight variation among transport measurements of different samples of the same TE material. The second reason is due to the aforementioned effects of finite contact size and probe placement near the edge, so the difference noted above is not unexpected.

## 2.3.Seebeck Coefficient Measurement

### 2.3.1. Construction

The measurement of the Seebeck coefficient in theory is the simplest transport measurement to make, requiring only the measurement of two temperatures and a voltage. In reality, however, the measurement at high temperatures is difficult due to the inaccuracy in determining the temperature. Because solder cannot be used at high temperature, there will always be some form of thermal contact resistance which will make the temperature being read greater than the actual temperature at the sample surface. In turn this will lead to the reading of a larger temperature gradient than what the sample is actually experiencing, thereby making a larger $\Delta T$ and so a smaller value of $S$. It has been experimentally demonstrated that solder negates almost any effect of thermal contact resistance, however solder at higher temperatures cannot be used. If thermal contact resistance could be calculated, it could be subtracted out, though trying to accurately model or account for the thermal contact resistance is quite a difficult task

[16].

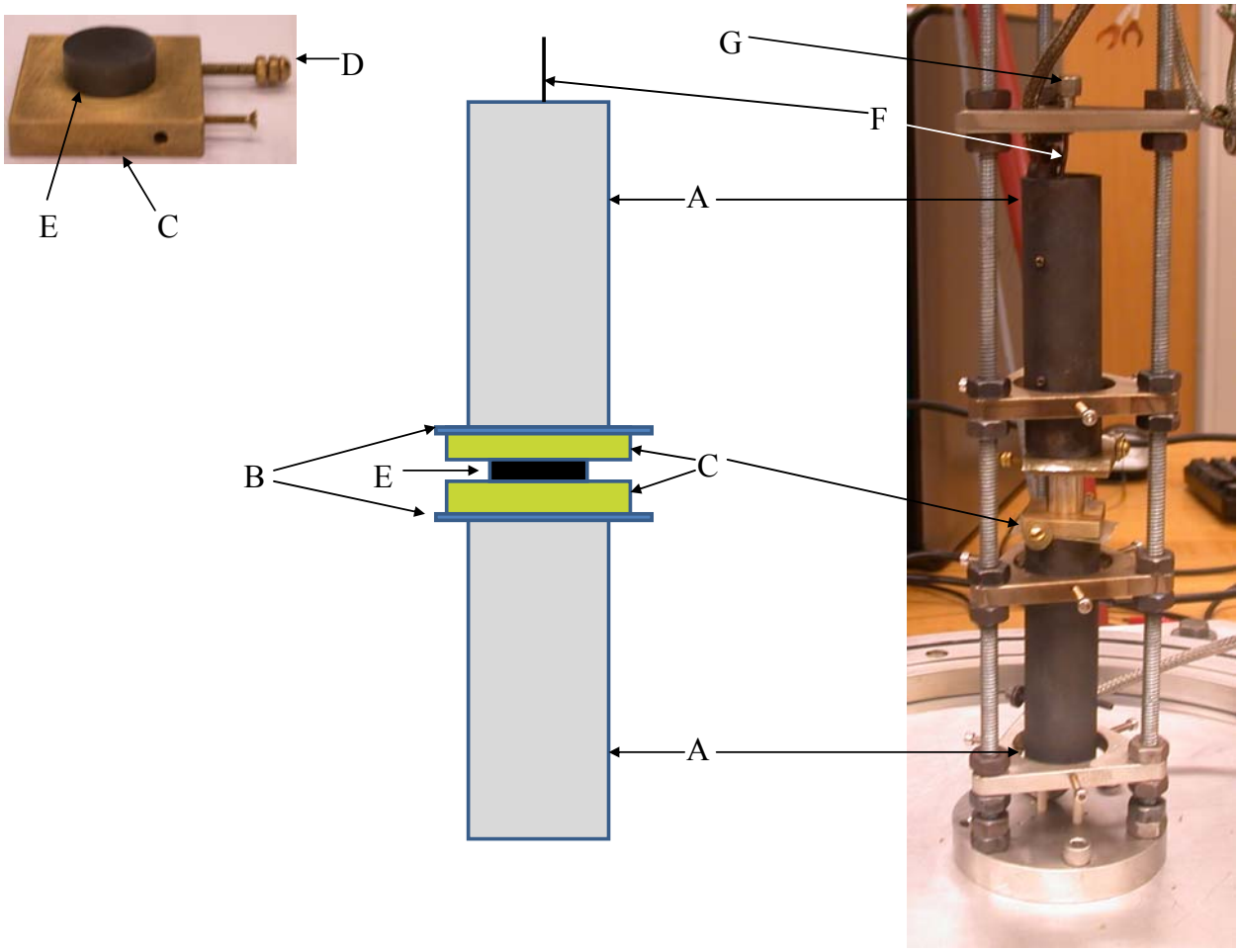


Figure 2.4: Actual picture along with a schematic diagram of the high temperature Seebeck setup.

The setup is run in the same vacuum chamber as the resistivity setup described in the previous section. Figure 2.4 shows both a schematic as well as a picture of the actual setup. The temperature is provided by a 3" long 3/8" diameter cartridge heater from Omega industries which is housed in a 1" diameter 3" long SS block (A). Again, as in the resistivity block, the vacuum chamber needs to be backfilled with an exchange gas and OFHC shim stock is used to create better thermal contact between the cartridge heater and the SS block. The SS block is separated from the contact via a thin layer of mica (B). This ensures that the SS block is electrically isolated from the electrical

contact (C) and therefore will have no effect on the voltage reading. The electrical contact is made out of brass and houses the thermocouple, which reads the temperature, as well as the Cu wire for the voltage measurement. A 30 gage N-type thermocouple wire is used to read the temperature and the thermocouple wire is embedded inside a hole in the brass and is electrically isolated from the brass contact through the use of a non-conducting high temperature epoxy, Omega 600, from Omega Industries. N-type thermocouple wire is used because it has the same operating temperature range as K-type thermocouple wire without concern of the effects of "green rot". Since there is no concern of green rot, thin thermocouple wire can be used which negates concern of any conductive heat loss out from the contact through the wires. Electrical connections are made to the brass contact by mechanically connecting 24 gage copper wire to a screw (D) specially fabricated out of OFHC copper that can screw directly into the brass block. By making both the wire as well as the screw out of copper, the thermoelectric loop created is simplified as shown in Figure 2.5. From elementary thermocouple loop analysis the total voltage can be expressed as [5],

$$V = S_{Cu}(T_H - T_o) + S_s(T_C - T_H) + S_{Cu}(T_o - T_C) = (S_{Cu} - S_s)(T_H - T_C) \qquad (2.7)$$

where $S_{cu}$ and $S_s$ are the absolute Seebeck coefficients of the Cu wire and the sample, respectively. The measurement yields the relative Seebeck coefficient with respect to the Cu wire. In order to obtain the absolute Seebeck coefficient of the sample, the well known absolute Seebeck coefficient of Cu can be subtracted [5]. The brass contacts are separated from the sample by a thin layer of conducting carbon foil (not shown). The foil

is necessary to prevent diffusion of Cu from the brass into the TE sample; Cu is known to be highly diffusive in several TE materials [17]. The carbon foil serves a secondary purpose of creating better thermal contact with the sample [16], which should decrease error in the determination of the temperature and therefore the Seebeck coefficient. Finally force is applied from the top by firmly pressing the heating block against the contact onto the sample (E). Increasing the applied force is known to decrease thermal resistance [16]. The force is applied by a 1/16" SS pin (F) which slides into both a ¼" screw (G) and the circular SS heating block, both of which have grooves machined in them for the pin to fit snuggly. The setup is aligned via external SS support rods.

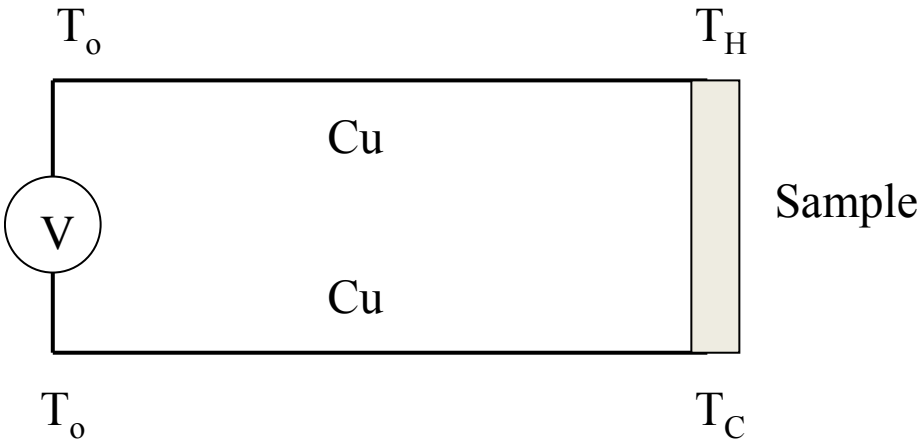

Figure 2.5: Simple schematic of how the Seebeck coefficient of a thermoelectric sample is measured relative to the Cu wire.

### 2.3.2. Results and Benchmarking

The voltage is measured by applying a static temperature gradient where a voltage is recorded at several different temperature gradients, with the average temperature being the sample temperature. The voltage is then plotted against the temperature and the slope of the line yields the relative Seebeck coefficient given by Equation 2.7. For each

temperature gradient, a total number of roughly 1000 data points were collected from which an average $T_H$, $T_C$, and $V$ are obtained with a standard deviation given by Equation 2.6. An example of a series of temperature gradients and a plot of $\Delta V/\Delta T$ are given in Figure 2.6. It is evident that the error bars are quite small due to the large number of points taken, however these error bars are not the actual uncertainty of the system. In order to measure the uncertainty in repeatability, a constantan sample was run on five different dates and the standard deviation calculated using Equation 2.6 was used to get an error bar of 3%.

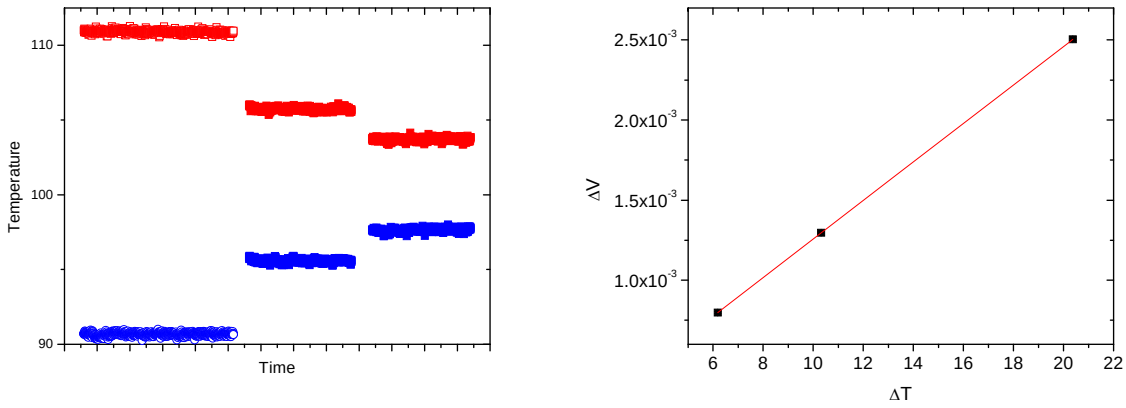


Figure 2.6: The left plots temperature as a function of time. It is seen that the temperature gradient remains constant over the time period. The two temperatures along with the voltage are averaged and plotted on the right. The slope of the ΔV/ΔT plot yields the Seebeck coefficient relative to the Cu wire.

Figure 2.7 shows the Seebeck coefficient, measured and calculated using the method described above, of $CoSb_3$ and constantan. The $CoSb_3$ sample was run on two separate occasions and the results agree within the 3% uncertainty as well as within the 7% error bar from the ZEM-3 system. This is excellent agreement and demonstrates the functionality of the setup. On the right is a plot of the Seebeck coefficient of constantan. From the plot it is evident that the difference exceeds the combined error bars of the ZEM and the apparatus, though it should be noted that the difference is constant over the entire

temperature range. Other "good" thermoelectric materials agree very well with the ZEM data and are presented in Appendix A.

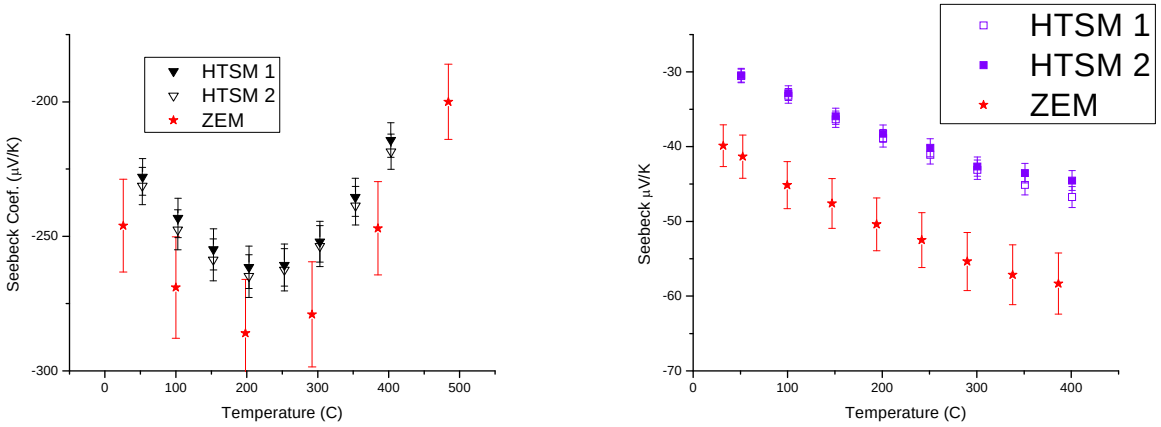


Figure 2.7: The Seebeck coefficients of $CoSb_3$ (left) and constantan (right) are plotted with temperature and compared to the ZEM-3 system.

Here a "good" thermoelectric is defined as having high S and low κ. However when trying to measure metals, or materials with a low Seebeck coefficient and high thermal conductivity, the system shows a deviation from the ZEM; the ZEM value directly matches literature values for constantan. The difference is due to thermal contact resistance as was previously mentioned. Thermal contact resistance is a complex function of $\kappa_{sample}$, $\kappa_{contact}$, exchange medium, pressure, surface area, hardness, surface roughness, etc [16]. In an attempt to try to account for thermal contact resistance the brass contacts were replaced by SS contacts because brass is very soft and dented when pressure was applied to the harder materials which made knowing the contact surface area impossible. Constantan was run using the SS contacts and the data is shown in Figure 2.8. It is obvious that the measurement with SS contacts does not show the constant difference that the brass contacts show. Since brass has a constant value for $\kappa$ over the entire range of measurement, it is believed that this is where the difference lies.

An attempt was made to use the model set forth by Ref. 16 to calculate the thermal contact resistance and correct for it, however this was unsuccessful. Further evidence for the fact that thermal contact resistance is leading to errors in the measurement can be seen in the fact that the maximum temperature that can be reached is 150 $^{o}$C less in the Seebeck setup than in the $\rho$ setup using the same cartridge heater. The heat has to pass through more interfaces and therefore has a greater thermal resistance.

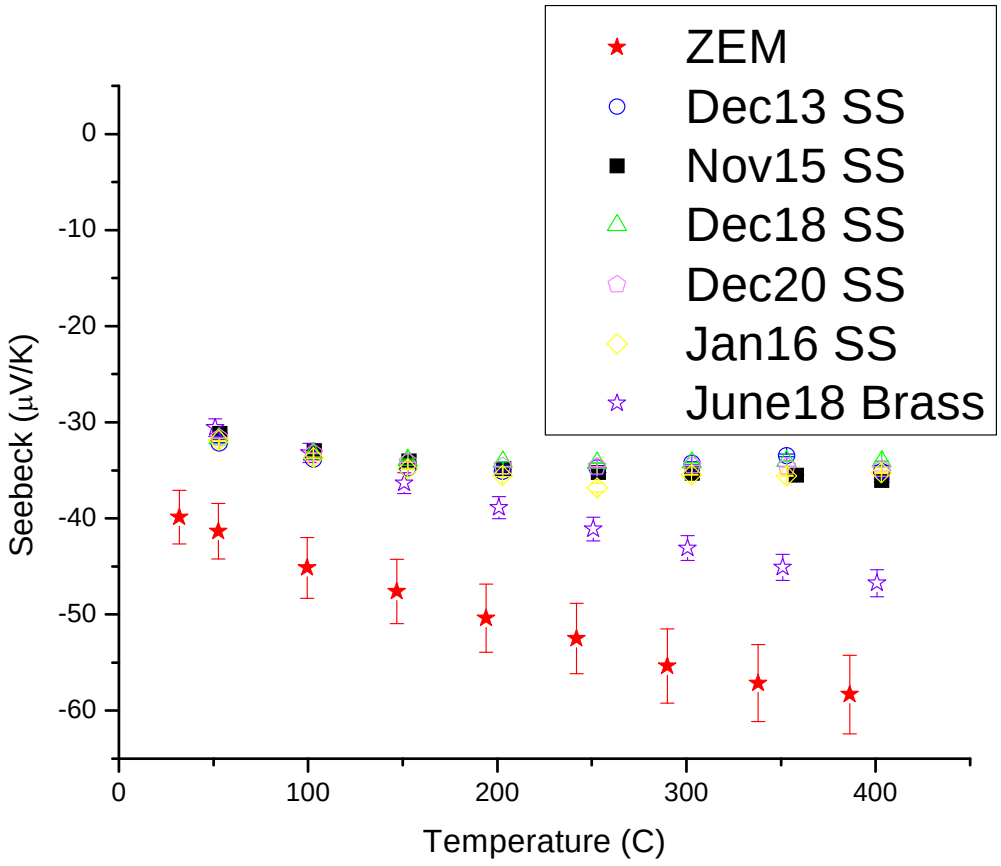


Figure 2.8: The Seebeck coefficient of constantan measured using SS contacts as well as brass contacts and compared to the ZEM. The system shows precision with the SS contacts, however accuracy is sacrificed due to the varying value of the thermal conductivity for SS.

The difference between measured values using the described apparatus and commercially available equipment is negligible for thermoelectric materials with a high

Seebeck coefficient. If this system is required to measure TE materials with a low thermopower, the measurement can be corrected to comparisons with commercially available equipment if the brass contacts are used. This method is used and has been used by Xu, *et al.* to correct a commercial system to a homebuilt system [18].

## 2.4. Apparatus Uses

The systems described above show specific advantages over other equipment. The most apparent are the ability to make continuous measurements. This capability allows a more accurate study of phase transitions, also shown in Appendix A for $Cu_2Se$, and *in situ* annealing and thermal stability measurements found in Appendix D. Both setups have the advantage of being able to measure arbitrary shapes as seen in the Van der Pauw method for $\rho$ and the fact that only two flat surface are required to measure $S$; this is opposite to the ZEM which has very strict requirements on the size and shape of the sample being rectangular, typically 2 x 2 x 12 $mm^3$. The final advantage is that the setup gives a secondary measurement that can be a confirmation of other measurements. This is especially important in thermoelectrics where as discussed before there is a lack of standard methodologies and reference materials to give confidence in a measurement. A secondary measurement gives much higher confidence in newly studied transport properties of TE materials.

## 2.5. References

1. M. S. Dresselhaus, G. Chen, M. Y. Tang,R. Yang, H. Lee, D. Z. Wang, Z. F. Ren, J. P. Fleurial, P. Gogna, Adv. Mater. **19**, 1043–1053 (2007).
2. G. J. Snyder, E. S. Toberer, Nature Materials. **7**, 105-114 (2008).
3. D. T. Morelli, Fifteenth Int. Conf. Thermoelectrics. 383-386 (1996).
4. D. Kraemer, B. Poudel, H. P. Feng, J. C. Caylor, B Yu, X. Yan, Y. Ma, X. Wang, D.Z. Wang, A. Muto, K. McEnaney, M. Chiesa, Z. F. Ren , G. Chen, Nature Materials. **10**, 532–538 (2011).
5. T. W. Kerlin, Practical Thermocouple Thermometry (Ins. Society of America, 1999**)**.
6. L. J. van der Pauw, Phil. Tech. Rev. **20**, 220-224 (1958).
7. T. M. Tritt, Recent Trends in Thermoelec. Mat. Research I. (Academic Press, Boston, 2001**)**.
8. D. M. Rowe, CRC Handbook of Thermoelectrics (CRC Press, New York, 1995**)**.
9. L. J. van der Pauw, Phil. Res. Rep. **13**, 1-9 (1958).
10. D. K. Schroder, Semicon. Mat. Device Charac. (John Wiley & Sons, Inc, New York, 1998**)**.
11. N. D. Lowhorn, W. Wong-Ng, Z. Q. Lu, E. Thomas, M. Otani, M. Green, N. Dilley, J. Sharp, T. N. Tran, Applied Physics A. **96**, 511-514 (2009).
12. J. R. Taylor, An Intro. to Error Analysis (University Science Books, Sausalito, 1997**)**.
13. R. Chwang, B. J. Smith , C. R. Crowell, Sol. St. Electron. **17**, 1217-1227 (1974).
14. T. Burkov, A. Heinrich, P. P. Konstantinov, T. Nakama, K Yagasaki, Meas. Sci. Technol. **12**, 264 (2007).

15. T. G. Kollie, Phys. Rev. B.**16**, 4872 (1977).

16. E. G. Wolff and D. A. Schneider, Int. J. of Heat and Mass Transfer. **41**, 3469 (1998).

17. D. M. Rowe, Thermoelectrics Handbook: Macro to Nano (Taylor & Francis, New York, 2006).

18. H. Xu, K.M. Kleinke, T. Holgate, D. Rossouw, G. Botton, T.M. Tritt, Kleinke, J. Alloys and Compounds.**504**, 314 (2010).

# Chapter 3: Low Temperature Measurements – Physical Properties Measurement System (PPMS)

## 3. Introduction

This chapter gives a brief overview of how the transport properties of the TE materials were measured for this thesis in the low temperature regime (2 – 350 K). A more in depth account is given of how the system was utilized in a slightly modified manner in order to separate the lattice and electronic portions of the thermal conductivity; this work has been published in *Physical Review B* and can be found in Appendix D.

## 3.2 Quantum Design Physical Properties Measurement System

The PPMS is a commercially available system that enables accurate materials characterization and is pictured in Figure 3.1. In this work the PPMS was used to determine the electrical resistivity, thermal conductivity, Seebeck coefficient, Hall coefficient, carrier concentration, carrier mobility, and magnetic susceptibility. The PPMS can operate in a temperature range of 2 – 400 K and with magnetic fields up to 9 T. The system accuracy was previously benchmarked [1], and in depth descriptions of the system can be found elsewhere [2-5]. The measurements made to determine TE material properties in this work are briefly described.

Figure 3.1: Picture of commercially available Physical Properties Measurement System (PPMS) from Quantum Design.

3.2.1 Thermal Transport Option

Thermoelectric properties S, ρ, and κ were measured, in the standard two probe method, from 5 to 350 K using the thermal transport option of the PPMS. Detailed descriptions of the system are described elsewhere [2]. Samples for the thermal transport option were cut with typical dimensions 2 x 2 x 4 mm. Samples were polished, chemically etched in a Bromine solution, and metallic contacts were sputtered onto the faces. Gold-coated OFHC (oxygen free high conductivity) copper disks provided by Quantum Design were soldered to the sputtered metallic contacts on the sample using Sn–Pb solder. An image of a typical sample is shown in Figure 3.2.

Figure 3.2: Image of a sample measured using the Thermal Transport Option of the PPMS.

### 3.2.2 AC Transport Option

The Hall coefficient, $R_H$, was also determined using the PPMS, under a magnetic field of 9 T and a current of 20 mA. Hall samples were rotated by $180^o$ in field using the PPMS AC Transport Rotator option, thereby allowing the field direction to be switched, thus averaging out any anomalous effects on the measurement due to the magnetic field. These samples were prepared in a five wire Hall configuration with typical dimensions 1 x 3 x 11 mm where 1 mil Pt wire was spark welded to the samples. Figure 3.3 shows a typical Hall sample. The carrier concentration was determined directly from the Hall coefficient using the relation $n = a_o/R_Hq$ where q is the electronic charge and $a_o$ is the Hall factor; we assume the Hall factor to be 1 in this work. Resistivity, $\rho$, was measured using a standard four point probe technique, with the same sample and orientation used to attain the Hall coefficient, and the mobility, $\mu_H$, was calculated from $R_H/q$.

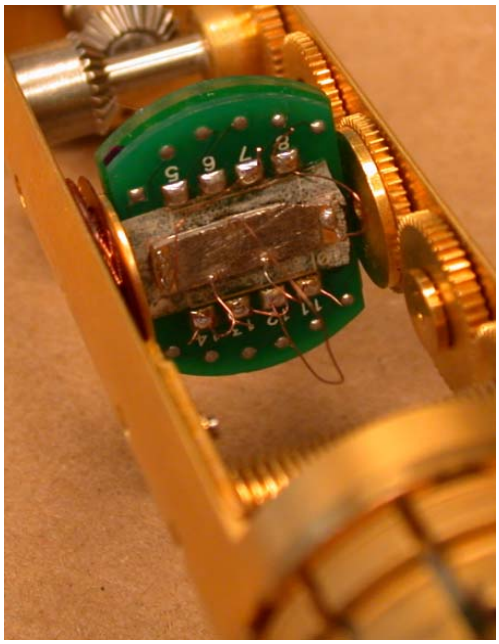

Figure 3.3: Image of a Hall sample on the AC Transport Rotator.

### 3.2.3 Homemade Torque Cantilever Magnetometer

A homemade torque cantilever magnetometer was constructed and used to qualitatively determine the inclusion of magnetic impurities in the samples. Figure 3.4 shows the image of the magnetometer. It is a capacitive based measurement based on the pioneering technique of Brooks [31], where one face of a parallel plate capacitor is the circular paddle, while the other is the large square plate. The sample is placed on the circular paddle where a torque, $\tau$, is created by the cross product of the magnetic moment in the sample, $\mu$, with the magnetic field, B. Since $\tau = \mu \times B$, the paddle will move which is measured as a change in the capacitance.

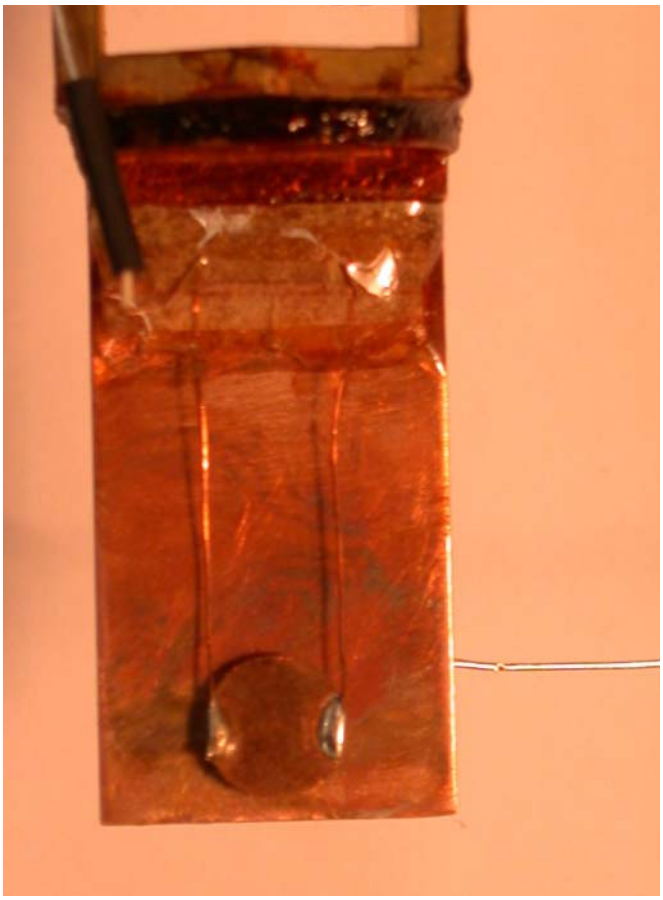

Figure 3.4: Homemade torque cantilever magnetometer. The square Cu plate is one face of a parallel plate capacitor while the circular Cu paddle is the other.

### 3.2.4 Vibrating Sample Magnetometer Option

To try to obtain a more quantitative analysis of the magnetic impurities, the susceptibility was measured using the vibrating sample magnetometer (VSM) option in the PPMS in a field of 0.1 T. Measurements were made at Los Alamos National Laboratory and the National Magnet Lab in Florida as we do not have a VSM option at Boston College. The details of the measurement can be found elsewhere [4].

## 3.3 Separation of $\kappa_{lattice}$ and $\kappa_{electronic}$

The determination of the Lorenz number is an important aspect in thermoelectric

research due to the fact that *ZT* enhancement is being realized through the reduction of thermal conductivity, specifically focusing on reducing the lattice portion of the thermal conductivity. The total thermal conductivity is given by

$$\kappa_{total} = \kappa_{carrier} + \kappa_{lattice} \qquad (3.1)$$

where $\kappa_{carrier}$ and $\kappa_{lattice}$ are the contributions to the thermal conductivity from the carriers and the lattice, respectively. Since only the total thermal conductivity can be measured, the contributions must be separated in some way. This is done using the Wiedemann-Franz Law and by defining a Lorenz number (L), which is the given by

$$L = \frac{\kappa_{carrier}}{\sigma T} \qquad (3.2)$$

where $\sigma$ is the electrical conductivity and T is the absolute temperature. In metals the Lorenz number can be determined by measuring the electrical conductivity and total thermal conductivity at a given temperature, from which the Lorenz number is calculated using Equation 3.2. This method is only useful in metals where the total thermal conductivity is approximately equal to $\kappa_{carrier}$. For the classical free electron model the Lorenz number is given as $2.44 \times 10^{-8}$ $V^2K^{-2}$[6]. It is important to note that the Lorenz number, as described by the free electron model, is not an accurate value for most materials and in a given material depends on the detailed band structure, position of the Fermi level, and the temperature; for semiconductors this relates to the carrier

concentration. Therefore, when $\kappa_{lattice}$ and $\kappa_{carrier}$ become comparable to each other, there must be a method for differentiating between the two components of $\kappa_{total}$. To date the separation of the two components has been accomplished through calculation by approximating the Lorenz number, and hence the carrier contribution, through various different formalisms [6,8-9]. Determinations of the Lorenz number have also been made experimentally [6], however there are few.

In order to separate $\kappa_{lattice}$ and $\kappa_{carrier}$ experimentally, two approaches have been used to determine the Lorenz number. Both methods utilize a transverse magnetic field in order to suppress the electronic component of the thermal conductivity. One approach uses a classically large magnetic field, while the other is performed in intermediate fields. A classically large magnetic field is described as $\mu_H B >> 1$ where $\mu_H$ is the carrier mobility and B is the magnetic field [1]. When this limit is reached, the electronic component of $\kappa$ is completely suppressed, so that the measurement yields only the lattice portion of the thermal conductivity, from which $\kappa_{carrier}$ and hence the Lorenz number can be calculated using equations 3.1 and 3.2.

Very often it is difficult to reach a classically large field, making this type of measurement not possible and therefore other methods have been developed for determining L. For example, Goldsmid et al. developed a Magneto-Thermal Resistance (MTR) method for extracting the Lorenz number at lower magnetic fields, specifically in the region where $\mu_H B \approx 1$ [10-13]. In the MTR method the sample is kept at a constant temperature while the field is varied. In this case both the electrical conductivity as well as the total thermal conductivity will change with the field due to the Lorentz force acting on the carriers, which is induced by the transverse magnetic field. Equation 3.1 can be

rewritten in the form

$$\kappa(B)_{total} = LT\sigma(B) + \kappa_{lattice} \qquad (3.3)$$

where now both κ and σ are dependent on magnetic field. It is noted that κ, σ, and L are all tensors, whose off diagonal components can have a non-negligible contributions in magnetic field [10,14]. Both σ(B) and κ(B) are measured along the same direction, which we define as $\sigma_{xx}$(B) and $\kappa_{xx}$(B). For an anisotropic sample, even to first order, the magnetic field affects the diagonal terms of the tensors as well as the non-diagonal terms. We show that by measuring only the diagonal terms we are able to extract the Lorentz number $L_{xx}$, which relates the $\sigma_{xx}$(B) and $\kappa_{xx}$(B). The reason behind the validity of this method is that both $\sigma_{xx}$(B) and $\kappa_{xx}$(B) have a similar magnetic field dependence and their ratio has only a weak dependence on the off-diagonal terms. Since the samples are isotropic [15] and extrinsic, it is assumed that off diagonal terms can be neglected because thermogalvanomagnetic effects are only dominant in intrinsic materials with a proportional number of positive and negative charge carriers [9,16]. As long as both have the same functional form with respect to the magnetic field, then $\sigma_{xx}$(B) vs. $\kappa_{xx}$(B) will have a linear relationship and the Lorenz number $L_{xx}$ at a given temperature can be directly taken from the slope as given in Equation 3.3. It is important to note that the analysis throughout this paper is based on the assumption that the Lorenz number is independent of magnetic field, which is true for some materials, but in general is not a valid assumption [17-19]. Analogous approximations have been used to study similar compounds in the past [11,17].

Neither method has been extensively used due to the fact that there are restrictions on the materials that can be measured because there must be a significant carrier contribution to the total thermal conductivity; also the experimental setup is rather difficult to realize [6,10-14]. The advent of the Physical Properties Measurement System (PPMS) from Quantum Design makes the experimental setup and measurement readily possible for either method. The purpose of this chapter is to present experimental techniques for the determination of the Lorenz number from which both the electronic and lattice contributions to the thermal conductivity can be directly extracted. Measurements are compared to literature values as well as simple model calculations. There are several different ways to analyze the raw experimental data; two different models will be used here and shown to yield similar results. The measurements are performed below 150 K so that bipolar terms will be negligible and therefore equations 3.1 and 3.3 accurately describe the contributions to the total thermal conductivity. While this technique has been used before, to the best of our knowledge, this experimental method has not previously been demonstrated on nanostructured thermoelectrics.

### 3.3.1 Experimental

Samples were prepared by combining the proper stoichiometric ratios of Cu (99.999%, Alfa Aesar), Bi (99.999%, Alfa Aesar), Te (99.999%, Alfa Aesar), and Se (99.999%, Alfa Aesar) for $Cu_{0.01}Bi_2Te_{2.7}Se_{0.3}$, while $Bi_{0.88}Sb_{0.12}$ was prepared with Bi (99.999%, Alfa Aesar) and Sb (99.999%, Alfa Aesar). Samples were then ball milled and hot pressed using dc hot-pressing techniques [15]. Metallic contacts were sputtered onto

the surfaces so that electrical contacts could be soldered to the sample.

MTR measurements were performed using the Thermal Transport Option (TTO) of the PPMS in which the sample was placed in an orientation where the magnetic field was perpendicular to the heat flow. A standard two point method was used for thermal conductivity and Seebeck coefficient (S) measurements with typical sample dimensions of 2 x 2 x 3 $mm^3$. In this case the temperature was held constant at 100 K and measurements were made while the field was swept over a range of 0.1 – 5 T. Since resistivity, ρ, values in a magnetic field are required, a four point technique must be used which was accomplished with the AC Transport option on a different sample of dimensions 1 x 2 x 12 $mm^3$ for the same temperature and field range. Since a four point technique is used, there is no concern of electrical contact resistance. For thermal contact resistance, our previous measurements show no difference in the thermal conductivity when a two or four point method is used which is included in Appendix C. Even so, any thermal contact resistance is assumed to be negligible in field and since we are looking at the change in thermal conductivity with field, there should be no influence on the slope (L) of the measurement. Geometrical effects on the magnetoresistance are considered to be negligible because the sample used for resistivity measurements in field has the appropriate aspect ratio. The sample dimensions for the thermal magnetoresistance measurements are restricted due to requirements to fit into the PPMS, however it is assumed there is a negligible contribution because there was no evidence previously of geometrical effects on a similar material which had an aspect ratio of 1 [17]. Error for the MTR measurements of L and $\kappa_{lattice}$ were calculated from the standard deviation and propagation of error, and determined to be 3% and 7% respectively. Hall measurements

to determine the mobility ($\mu_H$) from which the scattering factor (r) is obtained were made using the PPMS on the same sample as the four point ρ measurement.

When determining the Lorenz number in a classically large field, the Thermal Transport Option of the PPMS in which the magnetic field was perpendicular to the heat flow was again used. A standard two point method was used for all transport measurements on the same sample. The sample was run in magnetic fields of 0, 6, and 9 T. Only the thermal conductivity measurements in field are used, while electrical resistivity values are taken from the zero field data. Typical sample dimensions were 2x4x2 $mm^3$. Thermal contact resistance is assumed to be negligible for the reasons stated above, and electrical contact resistance is negligible from the comparison of two and four point resistivity measurements. There is no concern of geometrical effects on thermal conductivity measurements because saturation would not be obtained at higher magnetic fields. The measurements were performed over a temperature range of 5-150 K, with error for L and $\kappa_{lattice}$ being 2% and 6% respectively determined from the standard deviation and propagation of error.

### 3.3.2 Results

The MTR approach can be used only if the thermal and electrical conductivities have the same functional form with respect to the magnetic field. Since the MTR method is used in intermediate fields, or when $\mu_H B \approx 1$, only values in magnetic fields from 0.8 – 5 T were used, anything below 0.8 T was too low of a field. The top left inset in Figure 3.5 plots κ as a function of field while the lower right inset plots σ as a function of field

for $Cu_{0.01}Bi_2Te_{2.7}Se_{0.3}$. Both the electrical and thermal conductivity vary with field as $\frac{aB^2}{1+cB^2}$ where a and c are constants, which is valid for strong degeneracy [7, 21-22]. The fits are shown in the insets of Figure 3.5 along with the measured values. Figure 3.5 can be fit linearly and taking the slope yields LT in equation 3.3 from which we get L = $2.16 \times 10^{-8}$ $V^2K^{-2}$ by dividing by T = 100 K. The lattice portion of the thermal conductivity is given by the y-intercept and gives $\kappa_{lattice}$ = 1.49 W/mK. Care should be taken with the determination of $\kappa_{lattice}$ this way because a larger error is induced when extrapolating over six orders of magnitude to get $\kappa_{lattice}$ when κ(B) is zero. If $\kappa_{carrier}$ is calculated from the Lorenz number and the electrical conductivity in zero field, $\kappa_{lattice}$ can be calculated from $\kappa_{total} - \kappa_{carrier}$ which gives a value of 1.35 W/mK. For a comparison with the measured values, a simple model for the calculation of the Lorenz number is given by [8]

$$L = (\frac{k_B}{e})^2 \left[ \frac{(r+7/2)F_{r+5/2}(\xi)}{(r+3/2)F_{r+1/2}(\xi)} - \left[ \frac{(r+5/2)F_{r+3/2}(\xi)}{(r+3/2)F_{r+1/2}(\xi)} \right]^2 \right] \qquad (3.4)$$

where r is the scattering parameter, $k_B$ is Boltzmann's constant, e is the electron charge, and $F_n(\xi)$ is the Fermi integral given by

$$F_n(\xi) = \int_0^\infty \frac{\chi^n}{1+e^{\chi-\xi}} d\chi \qquad (3.5)$$

where ξ is the reduced Fermi energy that can be calculated from the Seebeck coefficient (S) as well as the scattering parameter (r) given by

$$S = \pm \frac{k_B}{e} \frac{(r+5/2)F_{r+3/2}(\xi)}{(r+3/2)F_{r+1/2}(\xi)} - \xi \qquad (3.6)$$

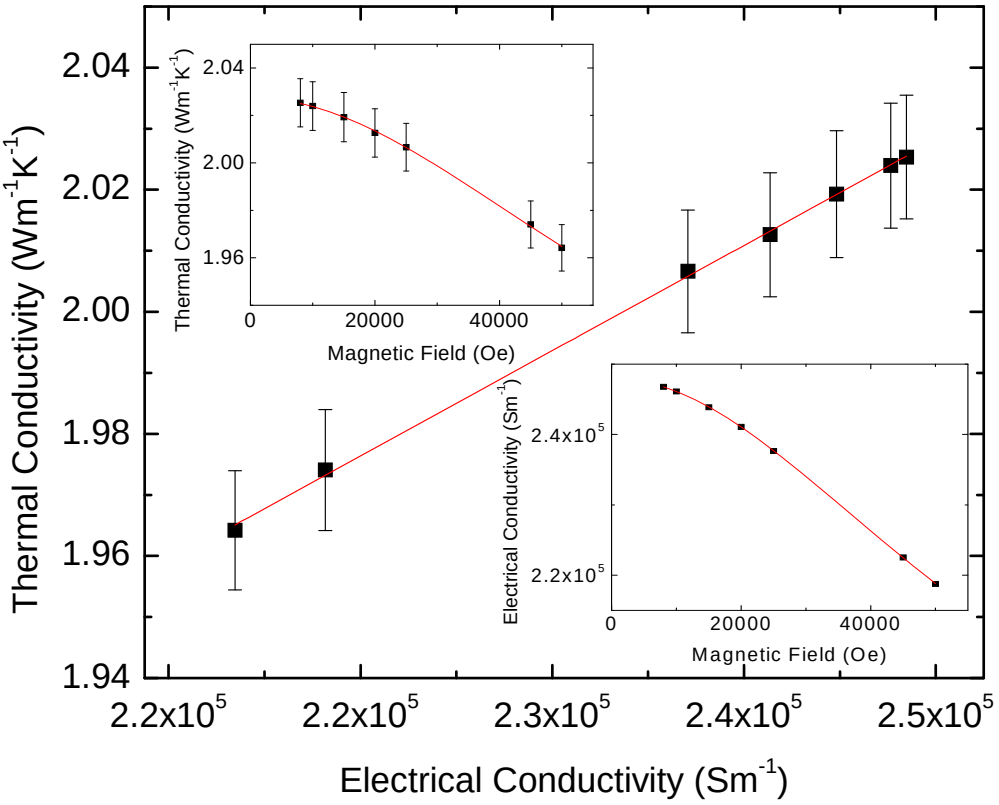


Figure 3.5: Thermal conductivity is plotted against electrical conductivity of $Cu_{0.01}Bi_2Te_{2.7}Se_{0.3}$ at 100 K with the magnetic field being varied from 0.8 T to 5 T. The slope of the linear fit provides the Lorenz number L = 2.16x10$^{-8}$ V$^2$K$^{-2}$ and the y-intercept gives $\kappa_{lattice}$ = 1.49 W/mK. The upper left inset plots the dependence of the total thermal conductivity on magnetic field. The lower right inset plots the dependence of electrical conductivity on magnetic field. Both the thermal and electrical conductivity varying with field can be fit using $\frac{aB^2}{1+cB^2}$ as shown in the insets.

In this model the Lorenz number can be calculated with knowledge of the Seebeck coefficient and the scattering parameter, both of which were measured at 100 K. The insets of Figure 3.6 show $\mu_H$ plotted as a function of temperature over the entire

temperature range (top left), as well as only the data around 100 K (lower right) which were used to calculate the scattering parameter (r). The data in Figure 3.6 are for $[Cu_{0.01}Bi_2Te_{2.7}Se_{0.3}]_{0.98}Ni_{0.02}$, the same method was used to calculate r for $Cu_{0.01}Bi_2Te_{2.7}Se_{0.3}$. The scattering parameter (r) was determined by taking the slope of $\ln(\mu_H)$ vs. ln(T) around 100 K, using the relationship $\mu \propto T^{r-1}$ [20]. The values for the mobility were nearly identical between the two samples with values for r being 0.26 and 0.27 for $Cu_{0.01}Bi_2Te_{2.7}Se_{0.3}$ and $[Cu_{0.01}Bi_2Te_{2.7}Se_{0.3}]_{0.98}Ni_{0.02}$ respectively. Though there is some error induced in the determination of r because the scattering parameter in general changes with temperature, these values should be more accurate than the commonly assumed r=-1/2 for acoustic phonon scattering. This fact is seen in the calculated values for L where using r=-1/2 yields values of L that are 3% higher than when r is calculated from the mobility. The calculated value using equations 3.4-3.6 and r=0.26 gives L = $2.34 \times 10^{-8}$ $V^2K^{-2}$ and $\kappa_{lattice}$ = 1.30 W/mK, both of which are close to the experimentally determined values.

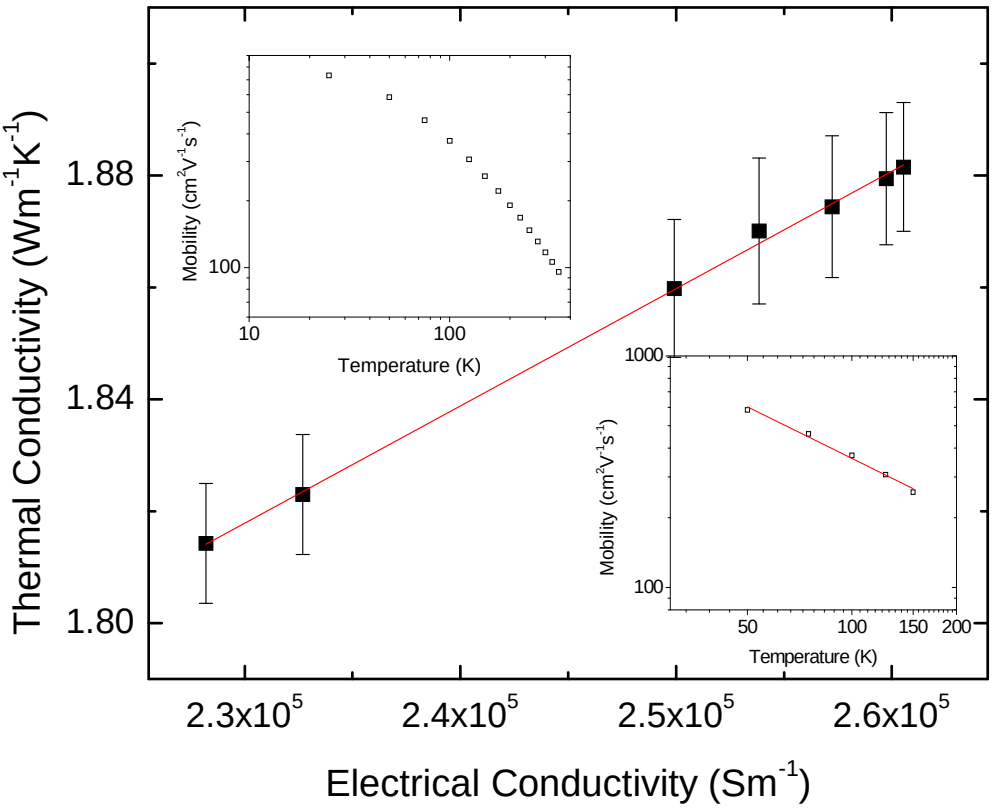


Figure 3.6: Thermal conductivity is plotted against electrical conductivity of $[Cu_{0.01}Bi_2Te_{2.7}Se_{0.3}]_{0.98}Ni_{0.02}$ at 100 K with the magnetic field being varied from 0.8 T to 5 T. The slope of the linear fit provides the Lorenz number L = 2.33x10$^{-8}$ V$^2$K$^{-2}$ and the y-intercept gives $\kappa_{lattice}$ = 1.27 W/mK. The upper left inset plots ln$\mu_H$ vs. lnT over the whole temperature range. The lower right inset plots only the points in the vicinity of 100 K from which the slope is taken to derive the scattering parameter.

The same procedure was followed for $[Cu_{0.01}Bi_2Te_{2.7}Se_{0.3}]_{0.98}Ni_{0.02}$ and Figure 3.6 shows again that κ(B) vs. σ(B) is linear. The measured value for the slope gives L = 2.33x10$^{-8}$ V$^2$K$^{-2}$ and from the y-intercept $\kappa_{lattice}$ = 1.27 W/mK. The calculated values using equations 3.4-3.6 give L = 2.36x10$^{-8}$ V$^2$K$^{-2}$ and $\kappa_{lattice}$ = 1.13 W/mK, again showing the validity of the measurement. Besides the MTR method the data can also be fit using the following expressions for the electrical and thermal conductivities as a function of

field for isotropic samples in the relaxation time approximation [23].

$$\sigma(B) = \frac{\sigma_0}{1 + (\mu_d B)^2} \qquad (3.7)$$

$$\kappa(B) = \kappa_{lattice} + \frac{\kappa_{carrier}}{1 + (\mu_d B)^2} \qquad (3.8)$$

where $\sigma_0$ is the electrical conductivity in zero field and $\mu_d$ is the drift mobility. The drift mobility determined by equation 3.7 and shown in Figure 3.7 is used in equation 3.8 in order to determine the carrier and lattice contributions to the thermal conductivity as shown in Figure 3.8. As opposed to the MTR method, the data must be fit using both weak and intermediate magnetic fields and so Figures 3.7 and 3.8 show the thermal and electrical conductivity in fields of 0.1 – 5 T. Fitting equation 3.8 to the thermal conductivity versus magnetic field data in Figure 3.8 yields $\kappa_{lattice}$ = 1.29 W/mK. It can be seen that using a completely different model presented in equations 3.7 and 3.8 produces a nearly identical value of $\kappa_{lattice}$ = 1.27 W/mK as determined by the MTR method.

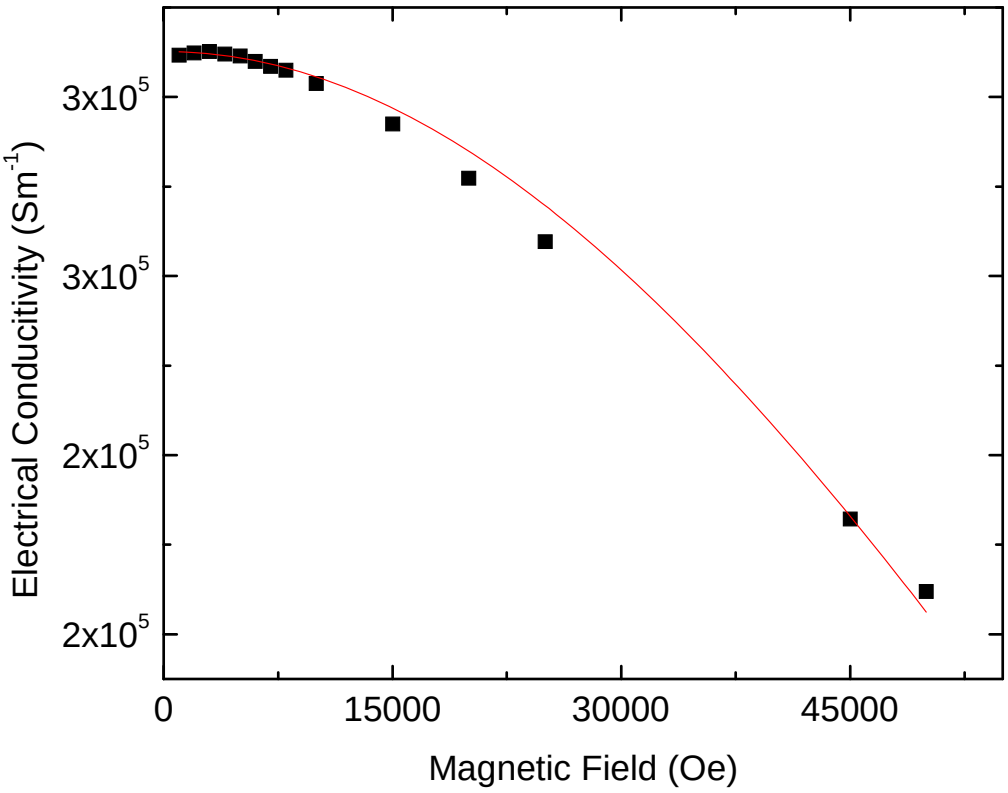


Figure 3.7: Electrical conductivity is plotted against magnetic field from 0.1-5 T and fit using equation 7. The electrical conductivity in zero field is used in order to determine the drift mobility, $\mu_d$ .

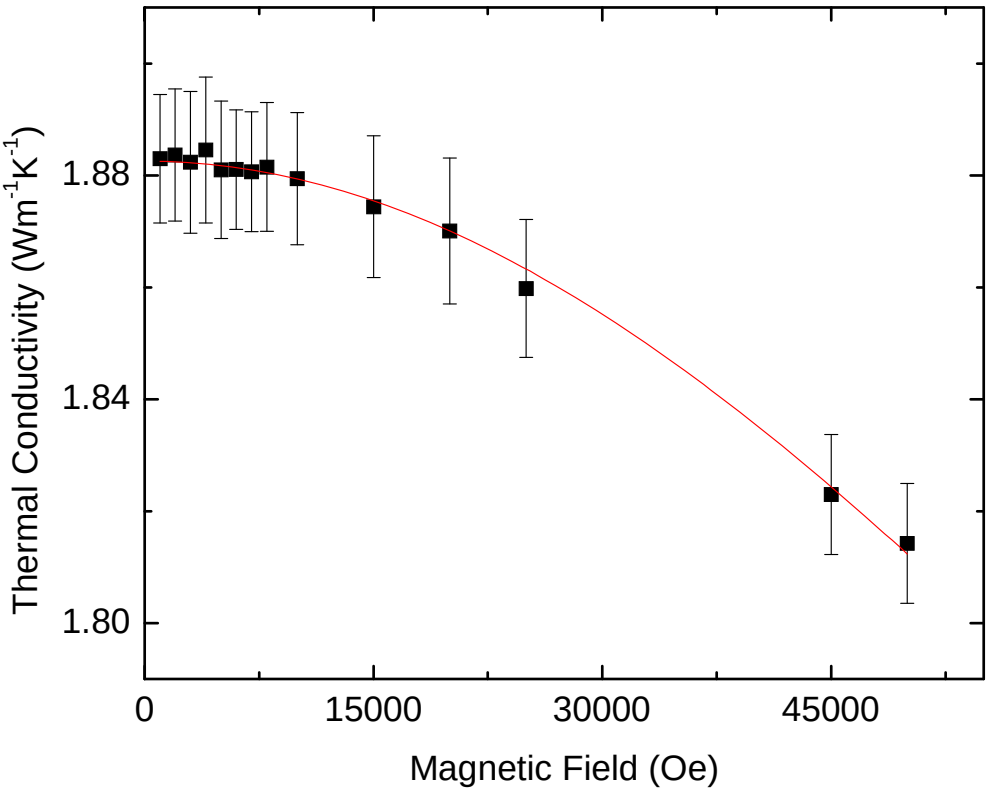


Figure 3.8: Thermal conductivity is plotted against magnetic field from 0.1-5 T and fit using equation 8 and $\mu_d$ from Figure 3.7. It is found that $\kappa_{lattice}$ = 1.29 W/mK.

Unlike $Cu_{0.01}Bi_2Te_{2.7}Se_{0.3}$, it was possible to reach the classical high field limit at lower temperatures for Bismuth Antimony compounds. Figure 3.9 plots the thermal conductivity of $Bi_{0.88}Sb_{0.12}$ versus temperature in magnetic fields of 0, 6, and 9 Tesla. The fact that the field is classically large in the temperature range of 5 – 150 K can be viewed by inspection of Figure 3.9. Since there is no change when increasing the field from 6 to 9 Tesla below 150 K, the high field limit has been reached and $\kappa_{carrier}$ has been completely suppressed. As can be seen in Fig. 3.9, there is the onset of the bipolar effect above 150 K, not radiation effects since these are negligible under 200 K, which is not

eliminated by the magnetic field and results in both the increase of the thermal conductivity and the lack of suppression of $\kappa_{carrier}$. The zero field values for the Seebeck coefficient and electrical resistivity are plotted in the insets, both confirming the onset of bipolar effects around 150 K. The fact that the electronic thermal conductivity is not suppressed due to the bipolar contribution has been described by Uher and Goldsmid and in pure Bismuth happens at around 150 K [10]. Therefore, extraction of the Lorenz number using this method is only possible for temperatures below 150 K where bipolar contributions are negligible. Once the lattice and total thermal conductivities are measured, the electronic portion was calculated using Equation 3.1. Equation 3.2 can be rewritten as LT = $\kappa_{carrier}\rho$ where $\rho$ is the zero field value for the electrical resistivity. Since in this case, the lattice portion is measured over a range of temperature, $\kappa_{carrier}\rho$ can be plotted versus temperature and the slope of the line will yield L for that temperature range. Figure 3.10 shows only the portion of the temperature range over which the plot is linear. At higher temperatures, above 150 K, the classical field approximation is no longer valid due to a drastic decrease in mobility as well as the onset of the bipolar contribution [10,12], while at lower temperatures $\kappa_{lattice}$ dominates and therefore $\kappa_{total}$ is unaffected by magnetic field as can be seen in Figure 3.9. Fitting linearly as shown in Figure 3.10, gives the measured value for the Lorenz number to be $2.21\text{x}10^{-8}$ $V^2K^{-2}$ in the temperature range 35-150 K; meaning L is constant over this range of temperature. Sharp et al. measured a sample of identical composition in fields up to 1 T where they were unable to reach the high field limit and therefore used the MTR method described above [11]. They obtained L = $2.31\text{x}10^{-8}$ $V^2K^{-2}$ at 100 K which is less than a 5% difference from our measurement. When comparing values for the lattice

portion of the thermal conductivity our measured value at 100 K yields 2.14 W/mK while the value determined using the MTR method from extrapolation is 2.19 W/mK [11]. It should be noted that the grain sizes in both samples are of the same order of magnitude, with average grain sizes being roughly one and five microns for our sample and that of Sharp respectively [11]. Again, as in the low field limit, the measured values are not only reasonable, but within 5% of published values on the same material.

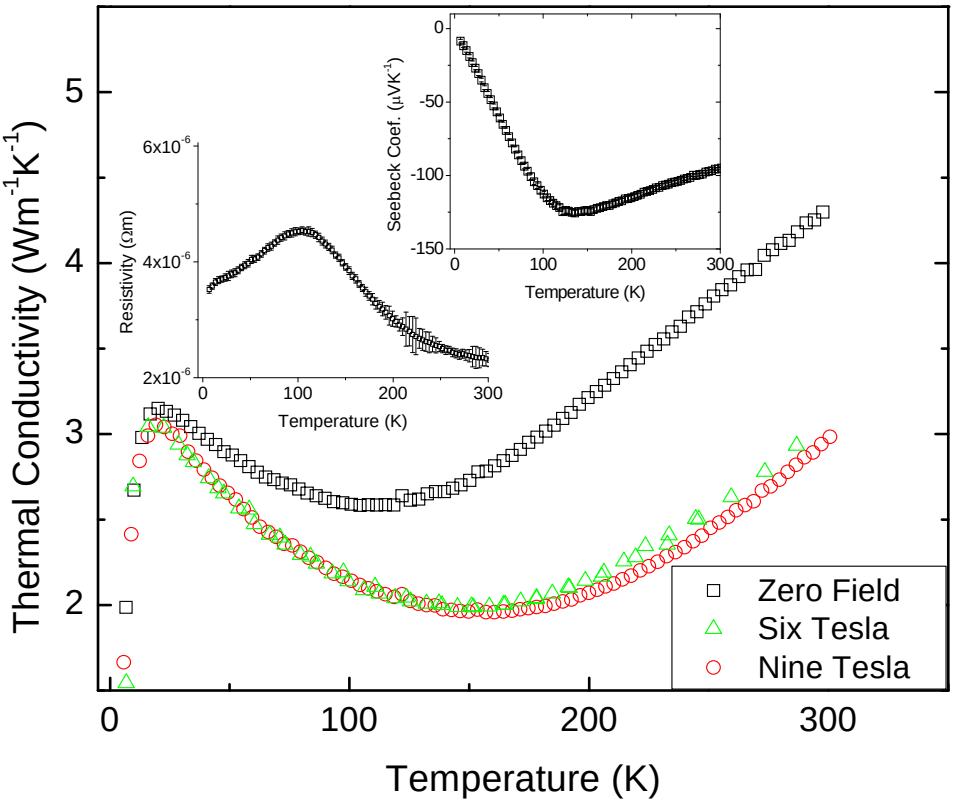


Figure 3.9: Thermal conductivity is plotted against temperature at magnetic fields of 0, 6, and 9 T for $Bi_{0.88}Sb_{0.12}$. The upper right inset plots the Seebeck coefficient against temperature while the upper left inset plots ρ vs. T from 5-300 K in zero magnetic field. It can be clearly seen that the bipolar contribution to the Seebeck coefficient becomes non negligible around 150 K.

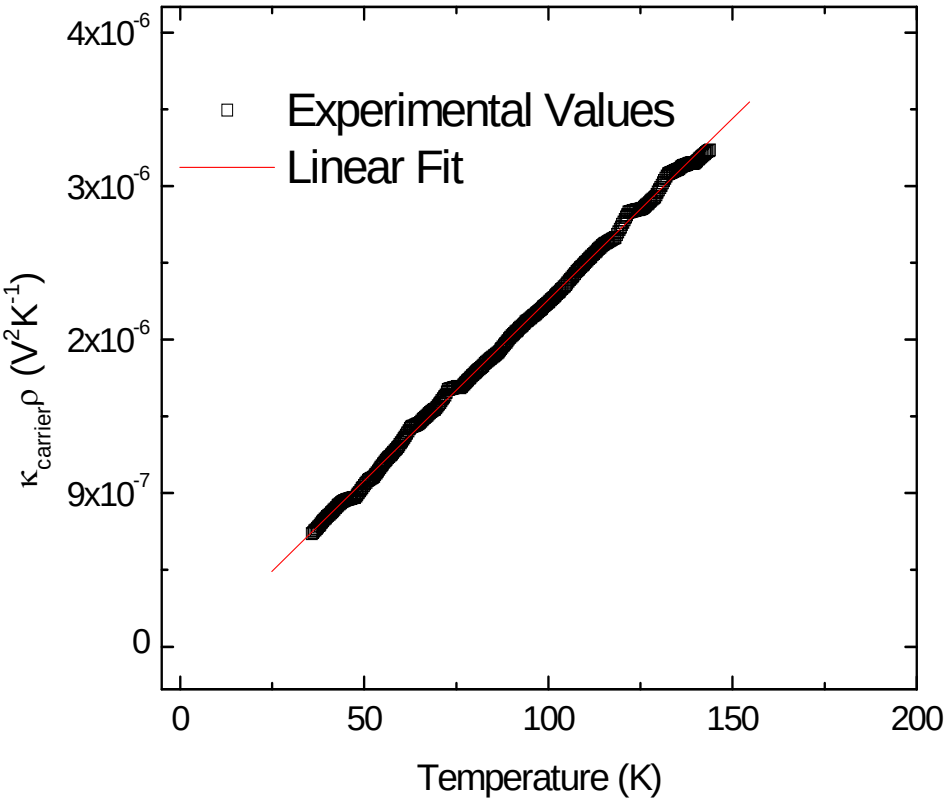


Figure 3.10: $\kappa_{carrier}\,\rho$ is plotted against temperature from 35-150 K. The black points represent the measured data while the red line is the linear fit. The slope of the linear fit provides the Lorenz number L = 2.21x10$^{-8}$ V$^2$K$^{-2}$ and the y-intercept gives $\kappa_{lattice}$ = 2.14 W/mK.

### 3.3.3 Discussion

There is excellent agreement between the two models used to fit the data in the low field limit for $Cu_{0.01}Bi_2Te_{2.7}Se_{0.3}$ and $[Cu_{0.01}Bi_2Te_{2.7}Se_{0.3}]_{0.98}Ni_{0.02}$ as well as decent agreement with simple parabolic band model theory. There is also excellent agreement between both low and high field methods as shown in the measurements of $Bi_{0.88}Sb_{0.12}$ and their comparison with literature values. While measurements for $Bi_{0.88}Sb_{0.12}$ were made near the typical temperature range of operation, these temperatures are far from optimal for $Cu_{0.01}Bi_2Te_{2.7}Se_{0.3}$ which operates in a much higher temperature range [15].

The purpose of measuring $Cu_{0.01}Bi_2Te_{2.7}Se_{0.3}$ was to see first if the measurement was possible in nanostructured materials, and second to see how high the temperature could be raised while performing the measurement. Therefore the measurement was also tried at 250 K, however there was no variation in the thermal conductivity data outside of experimental error. This is due to the fact that the mobility decreased by a factor of 3 at 250 K.

The requirement of high mobility is one of the limitations of this technique. Other limitations include the requirements for a high magnetic field, again to satisfy $\mu_H B >> 1$, as well as the electronic portion of the thermal conductivity being at least 5%. Ideal thermoelectric materials will have a high mobility along with a low lattice thermal conductivity which is comparable to the electronic portion, and so the use of magnetic field to separate out $\kappa_{carrier}$ would be perfect for the ideal nanostructured thermoelectric material [6,10-14].[1,5-9] The assumptions that are being made for the analysis (models used to fit the data) using this method are that: the Lorenz number is independent of magnetic field, the lattice is unaffected by magnetic field, there is no bipolar contribution, and electron-phonon interactions are negligible. The assumption that the Lorenz number and lattice are independent of magnetic field is true for some materials, which we take to be the case for these materials [17], but in general is not true and can be affected by secondary magnetic impurities; the authors are investigating the generality of this assumption further. Bipolar contributions should be negligible at 100 K. Electron-phonon interactions would manifest themselves when comparing the high and low field methods in $Bi_{0.88}Sb_{0.12}$. In the high field limit the carrier completes a full orbit and therefore should be more likely to scatter a phonon, this would lead to a difference in the

thermal conductivity between the high and low field measurements. Since there is no difference between the two methods, we believe the electron-phonon interactions to be negligible. It is noted that it would be interesting to devise an experiment from which electron-phonon interactions could be determined.

Because of the limitations on the material, only metals (W [18], Cu [24], Pb[25], Rb [26], etc.) along with a few alloyed compounds ($Cd_3P_2$[27], $Cd_3As_2$ [28]) have been measured using magnetic field; what the authors have found is referenced here and throughout the paper. Review articles written by Butler [22] and more recently by Kumar [15] attempt to give several literature values, though many were missed, for the Lorenz number of different elements and alloys determined by all types of experimental methods, not just in magnetic field. Another example of experimentally determining the Lorenz number being through the introduction of impurities in alloys, where the change in electrical conductivity and $\kappa_{carrier}$ is used to determine $\kappa_{lattice}$. A nice description, with examples as well as shortcomings, of the alloying method is given by Butler in reference 22.

Further investigation is required into higher temperature measurements as well as other types of materials [19-29] for which this technique can be useful. It should also be mentioned that we have only looked at the diagonal components, specifically $\kappa_{xx}$ and $\sigma_{xx}$, of the transport tensors and it could be possible to extract even more data from the off diagonal components through measurements of the Righi-Leduc and Hall coefficients [29-30]. Future work will include systematic measurements of the transport tensors on a specific material over a larger temperature range along with more complex theoretical analysis.

## 3.4 Conclusion

Two methods for experimentally determining the Lorenz number are presented for nanopolycrystalline $Bi_{0.88}Sb_{0.12}$, $Cu_{0.01}Bi_2Te_{2.7}Se_{0.3}$, and $[Cu_{0.01}Bi_2Te_{2.7}Se_{0.3}]_{0.98}Ni_{0.02}$. Measured values of $Cu_{0.01}Bi_2Te_{2.7}Se_{0.3}$ and $[Cu_{0.01}Bi_2Te_{2.7}Se_{0.3}]_{0.98}Ni_{0.02}$ analyzed using equations 3.1-3.3 as well as equations 3.7-3.8 yield similar results and are close to calculated values using the single parabolic band model presented in equations 3.4-3.6. The measured values for $Bi_{0.88}Sb_{0.12}$ are the same as previously published results. Now that the two methods have been clearly demonstrated to work on these nanopolycrystalline alloys at a given temperature, it is possible to look at other materials as well as the temperature range for which this technique can be used. A systematic study can then be done of the temperature dependence of the Lorenz number for a given material, making it possible for more complex theoretical models to be verified within experimental error leading to more accurate determinations of the lattice portion of the thermal conductivity.

## 3.5 References


1. M.Y. Tang, Ph. D. thesis, Massachusetts Institute of Technology, (2011).
2. Quantum Design, San Diego, CA, Physical Property Measurement System: Thermal Transport Option User's Manual, Third edition, (2002).
3. Quantum Design, San Diego, CA, Physical Property Measurement System: AC Transport Option User's Manual, Third edition, (2002).

4. Quantum Design, San Diego, CA, Physical Property Measurement System: Vibrating Sample Magnetometer Option User's Manual, Third edition, (2002).
5. N. R. Dilley, R. C. Black, L. Montes, A. Wilson, M. SimmondsMRS Symposium Proceedings, Boston, **691**, 85–90, (2002).
6. G. S. Kumar, M. E. Fine, J. Materials Science.**28**, 4261 (1993).
7. S. A. Aliev, L. L. Korenblit, S. S. Shalyt, Sov. Phys. Solid St.**8**, 565 (1966).
8. D. M. Rowe, C. M. Bhandari, Modern Thermoelectrics (Reston Publishing Co. Inc., Virginia, 1983**)**.
9. N. Hsieh, M. E. Fine, J. Appl. Phys.**52**, 2876 (1981).
10. C. Uher, H. J. Goldsmid, Phys. Stat. Sol. (b).**65**, 765 (1974).
11. J. W. Sharp, E. H. Volckmann, H. J. Goldsmid, Phys. Stat. Sol. (a).**2**, 185,257 (2001).
12. D. Armitage, H. J. Goldsmid, J. Phys. C. **2**, 2, 2138 (1969).
13. G. K. White, S. B. Woods, Phil. Mag., **3**, 28, 342 (1958).
14. R. T. Delves, Br. J. Appl. Phys.**15**, 105 (1964).
15. W. S. Liu, Q. Zhang, Y. Lan, S. Chen, X. Yan, Q. Zhang, H. Wang, D. Z. Wang, G. Chen, Z. F. Ren, Adv. Energy Mater.**1**, 577 (2011).
16. D. M. Rowe, CRC Handbook of Thermoelectrics (CRC Press, New York, 1995**)**.
17. A. E. Bowley, R. Delves, H. J. Goldsmid, Proc. Phys. Soc. LXXII.**3**, 401 (1958).
18. J. De Nobel, Physica XV.**5**, 532 (1949).
19. M. R. Stinson, R. Fletcher, C. R. Leavens, Physical Review B.**20**, 10, 3970 (1979).
20. A. F. Ioffe, Physics of Semiconductors (Infosearch, London, 1960**)**.

21. R. Laiho, S. A. Nemov, A. V. Lashkul, E. Lakhderanta, T. E. Svechnikova, D. S. Dvornik, Semiconductors.41, 546 (2007).

22. W. H. Butler, R. K. Williams, Phys. Rev. B.**18**, 12, 6483 (1978).

23. C. Jacoboni, Theory of Electron Transport in Semiconductors (Springer, Berlin, 2010**)**.

24. R. W. Arenz, C. F. Clark, W. N. Lawless, Phys. Rev. B.**26**, 6, 2727 (1982).

25. L. J. Challis, J. D. N. Cheeke, P. Wyder, Phys. Rev.**143**, 2, 499 (1966).

26. R. Fletcher, I. B. Verma, Phys. Rev. B.**36**, 18, 9482 (1987).

27. F. A. P. Blom, J. W. Burg, J. Phys. Chem. Solids.**38**, 19 (1977).

28. F. A. P. Blom, A. Huyser, Sol. State Comm.**7**, 1299 (1969).

29. M. Matusiak, T. Plackowski, W. Sadowski, Sol. State Comm.**132**, 25 (2004).

30. Y. Zhang, N. P. Ong, Z. A. Xu, K. Krishana, R. Gagnon, L. Taillefer, Phys. Rev. Lett.**84**, 10, 2219 (2000).

31. J. S. Brooks, M. j. Naughton, Y. P. Ma, P. M. Chaikin and R. V. Chamberlin Review of Scientific Instruments 58, 117 (1987)

# Chapter 4: Transport Properties of Ni, Co, Fe, Mn Doped $Cu_{0.01}Bi_2Te_{2.7}Se_{0.3}$ for Device Applications

## 4.1 Introduction

This chapter discusses a study performed on $Cu_{0.01}Bi_2Te_{2.7}Se_{0.3}$. The work has been published in the *Journal of Applied Physics* and can be found in Appendix D.

Much work has been done in recent years in an effort to improve the thermoelectric (TE) transport properties of several TE materials where efforts have specifically focused on the enhancement of the dimensionless figure of merit, $ZT$ where $ZT = (S^2/\rho\kappa)T$ with $S$ being the Seebeck coefficient, $\rho$ the resistivity, $\kappa$ the thermal conductivity, and $T$ the absolute temperature [1]. Efforts have focused on either the reduction of the lattice thermal conductivity, or the enhancement of the power factor $S^2/\rho$ through various approaches relying on physics at the nanoscale [2-5]. Ultimately however the material is going to be used in an actual device, where it is necessary for further optimization beyond that of the TE material used [2]. There have been previous studies on the fabrication of TE devices for cooling and power generation, along with the difficulties that arise during fabrication and operation [2]. TE devices are typically constructed with several p-n couples connected electrically in series and thermally in parallel as described by Ioffe [1]. A simple schematic of one p-n couple is shown in Figure 4.1. The efficiency of a TE device increases with both the material's $ZT$ and the temperature difference between the hot and the cold junction of the TE elements. One of the most important challenges in fabricating an efficient TE device is to develop

interfaces with low electrical and thermal contact resistance. Large electrical contact resistance results in parasitic Joule heating losses, while large thermal contact resistances result in a smaller temperature gradient across the TE material.

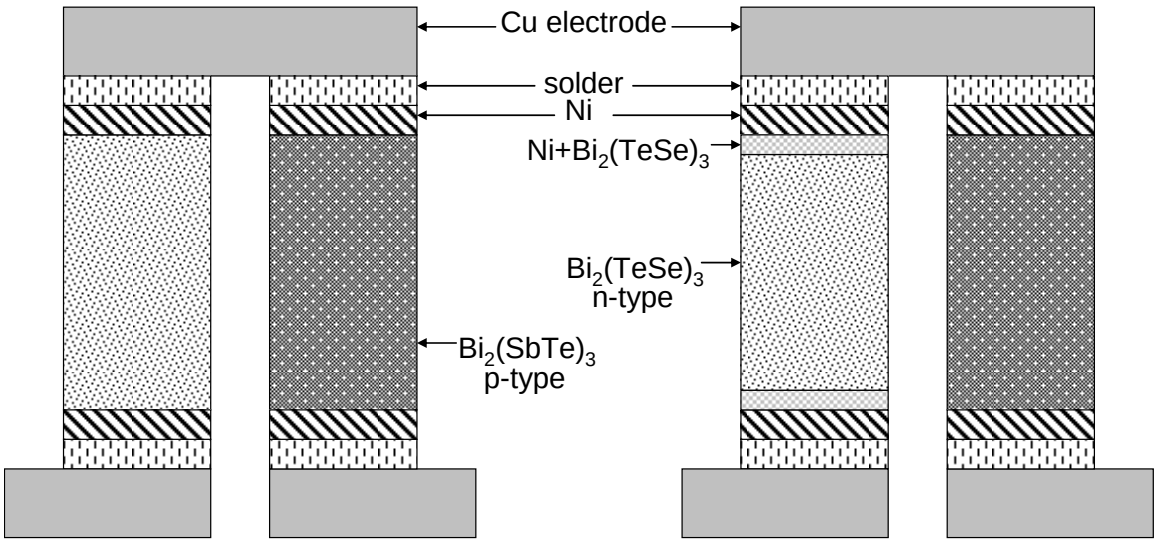


Figure 4.1: Both (a) and (b) show one p-n couple that can be used as a thermoelectric generator or Peltier cooler. Typical TE devices contain many couples. The ideal solder connection to the Ni diffusion barrier for a $Bi_2Te_3$ p-n couple shown in (a) where the Ni does not diffuse into the TE material. (b) shows the actual case during fabrication and operation where the Ni diffuses into the n-type TE material which is believed to be the cause of device degradation [4].

The best way to create good electrical and thermal connections is by soldering. However, it is known that typical solders as well as Cu metal (used for electrodes) readily diffuse into and degrade the properties of TE materials, specifically $Bi_2Te_3$ based materials [2-11]. In order to impede the diffusion of solder into the TE material, diffusion barriers are used [7]. These diffusion barriers are typically thin films of sputtered or electrochemically deposited metallic elements such as Fe for TAGS-85 and PbTe [10,12]. The deposition techniques ensure minimal thermal and electrical contact resistance.

Additionally, the thin films should have similar coefficients of thermal expansion (CTE) to ensure the mechanical longevity of the device [2,9].

It was previously demonstrated that nickel could be used successfully as a diffusion barrier for solder in p-type $Bi_2(SbTe)_3$ and n-type $Bi_2(TeSe)_3$ alloys [7]. The problem was that even though the nickel stopped the solder, the nickel itself diffused into the n-type $Bi_2(TeSe)_3$. A simple schematic of the Ni diffusion described in ref. 7 in one p-n couple is shown in Figure 4.1. Shown on the left is the ideal scenario where the Ni acts as a diffusion barrier without diffusing into the TE material. On the right is what actually happens during fabrication and operation. The Ni does not diffuse into the p-type element but does diffuse slightly into the n-type element. A later study demonstrated that using Co as a diffusion barrier prevented the solder from getting into the n-type $Bi_2(TeSe)_3$ while the Co itself did not diffuse into the material as readily as Ni [9]. Each study included only interfacial microstructure data and therefore it is unclear how the diffused Ni or Co affected the transport properties, though it was noted that the efficiency of the Peltier cooling devices degraded over time [7]. It was also noted that the Ni diffused further into the TE material as operation time increased. Therefore it seemed reasonable that TE device degradation was due to the diffusion of the Ni barrier into the TE material [7]. Based on this assumption, the device should perform at its lowest efficiency when the Ni fully diffused into the TE material.

In this study we intentionally dope two atomic percent Ni, Co, Fe, and Mn into $Cu_{0.01}Bi_2Te_{2.7}Se_{0.3}$ to study the maximum degradation in electrical and thermal transport properties that a TE material can undergo if these elements are used as a diffusion barrier. Based on a typical device height of 1 mm as well as the thickness of the applied diffusion

barrier of 3 μm, the amount of Ni, Co, Fe, or Mn that diffuses into the TE material should not exceed 2 percent [7]. Ni, Co, and Fe all have similar coefficients of thermal expansion which are reported to be similar to that of $Bi_2(TeSe)_3$ [9,12], and therefore would be ideal for device fabrication. Mn has a coefficient of thermal expansion roughly double that of Ni, Co, or Fe but is included in this study to see how transport is effected [12].

## 4.2 Experimental

Proper stoichiometric amounts of Cu (Alfa Aesar 99.999%), Bi (Alfa Aesar 99.999%), Te (Alfa Aesar 99.999%), Se (Alfa Aesar 99.999%), Ni (Alfa Aesar 99.999%), Co (Alfa Aesar 99.999%), Fe (Alfa Aesar 99.999%), and Mn (Alfa Aesar 99.999%) were prepared by ball milling and hot pressing methods described previously according to the formula $Cu_{0.01}Bi_2Te_{2.7}Se_{0.3}M_{0.02}$ (M=Ni, Co, Fe and Mn) [13]. Thermal conductivity $\kappa$, electrical resistivity $\rho$, Seebeck coefficient $S$, and Hall coefficient $R_H$ were measured using a PPMS from Quantum Design in a temperature range of 5-350 K as described in Chapter 3. Values for the electrical resistivity and Seebeck coefficient at temperatures of 300-525 K were made using a ZEM-3 from Ulvac Inc. Samples were also measured using the system described in Chapter 2. For clarity only values from the ZEM-3 are shown here while Appendix B shows data for the Seebeck coefficient from the homebuilt system (Chapter 2). Values for thermal conductivity were obtained using a LaserFlash system from Netzch. Low temperature measurements of $\kappa$, $\rho$, and $S$ were made on samples parallel to the press direction, while hall measurements as well as high

temperature measurements were made perpendicular to the press direction. It has been previously demonstrated that these materials are isotropic to within 10% [13]. Estimated errors for $\rho$, $\kappa$, $S$, $ZT$, $n$, and $\mu_H$ should not exceed 3, 8, 5, 14, 10, and 10%, respectively.

## 4.3 Results and Discussion

The Hall Coefficient is negative over the entire temperature range showing that the majority carriers are electrons as is to be expected for $Cu_{0.01}Bi_2Te_{2.7}Se_{0.3}$ [13]. Figure 4.2a shows the carrier concentration for all samples from 10 – 350 K. In contrast to $Cu_{0.01}Bi_2Te_{2.7}Se_{0.3}$ ($4.29\times10^{19}$ /cm$^{-3}$ at 300K), the carrier concentration at room temperature of $Cu_{0.01}Bi_2Te_{2.7}Se_{0.3}M_{0.02}$ is increased with the addition of Ni ($5.72\times10^{19}$ /cm$^{-3}$), Co ($4.88\times10^{19}$ /cm$^{-3}$), and Fe ($4.83\times10^{19}$ /cm$^{-3}$), while $n$ decreased with Mn ($3.11\times10^{19}$ /cm$^{-3}$). The increased carrier concentration for the Ni, Co and Fe, can be explained in the same manner as the increase in the case of Cu doped n-type $Bi_2Te_{2.7}Se_{0.3}$. It was previously shown that Cu easily diffuses into $Bi_2Te_3$ through the interstitial sites between two Te layers and acts as a strong donor providing 0.3 carrier/atom [13]. Ni, Co and Fe appear to get into the interstitial site of $Bi_2Te_{2.7}Se_{0.3}$ as well and also work as an n-type dopant providing 0.12, 0.05, and 0.04 carrier/atom, respectively. Such transition metals have also demonstrated n-type doping behavior when they are located at the interstitial site of layered compounds $TiSe_2$ [14] and $TiS_2$ [15]. The inability of Ni, Co, and Fe to donate the same number of free electrons in $Cu_{0.01}Bi_2Te_{2.7}Se_{0.3}M_{0.02}$, is likely associated with the difference in the number of outer valence electrons. Contrary to the other dopants, Mn decreases the carrier concentration. Based on previous work

demonstrating that Cu sitting in the interstitial site will donate carriers [13] along with the increase in carrier concentration from the addition of Ni, Co, and Fe, it is possible that Mn is does not sit in the interstitial site but substitutes for either Bi or Te. Figure 4.2b plots the mobility against temperature up to 350 K. It can be seen that the variation in mobility is quite small with the greatest change being roughly a 10% decrease in $\mu_H$ for the Fe doped sample. The lack of change in $\mu_H$ compared to $n$ with the addition of Ni, Co, Fe, and Mn is similar to the case of filled skutterudites. Filled skutterudites do not show as great a change in mobility compared to the carrier concentration because the dopants sit in the interstitial site [16].

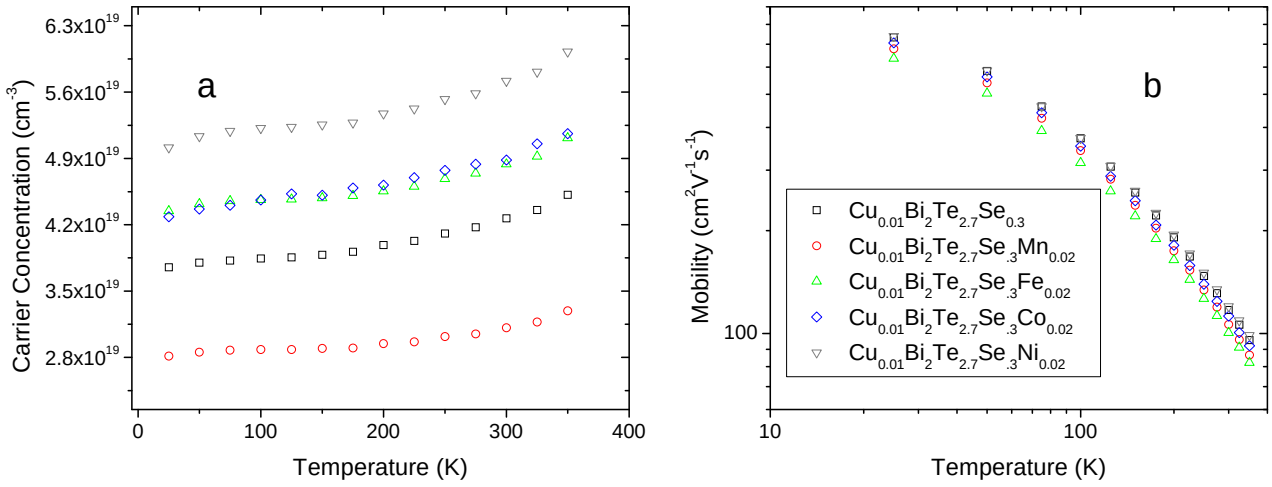


Figure 4.2: The carrier concentration (a) and carrier mobility (b) are plotted with temperature from 5-350 K. Carrier concentration changes with the doping element while the mobility remains unaffected.

In the range from 5-350 K the thermal and electrical transport properties of all doped TE samples show a small variation with the introduction of any of the doping impurities (Fig. 4.3). The electrical resistivities, Fig. 4.3a, show metallic like behavior. The addition of Ni slightly decreases the resistivity while the addition of Co, Fe, and Mn

slightly increases values for $\rho$ where Mn shows the largest increase which is due to a drop in carrier concentration. The Seebeck coefficient is negative over the entire temperature range confirming the majority carriers are electrons (Fig.4.3b). The Seebeck coefficient is slightly decreased by the addition of Ni due to the increased carrier concentration and unchanged mobility. Co and Fe do not strongly impact the values for *S*, while the addition of Mn slightly increases *S* again due to the decrease in *n*. The thermal conductivity decreases with the introduction of either Ni, Co, Fe, or Mn, all of which act as scattering sites in the lattice (Fig. 4.3c) as has been previously demonstrated with Cu in $Bi_2Te_{2.7}Se_{0.3}$ [13]. The values of *ZT* seen in Fig. 4.3d show that overall the figure of merit is unaffected by any of the above 3d transition metal doping.

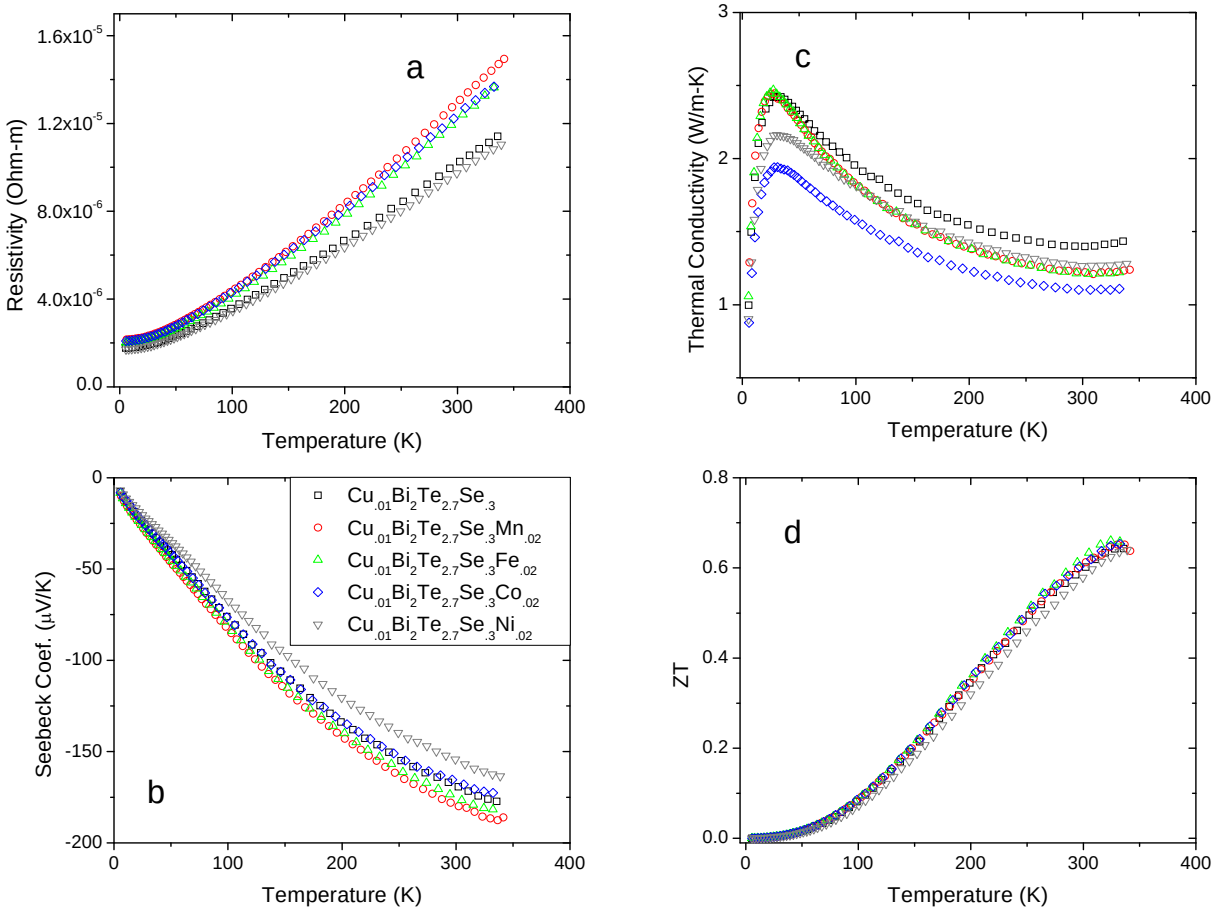

Figure 4.3: The electrical resistivity (a), Seebeck coefficient (b), thermal conductivity (c) and *ZT* (d) are plotted with temperature from 5-350 K. Though $\rho$ and *S* change with *n, ZT* remains unchanged in each sample.

In the temperature range from 300-525 K the inclusion of Ni gives a lower value for the electrical resistivity while Mn increases the resistivity (Fig. 4.4a). Figure 4.4b shows that within experimental error the Seebeck coefficient remains the same except for the Ni doped sample which is suppressed due to the increase in carrier concentration, though experimentally *n* is only measured up to 350 K. At these higher temperatures phonon-phonon scattering becomes dominant and all samples exhibit similar values for thermal conductivity, as expected (Fig. 4.4c). Overall, in each sample, an increase in $\rho$ comes with an increase in S and therefore all samples have similar values for *ZT* (Fig. 4.4d) just as in the low temperature data presented in Figure 4.3. The transport properties measured by the two commercial systems along different pressing directions match to within about 10% as is expected [13].

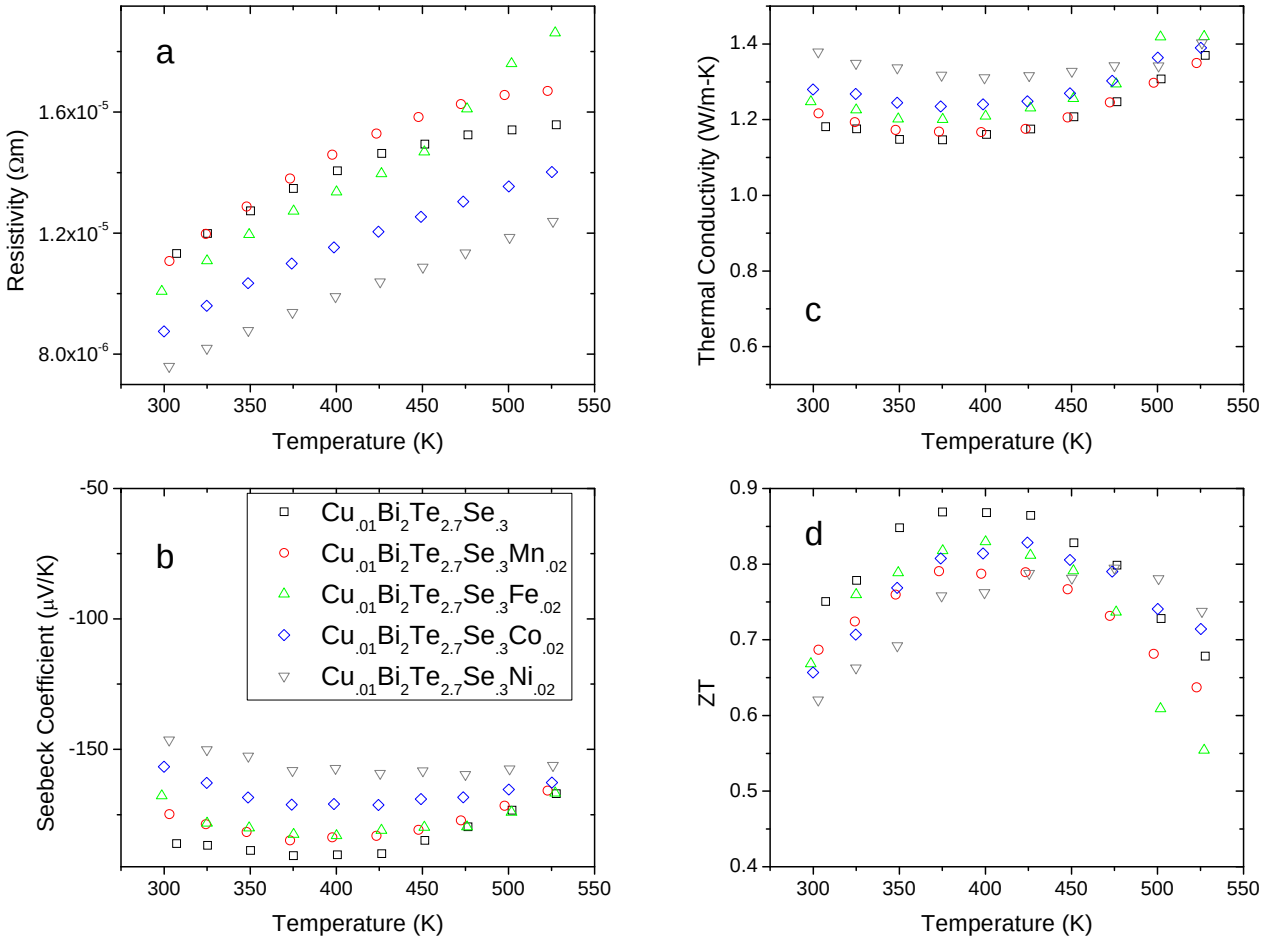


Figure 4.4: The electrical resistivity (a), Seebeck coefficient (b), thermal conductivity (b), and *ZT* (d) are plotted with temperature from 300-525 K. *ZT* is relatively unaltered by the introduction of different impurities just as in the low temperature measurements.

Both high and low temperature measurements made perpendicular and parallel to the press direction show similar quantitative trends due to the introduction of Ni, Fe, Co, and Mn, where overall there is negligible change to *ZT* with the addition of impurities. This means that if any of these elements are used as diffusion barriers, and diffuse into the TE material there should be negligible effects on the efficiency of the device. It was mentioned previously that former studies showed a decrease in device efficiency which was attributed to diffusion of Ni into the TE material [7]. However, these results are

contrary to that understanding because the device degradation is not due to deteriorating TE material performance. One possible explanation is that there is Cu already introduced into the $Bi_2Te_{2.7}Se_{0.3}$ material in this study. Previous studies by Liu, *et. al* added Cu in order to make the material properties reproducible [13]. And therefore with a further introduction of impurities at such a small percentage, there is not as drastic a change in the thermal or electrical transport properties as what is seen with the addition of slight amounts of Cu. Based on this understanding, any of the metallic elements, Ni, Co, Fe, and Mn, can be used as a diffusion barrier for $Cu_{0.01}Bi_2Te_{2.7}Se_{0.3}$ as long as they inhibit the solder from entering the TE material and have the proper mechanical properties during operation [2]. It would be interesting to create a device using $Cu_{0.01}Bi_2Te_{2.7}Se_{0.3}$ as the n-type TE material and Ni as a diffusion barrier. Based on the above data, the device should not degrade, as long as the solder does not diffuse, if a small amount of Ni diffuses into the TE material. If the device does degrade, then there are other issues with the device. Perhaps some special type of failure at the interface happens during operation or fabrication, but this failure would not be due to TE material degradation.

The above analysis only applies to bulk or "macro" TE devices. However the data can be useful in the construction of "micro" TE devices as well. Microelectromechanical systems (MEMS) and other thin film TE devices are also of interest and have become a widely studied area [2,6,17-19]. In thin films the diffusion barrier thickness is on the same order as the TE material [2,6], and so if Ni readily diffuses into $Cu_{0.01}Bi_2Te_{2.7}Se_{0.3}$ then the inclusion of Ni will be greater than the 2% addition studied here. However previous studies for Co show that it does not easily diffuse into $Bi_2(TeSe)_3$ and therefore the low doping percentage study here can be

applicable [9]. Co does go through a structural phase transition at 380 $^{o}$C [20], but this is higher than the typical operating temperature of $Bi_2(TeSe)_3$ based TE devices and therefore should be of no concern [2,7].

Due to the similarity in the coefficient of thermal expansion, minimal diffusion of Co into $Bi_2(TeSe)_3$ [9], and no significant change in *ZT* for Co doped $Cu_{0.01}Bi_2Te_{2.7}Se_{0.3}$, it appears that Co would be an excellent choice for the contact material in a $Cu_{0.01}Bi_2Te_{2.7}Se_{0.3}$ thin film TE device. I could find no information on the diffusion of Fe or Mn in $Bi_2(TeSe)_3$, however if they show similar diffusion tendencies to that of Co then they could also be a possible option for a contact material. However, because Fe oxidizes easily and Mn has a higher CTE, Co appears to be the ideal choice for contact materials in either macro or micro TE devices.

## 4.4 Conclusion

Thermoelectric transport properties of $Cu_{0.01}Bi_2Te_{2.7}Se_{0.3}$ doped with 2 atomic percent Ni, Co, Fe, and Mn are studied to reveal information on possible metallic elements for use as diffusion barriers in TE devices. It is shown that *ZT* is unaffected by the low percentage impurity doping and therefore the efficiency of TE devices should not be affected if any of these metals diffuse into the TE material while being used as a diffusion barrier for solder. And based on this and previous studies Co seems to be the optimal choice for a diffusion barrier. It is also noted that the addition of Cu into $Bi_2Te_{2.7}Se_{0.3}$ could be of great benefit to TE device fabrication because any excess introduction of impurities from the diffusion barriers would be negligible, if it is in fact

the impurities that are degrading the performance.

## 4.5 References


1. A. F. Ioffe, Semiconductor Thermoelements and Thermoelectric Cooling (Inforsearch Ltd., 1965)
2. D. M. Rowe, Thermoelectrics Handbook: Macro to Nano (Taylor & Francis, New York, 2006).
3. W. S. Liu, X. Yan, G. Chen, and Z. F. Ren, Nano Energy **1**, 42-56 (2012).
4. G. J. Snyder and E. S. Toberer, Nat. Mater. **7**, 105 (2008).
5. A. J. Minnich, M. S. Dresselhaus, Z. F. Ren, G. Chen, Energy & Env. Sci. 2, 466 (2009).
6. G. J. Snyder, J. R. Lim, C. K. Huang, and J. P. Fleurial, Nature **2**, 528 (2003).
7. Y. C. Lan, D. Z. Wang, G. Chen, and Z. F. Ren, App. Phys. Lett. **92**, 101910 (2008).
8. O. Ymashita, J. of Applied Phys. **95**, 1, 178, (2004).
9. R. P. Gupta, O. D. Iyore, K. Xiong, J. B. White, K. Cho, H.N. Alshareef, and B. E. Gnade, Electrochem. and Solid-State Lett **12**, H395, (2009).
10. A. Singh, S. Bhattacharya, C. Thinaharan, D. K. Aswal, S. K. Gupta, J. V. Yakhmi, and K. Bhanumurthy, J. Phys. D **42**, 015502, (2009).
11. V. M. Sokolova, L. D. Dudkin, and L. I. Petrova, Inorg. Mater. **36**, 21 (2000).
12. D. R. Lide, CRC Handbook of Chemistry and Physics, 84th Edition. (CRC Press. Boca Raton, 2003).

13. W. S. Liu, Q. Zhang, Y. C. Lan, S. Chen, X. Yan, Q. Zhang, H. Wang, D. Z. Wang, G. Chen, and Z. F. Ren, Adv. Energy Mater. **1**, 577 (2011).

14. F. Levy, J. Phys. C: Solid St. Phys., **13** 2901-12 (1980).

15. J. Zhang, X.Y. Qin, H.X. Xin, D. Li, and C.J. Song, J. Electronic Mater., **40**, 5, (2011).

16. J. Yang, Q. Hao, H. Wang, Y. C. Lan, Q. Y. He, A. Minnich, D. Z. Wang, J. A. Harriman, V. M. Varki, M. S. Dresselhaus, G. Chen, and Z. F. Ren, Phys. Rev. B **80**, 115329 (2009).

17. D. Bishop, A. Heuer, and D. Williams, Mater. Res. Bull. **26** (2001).

18. R. K. Kupka, F. Bouamran, C. Cremers, and S. Megtert, Appl. Surf. Sci. **164**, (2000).

19. R. Venkatasubramanian, E. Siivola, B. C. O'Quinn, K. Coonley, P. Addepalli, M. Napier, T. Colpitts, and M. Mantini, Proc. 2003 ACS Symp. Nanotech. & Environment (New Orleans, 2003).

20. C. Cabral, Jr., K. Barmak, J. Gupta, L. A. Clevenger, B. Arcot, D. A. Smith, and J. M. E. Harper, J. Vac. Sci. Tech. A, **11** 1435 (1993).

# Chapter 5: Cerium, Samarium, Holmium Doped $Bi_{88}Sb_{12}$

## 5.1 Introduction

This chapter discusses the electrical and thermal transport properties of Sm doped $Bi_{88}Sb_{12}$. Similar studies were done with the addition of both Ce and Ho and show comparable effects on the transport properties. The results for Ho doped $Bi_{88}Sb_{12}$ were published in the *Journal of Materials Science* and can be found in Appendix D along with the publication of the *2012 Spring MRS Conference Proceedings* for the Ce doped samples.

Bismuth – antimony alloys have long been noted for their beneficial thermoelectric properties below room temperature since the initial measurements by Smith and Wolf [1,2]. Thus far they have the highest figure of merit, *ZT*, below 200 K making them the best candidate for the n-type leg of thermoelectric refrigeration devices [3].

As group V semimetals bismuth and antimony form a solid solution over the entire composition range leading to many interesting physical features [4]. Lenoir *et al.* described in detail the changes in electronic band structure depending on the antimony content for $Bi_{1-x}Sb_x$ alloys [4]. The band structure for bulk $Bi_{1-x}Sb_x$ is shown in Figure 5.1. The solid solution is semimetallic when the Sb concentration is $x < 0.07$ and $x > 0.22$ while the alloy is semiconducting inside the region $0.07 < x < 0.22$ [4-9]. The best thermoelectric properties are found for single crystals, with $0.09 < x < 0.16$, when measured parallel to the trigonal axis [4, 10-11]. The very small band gap in the

semiconducting region, specifically the direct energy gap at the L point, along with the quasi-ellipsoidal electron Fermi surface leads to small electron effective masses, high electron mobilities, and a non parabolic dispersion relation [3]. The small direct energy gap at the L point leads to the dependence of the band structure on many different physical parameters including alloy composition [5,12-13], temperature [14], magnetic field [15,16], and pressure [17,18].

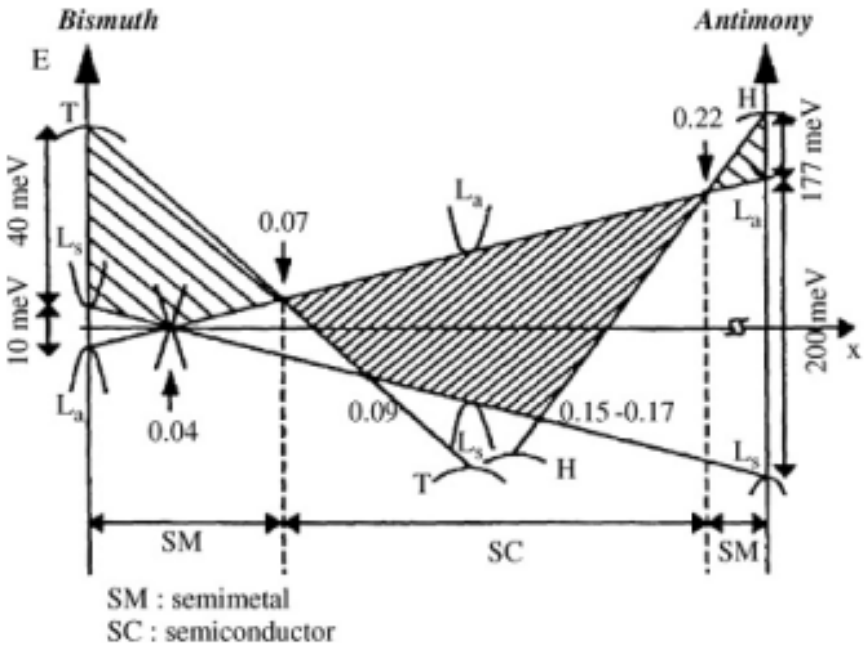


Figure 5.1: Depiction of energy band structure near the Fermi level for bulk $Bi_{1-x}Sb_x$ alloys at 0 K [4].

Single crystals exhibit the best transport properties, but they are difficult to grow and are mechanically weak making them unlikely candidates for commercial use. Several techniques for synthesizing polycrystalline BiSb have been studied, but none demonstrate a higher value for *ZT* than single crystals. These methods include: arc plasma [19], quenching [10], mechanical alloying [20], powder metallurgy [21], and doping [22, 23]. Devaux et al. [19] studied the effects of grain size on the thermoelectric

properties, specifically investigating the decrease of the lattice component of the thermal conductivity with the reduction of grain size. While the thermal conductivity was reduced due to phonon scattering, there was no benefit to *ZT* due to increased resistivity, as has also been seen in nanosized grains [24, 25]. Though it was initially thought that doping BiSb alloys would not enhance the transport properties, it was demonstrated in a few previous studies that doping impurities into BiSb can be another method for *ZT* enhancement [26].

We doped Ce, Sm, and Ho into $Bi_{88}Sb_{12}$ to study the effects of introducing a magnetic impurity into BiSb alloys [27]. While the ultimate goal was to study the magnetotransport properties, a slight enhancement was discovered in zero magnetic field. As mentioned above the band structure of BiSb alloys is very sensitive to different physical parameters, and changes at low temperatures have been interpreted as arising from lattice distortion as well as from varying spin-orbit interactions that arise from alloying [4]. Both Ho and Ce have a relatively large magnetic moment which could affect the spin-orbit interaction and therefore the band structure leading to enhanced transport properties. Samarium has a smaller magnetic moment while having an ionic mass in between that Ho and Ce. Therefore any difference in transport properties due to the differences in magnetic moment should be readily noticeable. The present study includes Sm doped $Bi_{88}Sb_{12}$ alloys synthesized under similar conditions and doping percentages for both Ho and Ce doped $Bi_{88}Sb_{12}$. The data for the Ce and Ho doped samples are similar to the Sm samples prepared under the same fabrication conditions and are presented in the publications found in Appendix D.

## 5.2 Experimental

Nano-polycrystalline $Bi_{88}Sb_{12}$ samples were prepared by ball milling and dc hot-pressing techniques described previously [27]. Two sets of samples were prepared using elemental chunks of bismuth (Bi) (99.99 %, Alfa Aesar), antimony (Sb) (99.99 %, Alfa Aesar), samarium (Sm) (99.9 %, Alfa Aesar), cerium (Ce) (99.9 %, Alfa Aesar), and holmium (Ho) (99.9 %, Alfa Aesar) according to the atomic composition $Bi_{88}Sb_{12}Ce_y$ (y = 0, 0.07, 0.7, and 4.2), $Bi_{88}Sb_{12}Sm_y$ (y = 0, 0.066, 0.66, 1.32 and 3.93), $Bi_{88}Sb_{12}Ho_y$ (y = 0, 1 and 3). One set of Sm samples was prepared, identically to the Ho doped samples, by ball milling elemental chunks with the proper stoichiometric ratio for 12 hours to form a powder which was hot pressed at 240 $^oC$ thereby creating a disk approximately 4 mm thick and 12 mm in diameter. For simplicity these samples are labeled 0.06Sm, 0.6Sm, 1Sm, and 3Sm respectively. The second set of samples was prepared, just as the Ce doped samples, by melting the constituent elements in quartz tubes for 6 hours at 450 $^oC$ and then quenching the solution in water to form an ingot. The ingot was then placed in a high energy ball mill for 6 hours then pressed at a temperature of 200 $^oC$.

From the pressed disks, two samples were cut to measure the thermoelectric properties where all transport properties were measured perpendicular to the pressing direction (parallel to the disk face). Thermoelectric transport properties including the Seebeck coefficient ($S$), electrical resistivity ($\rho$), and thermal conductivity ($\kappa$) were measured in the standard two probe method from 5 to 350 K as described in Chapter 3. The second sample was used to determine the Hall coefficient ($R_H$) again as described in Chapter 3 from which the carrier concentration and mobility were extracted. X-ray

diffraction was performed (Bruker AXS) to ensure the powders were alloyed into a single phase, and SEM (JEOL 7001F) images were taken from freshly fractured surfaces to observe the effects of grain growth during pressing. The magnetic susceptibility ($\chi$) was measured in a magnetic field of 0.1 T using a vibrating sample magnetometer (VSM) in the PPMS by our collaborators at The National Magnet Lab in Florida and Los Alamos National Laboratory. The lattice portion of the thermal conductivity was measured directly using a classically large magnetic field to completely suppress the electronic portion of $\kappa$, as previously described in detail in Chapter 3.

## 5.3 Discussion

Sm doped samples were prepared at various doping concentrations and through both fabrication methods. The 240 $^{o}$C hot pressed samples will be discussed in detail in this thesis and it will be seen that the data matches quite well with the similarly prepared Ho doped samples. Second the transport properties of the 200 $^{o}$C hot pressed samples will be shown to correlate well with what was seen in the study of Ce doped $Bi_{88}Sb_{12}$. A qualitative analysis similar to that used previously will be given since both the non parabolic energy-momentum dispersion relation and the narrow band gap make a quantitative analysis of the transport properties of BiSb alloys very difficult [3,4].

Figure 5.2 shows the XRD pattern for the samples hot pressed at 240 $^{o}$C and demonstrates that the material is single phase within the resolution of the system. SEM images are shown in Figure 5.3 where it is seen that for all doping concentrations, other than 3Sm, have similar grain sizes. The highest doping concentration has a much

different microstructure where the grains appear to be much smaller. This difference was also seen in the highest percentage of the Ce doped samples [28]. The difference at the highest doping concentration could be due to the low solubility of Sm in Bi, based on the Bi-Sm phase diagram; therefore it is reasonable that the solubility would be low in the Bi rich alloy $Bi_{88}Sb_{12}$.

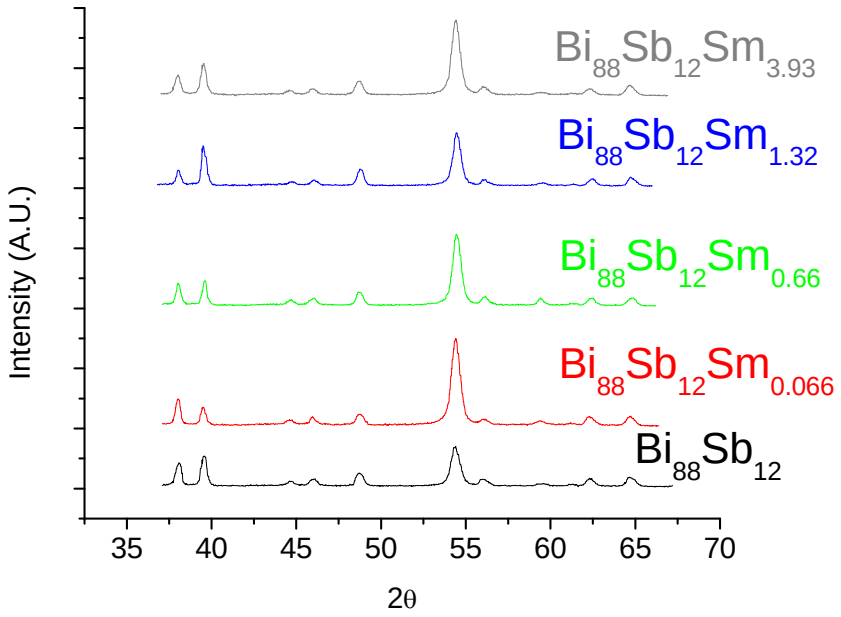


Figure 5.2: XRD patterns for all Sm doped samples. Data show the samples are single phase and alloyed similarly within the resolution of the machine.

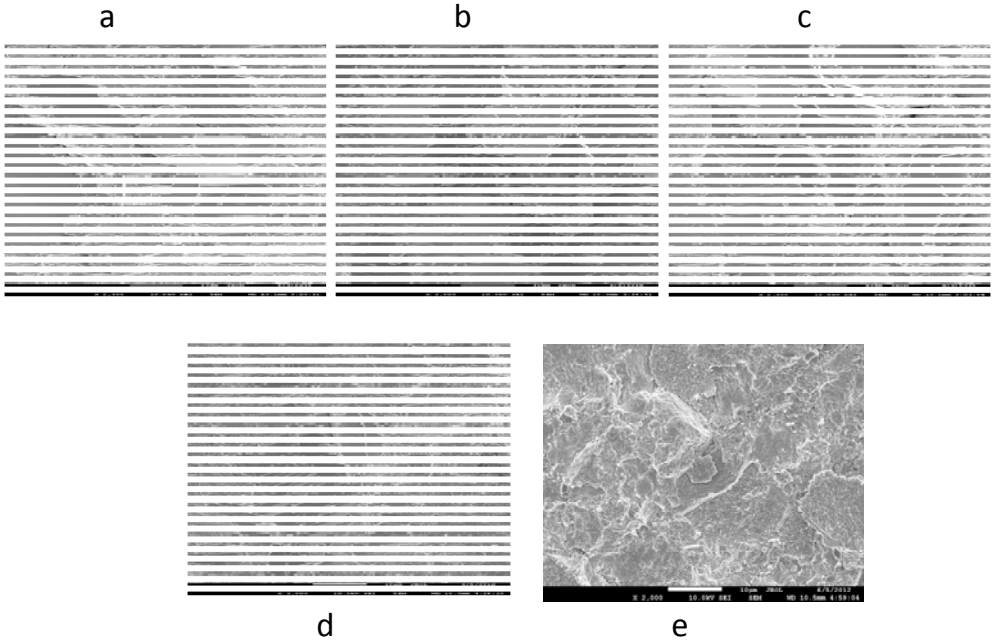


Figure 5.3: SEM images for samples $Bi_{88}Sb_{12}$ (a), 0.06Sm (b), 0.6Sm (c), 1Sm (d), and 3Sm (e).

The magnetic susceptibility of the Ce and Ho doped samples is plotted against temperature in Figure 5.4. The magnetic susceptibility is measured to ensure that the proper ratio of magnetic impurities are, in fact, in the sample. Problems arose in the VSM with our collaborators in Florida when trying to measure the Sm samples; based on the results of the Ce and Ho samples shown in Figure 5.4 and the similarity between the Ce-Bi, Sm-Bi, Ho-Bi phase diagrams, it is reasonable to assume as a first approximation that the intended percentage of Sm actually was incorporated into the sample. BiSb is typically diamagnetic; however, it can be seen that values for $\chi$ in Figure 5.4 are in fact positive demonstrating that the sample is paramagnetic. The shift to paramagnetism is due to the increased number of free carriers, as discussed below, free electrons are known to enhance paramagnetism [29]. The susceptibility is found to increase with increasing Ce and Ho doping concentration, as is expected from the introduction of magnetic

impurities, demonstrating that Ce and Ho are in fact assimilated into the solid solution. High enough temperatures could not be reached to perform an accurate Curie-Weiss fit for the magnetic susceptibility. However, it is interesting to note that we can still fit the data, though inaccurately, using the Curie-Weiss expression [29]

$$\chi = \chi_m + \frac{C}{\theta - T} \qquad 5.1$$

where $\chi_m$ is the diamagnetic susceptibility, $\theta$ is the Curie temperature, $T$ is the absolute temperature, and $C$ is a constant dependent upon the atomic mass of the magnetic impurity, the total J spin state, and the concentration of magnetic impurities in the sample. The atomic mass is constant and the value for J should remain unchanged, leading $C$ to only depend on the impurity concentration. If Figure 5.4 is fit using Eqn. 5.1, the values for $C$ can be calculated. While the fit is poor ($1/\chi$ vs. T is nonlinear), the value for $C$ scales with the Ce and Ho impurity concentration. This observation gives confidence that these impurities are not only assimilating into the BiSb solid solution but are also being incorporated in the solid solution according to the desired atomic ratios.

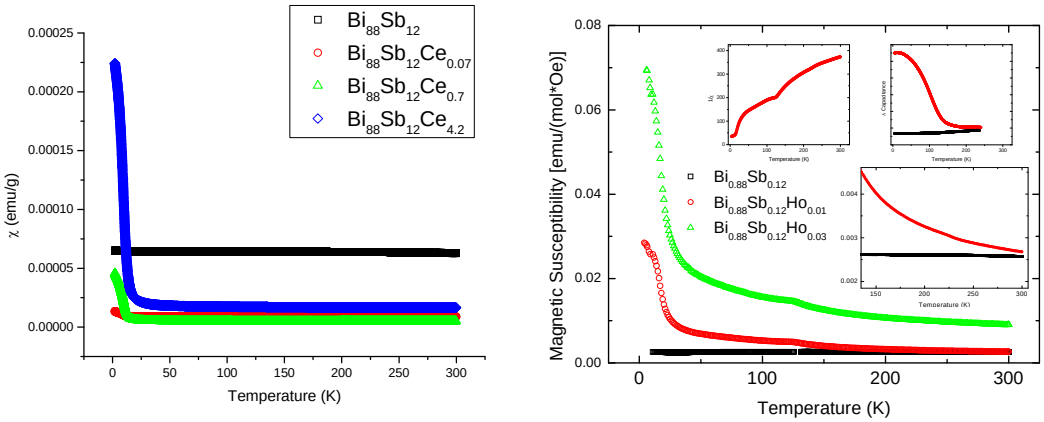

Figure 5.4: Magnetic susceptibility plotted against temperature for Ce doped (left) and Ho doped (right) $Bi_{88}Sb_{12}$. The insets of the right figure show the nonlinearity of $1/\chi$ vs. T as well as measurements made using a homemade torque cantilever magnetometer described in Chapter 3.

Electrical resistivity values for all samples are plotted versus temperature in Figure 5.5. From 5 K to approximately 100-200 K (depending on doping concentration), values of ρ for all samples, except 3Sm, increase with increasing temperature. This typical metallic-like behavior is due to an impurity band located in the conduction band; this impurity band has been experimentally measured and described by Lenoir *et al.* [3,4]. The impurity density dominates $\rho$ values up to a maximum at which point the temperature becomes high enough to excite carriers from the valence band to the conduction band across the thermal energy gap [4]. In this regime the intrinsic carrier concentration begins to dominate and all samples exhibit classical semiconducting behavior.

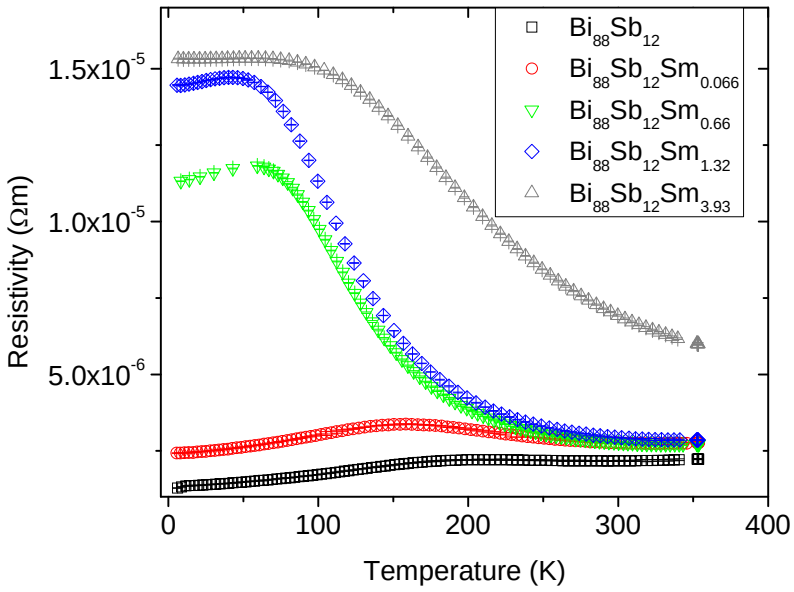


Figure 5.5: Resistivity plotted vs. temperature for all Sm doped samples.

Values for $\rho$ increase as the doping concentration is increased. Using a similar analysis to that of Lenoir, the thermal energy gap can be estimated using Arrhenius' Law [4]

$$\rho = \rho_o \exp\left(-\frac{\Delta E_g}{2k_B T}\right) \qquad 5.2$$

where $\rho_o$ is the zero temperature resistivity, $k_B$ is Boltzmann's constant, $T$ is the absolute temperature, and $\Delta E_g$ is the thermal gap size. Table 5.1 includes gap sizes from Sm samples as well as the previously studied Ho and Ce samples. It should be noted that the energy gaps for the parent compounds of both the Ce and Ho doped samples, 32 meV, are in agreement with previously determined gap sizes for similar stoichiometries [3,4]. The parent compounds for the Sm doped samples, however, exhibit more semimetallic behavior and have a negligible gap size. One possible explanation is that the sample is slightly off the desired $Bi_{88}Sb_{12}$ stoichiometry, and, as previously discussed, the band structure of BiSb is highly dependent on Sb concentration [5, 12-13]. In the present study, it is the relative change that is important, and for that reason each independently prepared set of samples (Ho, Ce, Sm) are doped from the same initial batch and the parent for each set is always measured. The addition of the smallest amount of Sm increases the gap size, and the energy gap is further increased with increasing Sm doping, reaching a maximum value of 47 meV for sample 3Sm. Similar results are found for both the Ce and Ho doped samples as shown in Table 5.1.

| Doping % | 0 Sm | 0.066 Sm | 0.66 Sm | 1.32 Sm | 3.93 Sm | 0 Sm | .066 Sm | .66 Sm | 1.32 Sm | 3.93 Sm | 0 Ce | .07 Ce | .7 Ce | 34.2 Ce | 0 Ho | 1 Ho | 3 Ho |
|---|---|---|---|---|---|---|---|---|---|---|---|---|---|---|---|---|---|
| BM (hours) | 12 | 12 | 12 | 12 | 12 | 6 | 6 | 6 | 6 | 6 | 6 | 6 | 6 | 6 | 12 | 12 | 12 |
| HP (°C) | 240 | 240 | 240 | 240 | 240 | 200 | 200 | 200 | 200 | 200 | 200 | 200 | 200 | 200 | 240 | 240 | 240 |
| $E_g$ (meV) | - | 17 | 40 | 40 | 47 | - | 40 | 47 | 44 | 45 | 32 | 41 | 42 | 44 | 30 | 40 | 47 |

Table 5.1: Estimated thermal energy gap, $E_g$, using equation 5.2 for Ce, Sm, and Ho doped samples under different fabrication conditions for ball milling (BM) time and hot pressing (HP) temperature.

The Hall coefficient is negative for all samples over the entire temperature range, signifying that the dominant carriers are electrons. The carrier concentrations and mobilities plotted in Figure 5.6 are in agreement with the impurity band model. The carrier concentration values are relatively constant at lower temperatures, where charge transfer is dominated by an impurity band, and the carrier density due to impurities should be independent of temperature. At higher temperatures $k_BT$ is near the energy required to excite carriers from the valence to the conduction band, and electronic conduction is due to both electrons and holes in this intrinsic region of the semiconductor, where values for $\rho$ begin to decrease as the temperature is increased. In the intrinsic region the single carrier expression for the Hall coefficient, $R_H=1/nq$, is no longer valid and must be replaced by the two carrier expression $R_H=1/(n+p)q$ [30]. The carrier concentration is much higher than previously reported values for single crystals at low temperatures [31] which leads to positive $\chi$ values as discussed above. The carrier concentration is slightly decreased with the addition of 0.066 % Sm doping, and further decreased with 0.66% and slightly further with 1.32% Sm addition. The widening of the band gap explains the decrease in carrier concentration. Sample 3Sm has a carrier

concentration slightly greater than the parent compound which is due to the fact that there is an increased number grain boundaries, as seen in Figure 5.3, and this increase in grin boundaries leads to an increased number of carriers [34].

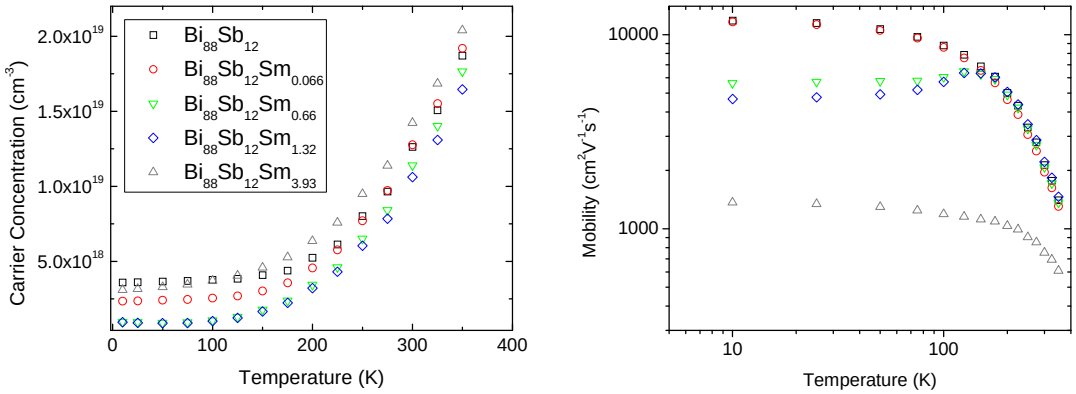


Figure 5.6: Carrier concentration (left) and carrier mobility (right) for all Sm doped samples plotted against temperature.

The magnitude of the mobility at lower temperature is very high due to the non parabolic band structure and quasi-ellipsoidal Fermi surfaces of Bi rich BiSb alloys [4]. From lower temperature, in the metallic-like regime, the mobility slightly decreases as the temperature increases, which leads to increasing values for $\rho$ with $T$. The mobility is unchanged by the addition of 0.066 % Sm and decreased by the addition of 0.66 and 1.32 % Sm. The introduction of 3.93 % Sm drastically reduces the mobility which could be due to both increased electron-electron interactions from the higher carrier concentration as well as the decreased carrier mean free path due to the smaller grain sizes as seen in the SEM images. It is interesting to note that there is a slight peak in the $\mu_H$ versus $T$ plot for samples 0.6Sm and 1Sm, which could be evidence of a change in the scattering parameter since $\mu_H$ is proportional to $T^{s-1}$ where $s$ is the scattering parameter. Another possible explanation for the peak in the mobility, which is found in the temperature range

where the electrical conduction is intrinsic, is that there is a slight alteration of the band structure due the Sm doping; as shown in Table 5.1 the gap size increases with increasing Sm doping. It is possible that initially only highly mobile carriers from the L valence band [4] contribute to electrical transport, and then as the temperature rises above 175 K the other heavier valence H and T bands [4] begin to contribute holes leading to identical mobility values as the parent compound. There are identical peaks in the optimally doped Ho and Ce $Bi_{88}Sb_{12}$ shown in Appendix D [27-28].

The Seebeck coefficient versus temperature is plotted in Figure 5.7 and is negative over the entire temperature range, confirming that electrons are the dominant carriers. The data qualitatively agrees quite well with the impurity band model. At lower temperatures the thermopower for all samples varies linearly with T which is typical of a degenerate system and is expected based on the metallic-like temperature dependence of the resistivity. The Seebeck coefficient increases with decreasing carrier concentration as the doping concentration is altered from 0.06Sm to 1Sm, typical of diffusive transport. As the temperature increases, carriers from the valence band are excited into the conduction band and the intrinsic semiconducting properties begin to dominate leading to a maximum in the *S* vs. *T* plot. While in the intrinsic region the electrical conductivity can be written as the simple sum of the hole and electron conductivities, the Seebeck coefficient is given as in Chapter 1

$$S = \frac{S_h \sigma_h + S_e \sigma_e}{S_h + S_e} \qquad 5.3$$

where $S_h$ and $S_e$ are the hole and electron contributions to the Seebeck coefficient and $\sigma_h$

and $\sigma_e$ are the hole and electron contributions to the electrical conductivity, respectively. The fact that $S$ remains negative even at higher temperatures is evidence that the hole conductivity is not the dominant contribution to the total electrical conductivity; this is in agreement with previous studies which demonstrate that the hole mobilities are much lower in alloyed BiSb than in pure Bi [4].

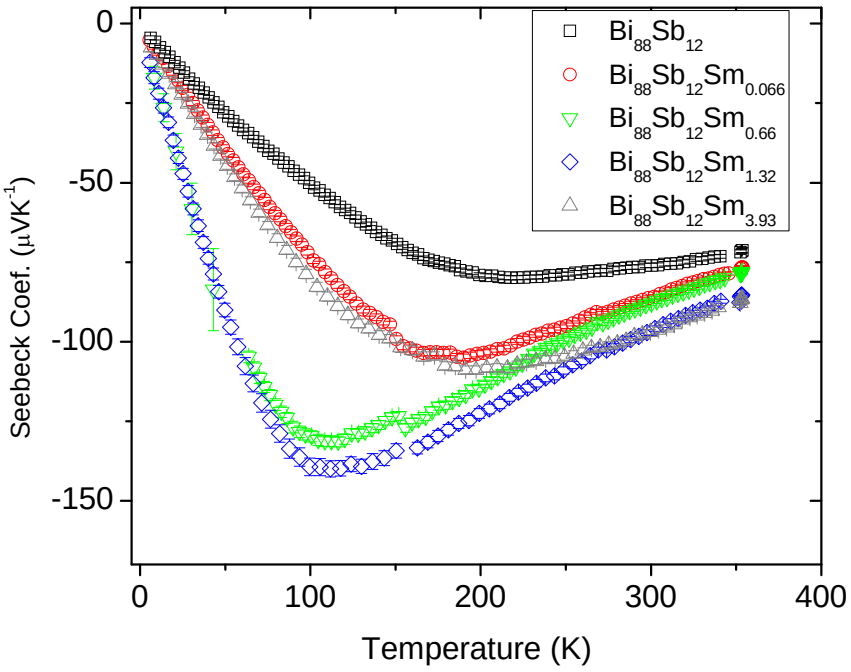


Figure 5.7: Seebeck coefficient for all Sm doped samples plotted against temperature.

The temperature dependence of the total thermal conductivity ($\kappa_{total}$) is plotted in Figure 5.8 for all samples where $\kappa_{total}$ decreases with increasing Sm doping concentration due to the Sm atoms scattering phonons, and for sample 3Sm the reduction in $\kappa$ is due to the increased number of grain boundaries as well. The total thermal conductivity is given by the sum of the individual contributions from the lattice and the carriers. For semiconducting materials the carrier contribution is given by the sum of both unipolar

and bipolar terms [32]. Therefore $\kappa_{total}$ can be written as [32]

$$\kappa_{total} = \kappa_l + \kappa_e + \kappa_b \qquad 5.4$$

where $\kappa_l$, $\kappa_e$, and $\kappa_b$ are the lattice, electronic, and bipolar thermal conductivities respectively. The total thermal conductivity rises from lower temperatures up to a maximum at around 20 K, then decreases down to a minimum before rising again as temperature continues to increase. The maximum at lower temperatures is typical of the interplay between different phonon scattering mechanisms [33]. The increase in $\kappa_{total}$ at higher temperatures is due to the bipolar contribution and can be seen to occur at the same temperature at which the magnitude of the Seebeck coefficient begins to decrease.

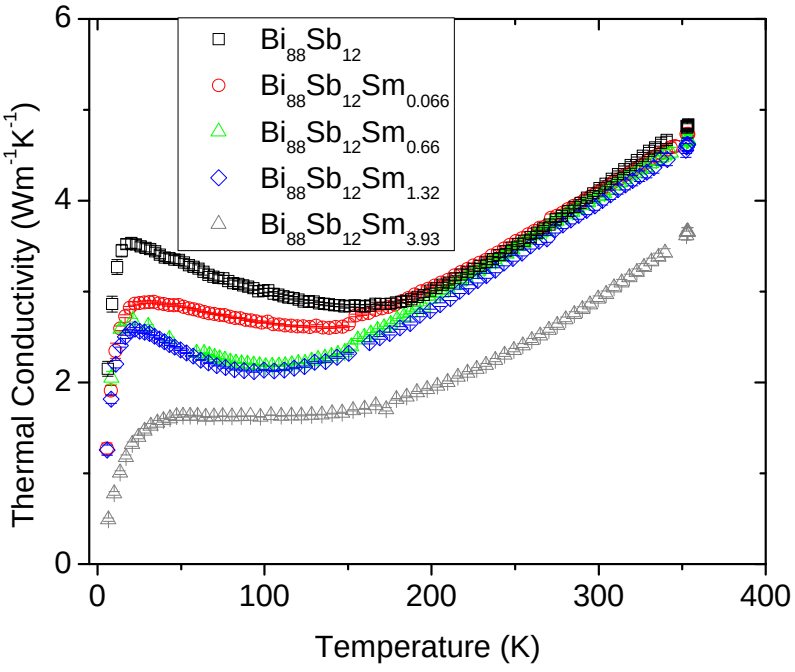


Figure 5.8: Thermal conductivity for all Sm doped samples plotted against temperature.

*ZT* is plotted in Figure 5.9 for all Sm doped samples and *ZT* increases with increasing Sm doping for all samples except 3Sm. The enhancement comes from the slight decrease in thermal conductivity as well as the increased Seebeck coefficient which is a result of the decreased carrier concentration. Sample 3Sm has a *ZT* value that is drastically lower than all samples which is completely due to the reduced mobility which both increases $\rho$ and decreases *S*.

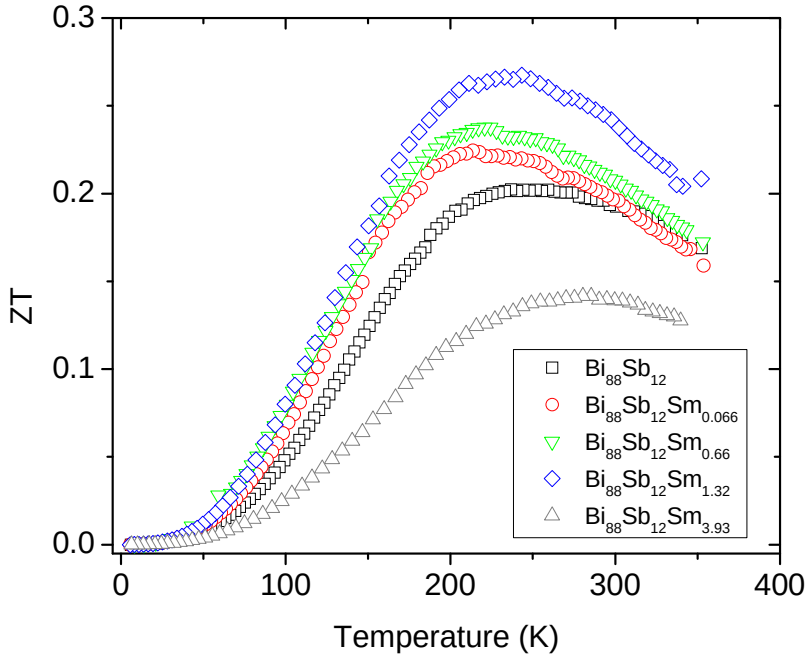


Figure 5.9: *ZT* for all Sm doped samples plotted against temperature

Figure 5.10 plots all transport data for the Sm doped samples prepared via ball milling for 6 hours and hot pressing at 200 $^{o}$C. The results are similar to the Sm samples that were ball milled for 12 hours and presented in Figures 5.2-5.9 and can be analyzed in the same manner. The electrical resistivity, shown in Figure 5.10a, increases with increasing Sm concentration; the largest change in the resistivity is due to the lowest

doping concentration. Figure 5.10b plots the temperature dependence of the Seebeck coefficient where the largest enhancement in the magnitude of *S* is due to the lowest doping concentration along with a shift in the peak of *S* to lower temperature. The total thermal conductivity is plotted in Figure 5.10c and is seen to decrease with increasing Sm doping. The overall effect on *ZT* is plotted in Figure 5.10d where there is a slight enhancement at the lower doping concentrations based on the enhancement in *S* and reduction in $\kappa_{total}$. The main difference between the two sets of Sm samples lies in that the transport properties are most drastically changed by the lowest doping concentration for the 200 $^{o}$C hot pressed samples.

The results in Figure 5.10 are identical to those of the Ce doped samples prepared under the same conditions [28], while the results for the Sm doped samples prepared by ball milling for 12 hours and hot pressing at 240 $^{o}$C are the same as the Ho doped samples [27]. The difference in the transport properties between the two different preparation methods is most likely due to the difference in ball milling time. It is known that high energy ball milling enhances the solubility of materials [34]. Also, there is no solubility at room temperature of Ce, Ho, and Sm in Bi according to the phase diagrams. It is likely that Bi rich $Bi_{88}Sb_{12}$ will have a solubility close to that of pure Bi, and therefore it is reasonable that the transport properties are enhanced at a higher doping concentration with longer ball milling times.

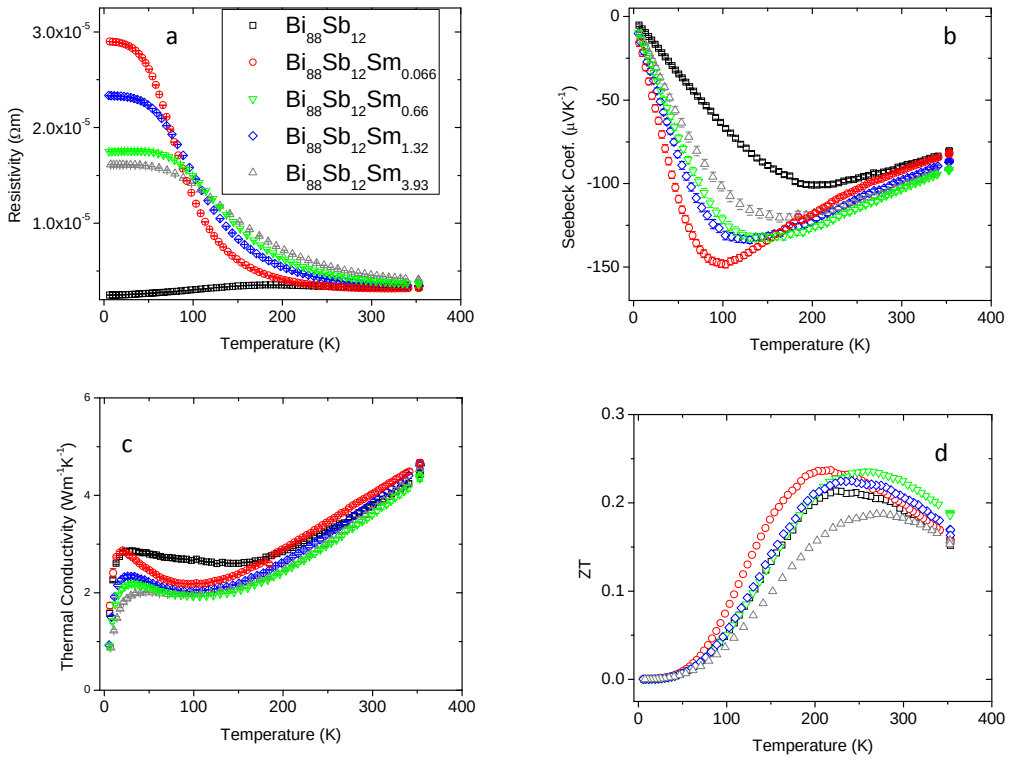


Figure 5.10: The temperature dependence of the resistivity (top left), Seebeck coefficient (top right), thermal conductivity (bottom left), and *ZT* (bottom right) for all Sm doped samples prepared at a hot pressing temperature of 200 $^{o}$C.

The present study of Ce, Sm, and Ho doped $Bi_{88}Sb_{12}$ all show similar enhancements in thermoelectric transport properties. From the current study it is believed that the differences in the effects of doping percentage are due to the difference in ball milling times. As mentioned previously Ce, Sm, and Ho all have quite different magnetic moments with effective Bohr magneton moments of 2.4, 1.5, and 10.4 respectively [35]. The fact that the transport properties are all similarly affected seems to lead to the conclusion that it is not the magnetic moment that is responsible for this enhancement. Fe has a similar moment to that of Ce and was also doped into the $Bi_{88}Sb_{12}$ alloy. While the resistivity increases, there is no enhancement of the Seebeck coefficient which further confirms that the change in transport properties is not due to the magnetic

moments of the impurities. From this study it seems probable that the changes seen in the Ce, Sm, and Ho doped samples are due to some other effect, likely a mass effect, though further investigation is required.

### 5.3.1 Separation of $\kappa_{lattice}$ and $\kappa_{carrier}$

At lower temperatures, T < 100 K, the bipolar contribution is negligible and $\kappa_{total}$ is the sum of $\kappa_{carrier}$ and $\kappa_{lattice}$. Because the mobility is so high in BiSb alloys, the condition for a classically large magnetic field $\mu B >> 1$ is satisfied and $\kappa_{carrier}$ and $\kappa_{lattice}$ can be separated using a magnetic field. This technique, described in detail previously in Chapter 3, is used to directly measure $\kappa_l$ below 100 K. It can be seen in Appendix C that the lattice portion of the thermal conductivity dominates at lower temperatures as has been previously determined [3]. It is our intention to fit the magnetic field data using the full phonon dispersion, as previously described, in order to quantify the effects of the doping on phonon scattering [36]. However, at this time further work is required theoretically in order to fit the data and so give a quantitative analysis, see Appendix C.

## 5.4 Conclusion

The $Bi_{88}Sb_{12}$ alloy has been doped with 0, 0.066, 0.66, 1.32, and 3.93 % Sm and prepared under two different fabrication conditions. The first being ball milled for 12 hours and hot pressed at 240 $^{o}$C and the second ball milled for 6 hours and hot pressed at 200 $^{o}$C. The results are in agreement with Ce and Ho samples prepared under similar

conditions. A slight *ZT* enhancement is seen due to doping which is the effect of an enhanced Seebeck coefficient as a result of a decrease in the carrier concentration, most likely caused by a widening band gap. The alteration of the band gap does not appear to be caused by the magnetic moments of Ce, Sm, and Ho based on the similar change to the gap size with the widely varying magnetic moments of the dopants. Also, similar results were not obtained with Fe doped samples, where Fe has a magnetic moment similar to Ce and greater than Sm.

## 5.5 References


1. G. E. Smith, R. Wolfe J Appl Phys **33**, 84 (1962).
2. R. Wolfe, G. E. Smith Appl. Phys. Lett. **1**, 5 (1962).
3. B. Lenoir, M. Cassart, J. P. Michenaud, H. Scherrer, S. Scherrer J. Phys. Chem. Solids **59**, 129 (1998).
4. B. Lenoir, M. Cassart, J. P. Michenaud, H. Scherrer, S. Scherrer J. Phys. Chem. Solids **57**, 89 (1996).
5. A. L. Jain Phys. Rev. **114**, 1518 (1959).
6. M. R. Ellet, R. B. Horst, L. R. Williams, K. F. Cuff J. Phys. Soc. Jpn. **21**, 666 (1966).
7. P. W. Chao, H. T. Chu, Y. H. Kao Phys. Rev. B **9**, 4030 (1974).
8. G. Oelgart, B. Schneider, W. Kraak, R. Herrmann Phys. Status Solidi (b) **74**, K75 (1976).
9. W. Kraak, G. Oelgart, G. Schneider, R. Herrmann Phys. Status Solidi (b) **88**, 105

(1978).

10. H. Kitagawa, H. Noguchi, T. Kiyabu, M. Itoh, Y. Noda J. Phys. Chem. Solids **65**, 1223 (2004).

11. W. M. Yim, A. Amith Solid-State Electron. **15**, 1141 (1972).

12. S. Golin Phys. Rev. **176**, 830 (1968).

13. N. B. Brandt, R. Hermann, G. I. Golysheva, L. I. Devyatkova, D. Kusnik, W. Kraak, Y. G. Ponomarev Sov. Phys. JETP **56**, 1247 (1982).

14. E. E. Mendez PhD Thesis (MIT 1979).

15. N. B. Brandt, E. A. Svistova J. Low Temp. Phys. **2**, 1 (1970).

16. K. Hiruma, G. Kido, K. Kawauchi, N. Miura Sol. St. Comm. **33**, 257 (1980).

17. N. B. Brandt, S. M. Chudinov Sov. Phys. JETP. **32**,815 (1971).

18. E. E. Mendez, A. Misu, M. S. Dresselhaus Phys. Rev. B **24**, 639 (1981).

19. X. Devaux, F. Brochin, R. Martin-Lopez, H. Scherrer J. Phys. Chem. Solids **63**, 119 (2002).

20. R. Martin-Lopez, A. Dauscher, H. Scherrer, J. Hejtmanek, H. Kenzari, B. Lenoir Appl. Phys. A **68**, 597 (1999).

21. J. W. Sharp, E. H. Volckmann, H. J. Goldsmid Phys. Status Solidi (a) **2**, 257 (2001).

22. A. D. Belaya, S. A. Zayakin, V. S. Zemskov J. Adv. Mater. **2**, 158 1994.

23. G. A. Ivanov, V. A. Kulikov, V. L. Naletov, A. F. Panarin, A. R. Regel Sov. Phys. Semicond. **7**, 1134 (1973).

24. H. J. Liu, L. F. Li J. Alloys Comp. **433**, 279 (2007).

25. S. Dutta, V. Shubha, T. G. Ramesh, F. D'Sa J. Alloys Comp. **467**, 305 (2009).

26. T. M. Tritt Recent Trends in Thermoelec. Mat. Research. (Academic Press, Boston 2001).

27. K. C. Lukas, G. Joshi, K. Modic, Z. F. Ren, C. P. Opeil J. Mater. Sci. **47**, 5729 (2012).

28. K. C. Lukas, H. Zhao, R. L. Stillwell, Z. F. Ren, C. P. Opeil MRS Online Proc. Library mrss12-1456-jj01-04 doi:10.1557/opl.2012.1368 (2012).

29. B. D. Cullity, C. D. Graham Intro. to Magnetic Materials (IEEE Press, New Jersey 2009).

30. D. K. Schroder Semicon. Mater. Device Charac. (John Wiley & Sons, Inc, New York 1998).

31. T. Hattori J. Phys. Soc. Jpn. **29**, 5, 1224 (1970).

32. G. S. Nolas, J. Sharp, H. J. Goldsmid Thermoelectrics: Basic Principles and New Materials Developments (Springer 2001).

33. T. M. Tritt Thermal conductivity (Kluwer Academic/Plenium Publishers, New York 2003).

34. C. Suryanarayana Prog. in Mater. Sci. **46**, 1 (2001).

35. N. E. Ashcroft, N. D. Mermin Solid State Physics (Saunders College Publishing, New York 1976).

36. M. Zebarjadi, J. Yang, K. Lukas, B. Kozinsky, B. Yu, M. S. Dresselhaus, C. P. Opeil , Z. F. Ren, G. Chen J. App. Phys **112**, 044305 (2012).

# Chapter 6: Conclusion

## 6.1. Overview

Overall during this research, measurement equipment has been built and utilized to study various thermoelectric compounds. The studies presented in this thesis have led to several publications in peer reviewed journals. Several collaborations have led to further publications, all of which can be found in Appendix D. A brief summary will be given along with possible future work.

Chapter 2 describes the construction of a high temperature apparatus to measure the Seebeck coefficient and electrical resistivity. The ability to make continuous measurements as well as measure arbitrarily shaped samples is the main benefit of the setup. Chapter 3 describes the PPMS from Quantum Design along with steps taken to use this equipment in a somewhat novel fashion in order to determine the individual components of the thermal conductivity. The agreement between low and high magnetic field measurements had not been previously demonstrated. And it had not been previously demonstrated that the low magnetic field techniques could be used on nanostructured thermoelectrics. Chapter 4 discusses a systematic study to determine why a particular thermoelectric device was degrading. It can be seen that the degradation is not due to the diffusion of the Ni barrier as previously thought leading the way to alternate solutions in device fabrication. Finally in Chapter 5 BiSb alloys are doped with Ce, Sm, and Ho. It is seen that the overall Figure of Merit is increased from the dopants most likely due to a size effect.

## 6.2. Future Work

While a great amount of work has been accomplished and presented in this thesis, there is always room for improvement and future work. The following will provide some direction as to how these projects can progress further.

For the high temperature setup in Chapter 2, the quickest improvement that can be made is to reach higher temperature. This can be accomplished through the addition of a second cartridge heater. Work is also currently underway to fabricate thin probes that can allow for the measurement of resistivity for small single crystals. The Seebeck measurement can be improved through an investigation into thermal contact resistance. I have put much time and effort into this study and after several attempts and discussions with NIST employees ceased in my efforts as this is a highly non trivial problem that would most likely require the majority of a thesis work to attempt to solve, if it can accurately be solved at all. The Seebeck setup can also be used to measure large temperature gradients which are of importance in thermoelectric devices.

The determination of the lattice and electronic portions of the thermal conductivity is quite interesting and future work is included in Chapter 3. Also of interest in the determination of the thermal conductivity are electron-phonon interactions. At this time there are limited experimental techniques that can probe this interaction. It is possible that the methods presented in Chapter 3 could aid in this study, though a distinct systematic study has not yet been devised.

As discussed in Chapter 4 it would be interesting to create a device out of the

material studied with a nickel diffusion barrier and study the efficiency. If there is degradation, there is most likely some other problem besides the diffusion of the contact material into the device. Also cobalt could be an interesting choice of diffusion barrier as it has a similar coefficient of thermal expansion to that of both the p-type and n-type legs.

Finally in Chapter 5 with the amount of experimental data taken it would be nice if more theoretical work can be done to determine the cause of the enhancement of the transport properties; this work is presently underway with our collaborators. It could also be beneficial to perform a study of the microstructure as well as look at fabricating single crystals containing a small doping percentage to see if any information can be gleaned from that.

## 6.3. Conclusion

In conclusion, many successful studies have been performed and have been discussed throughout this work. There have also been several collaborative efforts that have led to publications both in and out of the field of thermoelectrics. These works are included in Appendix D.

# Appendix A: High Temperature Apparatus

## A.1 Benchmarking

Figures A1-A9 plot the temperature dependence of the resistivities for different samples measured by both the commercially available ZEM and the constructed setup. Skutterudites, of varying stoichiometry and grain size, were used as they are pressed at higher temperatures and therefore have repeatable properties after cycling as demonstrated in the "Results" section of the main text. Differences between the measured samples are always within experimental uncertainty. The absolute deviation between the ZEM and VDP measurements never exceeds 9%, while deviation never exceeds 3% for bar shaped samples.

Figures A5 and A6 plot the resistivity of the same sample measured by the two different methods. A disk shaped sample was first polished to the proper thickness and then measured using the VDP technique (Figure A5). From the disk a bar was cut and measured in the ZEM, this same bar was then measured in the described setup using the four point method and is shown in Figure 6. It is seen that even when the bar is cut from the same disk shaped sample, there is a greater absolute deviation, though still showing agreement within experimental uncertainty, for the VDP technique as opposed to the four point probe technique. Reasons for the disagreement are discussed in the manuscript.

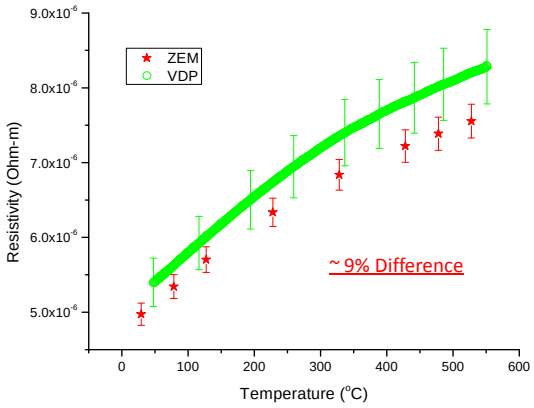


Figure A1: Resistivity for Sample 1 measured by both the ZEM and using the VDP technique. Absolute disagreement never exceeds 9%.

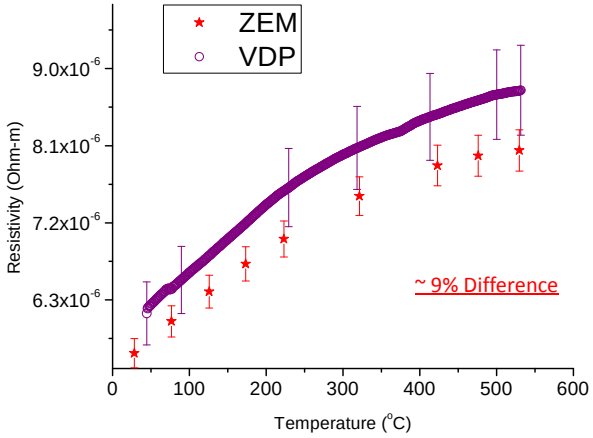


Figure A2: Resistivity for Sample 2 measured by both the ZEM and using the VDP technique. Absolute disagreement never exceeds 9%.

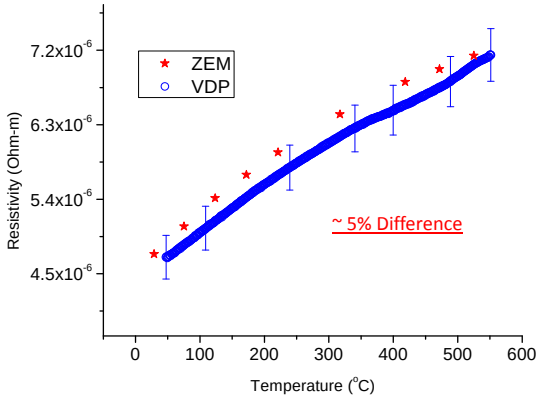


Figure A3: Resistivity for Sample 3 measured by both the ZEM and using the VDP

technique. Absolute disagreement never exceeds 5%.

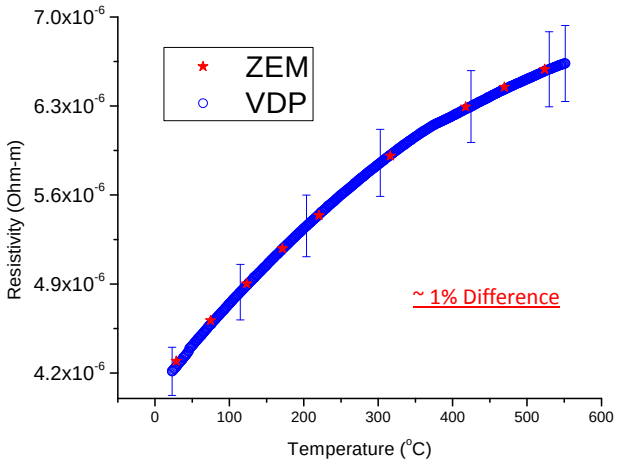


Figure A4: Resistivity for Sample 4 measured by both the ZEM and using the VDP technique. Absolute disagreement never exceeds 1%.

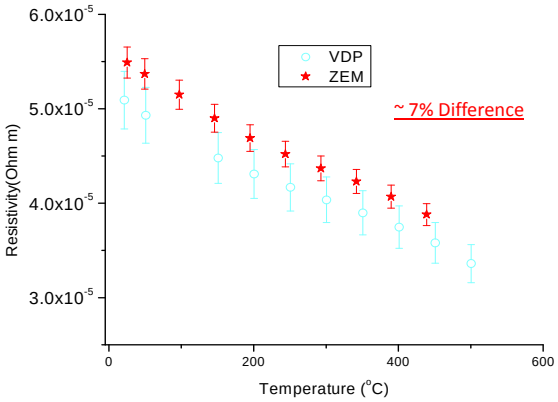


Figure A5: Resistivity for Sample 5 measured by both the ZEM and using the VDP technique. Absolute disagreement never exceeds 7%. A bar was cut from the disk and measured by the ZEM as well as using the four point probe technique as shown in Figure 6.

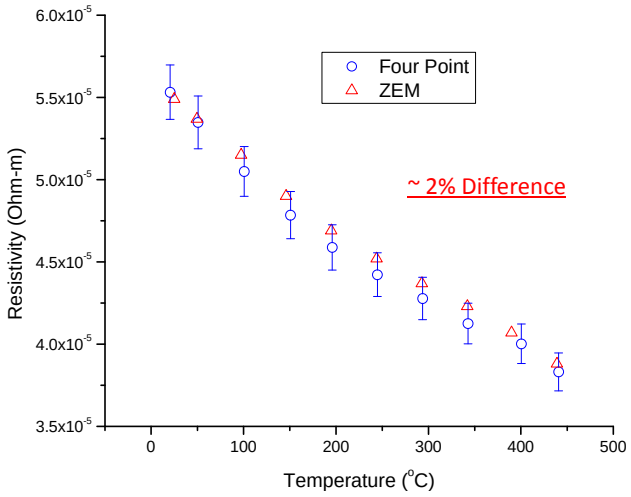


Figure A6: Resistivity for Sample 5 measured by both the ZEM and using the four point probe technique. This bar shaped sample was cut from the VDP disk measured in Figure 5. Absolute disagreement never exceeds 2%.

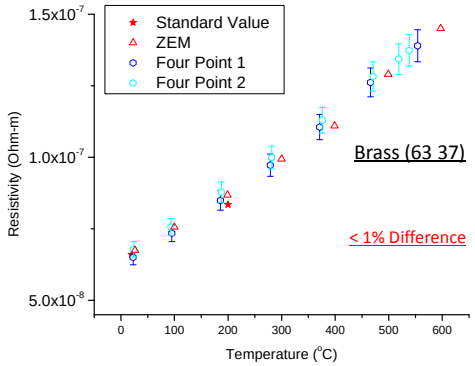


Figure A7: Resistivity for 63/37 Brass measured by both the ZEM the four point probe technique. Also included are standard values at two temperatures. Absolute disagreement never exceeds 1%.

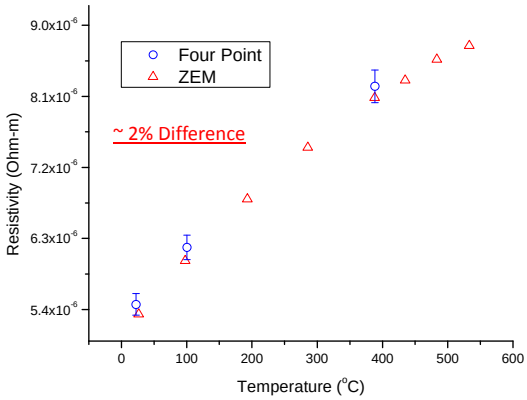


Figure A8: Resistivity for Sample 6 measured by both the ZEM and using the four point

probe technique. The measurements were made at three discrete temperatures. Absolute disagreement never exceeds 2%.

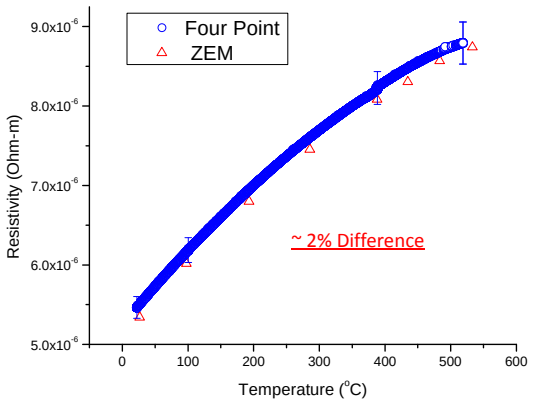


Figure A9: Resistivity for Sample 6 measured by both the ZEM and using the four point probe technique. The measurements were made continuously over the temperature range on the same sample measured in Figure 8. Absolute disagreement again never exceeds 2%.

Figures A10 – A13 plot the Seebeck coefficient as a function of temperature for different samples run on both the ZEM as well the high temperature setup (HTSM). Error bars are not shown, but there is excellent agreement between the two measurement methods. Measurements shown in Figures A10 and A11 were made on the same disk, one parallel to the pressing direction and one perpendicular to the pressing direction. In order to measure perpendicular to the pressing direction two cuts were made on the half inch diameter 3 mm thick disks to create two rectangular faces for the pressure contacts to be applied.

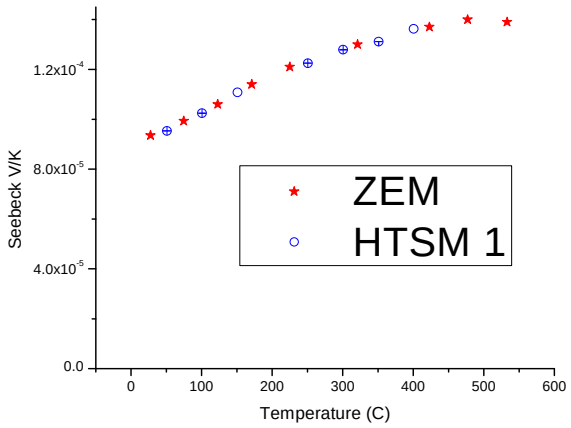


Figure A10: Seebeck coefficient for $Nd_{.9}Fe_{3.5}Co_{.5}Sb_{12.05}$ measured on a disk shaped sample parallel to the pressing direction measured by both the ZEM and HTSM. Disagreement does not exceed 8 %.

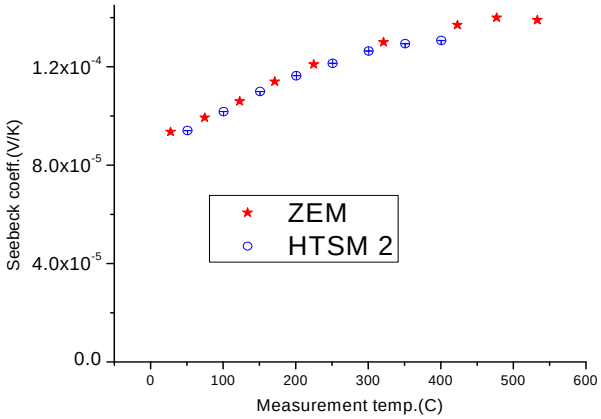


Figure A11: Seebeck coefficient for $Nd_{.9}Fe_{3.5}Co_{.5}Sb_{12.05}$ measured on a disk shaped sample perpendicular to the pressing direction measured by both the ZEM and HTSM. Disagreement does not exceed 10%.

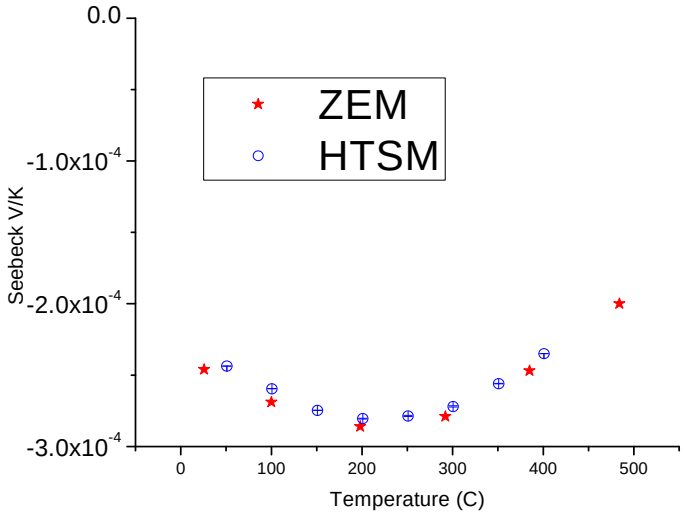


Figure A12: Seebeck coefficient for $CoSb_3$ measured on a disk shaped sample parallel to the pressing direction measured by both the ZEM and HTSM. Disagreement does not exceed 10%.

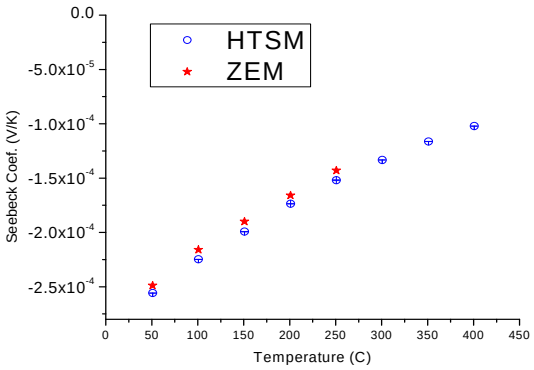


Figure A13: Seebeck coefficient for $Cu_{.01}Bi_2Te_3$ measured on a disk shaped sample perpendicular to the pressing direction measured by both the ZEM and HTSM. Disagreement does not exceed 4%.

A.2 Benefits of High Temperature Resistivity Measurement Setup

The ability to make continuous measurements can be of great advantage in trying to study and optimize materials. Below are some of the benefits of the system. Figure A14 plots $Cu_2Se$ measured by both the ZEM and the constructed setup. It is readily apparant that the continuous measurement gives a better idea of the transition temperature

as opposed to the discrete measurements made every twenty five degrees given by the ZEM. Other benefits are included in the published work that can be found in Appendix D.

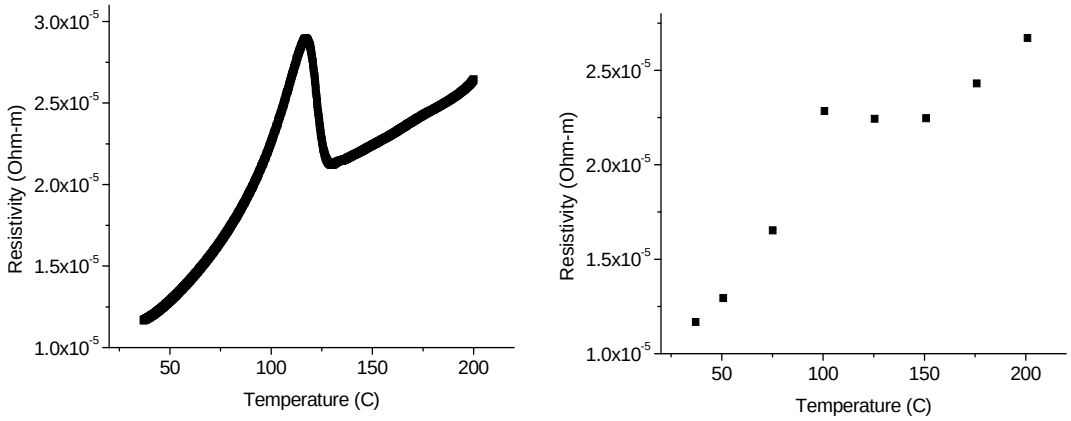


Figure A14: Comparison between the continuous measurement made on the constructed setup described in Chapter 2 (left) and data from the ZEM (right).

Appendix B: Comparison of Seebeck Coefficient

Values for the Seebeck coefficient as a function of temperature are plotted in Figures B1-B4. It can be seen that there is excellent agreement between the commercially available ZEM and PPMS as well as the constructed setup described in Chapter 2. Two separate sets of samples were fabricated and measured. All samples are plotted individually to demonstrate agreement on two separate sets of samples measured on all the available equipment. Here the SS contacts were used for the HTSM which leads to the slight deviation at higher temperature. If brass contacts were used, agreement would be enhanced as shown in Appendix A.

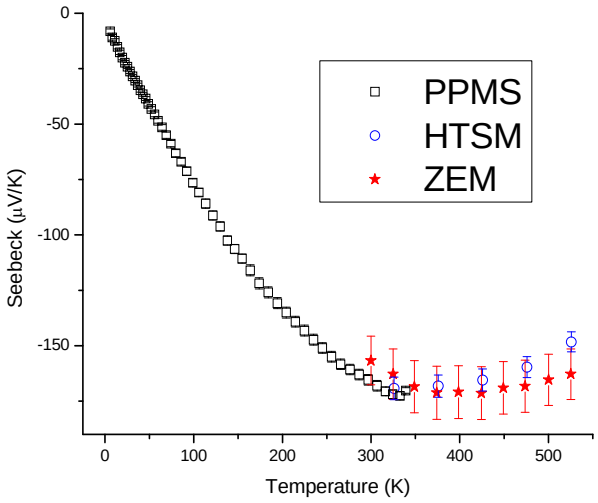


Figure B1: Seebeck coefficient plotted against temperature for $[Cu_{0.01}Bi_2Te_{2.7}Se_{0.3}]_{0.98}Co_{0.02}$ measured by the ZEM, PPMS, and constructed apparatus from Chapter 2. Measurements were made on two different samples. The PPMS and HTSM measurements were made on the same sample. An alternative sample was fabricated and measured on the ZEM.

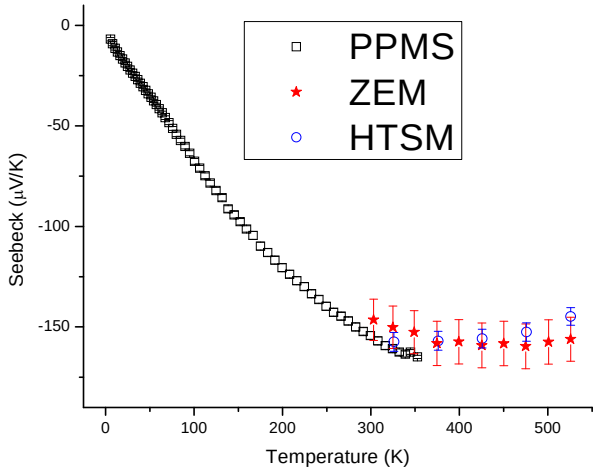


Figure B2: Seebeck coefficient plotted against temperature for $[Cu_{0.01}Bi_2Te_{2.7}Se_{0.3}]_{0.98}Ni_{0.02}$ measured by the ZEM, PPMS, and constructed apparatus from Chapter 2. Measurements were made on two different samples. The PPMS and HTSM measurements were made on the same sample. An alternative sample was fabricated and measured on the ZEM.

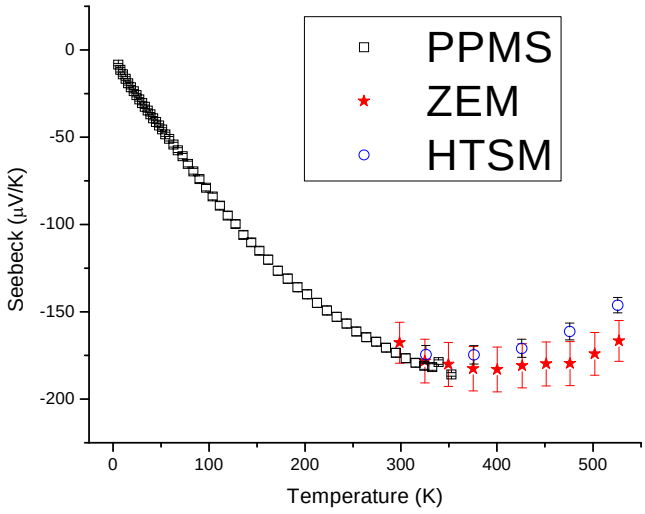


Figure B3: Seebeck coefficient plotted against temperature for $[Cu_{0.01}Bi_2Te_{2.7}Se_{0.3}]_{0.98}Fe_{0.02}$ measured by the ZEM, PPMS, and constructed apparatus from Chapter 2. Measurements were made on two different samples. The PPMS and HTSM measurements were made on the same sample. An alternative sample was fabricated and measured on the ZEM.

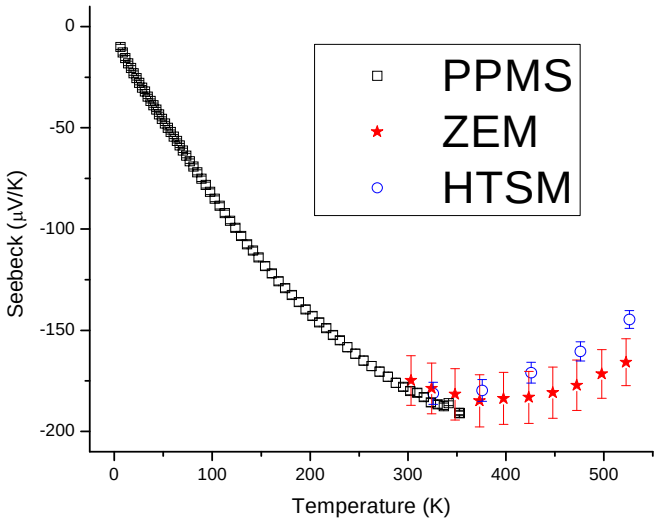


Figure B4: Seebeck coefficient plotted against temperature for $[Cu_{0.01}Bi_2Te_{2.7}Se_{0.3}]_{0.98}Mn_{0.02}$ measured by the ZEM, PPMS, and constructed apparatus from Chapter 2. Measurements were made on two different samples. The PPMS and HTSM measurements were made on the same sample. An alternative sample was fabricated and measured on the ZEM.

# Appendix C: $\kappa_{lattice}$ and $\kappa_{electronic}$ Separation

## C.1. Two Point Versus Four Point κ Measurement

Shown in Figure C1 is the comparison between the two point and four point thermal conductivity measurement taken on the sample of $FeSb_2$ shown in Figure C2. First the thermal conductivity was measured in the normal two point configuration as describd in Chapter 3. Second thin Cu wires were wrapped around the sample and soldered together, silver paint was then used to create a thermal link between the sample and the wire, and finally the thin portions of the gold coated OFHC disks were soldered to the wire so that the TTO shoe could be attached again as shown in Figure C2.

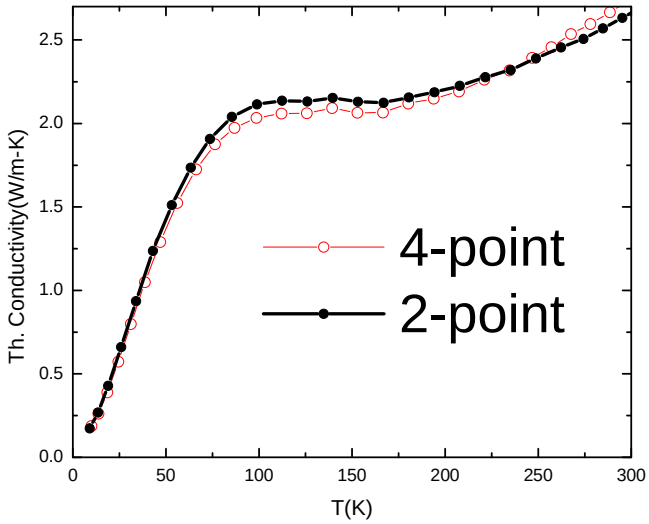


Figure C1: Comparison of thermal conductivity measurement made on the same sample of $FeSb_2$ hot pressed at 300 $^{o}$C in both a two point configuration as shown in Chapter 3 and a four point configuration as shown in Figure C2. There is negligible difference between the two methods demonstrating that effects of thermal contact resistance can be ignored.

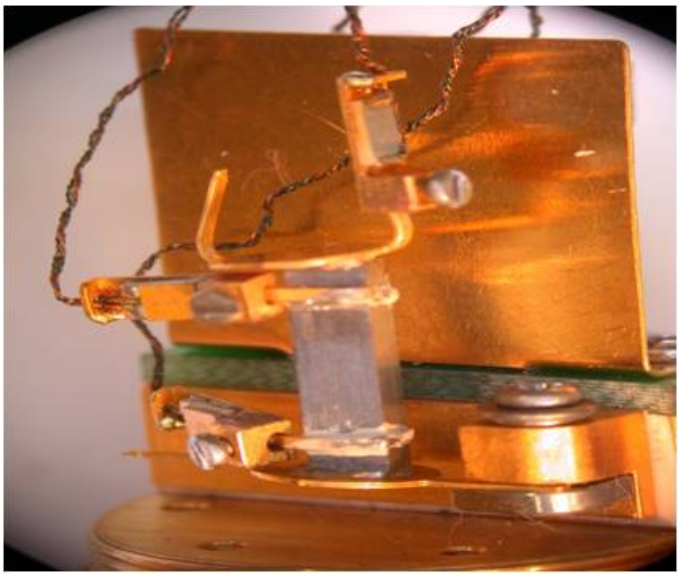

Figure C2: Sample prepared in a four point configuration for the thermal conductivity measurement plotted in Figure C1.

C.2. Thermal Conductivity Measurements in Magnetic Field

Figures C3-C12 plot the measured thermal conductivity in zero field as well as in nine Tesla. It is assumed that the nine Tesla measurement is a direct measurement of the lattice portion of the thermal conductivity. It is important to remember that this is only the case when there is no (or limited) bipolar contribution to $\kappa$ which should be below 100 K in these samples. It can be seen that the lattice portion of the thermal conductivity dominate the total thermal conductivity at lower temperatures as discussed in Chapters 3 and 5. The Ce doped samples are run in several fields to confirm experimentally that a classically large field is reached. For the Sm and Ho doped samples it is assumed the field is classically large because the carrier mobilities are lowest in the Ce doped samples due to the lower pressing temperature.

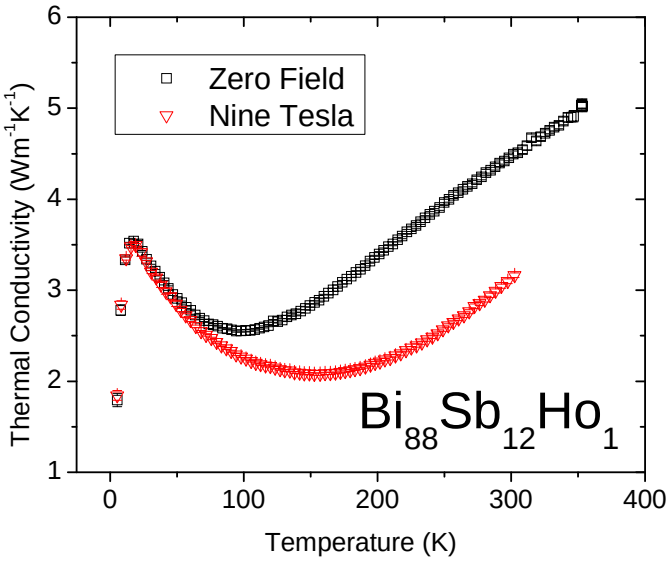


Figure C3: Thermal conductivity of $Bi_{88}Sb_{12}Ho_1$ in both zero field and nine Tesla.

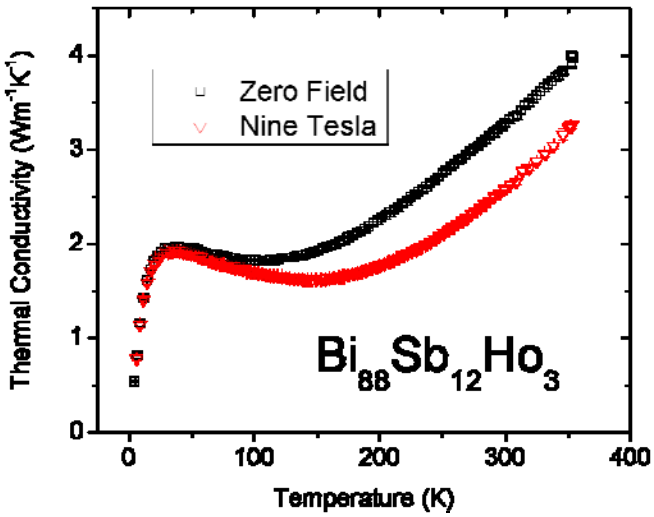


Figure C4: Thermal conductivity of $Bi_{88}Sb_{12}Ho_3$ in both zero field and nine Tesla.

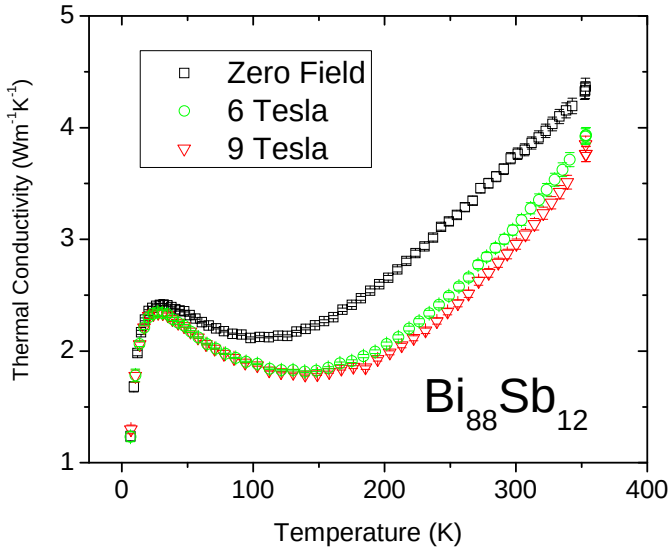


Figure C5: Thermal conductivity of $Bi_{88}Sb_{12}$ in both zero field and nine Tesla.

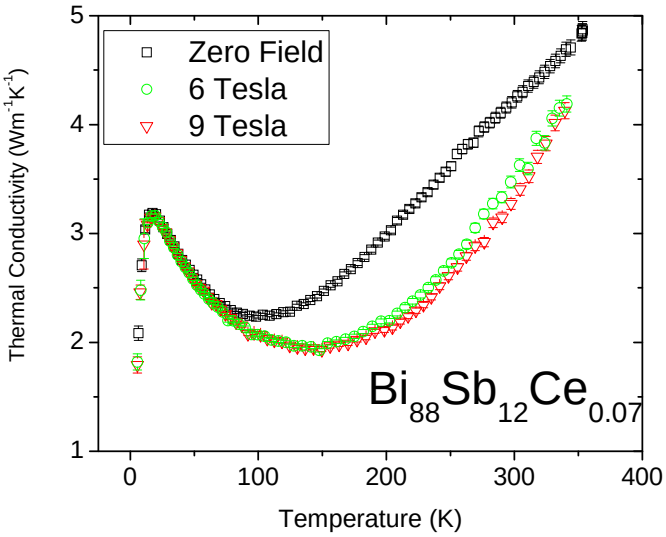


Figure C6: Thermal conductivity of $Bi_{88}Sb_{12}Ce_{0.07}$ in both zero field and nine Tesla.

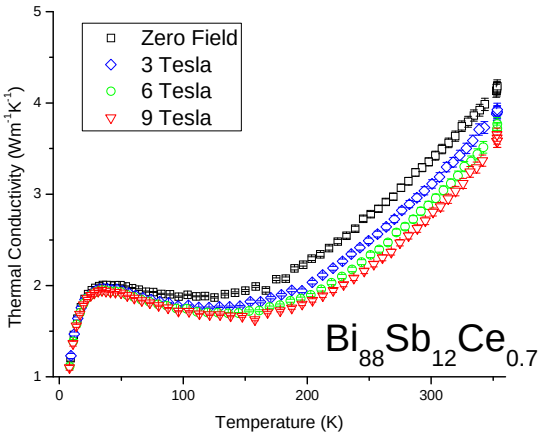


Figure C7: Thermal conductivity of $Bi_{88}Sb_{12}Ce_{0.7}$ in both zero field and nine Tesla.

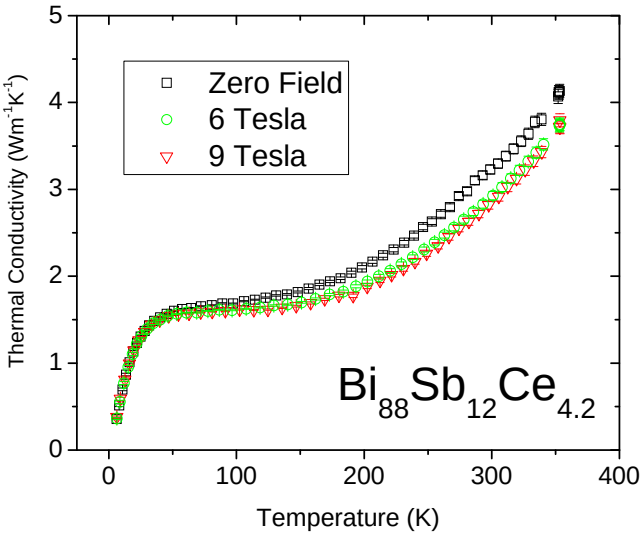


Figure C8: Thermal conductivity of $Bi_{88}Sb_{12}Ce_{4.2}$ in both zero field and nine Tesla.

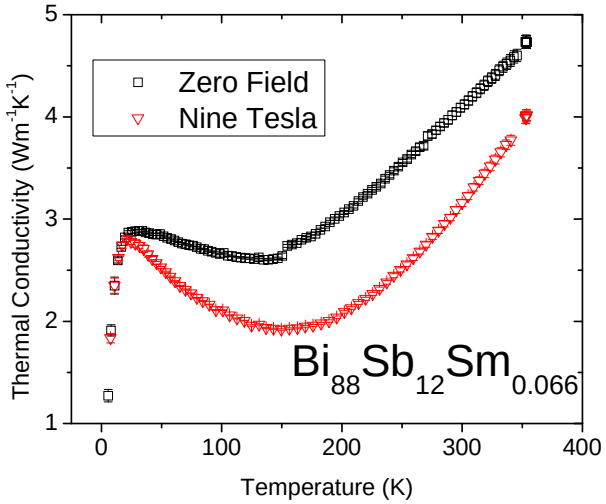


Figure C9: Thermal conductivity of $Bi_{88}Sb_{12}Sm_{0.066}$ in both zero field and nine Tesla.

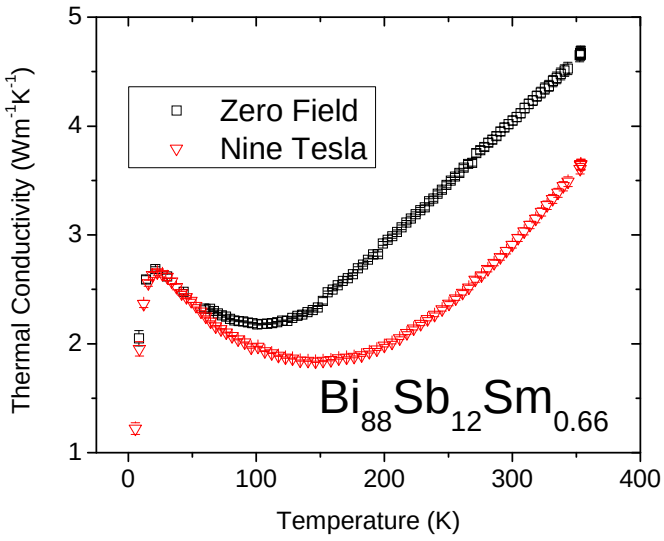


Figure C10: Thermal conductivity of $Bi_{88}Sb_{12}Sm_{0.66}$ in both zero field and nine Tesla.

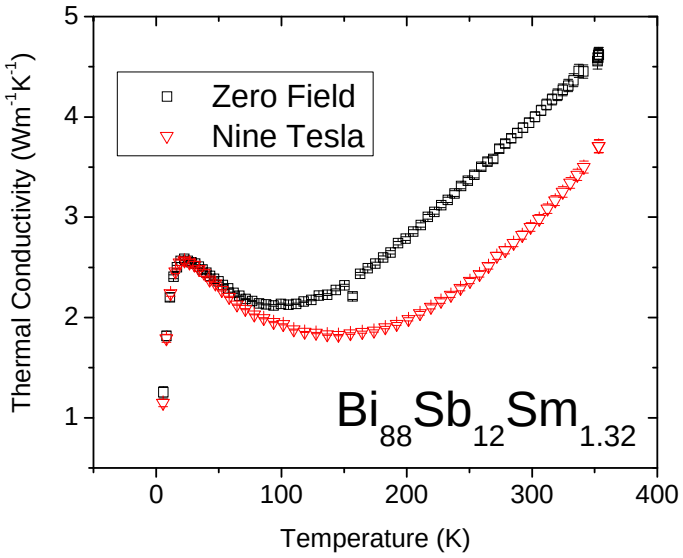


Figure C11: Thermal conductivity of $Bi_{88}Sb_{12}Sm_{1.32}$ in both zero field and nine Tesla.

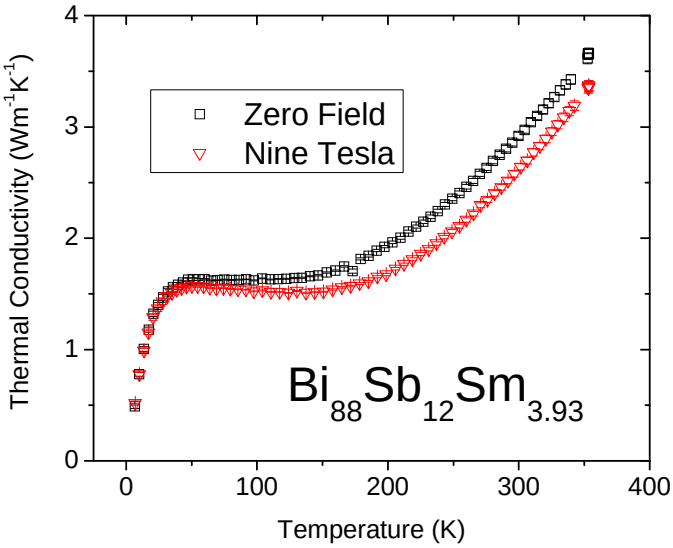


Figure C12: Thermal conductivity of $Bi_{88}Sb_{12}Sm_{3.93}$ in both zero field and nine Tesla.

Appendix D: Publications

16. W. Liu, **K. Lukas**, K. McEnaney, S. Lee, Q. Zhang, C. Opeil, G. Chen, Z. Ren, *Energy Env. Science,* 2012, doi: 10.1039/C2EE23549H

15. **K.C. Lukas**, W.S. Liu, Q. Jie, Z.F. Ren, C.P. Opeil, *Rev. Sci. Inst*., 2012, 83, 115114.

14. H. Zhao, M. Pokharel, S. Chen, B. Liao, **K. Lukas**, H. Wang, C. Opeil, G. Chen, Z.F. Ren, *Nanotechnology*, 2012, 23, 505402.

13. Q. Zhang, F. Cao, **K. Lukas**, W. Liu, K. Esfarjani, C. Opeil, D. Broido, D. Parker, D. Singh, G. Chen, Z. Ren, *J. American Chem. Soc.,* 2012, 134, 17731.

12. M. Pokheral, H. Zhao, **K.C. Lukas**, Z.F. Ren, C.P. Opeil, *MRS Online Proceedings Library*, 2012, 1456 , mrss12-1456-jj02-07 doi:10.1557/opl.2012.1505.

11. M. Zebarjadi, J. Yang, **K. Lukas**, B. Kozinsky, B. Yu, M.S.Dresselhaus, C. Opeil, Z. Ren, G. Chen, *J. App. Phys*., 2012, 112, 044305.

10. **K.C. Lukas**, W.S. Liu, Z.F. Ren, C.P. Opeil, *J. App. Phys*., 2012, 112, 054509.

9. **K.C. Lukas**, H. Zhao, R.L. Stillwell, Z.F. Ren, C.P. Opeil, *MRS Online Proceedings Library*, 2012, 1456 , mrss12-1456-jj01-04 doi:10.1557/opl.2012.1368.

8. C. Dhital, S. Khadka, Z. Yamani, C. de la Cruz, T.C. Hogan, S.M. Disseler, M. Pokharel, **K.C. Lukas**, W. Tian, C.P. Opeil, Z. Wang, S.D. Wilson, *Phys. Rev. B*, 2012, 86, 100401.

7. Q. Zhang, F. Cao, W. Liu, **K. Lukas**, B. Yu, S. Chen, C. Opeil, D. Broido, G. Chen, Z.F. Ren, *J. American Chem. Soc.* 2012, 134, 10031.

6. **K.C. Lukas**, W.S. Liu, G. Joshi, M. Zebarjadi, C. P. Opeil, G. Chen, M.S. Dresselhaus, Z.F. Ren, *Phys. Rev. B*, 2012, 85, 205410.

5. **K.C. Lukas**, G. Joshi, K. Modic, C.P. Opeil, Z.F. Ren, *J. of Mat. Sci*., 2012, 45, 15.

4. B. Yu, M. Zebarjadi, H. Wang, **K. Lukas**, H. Wang, D. Wang, C. Opeil, M. Dresselhaus, G. Chen, Z.F. Ren, *Nano Letters*, 2012, 12, 2077−2082.

3. Q. Zhang, Q. Zhang, S. Chen, W. Liu, **K. Lukas**, X. Yan, H. Wang, D. Wang, C.P. Opeil, G. Chen, Z.F. Ren. *Nano Energy*, 2012, 1, 1.

2. H. Zhao, M. Pokheral, G. Zhu, S. Chen, **K. Lukas**, Q. Jie, C.P. Opeil, G. Chen, Z.F. Ren. *App. Phys. Let*., 2011, 99.

**1.** **K. Lukas**, P. K. Lemaire, *Resonance*, 2009, 14, 8.

# Thermal stability of thermoelectric materials via *in situ* resistivity measurements

K. C. Lukas, W. S. Liu, Q. Jie, Z. F. Ren, and C. P. Opeil
*Department of Physics, Boston College, Chestnut Hill, Massachusetts 02467, USA*

(Received 8 June 2012; accepted 2 November 2012; published online 28 November 2012)

An experimental setup for determining the electrical resistivity of several types of thermoelectric materials over the temperature range $20 < T < 550\,^{\circ}C$ is described in detail. One resistivity measurement during temperature cycling is performed and explained for $Cu_{0.01}Bi_2Te_{2.7}Se_{0.3}$ and a second measurement is made on $Yb_{0.35}Co_4Sb_{12}$ as a function of time at 400 °C. Both measurements confirm that the materials are thermally stable for the temperature range and time period measured. Measurements made during temperature cycling show an irreversible decrease in the electrical resistivity of $Cu_{0.01}Bi_2Te_{2.7}Se_{0.3}$ when the measuring temperature exceeds the maximum sample fabrication temperature. Several other possible uses of such a system include but are not limited to studying the effects of annealing and/or oxidation as a function of both temperature and time. © *2012 American Institute of Physics*. [http://dx.doi.org/10.1063/1.4767904]

## INTRODUCTION

Thermoelectric materials have been widely studied over the last two decades with most of the research focused on increasing the dimensionless figure-of-merit ZT, $ZT = S^2T/\rho\kappa$, where S is the Seebeck coefficient, $\rho$ is the electrical resistivity, $\kappa$ is the thermal conductivity, and T is the absolute temperature.[1,2] However, ZT is not the only important parameter, especially when fabricating these materials for practical use, which is the ultimate goal. The materials should be relatively nontoxic, inexpensive, but most importantly their physical properties should remain stable over their temperature range of operation as well as during temperature cycling which most materials will experience in waste heat applications for cars,[3] solar panel use,[4] etc.

It is imperative when fabricating thermoelectric materials to ensure the materials are thermally stable. Much time and effort goes into the optimization of different synthesis parameters, such as pressing temperature, annealing temperature, annealing time. Thermoelectric samples measured in this work are prepared via ball milling and dc hot pressing techniques described previously.[5] Studies discussing the transport properties of thermoelectric materials often include thermal stability information based on temperature cycling, where the material is measured at different individual temperatures a number of times to see if the transport properties degrade after several runs.[5] Another method to test the stability is to anneal the samples in a furnace at different temperatures for a varying amount of time and then measure their properties to study the effects of both the annealing time and temperature.[6–9] Both methods are useful for basic information about the thermal stability, however, both have shortcomings. Measurements taken at individual temperature intervals can miss important information such as phase transitions. And annealing samples in an oven at different temperatures for different times is useful, but the question of how many different temperature or time intervals should be established is difficult to answer. If there are not enough intervals, information may be missed or misinterpreted. If there are too many intervals, then a great deal of time and/or sample preparation is required in order to obtain accurate information.

A solution to this problem can be made by measuring the transport properties *in situ* as the material is being annealed and/or cycled. The difficulty in decoupling the parameters in $ZT^2$ can now be seen as beneficial because by only measuring one transport property, accurate information about the material can be obtained as a function of both temperature and time; two important variables upon which thermal stability is dependent. We measure resistivity *in situ* as it is the most accurate measurement among the transport properties contributing to ZT. *In situ* resistivity measurements are commonly made on thin films to determine their temperature stability, but the authors have found no evidence or description of an experimental setup for *in situ* resistivity measurements on bulk thermoelectric materials to determine how properties change as a function of both annealing time and temperature. The Experimental details section describes the developed setup to measure the resistivity of a bulk sample from room temperature to 550 °C. It will be shown that accurate temperature control and continuous measurement allow for much quicker and more accurate results for the determination of the thermal stability.

The paper is divided into two sections. The first section describes in detail the experimental apparatus and configuration where standard materials are compared to ensure an accurate resistivity measurement as a function of temperature. The second section uses *in situ* resistivity measurements during temperature cycling to demonstrate the quick and easy extraction of additional information on the thermal stability of a material. Finally, other potential uses for the setup are stated but these data are not included.

## EXPERIMENTAL DETAILS

Resistivity measurements can be made either using a four point probe method on a bar shaped sample, or the Van der Pauw (VdP) technique.[11] The use of four probes negates any

 © 2012 American Institute of Physics

Downloaded 03 Dec 2012 to 136.167.55.68. Redistribution subject to AIP license or copyright; see http://rsi.aip.org/about/rights_and_permissions

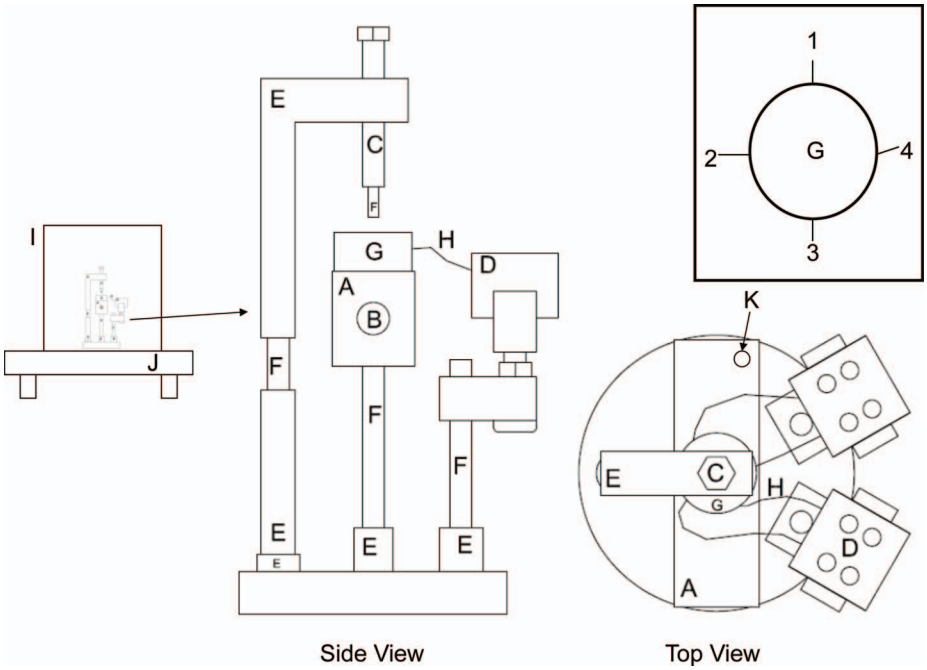


FIG. 1. Diagram of experimental setup for *in situ* resistivity measurements. Alumina rods, 1/4 in., (F) are connected to SS pieces (E) machined with hole sizes a fraction larger than the alumina rods. The sample (G), not drawn to scale, is mechanically pressed with a Ti screw (C) against the heating block (A) which houses a cartridge heater (B). Ni wire (H) is sparkwelded to the sample and mechanically connected (D) to external feedthroughs. The temperature is read by a mechanically clamped K-type thermocouple (K). The inset shows the wiring configuration for a sample being measured using the VdP technique.

concerns about contact resistance.[12,13] For thermoelectric materials alternating current (ac) is used to negate any voltage build up due to the Peltier and Seebeck effects.[12] A frequency of 13.7 Hz is used in the described setup, which is sufficient because the Peltier effect takes a finite amount of time to manifest itself which is usually on the order of 1 s.[12]

The resistivity of samples is measured by the experimental setup (Figs. 1 and 2) in a helium backfilled vacuum chamber. The resistivity measurements must be performed in an oxygen free environment at elevated temperature to prevent the oxidation of the material, unless that is the purpose of the measurements. Since the chamber must create an isolated environment, Viton o-rings are used to seal the chamber. The o-rings have a maximum operating temperature which when exceeded cause the o-rings to fail. In order to maintain an optimal operating temperature, a coolant plate (J) is used to dissipate excess heat. The coolant plate is kept at roughly 14 °C via a closed loop water coolant system. This has proven to be enough cooling power to keep the o-rings under their maximum operating temperature, 100 °C, while the inside of the chamber reaches temperatures in excess of 550 °C. The chamber is evacuated with a mechanical pump down to pressures of 10 Pa. The chamber is then backfilled with He gas, typically ambient pressure because it was determined that the cartridge heaters (B), which supply the heat, function better when in the presence of an exchange gas as opposed to in vacuum. Feedthroughs for electrical leads for current, voltage, heater power, and thermocouple inputs were mechanically fabricated. A sketch of the setup is shown in Figure 1. Nickel wire (3 mil) (H) is spark welded to each sample and then mechanically connected (D) to copper wire leads which

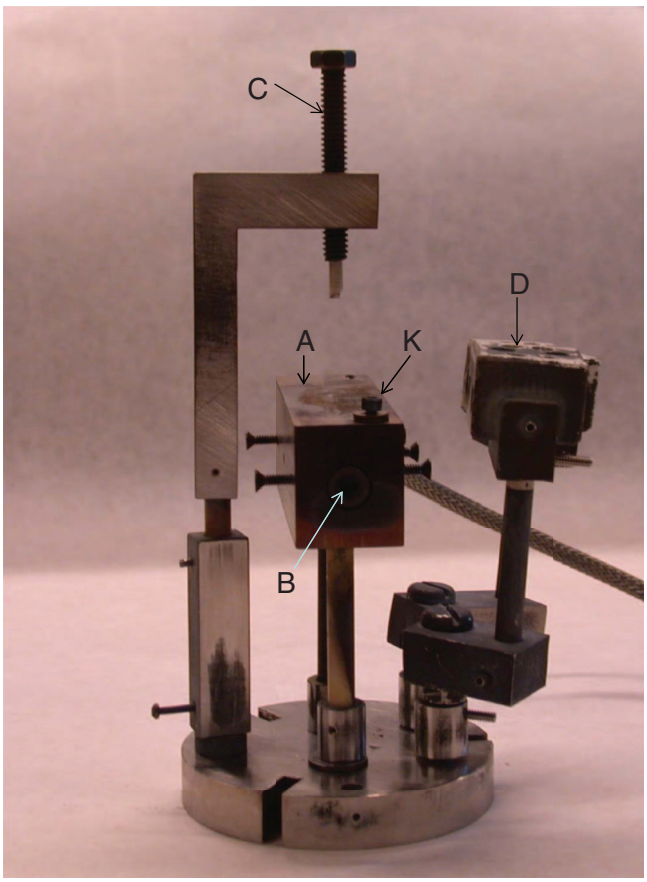


FIG. 2. Actual photograph of the side view schematic drawing shown in Fig. 1. There is no sample on the heating block. The slots in the base are to screw into the coolant plate for stability.

Downloaded 03 Dec 2012 to 136.167.55.68. Redistribution subject to AIP license or copyright; see http://rsi.aip.org/about/rights_and_permissions

in turn are mechanically connected to the vacuum chamber feedthroughs leading out of the chamber where the instrumentation for data acquisition are attached. Ni wire is used because it does not diffuse into the sample as readily as Cu, Au, or Ag which is of concern at high temperature. Temperature is read using 24 gage K-type thermocouple wire from Omega Engineering Inc. which is mechanically attached to the heating block with a screw (K); the 24 gage wire should be thick enough to negate any effects of "green rot" on the positive element which is a problem in oxygen depleted environments.[10] Mechanical connections are used at higher temperatures because solder or other electrically conducting epoxies are more difficult to use due to their lower operating temperatures. Heat is provided by a 120 V, 400 W cartridge heater (B) from Omega with a length of 3 in. and a 3/8 in. diameter. The cartridge heater is placed into a $1 \times 1 \times 3$ in. stainless steel (SS) block (A) with a hole size slightly larger than the diameter of the cartridge heater.

In an ambient environment the cartridge heater resting in the SS block can typically reach 700 °C. In vacuum this temperature is much more difficult to reach, and it is found that placing oxygen-free high thermal conductivity Cu shimstock inside the hole of the SS block creates greater surface contact area so that the SS block can remove the heat away from the cartridge heater, allowing the heater to reach higher temperatures without electrically shorting. The use of braze as thermal contact material could be beneficial; however, its use is avoided so that the cartridge heater can be easily removed in the case of a short or failure. Another necessity is to backfill the chamber with an exchange gas which enhances heat transfer from the heater to the SS block. Combining these two methods allows the temperature to easily be raised to 550 °C, and if necessary to reach up to 600 °C. The sample (G), which is not drawn to scale as discussed later, sits on top of a 0.1 mm thick layer of mica which is on top the of the SS block providing electrical insulation but the mica is also thin enough where it can be assumed that the sample temperature is the same as that of the heating block. To ensure the sample is thermally connected to the heating block, it is mechanically pressed down onto the block from above with a thin, 1/16 in. diameter, alumina rod (F) which fits in a tungsten screw (C). Enough force is applied to ensure good thermal contact without fracturing the sample. The rod must apply pressure so that the sample contacts the heating block evenly. Excellent thermal contact is imperative, as any temperature non-uniformity will generate a Seebeck voltage thereby creating error in the resistivity measurement. Temperature inhomogeneity can be due to heat loss from conduction through the rod, from convection due to the surrounding gas, and from radiation. Temperature inhomogeneity can also be caused by non-uniform heating which can manifest itself in thicker materials of low thermal conductivity heated at a fast rate; the sample base contacting the heating block will be much hotter than the top creating and internal temperature difference. An accurate theoretical determination of heat loss is difficult. Therefore to determine whether temperature differences due to heat loss and sample thickness are negligible, several measurements of different materials are compared with both standards and commercial equipment. All results agree within experimental error, described below, and so any effects on the measurement due to temperature differentials are considered negligible. It is determined that for materials with thermal conductivity values between 1 and 5 W/m-K the geometry for bar shaped samples with dimensions $2 \times 2 \times 12$ mm$^3$ and for disk shaped samples with a thickness to diameter ratio of 1:11 are required for accurate measurements. For the VdP technique, a smaller sample thickness should provide more uniform temperature, though at the sacrifice of mechanical strength. It is important in either geometry that the sample surfaces are flat to ensure uniform contact to the heating block.

The temperature is read and controlled by a PXR 4 (PID) temperature controller from Fuji Electric to which both the heater and K-type thermocouple are connected. The PXR 4 allows the rate at which the temperature is increased or decreased to be accurately controlled. Temperature is simultaneously read using a NI 9211 data acquisition system from National Instruments. The resistance is read using the 370 AC Resistance Bridge from LakeShore which uses an (ac) with a frequency of 13.7 Hz. A LabVIEW program records the temperature (NI 9211), resistance (LS 370), time, and allows the user to set the time interval at which data are recorded. Unless otherwise noted, data are recorded roughly once every second. There is again concern of temperature uniformity in the sample when slewing the temperature, too fast a rate will lead to incorrect resistivity values, while too slow a rate is impractical. Again measurements are compared with standards and commercial measurements. Also, measurements made at discrete temperatures are compared with measurements made on the same sample while slewing the temperature. It is determined that a slew rate of 1 °C/min is optimal for this system and investigated samples.

For a bar shaped sample the resistivity is obtained from $\rho = RA/L$ where $R$ is the resistance, $A$ is the cross sectional area, and $L$ is the voltage lead separation. The placement of voltage leads always satisfies the ratio $2w < L_s - L$ where $w$ is the thickness of the sample, $L_s$ is the length of the sample, and $L$ is the voltage lead separation which ensures uniformity of the electric field, or one-dimensional current flow, at the voltage leads.[12]

The VdP technique can be used to measure a sample of any arbitrary shape as long as the sample is flat and is singly connected, meaning it does not contain any holes.[11,14] The resistivity using the VdP technique is given by the expression[11,14,15]

$$\rho = \frac{t\pi}{\ln(2)} \frac{(R_{12,34} + R_{23,41})}{2} F. \quad (1)$$

Where $R_{12,34}$ is defined as the current flowing between points 1 and 2, while the voltage is read between points 3 and 4 (inset Figure 1), $R_{23,41}$ has the current between points 2 and 3 with voltage read between 1 and 4, $t$ is the thickness of the sample, and $F$ is a correction factor which can be solved graphically and is given by[15]

$$\frac{R_r - 1}{R_r + 1} = \frac{F}{\ln(2)} \operatorname{arccosh}\left(\frac{\exp[\ln(2)/\mathrm{F}]}{2}\right). \quad (2)$$

Where the ratio $R_r = R_{12,34}/R_{23,41}$. Thermoelectric materials have no widely accepted standard at high temperature

Downloaded 03 Dec 2012 to 136.167.55.68. Redistribution subject to AIP license or copyright; see http://rsi.aip.org/about/rights_and_permissions

(NIST only recently developed a low temperature standard[16]), thus it is imperative to accurately understand and account for any sources of error in the measurement so that data can be more accurately understood and communicated among research groups. The error bars for bar shaped samples from the propagation of independent errors are given by[17]

$$\frac{\sigma(\rho)}{\rho} = \sqrt{\left(\frac{\sigma(R)}{R}\right)^2 + \left(\frac{\sigma(L)}{L}\right)^2 + \left(\frac{\sigma(A)}{A}\right)^2}. \quad (3)$$

Where $\sigma(R)$ is the standard deviation obtained from binning the resistance values ($R$) at a given temperature, $\sigma(L)$ is the uncertainty in the voltage lead separation ($L$), and $\sigma(A)$ is the uncertainty in the cross sectional area ($A$). The error bars displayed for the VdP method are given by

$$\frac{\sigma_{\mathrm{VdP}}(\rho)}{\rho} = \sqrt{\left(\frac{\sigma_{\mathrm{VdP}}(R)}{R}\right)^2 + \left(\frac{\sigma(t)}{t}\right)^2 + \left(\frac{\sigma(F)}{F}\right)^2}. \quad (4)$$

Where $\sigma(t)$ is the uncertainty in the thickness of the sample ($t$), $\sigma(F)$ is the uncertainty in the graphical determination of the correction factor ($F$) which we take to not exceed 3%, and

$$\sigma_{\mathrm{VdP}}(R) = \sqrt{\sigma(R_{12,34})^2 + \sigma(R_{23,41})^2}. \quad (5)$$

Where $\sigma(R_{12,34})$ and $\sigma(R_{23,41})$ are the standard deviation of binned resistance values for a given temperature, typical bin size is every 1 °. It should be noted that Eq. (1) is written under the assumption that the size of the contact points are infinitesimal and the contacts are made directly on the edge of the specimen. In reality, the wire will always have some finite thickness and it is not possible to place the wire exactly on the edge of the sample, leading to additional error. This error is difficult to quantify but should not be exceed 2% as long as care is taken in wire placement.[18] Therefore, it is not taken into account in the expression for the error given in Eq. (4).

Figure 3 shows the resistivity data for constantan while the temperature is increased at discrete intervals, while Figure 4 plots the dependence of the resistivity of nickel measured continuously over the temperature range. Constantan is measured at discrete temperatures on a bar shaped sample of dimensions $2 \times 2 \times 14$ mm$^3$. The resistance values at each temperature are binned which gives the value of $\sigma(R)$ in Eq. (3). It can be seen that the data measured by the constructed setup matches within 1% of the data taken by the ZEM-3 (ULVAC) on the standard constantan bar provided by ULVAC. The resistivity data of nickel (Fig. 4) are measured on a flat square shaped sample of dimensions $16 \times 16 \times 2$ mm$^3$ using the VdP technique. The temperature is increased continuously from 20 °C – to 550 °C at a rate of 1 °C/min to measure $R_{12,34}$. The sample is then cooled and wires reconfigured to measure $R_{23,41}$. The sample is again measured, while the temperature is increased at 1 °C/min. Resistance values are binned every degree to obtain the standard deviation. The experiments are performed from room temperature to up to 550 °C. The agreement with the literature data, we take their uncertainty as 7%,[19] is within the experimental uncertainty of the two measurement systems with the absolute deviation at higher temperatures never exceeding 6%.[19] The ferromagnetic transition temperature is in very good agreement with the literature.[20] The transition takes place at 355.5 °C according to the literature,[20] while the measurement here gives a transition temperature of 354 °C which is well within the industrial error of 0.75% given for K-type thermocouples by Omega Engineering Inc.

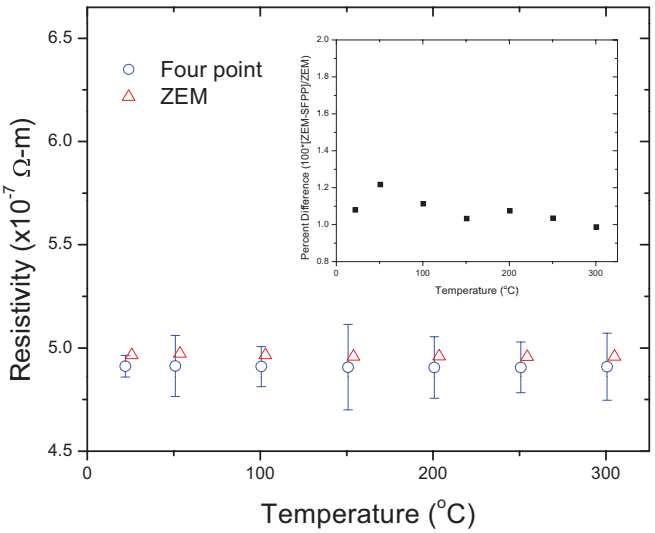


FIG. 3. The resistivity of a standard bar-shape constantan sample is plotted versus temperature along with the uncertainty calculated from Eq. (3) demonstrating agreement between both systems. The inset plots the percent difference in the resistivity between the developed setup and the commercially available ZEM-3.

Nickel and constantan are standard metals, but both have lower Seebeck coefficients and higher thermal conductivities than commonly used thermoelectrics. Therefore, several other thermoelectric samples were run in order to validate the accuracy of the machine. These data are included in a supplementary material;[21] however, the results are summarized. For bar shaped samples measured in both the developed setup as well as the ZEM-3, disagreement never exceeds 3% which is within the experimental uncertainty of the above system.

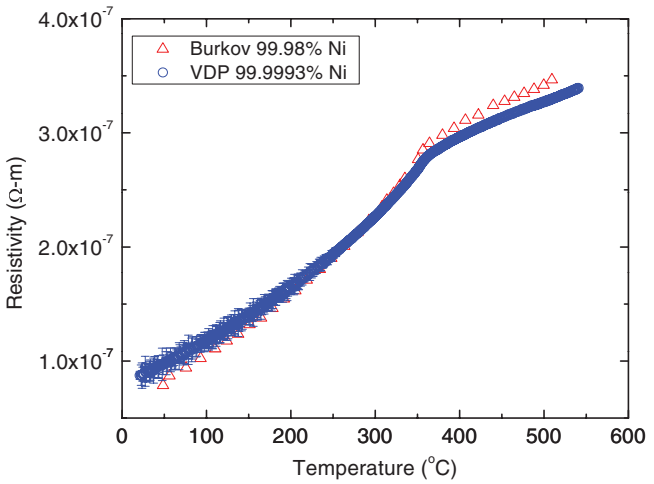


FIG. 4. Resistivity of nickel is plotted against temperature. Measurements were made using the VdP technique on a sample of 99.9993% purity from AJA International, Inc. Values obtained from Ref. 19 for Ni of 99.98% purity are shown for comparison. Agreement is seen between the two data sets validating the system. The slight deviation at higher temperatures could be due to the difference in sample purity.

Downloaded 03 Dec 2012 to 136.167.55.68. Redistribution subject to AIP license or copyright; see http://rsi.aip.org/about/rights_and_permissions

The absolute difference for VdP measurements never exceeds 9%, which is still within experimental error when the uncertainty of 3% of the ZEM-3 is taken into account. There are two probable reasons for a greater disagreement in the VdP measurements. The first is that the resistivity is being compared between two different samples. One is a thin disk used for VdP measurements, while the other is a bar that is not cut from the same disk; the ZEM can only measure bar shaped samples. There can be slight variations among transport measurements of different samples of the same TE material. The second reason is due to the aforementioned effects of finite contact size and probe placement near the edge, so the difference noted above is not unexpected.

The apparatus has been designed and benchmarked to study thermoelectric materials, in particular, bar shaped samples of dimensions $2 \times 2 \times 12$ mm$^3$ and disk shaped samples of 12 mm diameter and 1 mm thickness. Caution and care should be taken if measuring samples of alternate dimensions and/or non-thermoelectric materials. As mentioned previously, samples that are too thick can have internal temperature gradients that lead to additional voltages thereby altering the measurement. The other potential cause of a temperature gradient could come from heat loss through radiation, convection due to the surrounding gas, or conduction through the alumina rod. While multiple comparisons made between standards, commercial equipment, and the described apparatus demonstrate any effect outside of statistical error is negligible, accuracy could be affected by varying the sample geometry or for non-thermoelectrics. A heat shield surrounding the sample along with narrowing the contacting cross sectional area of the alumina rod could be introduced as improvements if systematic errors are discovered. Another potential improvement could be made by introducing a constant force spring as the method of applying force down on the sample instead of the tungsten screw. With the spring, any change in sample thickness due to thermal expansion or softening would not affect the contacting force and so maintain uniform contact with the heating block; this is not of concern in our samples as any thermoelectric materials of interest for commercial use need to have stable mechanical properties and, therefore, any material that expands or softens would not be systematically investigated. The described setup has also been used to measure small, 1 mm$^3$, single crystal samples. Due to the sample size 1 mil Pt wire was used and the sample was thermally connected to the heating block by embedding the sample in a high temperature dielectric epoxy (Omega 600 from Omega Engineering Inc.). Slight error could be introduced in this instance from the difference between the sample temperature and the measured temperature. However, by heating the block at a slower ramp rate the difference between the sample and measured temperature should not exceed a few degrees. Work is currently underway to improve and benchmark the apparatus and accurately determine the error for smaller single crystal samples.

## RESULTS

To demonstrate the developed experimental apparatus, the resistivities of two thermoelectric material samples are measured during *in situ* annealing and/or temperature cycling. Figure 5 shows raw, not binned, data for a $Cu_{0.01}Bi_2Te_{2.7}Se_{0.3}$ sample that has been temperature cycled. The sample is prepared via ball milling and dc hot pressing techniques described previously;[5] the sample in Figure 5 is hot pressed at 450 °C. The temperature is incrementally cycled by running from 40 °C up to 200 °C at a rate of 5 °C/min, then from 200 °C back to 40 °C at a rate of 5 °C/min. The temperature is then ramped from 40 °C to 225 °C and then from 225 °C back to 40 °C. The system remains at each maximum temperature for 10 min before cooling back down. This procedure is continued while increasing the maximum temperature each time by 25 °C up to a temperature of 450 °C. A ramp rate of 5 °C/min is used to expedite the measurement time, though there is a slight error introduced due to the higher ramp rate, the difference between the warming and cooling curves for the 200 °C run is seen to fall on top of each other indicating a negligible difference from the ramp rate. It can be seen that the sample exhibits metallic-like behavior. While several different runs were recorded, only the first run to a temperature of 200 °C and the final run to 450 °C are shown for clarity; the data from all intermediate temperatures lie in between the warming curves for both 200 °C and 450 °C. The values for the resistivity change by less than 5%, while the temperature remains below the pressing temperature. However, once the pressing temperature is reached and slightly exceeded due to the overshooting of the system temperature at large ramp rates, the resistivity value is lowered by about 13% from its initial value. The reason is that the dc hot press method essentially anneals the sample at the pressing temperature, and if the pressing temperature is exceeded during measurement or operation, there are irreversible changes to the transport properties of the material due to further annealing. While both Seebeck coefficient and thermal conductivity values are just as important as resistivity values for overall optimization, it is evident how quickly information about annealing time, temperature and phase transitions can be ascertained from the continuous measurement capability.

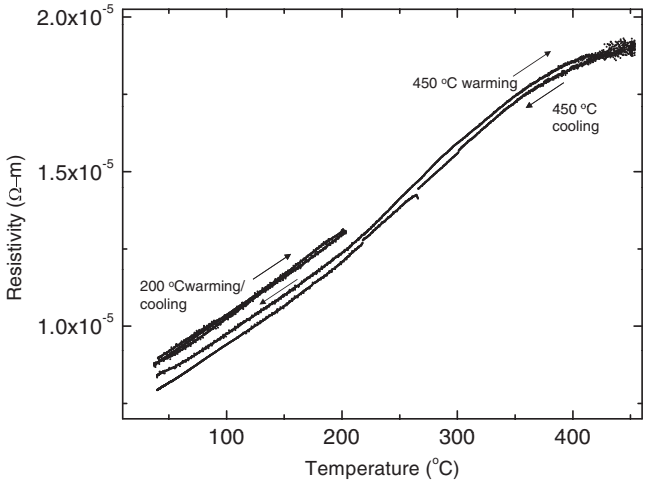


FIG. 5. Resistivity is plotted against temperature for two temperature cycles for $Cu_{0.01}Bi_2Te_{2.7}Se_{0.3}$ hot pressed at 450 °C. Negligible change is seen in the material, while the temperature remains below the pressing temperature.

Downloaded 03 Dec 2012 to 136.167.55.68. Redistribution subject to AIP license or copyright; see http://rsi.aip.org/about/rights_and_permissions

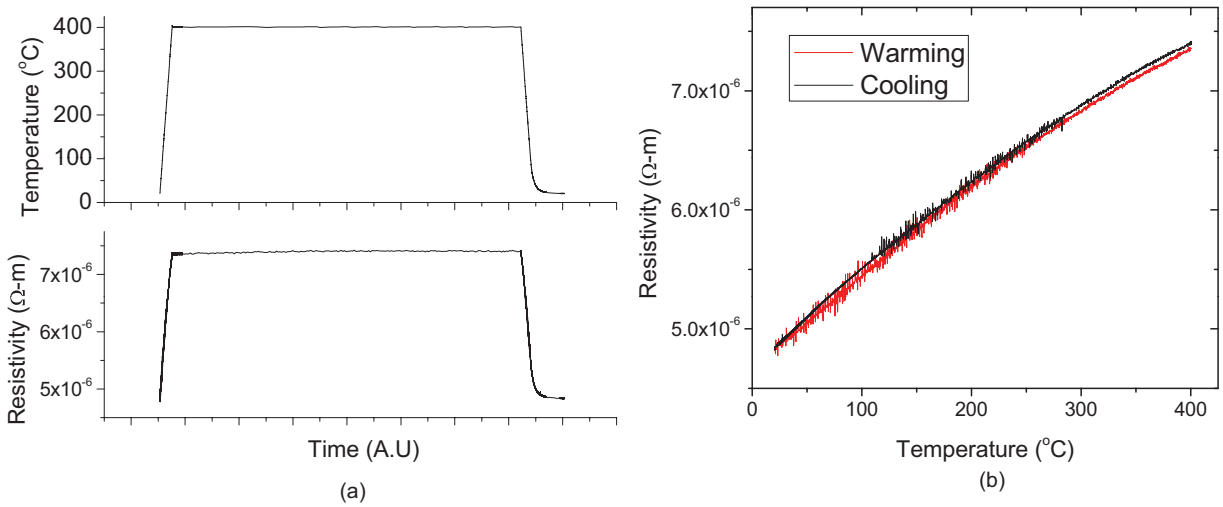


FIG. 6. (a) Resistivity and temperature are plotted against time. (b) The resistivity is plotted with temperature showing negligible difference in the warming and cooling curves, even at different cooling rates.

Another possibility that is easy to realize besides temperature cycling is *in situ* annealing measurements as a function of time, which is measured for $Yb_{0.35}Co_4Sb_{12}$ (Fig. 6). The sample can be brought to a specific temperature and remain at that temperature to study the effects of annealing or operating temperature over a period of time. The typical hot junction temperature range of operation for skutterudites is between 400 °C and 500 °C for waste heat applications.[13] The sample is heated from 20 °C to 400 °C at a rate of 5 °C/min (Fig. 6). The temperature is then held at 400 °C for 36 h. Then the temperature is lowered from 400 °C to 20 °C again at a rate of 5 °C/min. As mentioned previously the time interval at which data are recorded can be changed. During warming and cooling the data are recorded roughly every second. To minimize the number of data points during the 36 h period, data are recorded every 10 min. The recording time for the data can be adjusted in a wide range, commonly between 1 and 3600 s for the developed setup. In the experiments, the ramp rate is constant on the way up as expected and the temperature is stable at 400 °C for the entire 36 h. The resistivity at 400 °C changes by less than 1% over the 36 h period (Fig. 6(a) bottom). The cooling rate is constant until a temperature of 80 °C is reached and the system does not have the ability to cool at the 5 °C/min through convective and conductive cooling (Fig. 6(a) top). The resistivity shows no hysteresis even with the different cooling rates below 80 °C, the difference in the room temperature values of the resistivity before and after heating is about 1%. The data sets show both compounds are thermally stable over the studied regions. It should be noted that at higher temperatures and for longer operation times these materials are not thermally stable. Further investigation is currently underway and much future work is to be done utilizing the newly constructed apparatus to establish optimal operating conditions and fabrication parameters.

Only brief mention will be made of yet another capability for the setup which would be to study oxidation effects on thermoelectric materials. It was stated previously that the chamber is either evacuated or backfilled with an inert gas. It is possible to leave air in the chamber to study the effects of oxygen with both time and temperature. No data are presented here but it is straightforward to see how these measurements can readily be made. The ability to measure the resistivity continuously as the temperature is being cycled and/or held constant leads to much more information than would be obtained with simple incremental measurements. The benefits are evident in the study of phase transitions, temperature cycling, or annealing as is demonstrated above in the measurements of $Cu_{0.01}Bi_2Te_{2.7}Se_{0.3}$ and $Yb_{0.35}Co_4Sb_{12}$.

## CONCLUSION

An experimental setup for accurately determining the electrical resistivity of thermoelectric materials in a temperature range of 20 °C–550 °C is described in detail. The accuracy of the setup is benchmarked against standard samples of constantan and nickel, as well as several thermoelectric materials measured on a commercial system. Two *in situ* resistivity measurements are also described. $Cu_{0.01}Bi_2Te_{2.7}Se_{0.3}$ is stable upon temperature cycling, while the temperature does not exceed the fabrication temperature. Measurements are also made on $Yb_{0.35}Co_4Sb_{12}$ held at its operating temperature for 36 h. The material is again stable over this time period. Other possible measurements including the study of annealing as well as oxidation effects can be easily realized with the apparatus.

## ACKNOWLEDGMENTS

The authors gratefully acknowledge funding for this work through the "Solid State Solar-Thermal Energy Conversion Center (S3TEC)," an Energy Frontier Research Center founded by the U.S. Department of Energy, Office of Basic Energy Science under Award No. DE-SC0001299/DE-FG02-09ER46577.

[1]M. S. Dresselhaus, G. Chen, M. Y. Tang, R. Yang, H. Lee, D. Z. Wang, Z. F. Ren, J. P. Fleurial, and P. Gogna, Adv. Mater. **19**, 1043–1053 (2007).
[2]G. J. Snyder and E. S. Toberer, Nature Mater. **7**, 105–114 (2008).

Downloaded 03 Dec 2012 to 136.167.55.68. Redistribution subject to AIP license or copyright; see http://rsi.aip.org/about/rights_and_permissions

[3]D. T. Morelli, in *Proceedings of the 15th International Conference on Thermoelectrics* (IEEE Publishing, 1996), pp. 383–386.
[4]D. Kraemer, B. Poudel, H. P. Feng, J. C. Caylor, B Yu, X. Yan, Y. Ma, X. Wang, D. Z. Wang, A. Muto, K. McEnaney, M. Chiesa, Z. F. Ren, and G. Chen, Nature Mater. **10**, 532–538 (2011).
[5]W. S. Liu, Q. Zhang, Y. Lan, S. Chen, X. Yan, Q. Zhang, H. Wang, D. Z. Wang, G. Chen, and Z. F. Ren, Adv. Energy Mater. **1**, 577 (2011).
[6]O. Yamashita and S. Tomiyoshi, Jpn. J. Appl. Phys. **42**, 492 (2003).
[7]H. Kaibe, M. Sakata, Y. Isoda, and I. Nishida, J. Jpn. Inst. Met. **53**, 958 (1989).
[8]W. M. Yim and F. D. Rosi, Solid-State Electron. **15**, 1121 (1972).
[9]O. Yamashita and S. Sugihara, J. Mater. Sci. **40**, 6439–6444 (2005).
[10]T. W. Kerlin, *Practical Thermocouple Thermometry* (Instrumental Society of America, 1999).
[11]L. J. Van der Pauw, Philips Tech. Rev. **20**, 220–224 (1958).
[12]T. M. Tritt, *Recent Trends in Thermoelectric Materials Research I* (Academic, Boston, 2001).
[13]D. M. Rowe, *CRC Handbook of Thermoelectrics* (CRC, New York, 1995).
[14]L. J. Van der Pauw, Philips Res. Rep. **13**, 1–9 (1958).
[15]D. K. Schroder, *Semiconductor Material and Device Characterization* (Wiley, New York, 1998).
[16]N. D. Lowhorn, W. Wong-Ng, Z. Q. Lu, E. Thomas, M. Otani, M. Green, N. Dilley, J. Sharp, and T. N. Tran, Appl. Phys. A **96**, 511–514 (2009).
[17]J. R. Taylor, *An Introduction to Error Analysis* (University Science Books, Sausalito, 1997).
[18]R. Chwang, B. J. Smith, and C. R. Crowell, Solid-State Electron. **17**, 1217–1227 (1974).
[19]T. Burkov, A. Heinrich, P. P. Konstantinov, T. Nakama, and K. Yagasaki, Meas. Sci. Technol. **12**, 264 (2001).
[20]T. G. Kollie, Phys. Rev. B **16**, 4872 (1977).
[21]See supplementary material at http://dx.doi.org/10.1063/1.4767904 for information on the other thermoelectric samples measured to benchmark the system.

Downloaded 03 Dec 2012 to 136.167.55.68. Redistribution subject to AIP license or copyright; see http://rsi.aip.org/about/rights_and_permissions

# Experimental determination of the Lorenz number in $Cu_{0.01}Bi_2Te_{2.7}Se_{0.3}$ and $Bi_{0.88}Sb_{0.12}$

K. C. Lukas,[1] W. S. Liu,[1] G. Joshi,[1] M. Zebarjadi,[2] M. S. Dresselhaus,[3] Z. F. Ren,[1] G. Chen,[2] and C. P. Opeil[1]

[1]*Department of Physics, Boston College, Chestnut Hill, Massachusetts 02467, USA*

[2]*Department of Mechanical Engineering and Computer Science, Massachusetts Institute of Technology, Cambridge, Massachusetts 02139, USA*

[3]*Department of Physics and Department of Electrical Engineering and Computer Science, Massachusetts Institute of Technology, Cambridge, Massachusetts 02139, USA*

(Received 3 January 2012; revised manuscript received 6 April 2012; published 7 May 2012)

Nanostructuring has been shown to be an effective approach to reduce the lattice thermal conductivity and improve the thermoelectric figure of merit. Because the experimentally measured thermal conductivity includes contributions from both carriers and phonons, separating out the phonon contribution has been difficult and is mostly based on estimating the electronic contributions using the Wiedemann-Franz law. In this paper, an experimental method to directly measure electronic contributions to the thermal conductivity is presented and applied to $Cu_{0.01}Bi_2Te_{2.7}Se_{0.3}$, $[Cu_{0.01}Bi_2Te_{2.7}Se_{0.3}]_{0.98}Ni_{0.02}$, and $Bi_{0.88}Sb_{0.12}$. By measuring the thermal conductivity under magnetic field, electronic contributions to thermal conductivity can be extracted, leading to knowledge of the Lorenz number in thermoelectric materials.

DOI: 10.1103/PhysRevB.85.205410 PACS number(s): 72.15.Jf, 72.20.Pa, 66.70.Df

## I. INTRODUCTION

The determination of the Lorenz number is an important aspect in thermoelectric research due to the fact that $ZT$ enhancement is being realized through the reduction of thermal conductivity, specifically focusing on reducing the lattice portion of the thermal conductivity. The total thermal conductivity is given by

$$\kappa_{\text{total}} = \kappa_{\text{carrier}} + \kappa_{\text{lattice}}, \tag{1}$$

where $\kappa_{\text{carrier}}$and $\kappa_{\text{lattice}}$ are the contributions to the thermal conductivity from the carriers and the lattice, respectively. Since only the total thermal conductivity can be measured, the contributions must be separated in some way. This is done using the Wiedemann-Franz law and by defining a Lorenz number $L$, which is the given by

$$L = \frac{\kappa_{\text{carrier}}}{\sigma T}, \tag{2}$$

where $\sigma$ is the electrical conductivity and $T$ is the absolute temperature. In metals the Lorenz number can be determined by measuring the electrical conductivity and total thermal conductivity at a given temperature, from which the Lorenz number is calculated using Eq. (2). This method is only useful in metals where the total thermal conductivity is approximately equal to $\kappa_{\text{carrier}}$. For the classical free-electron model the Lorenz number is given as $2.44 \times 10^{-8}$ $V^2$ $K^{-2}$.[1] It is important to note that the Lorenz number, as described by the free-electron model, is not an accurate value for most materials and in a given material depends on the detailed band structure, position of the Fermi level, and the temperature; for semiconductors this relates to the carrier concentration. Therefore, when $\kappa_{\text{lattice}}$ and $\kappa_{\text{carrier}}$ become comparable to each other, there must be a method for differentiating between the two components of $\kappa_{\text{total}}$. To date the separation of the two components has been accomplished through calculation by approximating the Lorenz number, and hence the carrier contribution, through various different formalisms.[1,3,4] Determinations of the Lorenz number have also been made experimentally;[1] however, there are few.

In order to separate $\kappa_{\text{lattice}}$ and $\kappa_{\text{carrier}}$ experimentally, two approaches have been used to determine the Lorenz number. Both methods utilize a transverse magnetic field in order to suppress the electronic component of the thermal conductivity. One approach uses a classically large magnetic field, while the other is performed in intermediate fields. A classically large magnetic field is described as $\mu B \gg 1$, where $\mu$ is the carrier mobility and $B$ is the magnetic field.[1] When this limit is reached, the electronic component of $\kappa$ is completely suppressed so that the measurement yields only the lattice portion of the thermal conductivity, from which $\kappa_{\text{carrier}}$and hence the Lorenz number can be calculated using Eqs. (1) and (2).

Very often it is difficult to reach a classically large field, making this type of measurement impossible, and therefore other methods have been developed for determining $L$. For example, Goldsmid *et al.* developed a magnetothermal resistance (MTR) method for extracting the Lorenz number at lower magnetic fields, specifically in the region where $\mu B \approx 1$.[5–8] In the MTR method the sample is kept at a constant temperature while the field is varied. In this case both the electrical conductivity and the total thermal conductivity will change with the field due to the Lorentz force acting on the carriers, which is induced by the transverse magnetic field. Equation (1) can be rewritten in the form

$$\kappa(B)_{\text{total}} = LT\sigma(B) + \kappa_{\text{lattice}}, \tag{3}$$

where now both $\kappa$ and $\sigma$ are dependent on the magnetic field. It is noted that $\kappa$, $\sigma$, and $L$ are all tensors, whose off-diagonal components can have non-negligible contributions in magnetic field.[5,9] Both $\kappa(B)$ and $\sigma(B)$ are measured along the same direction, which we define as $\kappa_{xx}(B)$ and $\sigma_{xx}(B)$. For an anisotropic sample, even to first order, the magnetic field affects the diagonal terms of the tensors as well as the nondiagonal terms. We show that by measuring only the diagonal terms we are able to extract the Lorenz number $L_{xx}$,

 ©2012 American Physical Society

which relates $\kappa_{xx}$ to $\sigma_{xx}$. The reason behind the validity of this method is that both $\kappa(B)_{xx}$ and $\sigma(B)_{xx}$ have a similar magnetic field dependence and their ratio has only a weak dependence on the off-diagonal terms. Since the samples are isotropic[10] and extrinsic, it is assumed that off-diagonal terms can be neglected because thermogalvanomagnetic effects are only dominant in intrinsic materials with a proportional number of positive and negative charge carriers.[4,11] As long as both have the same functional form with respect to the magnetic field, then $\kappa(B)$ vs $\sigma(B)$ will have a linear relationship, and the Lorenz number $L_{xx}$ at a given temperature can be directly taken from the slope as given in Eq. (3). It is important to note that the analysis throughout this paper is based on the assumption that the Lorenz number is independent of magnetic field, which is true for some materials but, in general, is not a valid assumption.[12–14] Analogous approximations have been used to study similar compounds in the past.[6,12]

Neither method has been extensively used due to the fact that there are restrictions on the materials that can be measured because there must be a significant carrier contribution to the total thermal conductivity; also the experimental setup is rather difficult to realize.[1,5–9] The advent of the Physical Properties Measurement System (PPMS) from Quantum Design makes the experimental setup and measurement readily possible for either method. The purpose of this paper is to present experimental techniques for the determination of the Lorenz number from which both the electronic and lattice contributions to the thermal conductivity can be directly extracted. Measurements are compared to literature values as well as simple model calculations. There are several different ways to analyze the raw experimental data; two different models will be used here and are shown to yield similar results. The measurements are performed below 150 K so that bipolar terms will be negligible, and therefore Eqs. (1) and (3) accurately describe the contributions to the total thermal conductivity.

## II. EXPERIMENT

Samples were prepared by combining the proper stoichiometric ratios of Cu (99.999%, Alfa Aesar), Bi (99.999%, Alfa Aesar), Te (99.999%, Alfa Aesar), and Se (99.999%, Alfa Aesar) for $Cu_{0.01}Bi_2Te_{2.7}Se_{0.3}$, while $Bi_{0.88}Sb_{0.12}$ was prepared with Bi (99.999%, Alfa Aesar) and Sb (99.999%, Alfa Aesar). Samples were then ball milled and pressed using dc hot-pressing techniques.[10] Metallic contacts were sputtered onto the surfaces so that electrical contacts could be soldered to the sample.

MTR measurements were performed using the thermal transport option (TTO) of the PPMS in which the sample was placed in an orientation where the magnetic field was perpendicular to the heat flow. A standard two-point method was used for thermal conductivity and Seebeck coefficient $S$ measurements with typical sample dimensions of $2 \times 2 \times 3$ mm$^3$. In this case the temperature was held constant at 100 K, and measurements were made while the field was swept over a range of 0.1–5 T. Since resistivity $\rho$ values in a magnetic field are required, a four-point technique must be used, which was accomplished with the ac transport option on a different sample of dimensions $1 \times 2 \times 12$ mm$^3$ for the same temperature and field range. Since a four-point technique is used, there is no concern of electrical contact resistance. For thermal contact resistance, our previous measurements show no difference in the thermal conductivity when a two- or four-point method is used. Even so, any thermal contact resistance is assumed to be negligible in field, and since we are looking at the change in thermal conductivity with field, there should be no influence on the slope $L$ of the measurement. Geometrical effects on the magnetoresistance are considered to be negligible because the sample used for resistivity measurements in field has the appropriate aspect ratio. The sample dimensions for the thermal magnetoresistance measurements are restricted due to requirements to fit into the PPMS; however, it is assumed there is a negligible contribution because there was no evidence previously of geometrical effects on a similar material which had an aspect ratio of 1.[12] Errors for the MTR measurements of $L$ and $\kappa_{\text{lattice}}$ were calculated from the standard deviation and propagation of error and were determined to be 3% and 7%, respectively. Hall measurements to determine the mobility $\mu_H$ from which the scattering factor $r$ is obtained were made using the PPMS on the same sample as the four-point $\rho$ measurement.

When determining the Lorenz number in a classically large field, the TTO of the PPMS in which the magnetic field was perpendicular to the heat flow was again used. A standard two-point method was used for all transport measurements on the same sample. The sample was run in magnetic fields of 0, 6, and 9 T. Only the thermal conductivity measurements in field are used, while electrical resistivity values are taken from the zero-field data. Typical sample dimensions were $2 \times 4 \times 2$ mm$^3$. Thermal contact resistance is assumed to be negligible for the reasons stated above, and electrical contact resistance is negligible from the comparison of two- and four-point resistivity measurements. There is no concern of geometrical effects on thermal conductivity measurements because saturation would not be obtained at higher magnetic fields. The measurements were performed over a temperature range of 5–150 K, with the error for $L$ and $\kappa_{\text{lattice}}$ being 2% and 6%, respectively, determined from the standard deviation and propagation of error.

## III. RESULTS

The MTR approach can be used only if the thermal and electrical conductivities have the same functional form with respect to the magnetic field. Since the MTR method is used in intermediate fields, or when $\mu B \approx 1$, only values in magnetic fields from 0.8 to 5 T were used; anything below 0.8 T was too low of a field. The top left inset in Fig. 1 plots $\kappa$ as a function of field, while the bottom right inset plots $\sigma$ as a function of field for $Cu_{0.01}Bi_2Te_{2.7}Se_{0.3}$. Both the electrical and thermal conductivities vary with field as $\frac{aB^2}{1+cB^2}$, where $a$ and $c$ are constants, which is valid for strong degeneracy.[2,16,17] The fits are shown in the insets of Fig. 1 along with the measured values. Figure 1 can be fit linearly, and taking the slope yields $LT$ in Eq. (3), from which we get $L = 2.16 \times 10^{-8}$ V$^2$ K$^{-2}$ by dividing by $T = 100$ K. The lattice portion of the thermal conductivity is given by the $y$ intercept and gives $\kappa_{\text{lattice}} = 1.49$ W mK$^{-1}$. Care should be taken with the determination of $\kappa_{\text{lattice}}$ this way because a larger error is induced when extrapolating over six orders of magnitude to

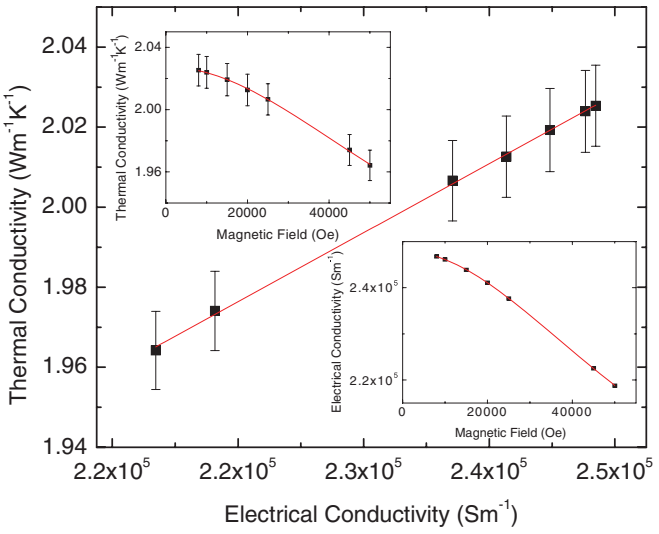


FIG. 1. (Color online) Thermal conductivity is plotted against electrical conductivity of $Cu_{0.01}Bi_2Te_{2.7}Se_{0.3}$ at 100 K with the magnetic field being varied from 0.8 to 5 T. The slope of the linear fit provides the Lorenz number $L = 2.16 \times 10^{-8}$ V$^2$ K$^{-2}$, and the $y$ intercept gives $\kappa_{\text{lattice}} = 1.49$ W mK$^{-1}$. The top left inset plots the dependence of the total thermal conductivity on magnetic field. The bottom right inset plots the dependence of electrical conductivity on magnetic field. Both the thermal conductivity and electrical conductivity varying with field can be fit using $\frac{aB^2}{1+cB^2}$, as shown in the insets.

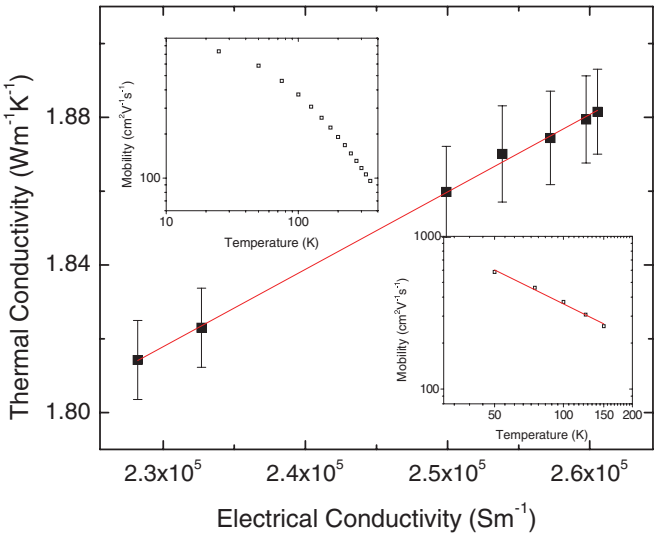


FIG. 2. (Color online) Thermal conductivity is plotted against electrical conductivity of $[Cu_{0.01}Bi_2Te_{2.7}Se_{0.3}]_{0.98}Ni_{0.02}$ at 100 K with the magnetic field being varied from 0.8 to 5 T. The slope of the linear fit provides the Lorenz number $L = 2.33 \times 10^{-8}$ V$^2$ K$^{-2}$, and the $y$ intercept gives $\kappa_{\text{lattice}} = 1.27$ W mK$^{-1}$. The top left inset plots $\ln(\mu_H)$ vs $\ln(T)$ over the whole temperature range. The bottom right inset plots only the points in the vicinity of 100 K from which the slope is taken to derive the scattering parameter.

get $\kappa_{\text{lattice}}$ when $\sigma(B)$ is zero. If $\kappa_{\text{carrier}}$ is calculated from the Lorenz number and the electrical conductivity in zero field, $\kappa_{\text{lattice}}$can be calculated from $\kappa_{\text{total}}$–$\kappa_{\text{carrier}}$, which gives a value of 1.35 W mK$^{-1}$. For a comparison with the measured values, a simple model for the calculation of the Lorenz number is given by[3]

$$L = \left(\frac{k_B}{e}\right)^2 \left[\frac{(r+7/2)F_{r+5/2}(\xi)}{(r+3/2)F_{r+1/2}(\xi)} - \left(\frac{(r+5/2)F_{r+3/2}(\xi)}{(r+3/2)F_{r+1/2}(\xi)}\right)^2\right], \quad (4)$$

where $r$ is the scattering parameter, $k_B$ is Boltzmann's constant, $e$ is the electron charge, and $F_n(\xi)$ is the Fermi integral given by

$$F_n(\xi) = \int_0^\infty \frac{\chi^n}{1+e^{\chi-\xi}} d\chi, \quad (5)$$

where $\xi$ is the reduced Fermi energy that can be calculated from the Seebeck coefficient $S$ as well as the scattering parameter $r$, which is given by

$$S = \pm\frac{k_B}{e}\frac{(r+5/2)F_{r+3/2}(\xi)}{(r+3/2)F_{r+1/2}(\xi)} - \xi. \quad (6)$$

In this model the Lorenz number can be calculated with knowledge of the Seebeck coefficient and the scattering parameter, both of which were measured at 100 K. The insets of Fig. 2 show $\mu_H$ plotted as a function of temperature over the entire temperature range (top left) as well as only the data around 100 K (bottom right), which were used to calculate the scattering parameter $r$. The data in Fig. 2 are for $[Cu_{0.01}Bi_2Te_{2.7}Se_{0.3}]_{0.98}Ni_{0.02}$; the same method was used to calculate $r$ for $Cu_{0.01}Bi_2Te_{2.7}Se_{0.3}$. The scattering parameter $r$ was determined by taking the slope of $\ln(\mu_H)$ vs $\ln(T)$ around 100 K, using the relationship $\mu \propto T^{r-1}$.[15] The values for the mobility were nearly identical between the two samples, with values for $r$ being 0.26 and 0.27 for $Cu_{0.01}Bi_2Te_{2.7}Se_{0.3}$ and $[Cu_{0.01}Bi_2Te_{2.7}Se_{0.3}]_{0.98}Ni_{0.02}$, respectively. Though there is some error induced in the determination of $r$ because the scattering parameter in general changes with temperature, these values should be more accurate than the commonly assumed $r = -1/2$ for acoustic phonon scattering. This fact is seen in the calculated values for $L$ where using $r = -1/2$ yields values of $L$ that are 3% higher than when $r$ is calculated from the mobility. The calculated value using Eqs. (4)–(6) and $r = 0.26$ gives $L = 2.34 \times 10^{-8}$ V$^2$ K$^{-2}$ and $\kappa_{\text{lattice}} = 1.30$ W mK$^{-1}$, both of which are close to the experimentally determined values.

The same procedure was followed for $[Cu_{0.01}Bi_2Te_{2.7}Se_{0.3}]_{0.98}Ni_{0.02}$, and Fig. 2 shows again that $\kappa(B)$ vs $\sigma(B)$ is linear. The measured value for the slope gives $L = 2.33 \times 10^{-8}$ V$^2$ K$^{-2}$, and from the $y$ intercept $\kappa_{\text{lattice}} = 1.27$ W mK$^{-1}$. The calculated values using Eqs. (4)–(6) give $L = 2.36 \times 10^{-8}$ V$^2$ K$^{-2}$ and $\kappa_{\text{lattice}} = 1.13$ W mK$^{-1}$, again showing the validity of the measurement. Besides the MTR method the data can also be fit using the following expressions for the electrical and thermal conductivities as a function of field for isotropic samples in the relaxation-time approximation:[18]

$$\sigma(B) = \frac{\sigma_0}{1+(\mu_d B)^2}, \quad (7)$$

$$\kappa(B) = \kappa_{\text{lattice}} + \frac{\kappa_{\text{carrier}}}{1+(\mu_d B)^2}, \quad (8)$$

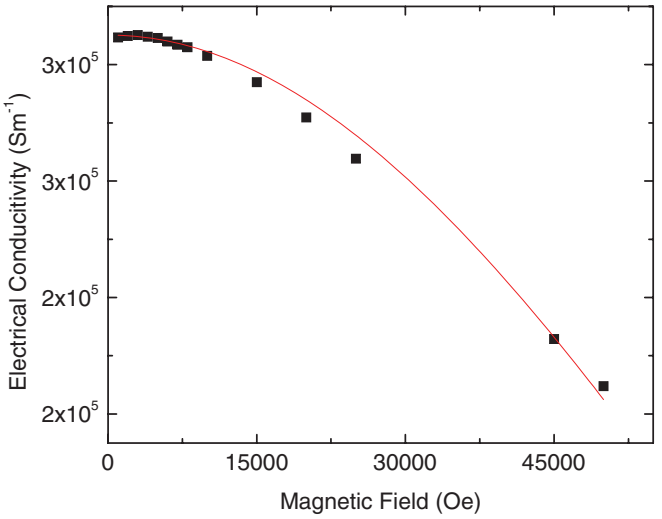


FIG. 3. (Color online) Electrical conductivity is plotted against magnetic field from 0.1 to 5 T and fit using Eq. (7). The electrical conductivity in zero field is used in order to determine the drift mobility $\mu_d$.

where $\sigma_0$ is the electrical conductivity in zero field and $\mu_d$ is the drift mobility. The drift mobility determined by Eq. (7) and shown in Fig. 3 is used in Eq. (8) in order to determine the carrier and lattice contributions to the thermal conductivity, as shown in Fig. 4. As opposed to the MTR method, the data must be fit using both weak and intermediate magnetic fields, and so Figs. 3 and 4 show the thermal and electrical conductivities in fields of 0.1–5 T. Fitting Eq. (8) to the thermal conductivity vs magnetic field data in Fig. 4 yields $\kappa_{\text{lattice}} = 1.29$ W mK$^{-1}$. It can be seen that using the completely different model presented in Eqs. (7) and (8) produces a nearly identical value of $\kappa_{\text{lattice}} = 1.27$ W mK$^{-1}$ as determined by the MTR method.

Unlike $Cu_{0.01}Bi_2Te_{2.7}Se_{0.3}$, it was possible to reach the classical high-field limit at lower temperatures for bismuth antimony compounds. Figure 5 plots the thermal conductivity

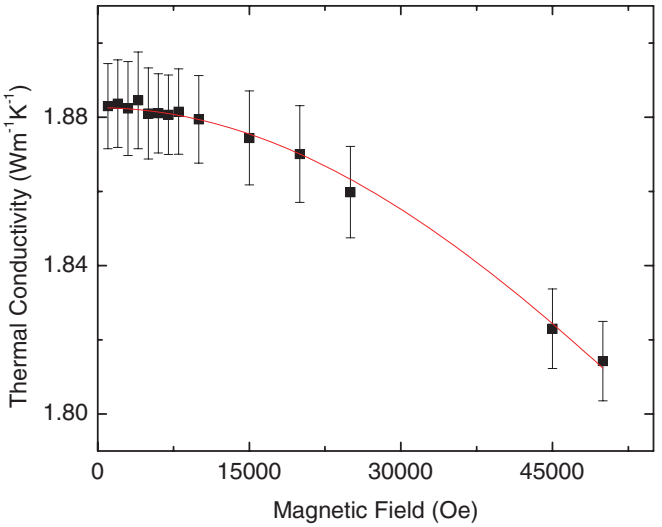


FIG. 4. (Color online) Thermal conductivity is plotted against magnetic field from 0.1 to 5 T and fit using Eq. (8) and $\mu_d$ from Fig. 3. It is found that $\kappa_{\text{lattice}} = 1.29$ W mK$^{-1}$.

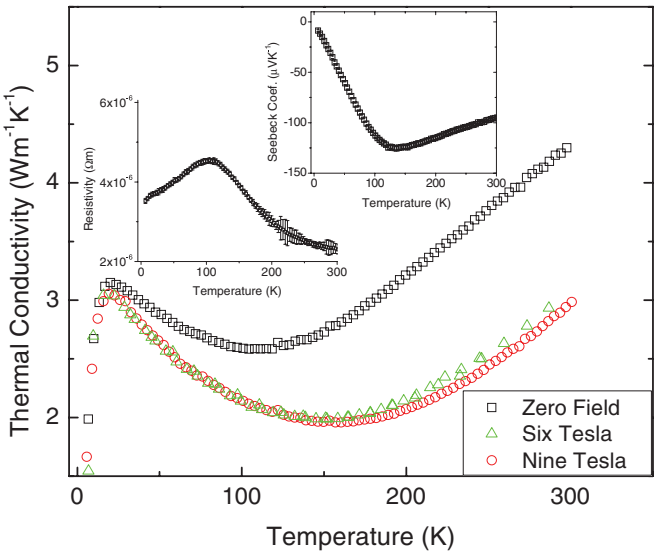


FIG. 5. (Color online) Thermal conductivity is plotted against temperature at magnetic fields of 0, 6, and 9 T for $Bi_{0.88}Sb_{0.12}$. The top right inset plots the Seebeck coefficient against temperature, while the top left inset plots $r$ vs $T$ from 5 to 300 K in zero magnetic field. It can be clearly seen that the bipolar contribution to the Seebeck coefficient becomes non-negligible around 150 K.

of $Bi_{0.88}Sb_{0.12}$ vs temperature in magnetic fields of 0, 6, and 9 T. The fact that the field is classically large in the temperature range of 5–150 K can be seen by inspection of Fig. 5. Since there is no change when increasing the field from 6 to 9 T below 150 K, the high-field limit has been reached, and $\kappa_{\text{carrier}}$has been completely suppressed. As can be seen in Fig. 5, the onset of the bipolar effect occurs above 150 K but not radiation effects since these are negligible under 200 K, which is not eliminated by the magnetic field and results in both the increase of the thermal conductivity and the lack of suppression of $\kappa_{\text{carrier}}$. The zero-field values for the Seebeck coefficient and electrical resistivity are plotted in the insets, both of which confirm the onset of bipolar effects around 150 K. The fact that the electronic thermal conductivity is not suppressed due to the bipolar contribution has been described by Uher and Goldsmid, and in pure bismuth happens at around 150 K.[5] Therefore, extraction of the Lorenz number using this method is only possible for temperatures below 150 K, where bipolar contributions are negligible. Once the lattice and total thermal conductivities are measured, the electronic portion was calculated using Eq. (1). Equation (2) can be rewritten as $LT = \kappa_{\text{carrier}}\rho$, where $\rho$ is the zero-field value for the electrical resistivity. Since, in this case, the lattice portion is measured over a range of temperatures, $\kappa_{\text{carrier}}\rho$ can be plotted versus temperature, and the slope of the line will yield $L$ for that temperature range. Figure 6 shows only the portion of the temperature range over which the plot is linear. At higher temperatures, above 150 K, the classical field approximation is no longer valid due to a drastic decrease in mobility as well as the onset of the bipolar contribution,[5,7] while at lower temperatures $\kappa_{\text{lattice}}$ dominates and therefore $\kappa_{\text{total}}$ is unaffected by magnetic field, as can be seen in Fig. 5. Fitting linearly, as shown in Fig. 6, gives the measured value for the Lorenz number as $2.21 \times 10^{-8}$ V$^2$ K$^{-2}$ in the

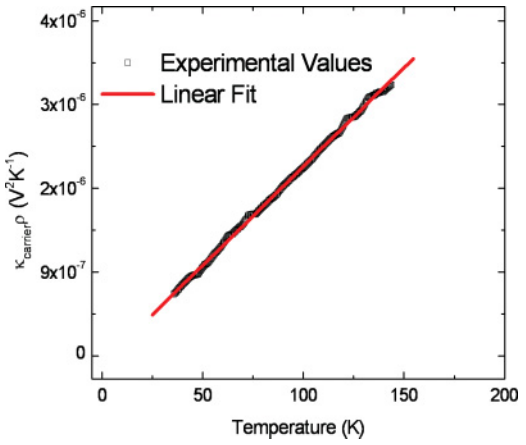


FIG. 6. (Color online) $\kappa_{\text{carrier}}\rho$ is plotted against temperature from 35 to 150 K. The black points represent the measured data, while the red line is the linear fit. The slope of the linear fit provides the Lorenz number $L = 2.21 \times 10^{-8}$ V$^2$ K$^{-2}$, and the $y$ intercept gives $\kappa_{\text{lattice}} = 2.14$ W mK$^{-1}$.

temperature range 35–150 K, meaning $L$ is constant over this range of temperature. Sharp *et al.* measured a sample of identical composition in fields up to 1 T, where they were unable to reach the high-field limit and therefore used the MTR method described above.[6] They obtained $L = 2.31 \times 10^{-8}$ V$^2$ K$^{-2}$ at 100 K, which is less than a 5% difference from our measurement. When comparing values for the lattice portion of the thermal conductivity, our measured value at 100 K yields 2.14 W mK$^{-1}$, while the value determined using the MTR method from extrapolation is 2.19 W mK$^{-1}$.[6] It should be noted that the grain sizes in both samples are of the same order of magnitude, with average grain sizes being roughly 1 and 5 $\mu$m for our sample and that of Sharp, respectively.[6] Again, as in the low-field limit, the measured values are not only reasonable but also within 5% of published values on the same material.

## IV. DISCUSSION

There is excellent agreement between the two models used to fit the data in the low-field limit for $Cu_{0.01}Bi_2Te_{2.7}Se_{0.3}$ and $[Cu_{0.01}Bi_2Te_{2.7}Se_{0.3}]_{0.98}Ni_{0.02}$ as well as decent agreement with simple parabolic band model theory. There is also excellent agreement between both low- and high-field methods, as shown in the measurements of $Bi_{0.88}Sb_{0.12}$ and their comparison with literature values. While measurements for $Bi_{0.88}Sb_{0.12}$ were made near the typical temperature range of operation, these temperatures are far from optimal for $Cu_{0.01}Bi_2Te_{2.7}Se_{0.3}$, which operates in a much higher temperature range.[10] The purpose of measuring $Cu_{0.01}Bi_2Te_{2.7}Se_{0.3}$ was to see first if the measurement was possible in nanostructured materials and second to see how high the temperature could be raised while performing the measurement. Therefore the measurement was also tried at 250 K; however, there was no variation in the thermal conductivity data outside of experimental error. This is due to the fact that the mobility decreased by a factor of 3 at 250 K.

The requirement of high mobility is one of the limitations of this technique. Other limitations include the requirements for a high magnetic field, again to satisfy $\mu B \gg 1$, as well as the electronic portion of the thermal conductivity being at least 5%. Ideal thermoelectric materials will have a high mobility along with a low lattice thermal conductivity, which is comparable to the electronic portion, and so the use of magnetic field to separate out $\kappa_{\text{carrier}}$ would be perfect for the ideal nanostructured thermoelectric material.[1,5–9] The assumptions that are being made for the analysis (models used to fit the data) using this method are that the Lorenz number is independent of magnetic field, the lattice is unaffected by magnetic field, there is no bipolar contribution, and electron-phonon interactions are negligible. The assumption that the Lorenz number and lattice are independent of magnetic field is true for some materials, which we take to be the case for these materials,[12] but in general it is not true and can be affected by secondary magnetic impurities. We are investigating the generality of this assumption further. Bipolar contributions should be negligible at 100 K. We assume electron-phonon interactions would manifest themselves when comparing the high- and low-field methods in $Bi_{0.88}Sb_{0.12}$. In the high-field limit the carrier completes a full orbit and therefore should be more likely to scatter a phonon, which would lead to a difference in the thermal conductivity between the high- and low-field measurements. Since there is no difference between the two methods, we believe the electron-phonon interactions to be negligible. It is noted that it would be interesting to devise an experiment from which electron-phonon interactions could be determined.

Because of the limitations on the material, only metals (W,[13] Cu,[19] Pb,[20] Rb,[21] etc.) along with a few alloyed compounds [$Cd_3P_2$ (Ref. 22) and $Cd_3As_2$ (Ref. 23)] have been measured using magnetic field; what we have found is referenced here and throughout the paper. Review articles written by Butler and Williams[17] and, more recently, by Kumar[1] attempt to give several literature values, though many were missed, for the Lorenz number of different elements and alloys determined by all types of experimental methods, not just in magnetic field. Another example of experimentally determining the Lorenz number is through the introduction of impurities in alloys, where the change in electrical conductivity and $\kappa_{\text{carrier}}$ is used to determine $\kappa_{\text{lattice}}$. A nice description, with examples as well as shortcomings, of the alloying method is given by Butler and Williams.[17]

Further investigation is required into higher-temperature measurements as well as other types of materials[14,24] for which this technique can be useful. It should also be mentioned that we have only looked at the diagonal components, specifically $\kappa_{xx}$ and $\sigma_{xx}$, of the transport tensors, and it could be possible to extract even more data from the off-diagonal components through measurements of the Righi-Leduc and Hall coefficients.[24,25] Future work will include systematic measurements of the transport tensors on a specific material over a larger temperature range along with more complex theoretical analysis.

## V. CONCLUSION

Two methods for experimentally determining the Lorenz number are presented for nanopolycrystalline $Bi_{0.88}Sb_{0.12}$, $Cu_{0.01}Bi_2Te_{2.7}Se_{0.3}$, and $[Cu_{0.01}Bi_2Te_{2.7}Se_{0.3}]_{0.98}Ni_{0.02}$.

Measured values of $Cu_{0.01}Bi_2Te_{2.7}Se_{0.3}$ and $[Cu_{0.01}Bi_2Te_{2.7}Se_{0.3}]_{0.98}Ni_{0.02}$ analyzed using Eqs. (1)–(3) as well as Eqs. (7) and (8) yield similar results and are close to calculated values using the single parabolic band model presented in Eqs. (4)–(6). The measured values for $Bi_{0.88}Sb_{0.12}$ are the same as previously published results. Now that the two methods have been clearly demonstrated to work on these nanopolycrystalline alloys at a given temperature, it is possible to look at other materials as well as the temperature range for which this technique can be used. A systematic study can then be done of the temperature dependence of the Lorenz number for a given material, making it possible for more complex theoretical models to be verified within experimental error, leading to more accurate determinations of the lattice portion of the thermal conductivity.

## ACKNOWLEDGMENTS

This work is supported by the "Solid State Solar-Thermal Energy Conversion Center (S3TEC)," an Energy Frontier Research Center founded by the US Department of Energy, Office of Science, Office of Basic Energy Science, under Award No. DE-SC0001299/DE-FG02-09ER46577.

[1] G. S. Kumar and M. E. Fine, J. Mater. Sci. **28**, 4261 (1993).
[2] S. A. Aliev, L. L. Korenblit, and S. S. Shalyt, Sov. Phys. Solid State **8**, 565 (1966).
[3] D. M. Rowe and C. M. Bhandari, *Modern Thermoelectrics* (Reston Publishing, Reston, VA, 1983).
[4] N. Hsieh and M. E. Fine, J. Appl. Phys. **52**, 2876 (1981).
[5] C. Uher and H. J. Goldsmid, Phys. Status Solidi B **65**, 765 (1974).
[6] J. W. Sharp, E. H. Volckmann, and H. J. Goldsmid, Phys. Status Solidi A **185**, 257 (2001).
[7] D. Armitage and H. J. Goldsmid, J. Phys. C **2**, 2138 (1969).
[8] G. K. White and S. B. Woods, Philos. Mag. **3**, 342 (1958).
[9] R. T. Delves, Br. J. Appl. Phys. **15**, 105 (1964).
[10] W. S. Liu, Q. Zhang, Y. Lan, S. Chen, X. Yan, Q. Zhang, H. Wang, D. Z. Wang, G. Chen, and Z. F. Ren, Adv. Energy Mater. **1**, 577 (2011).
[11] D. M. Rowe, *CRC Handbook of Thermoelectrics* (CRC Press, New York, 1995).
[12] A. E. Bowley, R. Delves, and H. J. Goldsmid, Proc. Phys. Soc. London **72**, 401 (1958).
[13] J. De Nobel, Physica **15**, 532 (1949).
[14] M. R. Stinson, R. Fletcher, and C. R. Leavens, Phys. Rev. B **20**, 3970 (1979).
[15] A. F. Ioffe, *Physics of Semiconductors* (Infosearch, London, 1960).
[16] R. Laiho, S. A. Nemov, A. V. Lashkul, E. Lakhderanta, T. E. Svechnikova, and D. S. Dvornik, Semiconductors **41**, 546 (2007).
[17] W. H. Butler and R. K. Williams, Phys. Rev. B. **18**, 6483 (1978).
[18] C. Jacoboni, *Theory of Electron Transport in Semiconductors* (Springer, Berlin, 2010).
[19] R. W. Arenz, C. F. Clark, and W. N. Lawless, Phys. Rev. B. **26**, 2727 (1982).
[20] L. J. Challis, J. D. N. Cheeke, and P. Wyder, Phys. Rev. **143**, 499 (1966).
[21] R. Fletcher and I. B. Verma, Phys. Rev. B. **36**, 9482 (1987).
[22] F. A. P. Blom and J. W. Burg, J. Phys. Chem. Solids. **38**, 19 (1977).
[23] F. A. P. Blom and A. Huyser, Sol. State Commun. **7**, 1299 (1969).
[24] M. Matusiak, T. Plackowski, and W. Sadowski, Sol. State Commun. **132**, 25 (2004).
[25] Y. Zhang, N. P. Ong, Z. A. Xu, K. Krishana, R. Gagnon, and L. Taillefer, Phys. Rev. Lett. **84**, 2219 (2000).

# Transport properties of Ni, Co, Fe, Mn doped $Cu_{0.01}Bi_2Te_{2.7}Se_{0.3}$ for thermoelectric device applications

K. C. Lukas, W. S. Liu, Z. F. Ren, and C. P. Opeil
*Department of Physics, Boston College, Chestnut Hill, Massachusetts 02467, USA*

(Received 24 May 2012; accepted 9 August 2012; published online 11 September 2012)

$Bi_2Te_3$ based thermoelectric devices typically use a nickel layer as a diffusion barrier to block the diffusion of solder or copper atoms from the electrode into the thermoelectric material. Previous studies have shown degradation in the efficiency of these thermoelectric devices may be due to the diffusion of the barrier layer into the thermoelectric material. In this work, Ni, Co, Fe, and Mn are intentionally doped into $Cu_{0.01}Bi_2Te_{2.7}Se_{0.3}$ in order to understand their effects on the thermoelectric material. Thermoelectric transport properties including the Seebeck coefficient, thermal conductivity, electrical resistivity, carrier concentration, and carrier mobility of $Cu_{0.01}Bi_2Te_{2.7}Se_{0.3}$ doped with 2 atomic percent M (M = Ni, Co, Fe, Mn) as $Cu_{0.01}Bi_2Te_{2.7}Se_{0.3}M_{0.02}$ are studied in a temperature range of 5-525 K. It is seen that the introduction of Ni, Co, Fe, or Mn does not affect the overall figure of merit, and therefore demonstrates that the diffusion barrier is not leading to device degradation as previously hypothesized. Any of these elements may be used as a diffusion barrier with Co being the best candidate based on both its electrical and mechanical properties. © *2012 American Institute of Physics*. [http://dx.doi.org/10.1063/1.4749806]

## INTRODUCTION

Much work has been done in recent years in an effort to improve the thermoelectric (TE) transport properties of several TE materials where efforts have specifically focused on the enhancement of the dimensionless figure of merit, $ZT$ where $ZT = (S^2/\rho\kappa)T$ with $S$ being the Seebeck coefficient, $\rho$ the resistivity, $\kappa$ the thermal conductivity, and $T$ the absolute temperature.[1] Efforts have focused on either the reduction of the lattice thermal conductivity, or the enhancement of the power factor $S^2/\rho$ through various approaches relying on physics at the nanoscale.[2–5] Ultimately, however, the material is going to be used in an actual device, where it is necessary for further optimization beyond that of the TE material used.[2] There have been previous studies on the fabrication of TE devices for cooling and power generation, along with the difficulties that arise during fabrication and operation.[2] TE devices are typically constructed with several p-n couples connected electrically in series and thermally in parallel as described by Ioffe.[1] A simple schematic of one p-n couple is shown in Fig. 1. The efficiency of a TE device increases with both the material's ZT and the temperature difference between the hot and the cold junction of the TE elements. One of the most important challenges in fabricating an efficient TE device is to develop interfaces with low electrical and thermal contact resistance. Large electrical contact resistance results in parasitic Joule heating losses, while large thermal contact resistances result in a smaller temperature gradient across the TE material.

The best way to create good electrical and thermal connections is by soldering. However, it is known that typical solders as well as Cu metal (used for electrodes) readily diffuse into and degrade the properties of TE materials, specifically $Bi_2Te_3$ based materials.[2–11] In order to impede the diffusion of solder into the TE material, diffusion barriers are used.[7] These diffusion barriers are typically thin films of sputtered or electrochemically deposited metallic elements such as Fe for TAGS-85 and PbTe.[10,12] The deposition techniques ensure minimal thermal and electrical contact resistance. Additionally, the thin films should have similar coefficients of thermal expansion (CTE) to ensure the mechanical longevity of the device.[2,9]

It was previously demonstrated that nickel could be used successfully as a diffusion barrier for solder in p-type $Bi_2(SbTe)_3$ and n-type $Bi_2(TeSe)_3$ alloys.[7] The problem was that, even though the nickel stopped the solder, the nickel itself diffused into the n-type $Bi_2(TeSe)_3$. A simple schematic of the Ni diffusion described in Ref. 7 in one p-n couple is shown in Fig. 1. Shown on the left is the ideal scenario where the Ni acts as a diffusion barrier without diffusing into the TE material. On the right is what actually happens during fabrication and operation. The Ni does not diffuse into the p-type element but does diffuse slightly into the n-type element. A later study demonstrated that using Co as a diffusion barrier prevented the solder from getting into the n-type $Bi_2(TeSe)_3$ while the Co itself did not diffuse into the material as readily as Ni.[9] Each study included only interfacial microstructure data and therefore it is unclear how the diffused Ni or Co affected the transport properties, though it was noted that the efficiency of the Peltier cooling devices degraded over time.[7] It was also noted that the Ni diffused further into the TE material as operation time increased. Therefore it seemed reasonable that TE device degradation was due to the diffusion of the Ni barrier into the TE material.[7] Based on this assumption, the device should perform at its lowest efficiency when the Ni fully diffused into the TE material.

In this study we intentionally dope two atomic percent Ni, Co, Fe, and Mn into $Cu_{0.01}Bi_2Te_{2.7}Se_{0.3}$ to study the maximum degradation in electrical and thermal transport properties that a TE material can undergo if these elements

 © 2012 American Institute of Physics

Downloaded 28 Sep 2012 to 136.167.55.68. Redistribution subject to AIP license or copyright; see http://jap.aip.org/about/rights_and_permissions

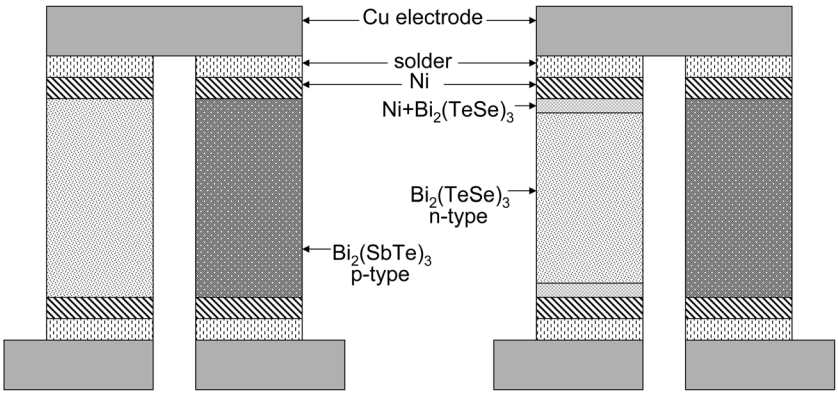


FIG. 1. Both (a) and (b) show one p-n couple that can be used as a thermoelectric generator or Peltier cooler. Typical TE devices contain many couples. The ideal solder connection to the Ni diffusion barrier for a $Bi_2Te_3$ p-n couple is shown in (a) where the Ni does not diffuse into the TE material. (b) The actual case during fabrication and operation where the Ni diffuses into the n-type TE material which is believed to be the cause of device degradation.[4]

are used as a diffusion barrier. Based on a typical device height of 1 mm as well as the thickness of the applied diffusion barrier of 3 $\mu$m, the amount of Ni, Co, Fe, or Mn that diffuses into the TE material should not exceed 2 percent.[7] Ni, Co, and Fe all have similar coefficients of thermal expansion which are reported to be similar to that of $Bi_2(TeSe)_3$,[9,12] and therefore would be ideal for device fabrication. Mn has a coefficient of thermal expansion roughly double that of Ni, Co, or Fe but is included in this study to see how transport is effected.[12]

## EXPERIMENTAL

Proper stoichiometric amounts of Cu (Alfa Aesar 99.999%), Bi (Alfa Aesar 99.999%), Te (Alfa Aesar 99.999%), Se (Alfa Aesar 99.999%), Ni (Alfa Aesar 99.999%), Co (Alfa Aesar 99.999%), Fe (Alfa Aesar 99.999%), and Mn (Alfa Aesar 99.999%) were prepared by ball milling and hot pressing methods described previously according to the formula $Cu_{0.01}Bi_2Te_{2.7}Se_{0.3}M_{0.02}$ (M = Ni, Co, Fe and Mn).[13] Thermal conductivity $\kappa$, electrical resistivity $\rho$, Seebeck coefficient $S$, and Hall coefficient $R_H$ were measured using a physical properties measurement system (PPMS) from Quantum Design in a temperature range of 5–350 K. The carrier concentration $n$ and mobility $\mu_H$ were obtained from Hall measurements and the relations $n = 1/R_H q$ and $\mu_H = R_H/\rho$ where $q$ is the electronic charge. Values for the electrical resistivity and Seebeck coefficient at temperatures 300–525 K were made using both a ZEM-3 from Ulvac Inc. as well as a homebuilt system. For clarity, only values from the ZEM-3 are shown, but all data agree within experimental error. Values for thermal conductivity were obtained using a LaserFlash system from Netzch. Low temperature measurements of $\kappa$,$\rho$, and $S$ were made on samples parallel to the press direction, while Hall measurements as well as high temperature measurements were made perpendicular to the press direction. It has been previously demonstrated that these materials are isotropic to within 10%.[13] Estimated errors for $\rho$, $\kappa$, $S$, $ZT$, $n$, and $\mu_H$ should not exceed 3%, 8%, 5%, 14%, 10%, and 10%, respectively.

## RESULTS AND DISCUSSION

The Hall coefficient is negative over the entire temperature range showing that the majority carriers are electrons as is to be expected for $Cu_{0.01}Bi_2Te_{2.7}Se_{0.3}$.[13] Figure 2(a) shows the carrier concentration for all samples from 10 to 350 K. In contrast to $Cu_{0.01}Bi_2Te_{2.7}Se_{0.3}$ ($4.29 \times 10^{19}/cm^{-3}$ at 300 K), the carrier concentration at room temperature of $Cu_{0.01}Bi_2Te_{2.7}Se_{0.3}M_{0.02}$ is increased with the addition of Ni ($5.72 \times 10^{19}$ / $cm^{-3}$), Co ($4.88 \times 10^{19}$ /$cm^{-3}$), and Fe ($4.83 \times 10^{19}$ /$cm^{-3}$), while $n$ decreased with Mn ($3.11 \times 10^{19}/cm^{-3}$). The increased carrier concentration for the Ni, Co, and Fe can be explained in the same manner as the increase in the case of Cu doped n-type $Bi_2Te_{2.7}Se_{0.3}$. It was previously shown that Cu easily

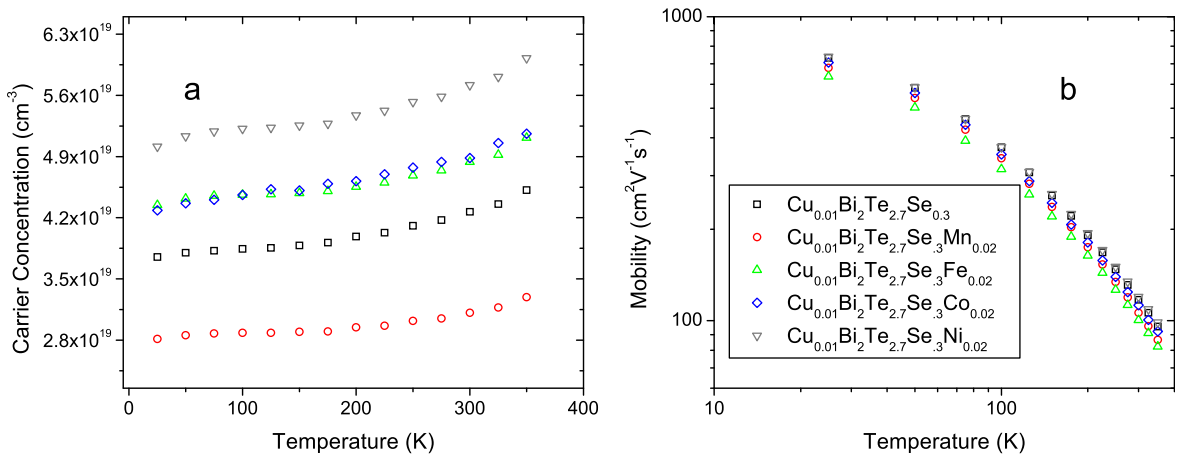


FIG. 2. The carrier concentration (a) and carrier mobility (b) are plotted with temperature from 5–350 K. Carrier concentration changes with the doping element while the mobility remains unaffected.

Downloaded 28 Sep 2012 to 136.167.55.68. Redistribution subject to AIP license or copyright; see http://jap.aip.org/about/rights_and_permissions

diffuses into $Bi_2Te_3$ through the interstitial sites between two Te layers and acts as a strong donor providing 0.3 carrier/atom.[13] Ni, Co, and Fe appear to get into the interstitial site of $Bi_2Te_{2.7}Se_{0.3}$ as well and also work as an n-type dopant providing 0.12, 0.05, and 0.04 carrier/atom, respectively. Such transition metals have also demonstrated n-type doping behavior when they are located at the interstitial site of layered compounds $TiSe_2$[14] and $TiS_2$.[15] The inability of Ni, Co, and Fe to donate the same number of free electrons in $Cu_{0.01}Bi_2Te_{2.7}Se_{0.3}M_{0.02}$ is likely associated with the difference in the number of outer valence electrons. Contrary to the other dopants, Mn decreases the carrier concentration. Based on previous work demonstrating that Cu sitting in the interstitial site will donate carriers[13] along with the increase in carrier concentration from the addition of Ni, Co, and Fe, it is possible that Mn does not sit in the interstitial site but substitutes for either Bi or Te. Figure 2(b) plots the mobility against temperature up to 350 K. It can be seen that the variation in mobility is quite small with the greatest change being roughly a 10% decrease for the Fe doped sample. The lack of change in $\mu_H$ compared to $n$ with the addition of Ni, Co, Fe, and Mn is similar to the case of filled skutterudites. Filled skutterudites do not show as a great change in mobility compared to the carrier concentration because the dopants sit in the interstitial site.[16]

In the range from 5-350 K, the thermal and electrical transport properties of all doped TE samples show a small variation with the introduction of any of the doping impurities (Fig. 3). The electrical resistivities, Fig. 3(a), show metallic like behavior. The addition of Ni slightly decreases the resistivity while the addition of Co, Fe, and Mn slightly increases the values for $\rho$ where Mn shows the largest increase which is due to a drop in carrier concentration. The Seebeck coefficient is negative over the entire temperature range confirming the majority carriers are electrons (Fig. 3(b)). The Seebeck coefficient is slightly decreased by the addition of Ni due to the increased carrier concentration and unchanged mobility. Co and Fe do not strongly impact the values for $S$, while the addition of Mn slightly increases $S$ again due to the decrease in $n$. The thermal conductivity decreases with the introduction of either Ni, Co, Fe, or Mn, all of which act as scattering sites in the lattice (Fig. 3(c)) as has been previously demonstrated with Cu in $Bi_2Te_{2.7}Se_{0.3}$.[13] The values of $ZT$ seen in Fig. 3(d) show that overall the figure of merit is unaffected by any of the above 3d transition metal doping.

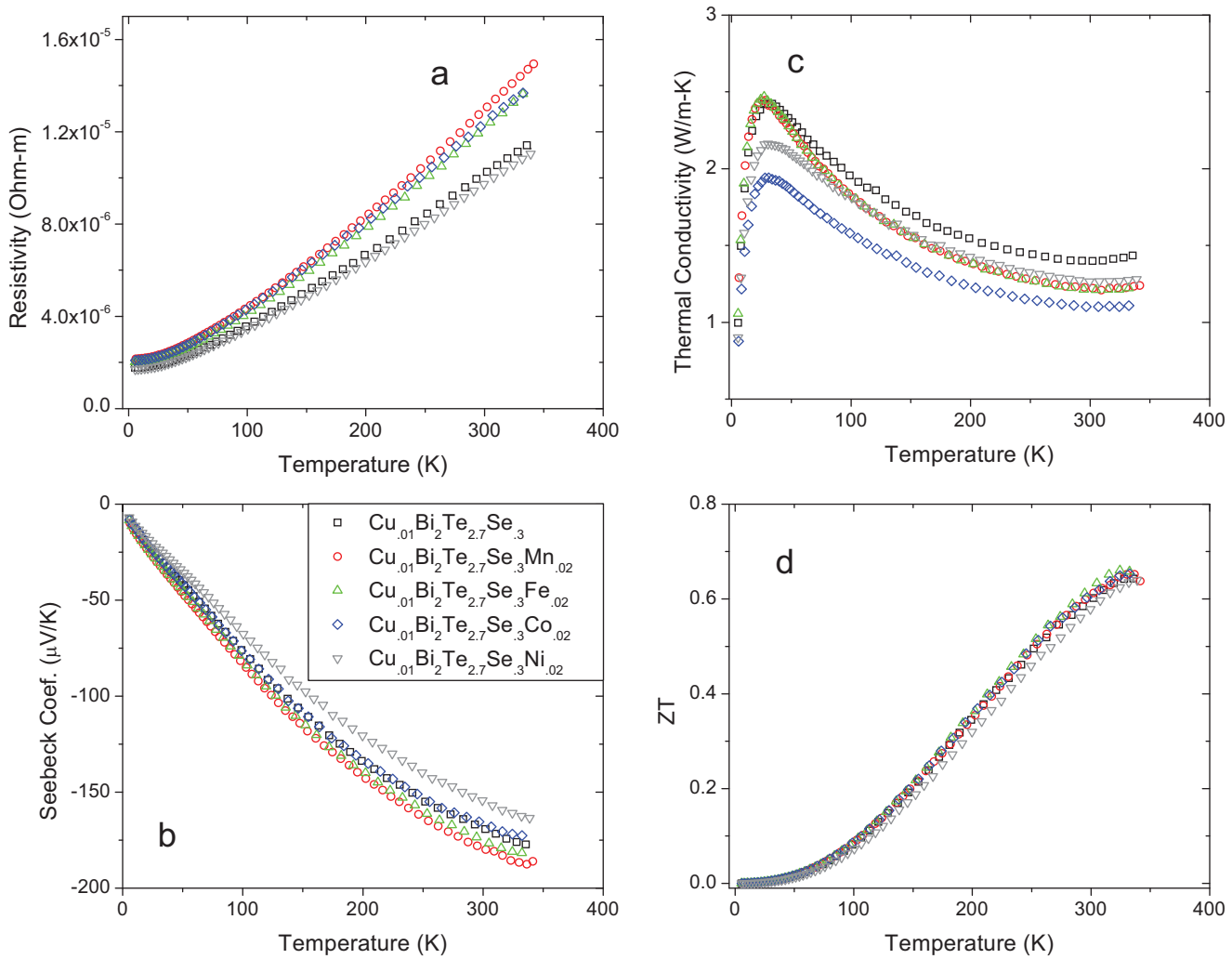


FIG. 3. The electrical resistivity (a), Seebeck coefficient (b), thermal conductivity (c), and $ZT$ (d) are plotted with temperature from 5–350 K. Though $\rho$ and $S$ change with $n$, $ZT$ remains unchanged in each sample.

Downloaded 28 Sep 2012 to 136.167.55.68. Redistribution subject to AIP license or copyright; see http://jap.aip.org/about/rights_and_permissions

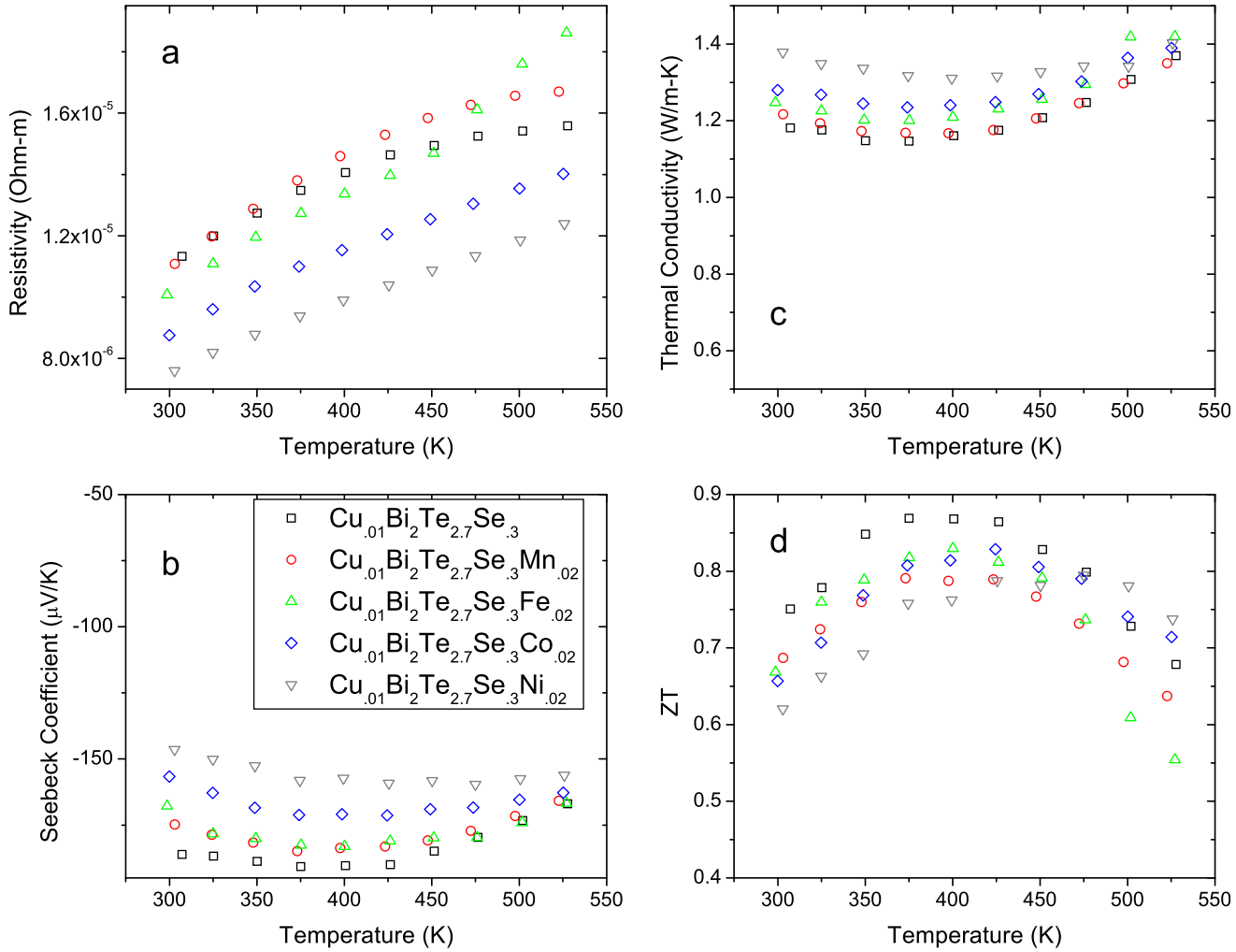


FIG. 4. The electrical resistivity (a), Seebeck coefficient (b), thermal conductivity (b), and *ZT* (d) are plotted with temperature from 300–525 K. *ZT* is relatively unaltered by the introduction of different impurities just as in the low temperature measurements.

In the temperature range from 300–525 K, the inclusion of Ni gives a lower value for the electrical resistivity while Mn increases the resistivity (Fig. 4(a)). Figure 4(b) shows that within experimental error the Seebeck coefficient remains the same except for the Ni doped sample which is suppressed due to the increase in carrier concentration, though experimentally $n$ is only measured up to 350 K. At these higher temperatures, phonon-phonon scattering becomes dominant and all samples exhibit similar values for thermal conductivity, as expected (Fig. 4(c)). Overall, in each sample, an increase in $\rho$ comes with an increase in S and therefore all samples have similar values for *ZT* (Fig. 4(d)) just as in the low temperature data presented in Fig. 3. The transport properties measured by the two commercial systems along different pressing directions match to within about 10% as is expected.[13]

Both high and low temperature measurements made perpendicular and parallel to the press direction show similar quantitative trends due to the introduction of Ni, Fe, Co, and Mn, where overall there is negligible change to *ZT* with the addition of impurities. This means that if any of these elements are used as diffusion barriers, and diffuse into the TE material, there should be negligible effects on the efficiency of the device. It was mentioned previously that former studies showed a decrease in device efficiency which was attributed to diffusion of Ni into the TE material.[7] However, these results are contrary to that understanding because the device degradation is not due to deteriorating TE material performance. One possible explanation is that there is Cu already introduced into the $Bi_2Te_{2.7}Se_{0.3}$ material in this study. Previous studies by Liu *et al.*, added Cu in order to make the material properties reproducible.[13] And therefore with a further introduction of impurities at such a small percentage, there is not as drastic change in the thermal or electrical transport properties as what is seen with the addition of slight amounts of Cu. Based on this understanding, any of the metallic elements, Ni, Co, Fe, and Mn, can be used as a diffusion barrier for $Cu_{0.01}Bi_2Te_{2.7}Se_{0.3}$ as long as they inhibit the solder from entering the TE material and have the proper mechanical properties during operation.[2] It would be interesting to create a device using $Cu_{0.01}Bi_2Te_{2.7}Se_{0.3}$ as the n-type TE material and Ni as a diffusion barrier. Based on the above data, the device should not degrade, as long as the solder does not diffuse, if a small amount of Ni diffuses into the TE material. If the device does degrade, then there are other issues with the device. Perhaps some special type of

Downloaded 28 Sep 2012 to 136.167.55.68. Redistribution subject to AIP license or copyright; see http://jap.aip.org/about/rights_and_permissions

failure at the interface happens during operation or fabrication, but this failure would not be due to TE material degradation.

The above analysis only applies to bulk or "macro" TE devices. However the data can be useful in the construction of "micro" TE devices as well. Microelectromechanical systems (MEMS) and other thin film TE devices are also of interest and have become a widely studied area.[2,6,17–19] In thin films, the diffusion barrier thickness is on the same order as the TE material,[2,6] and so if Ni readily diffuses into $Cu_{0.01}Bi_2Te_{2.7}Se_{0.3}$ then the inclusion of Ni will be greater than the 2% addition studied here. However previous studies for Co show that it does not easily diffuse into $Bi_2(TeSe)_3$ and therefore the low doping percentage study here can be applicable.[9] Co does go through a structural phase transition at 380 °C,[20] but this is higher than the typical operating temperature of $Bi_2(TeSe)_3$ based TE devices and therefore should be of no concern.[2,7]

Due to the similarity in the coefficient of thermal expansion, minimal diffusion of Co into $Bi_2(TeSe)_3$,[9] and no significant change in *ZT* for Co doped $Cu_{0.01}Bi_2Te_{2.7}Se_{0.3}$, it appears that Co would be an excellent choice for the contact material in a $Cu_{0.01}Bi_2Te_{2.7}Se_{0.3}$ thin film TE device. The authors could find no information on the diffusion of Fe or Mn in $Bi_2(TeSe)_3$, however if they show similar diffusion tendencies to that of Co then they could also be a possible option for a contact material. However, because Fe oxidizes easily and Mn has a higher CTE, Co appears to be the ideal choice for contact materials in either macro or micro TE devices.

## CONCLUSION

Thermoelectric transport properties of $Cu_{0.01}Bi_2Te_{2.7}Se_{0.3}$ doped with 2 atomic percent Ni, Co, Fe, and Mn are studied to reveal information on possible metallic elements for use as diffusion barriers in TE devices. It is shown that *ZT* is unaffected by the low percentage impurity doping and therefore the efficiency of TE devices should not be affected if any of these metals diffuse into the TE material while being used as a diffusion barrier for solder. And based on this and previous studies, Co seems to be the optimal choice for a diffusion barrier. It is also noted that the addition of Cu into $Bi_2Te_{2.7}Se_{0.3}$ could be of great benefit to TE device fabrication because any excess introduction of impurities from the diffusion barriers would be negligible.

## ACKNOWLEDGMENTS

We gratefully acknowledge funding for this work through the "Solid State Solar-Thermal energy conversion Center (S3TEC)," an Energy Frontier research Center founded by the U.S. Department of Energy, Office of Basic Energy Science under award number: DE-SC0001299/DE-FG02-09ER46577.

[1]A. F. Ioffe, *Semiconductor Thermoelements and Thermoelectric Cooling* (Inforsearch Limited, 1965).
[2]D. M. Rowe, *Thermoelectrics Handbook: Macro to Nano* (Taylor & Francis, New York, 2006).
[3]W. S. Liu, X. Yan, G. Chen, and Z. F. Ren, Nano Energy **1**, 42–56 (2012).
[4]G. J. Snyder and E. S. Toberer, Nature Mater. **7**, 105 (2008).
[5]A. J. Minnich, M. S. Dresselhaus, Z. F. Ren, and G. Chen, Energy Environ. Sci. **2**, 466 (2009).
[6]G. J. Snyder, J. R. Lim, C. K. Huang, and J. P. Fleurial, Nature **2**, 528 (2003).
[7]Y. C. Lan, D. Z. Wang, G. Chen, and Z. F. Ren, Appl. Phys. Lett. **92**, 101910 (2008).
[8]O. Ymashita, J. Appl. Phys. **95**, 178 (2004).
[9]R. P. Gupta, O. D. Iyore, K. Xiong, J. B. White, K. Cho, H. N. Alshareef, and B. E. Gnade, Electrochem. Solid-State Lett. **12**, H395 (2009).
[10]A. Singh, S. Bhattacharya, C. Thinaharan, D. K. Aswal, S. K. Gupta, J. V. Yakhmi, and K. Bhanumurthy, J. Phys. D **42**, 015502 (2009).
[11]V. M. Sokolova, L. D. Dudkin, and L. I. Petrova, Inorg. Mater. **36**, 16 (2000).
[12]D. R. Lide, *CRC Handbook of Chemistry and Physics*, 84th ed. (CRC Press, Boca Raton, 2003).
[13]W. S. Liu, Q. Zhang, Y. C. Lan, S. Chen, X. Yan, Q. Zhang, H. Wang, D. Z. Wang, G. Chen, and Z. F. Ren, Adv. Energy Mater. **1**, 577 (2011).
[14]F. Levy, J. Phys. C: Solid State Phys. **13**, 2901–12 (1980).
[15]J. Zhang, X. Y. Qin, H. X. Xin, D. Li, and C. J. Song, J. Electron. Mater. **40**, 5 (2011).
[16]J. Yang, Q. Hao, H. Wang, Y. C. Lan, Q. Y. He, A. Minnich, D. Z. Wang, J. A. Harriman, V. M. Varki, M. S. Dresselhaus, G. Chen, and Z. F. Ren, Phys. Rev. B **80**, 115329 (2009).
[17]D. Bishop, A. Heuer, and D. Williams, Mater. Res. Bull. **26**, 282 (2001).
[18]R. K. Kupka, F. Bouamran, C. Cremers, and S. Megtert, Appl. Surf. Sci. **164**, 97 (2000).
[19]R. Venkatasubramanian, E. Siivola, B. C. O'Quinn, K. Coonley, P. Addepalli, M. Napier, T. Colpitts, and M. Mantini, Proceedings of 2003 ACS Symposium on Nanotechnology and the Environment (New Orleans, 2003).
[20]C. Cabral, Jr., K. Barmak, J. Gupta, L. A. Clevenger, B. Arcot, D. A. Smith, and J. M. E. Harper, J. Vac. Sci. Technol. A **11**, 1435 (1993).

Downloaded 28 Sep 2012 to 136.167.55.68. Redistribution subject to AIP license or copyright; see http://jap.aip.org/about/rights_and_permissions

J Mater Sci
DOI 10.1007/s10853-012-6463-6

# Thermoelectric properties of Ho-doped $Bi_{0.88}Sb_{0.12}$

**K. C. Lukas · G. Joshi · K. Modic · Z. F. Ren · C. P. Opeil**

Received: 19 December 2011 / Accepted: 30 March 2012
© Springer Science+Business Media, LLC 2012

**Abstract** The Seebeck coefficients, electrical resistivities, total thermal conductivities, and magnetization are reported for temperatures between 5 and 350 K for n-type $Bi_{0.88}Sb_{0.12}$ nano-composite alloys made by Ho-doping at the 0, 1, and 3 % atomic levels. The alloys were prepared using a dc hot-pressing method, and are shown to be single phase for both Ho contents with grain sizes on the average of 900 nm. We find the parent compound has a maximum of ZT = 0.28 at 231 K, while doping 1 % Ho increases the maximum ZT to 0.31 at 221 K and the 3 % doped sample suppresses the maximum ZT = 0.24 at a temperature of 260 K.

## Introduction

Since the work of Smith and Wolfe [1], Bi-rich Bismuth Antimony n-type alloys have long been noted for their beneficial thermoelectric and magneto-thermoelectric properties below room temperature [2]. Similar results were found for different Bi–Sb compositions of single crystal alloys prepared by different growth techniques [3, 4]. New technological applications and work on $Bi_{1-x}Sb_x$ in zero field slowed for several years due to the lack of a comparable p-type material, because commercial devices rely on a combination of both n and p-type materials whose overall thermoelectric figure of merit is given by [5]

$$ZT = \frac{(\alpha_p - \alpha_n)^2}{\left[(\kappa_n \rho_n)^{\frac{1}{2}} + (\kappa_p \rho_p)^{\frac{1}{2}}\right]^2}$$

in which $\alpha$, $\rho$, and $\kappa$ are the Seebeck coefficient, resistivity, and thermal conductivity, respectively. Interest in the alloy was revived by the discovery of high $T_c$ superconductors and the work of Dashevskii et al. showing that the total dimensionless figure of merit is approximately equal to the value of ZT for the n-type couple [6–9].

As group V metals, $Bi_{1-x}Sb_x$ forms a solid solution over the entire composition range, being semimetallic outside the range $0.07 < x < 0.22$ where the alloy is semiconducting with the largest gap occurring around 17 % Sb concentration [10–15]. The best thermoelectric properties are found for single crystals, with $0.09 < x < 0.16$, when measured parallel to the trigonal axis [4, 11, 16]. Single crystals are not ideal for large scale manufacturing due to their difficulty in growing and cleaving, as well as their slow growth rate. More importantly, single crystals are mechanically weak [16], limiting their use in commercial applications. In an effort to increase their mechanical strength, polycrystalline alloys have been produced, but all have a lower ZT, dimensionless figure of merit, than single crystals. Several methods have been developed to improve ZT for n-type polycrystalline samples. These methods include: arc plasma [17], quenching [16], mechanical alloying [18], powder metallurgy [19], and doping [20, 21]. Devaux et al. [17] studied the effects of grain size on the thermoelectric properties, specifically investigating the decrease of the lattice component of the thermal conductivity with the reduction of grain size. While the thermal conductivity was reduced due to phonon scattering, there

K. C. Lukas (✉) · G. Joshi · Z. F. Ren · C. P. Opeil
Department of Physics, Boston College, Chestnut Hill, MA 02467, USA
e-mail: lukaske@bc.edu

K. Modic
Los Alamos National Laboratory, Los Alamos, NM 87545, USA

Published online: 17 April 2012

was no benefit to ZT due to increased resistivity, as has also been seen in nanosized grains [22, 23].

We present here the effects of doping atomic 1 and 3 % Ho into nano-polycrystalline $Bi_{0.88}Sb_{0.12}$ prepared by ball milling and dc hot-pressing. The motivation for using Ho was to study the effects on the magneto-thermoelectric properties due to a dopant with a large magnetic moment. Ho not only has a large magnetic moment, but it exhibits two magnetic transitions over the studied temperature range. Ho is antiferromagnetic over a large portion of the temperature range having a Neel temperature of approximately 133 K and is ferromagnetic at lower temperatures with a Curie temperature of about 20 K [24–28].

## Experimental

Nano-polycrystalline $Bi_{1-x}Sb_x$ samples were prepared by ball milling and dc hot-pressing techniques described previously [29–32] where $x = 0.12$ was determined to be the optimal Sb concentration for this process. Alloyed nanopowders were prepared by ball milling elemental chunks of bismuth (Bi) (99.99 %, Alfa Aesar) and antimony (Sb) (99.99 %, Alfa Aesar) with holmium (Ho) (99.9 %, Alfa Aesar) according to the required composition $Bi_{0.88}Sb_{0.12-y}Ho_y$ ($y = 0.01$ and 0.03) for 5–12 h, and then pressed at a temperature of 240 °C thereby creating disks 4 mm thick and 12 mm in diameter. X-ray diffraction was performed (Bruker AXS) to insure the powders were alloyed into a single phase, and SEM (JEOL 7001F) images were taken of freshly fractured surfaces to observe the effects of grain growth during pressing. The pressed disks were then polished, chemically etched in a Bromine solution and metallic contacts were sputtered onto the faces.

From the disks, two samples were cut to measure the thermoelectric properties. Thermoelectric properties $\alpha$, $\rho$, and $\kappa$ were measured, in the standard two probe method, from 5 to 350 K using the thermal transport option of the physical properties measurement system (PPMS) from Quantum Design. Samples for the thermal transport option were cut and measured perpendicular to the face of the disk (parallel with the press direction) with typical dimensions $3 \times 3 \times 4$ mm. Gold-coated OFHC (oxygen free high conductivity) copper disks provided by Quantum Design were soldered to the sputtered metallic contacts on the sample using Sn–Pb solder. A second sample was used to determine the Hall coefficient. The Hall coefficient was also determined using the PPMS, under a magnetic field of 9 T and a current of 20 mA. Our Hall sample was rotated by 180° in field using the QD-PPMS AC Rotator option, thereby allowing the current direction to be switched and thus averaging out any anomalous effects on the measurement due to the field. These samples were prepared in a five wire Hall configuration with typical dimensions $1 \times 3 \times 11$ mm. These samples were cut and measured perpendicular to the press direction. The carrier concentration was determined directly from the Hall coefficient. Resistivity, $\rho$, was measured using a standard four point probe technique, with the same sample and orientation used to attain the Hall coefficient, and mobility, $\mu$, was calculated from $R_H/\rho$. We assume the mobility to be essentially isotropic because the thermoelectric properties for alloys prepared by single dc hot-pressing techniques have been shown to be isotropic to within 10 % [32]. Susceptibility was measured using the vibrating sample magnetometer (VSM) option in the PPMS in a field of 0.1 T.

## Results and discussion

Figures 1 and 2 show the X-ray diffraction patterns and SEM images of $Bi_{0.88}Sb_{0.12}$, $Bi_{0.88}Sb_{0.12}Ho_{.01}$, and $Bi_{0.88}Sb_{0.12}Ho_{0.03}$, respectively. X-ray peak positions confirm that the samples are alloyed and no second phases exist, while SEM images confirm that the average grain growth is proportional in each sample, and independent of the doping concentration. We confirm that the addition of Ho does not affect grain growth, which is known to alter thermoelectric properties [17]. The changes in $\alpha$, $\rho$, $\kappa$ are due to contributions from the magnetic moment, as well as the different size and mass of Ho. It should be noted that the grains are larger than usual for this process because the dc hot-pressing process was not optimized.

The data in Fig. 3 shows the change in susceptibility due to the addition of Ho. Due to the large magnetic moment of Ho the susceptibility increases with the addition of 1 % Ho

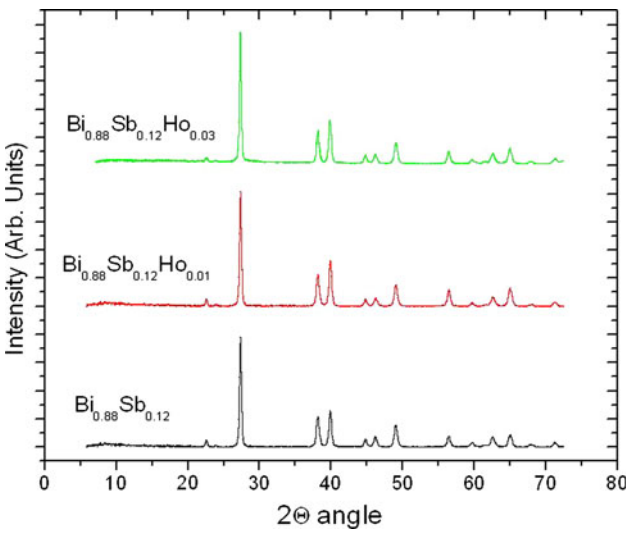


**Fig. 1** XRD pattern for $Bi_{0.88}Sb_{0.12}$ (*Black*), $Bi_{0.88}Sb_{0.12}Ho_{0.01}$ (*Red*), $Bi_{0.88}Sb_{0.12}Ho_{0.03}$ (*Green*) (Color figure online)

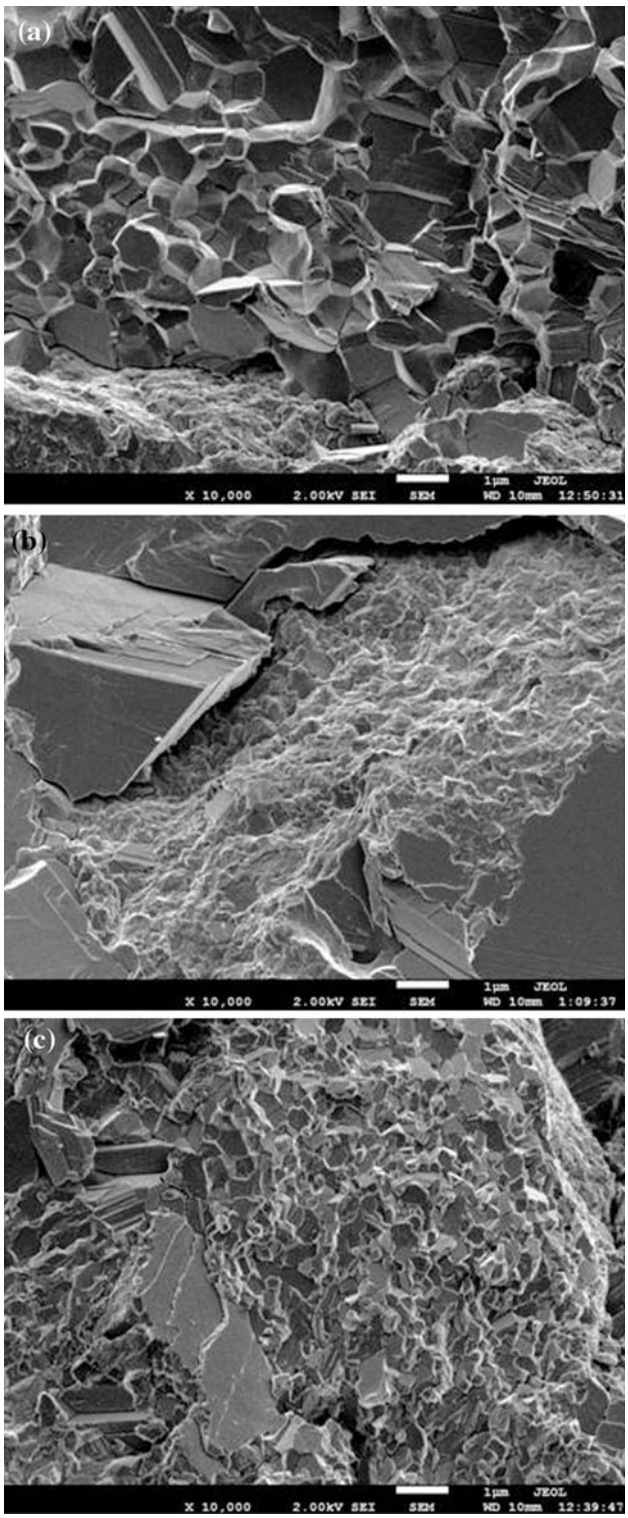


**Fig. 2** SEM images for **a** $Bi_{0.88}Sb_{0.12}$, **b** $Bi_{0.88}Sb_{0.12}Ho_{0.01}$ and **c** $Bi_{0.88}Sb_{0.12}Ho_{0.03}$. The scale bar is 1 μm

and further increases with 3 % Ho, where the Neel and Curie temperatures can also be seen more distinctly as the percentage of Ho increases. High enough temperatures could not be reached in the VSM to perform a Curie–Weiss fit as can be seen in the left inset of Fig. 3. The top right inset plots Δ capacitance versus temperature for 1 % Ho on a home built torque cantilever magnetometer, giving the same trend as the VSM.

The Hall coefficient is negative throughout the temperature range, showing that electrons are the majority carriers. The carrier concentration is presented in Fig. 4. It can be seen that there is almost no change from the addition of 1 % Ho at temperatures above 200 K while there is a decrease in carrier concentration below 200 K. The addition of 3 % Ho increases the carrier concentration throughout the temperature range. The decrease in carrier concentration with the addition of 1 % Ho while increasing with the addition of 3 % Ho over the parent compound may be due to the fact that the Ho begins to replace a different site in the lattice as the dopant concentration increases, which has been seen in co-doped PbTe [33]. The values for $Bi_{0.88}Sb_{0.12}$ are slightly higher than those reported in the literature for polycrystalline samples prepared by quenching and annealing [16], and three orders of magnitude higher than values reported for single crystals at 4.2 K [34]. Figure 5 shows the mobility, where again 1 and 0 % Ho are nearly equal for higher temperatures ($T > 200$ K) but deviate from one another at lower temperatures, where 0 % Ho has a higher mobility than the 1 % Ho sample. Again the 3 % Ho-doped sample has a consistently lower mobility throughout the temperature range. The values for mobility, Fig. 5, are again lower than in the literature [16, 34]; however, the log $\mu_H$ vs. log $T$ curve is linear for $Bi_{0.88}Sb_{0.12}$ showing the same qualitative trend throughout the temperature range. The addition of Ho causes a more defined change in the slope of the lines at 150 K, creating two different relationships for $\mu(T)$ above and below 150 K.

Figure 6 shows the temperature dependence of the resistivity for the different doping concentrations. Each sample shows typical semiconducting behavior at lower temperatures, with the maximum value for $\rho$ at temperatures below 150 K increasing with doping concentration. At temperatures exceeding 150 K, the 0 and 1 % Ho samples have nearly the same resistivity, while the 3 % Ho sample always has a greater resistivity than the other compositions. The increase in resistivity at lower temperatures for the 1 % Ho sample is due to both a decrease in carrier concentration as well as a decrease in mobility, while the increase in $\rho$ for the 3 % Ho sample is due entirely to a decrease in mobility. The values for $\rho$ of $Bi_{0.88}Sb_{0.12}$ are higher than those of single crystal [11], which is typically the case, but comparable with those of different polycrystalline samples [16, 17, 19], including those from the work by Belaya et al. [20] and Dutta et al. [23].

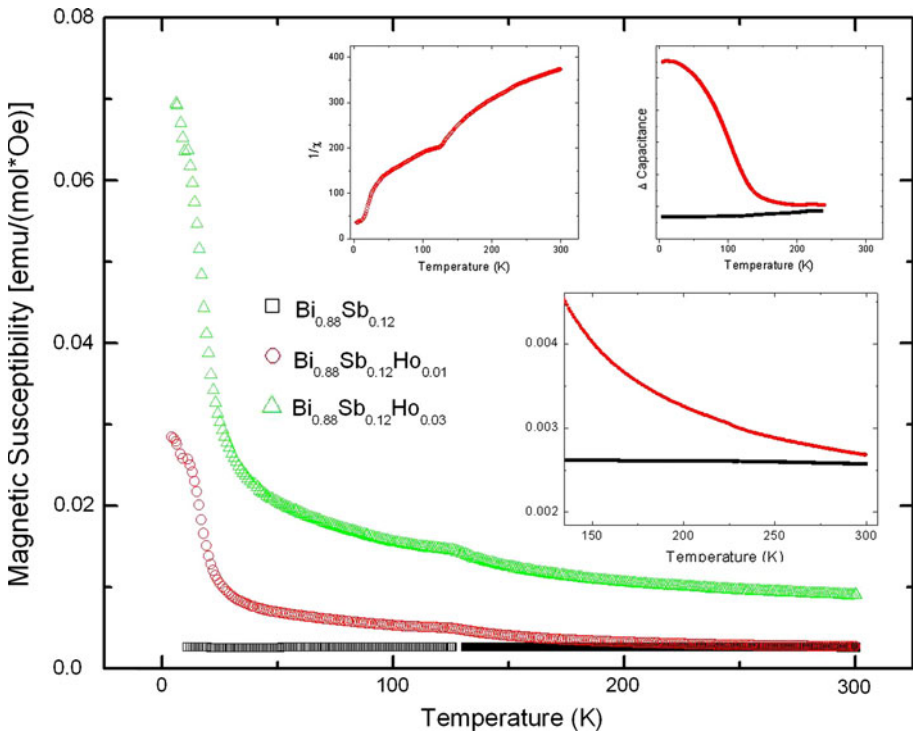


**Fig. 3** Temperature dependence of the magnetic susceptibility for $Bi_{0.88}Sb_{0.12}$ (*Black*), $Bi_{0.88}Sb_{0.12}Ho_{0.01}$ (*Red*), $Bi_{0.88}Sb_{0.12}Ho_{0.03}$ (*Green*) given by the VSM option in the PPMS. The bump in the data at 10 K is caused by the PPMS changing cooling modes and not by the sample. The *upper right inset* shows Δ capacitance vs. temperature on a home built torque cantilever magnetometer for $Bi_{0.88}Sb_{0.12}$ (*Black*) and $Bi_{0.88}Sb_{0.12}Ho_{0.01}$ (*Red*) giving the same trend as the VSM data. The *left inset* plots $1/\chi$ vs. temperature and shows that a Curie–Weiss analysis is not possible for this temperature range. The *lower right inset* gives an expanded view of $\chi$ vs. temperature from 150 to 300 K for $Bi_{0.88}Sb_{0.12}$ (*Black*) and $Bi_{0.88}Sb_{0.12}Ho_{0.01}$ (*Red*) (Color figure online)

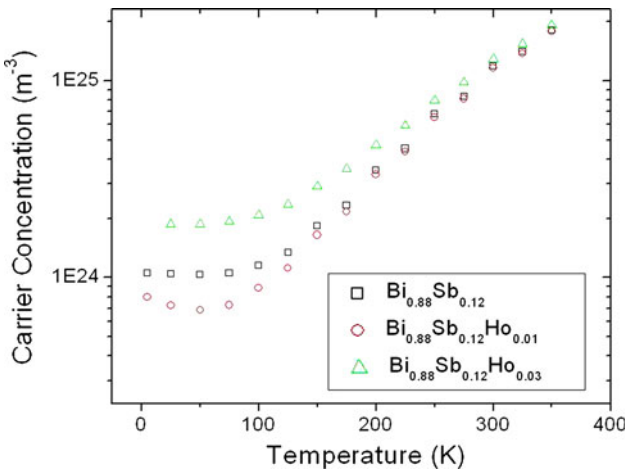


**Fig. 4** Temperature dependence of the carrier concentration of $Bi_{0.88}Sb_{0.12}$ (*Black*), $Bi_{0.88}Sb_{0.12}Ho_{0.01}$ (*Red*), $Bi_{0.88}Sb_{0.12}Ho_{0.03}$ (*Green*) (Color figure online)

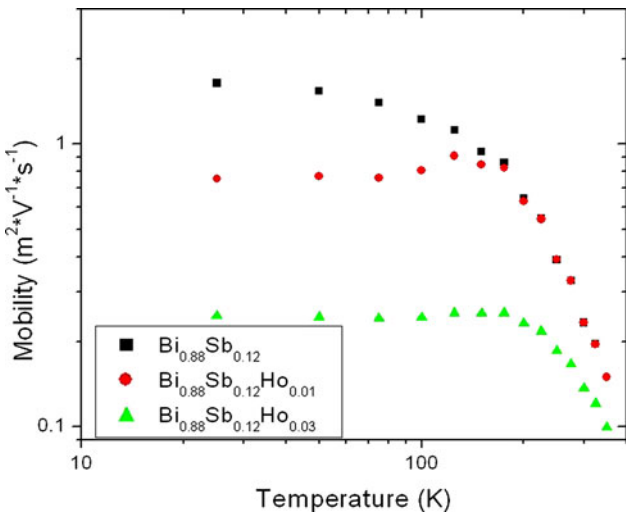


**Fig. 5** Temperature dependence of mobility for $Bi_{0.88}Sb_{0.12}$ (*Black*), $Bi_{0.88}Sb_{0.12}Ho_{0.01}$ (*Red*), $Bi_{0.88}Sb_{0.12}Ho_{0.03}$ (*Green*) (Color figure online)

The temperature dependence of the Seebeck coefficients are shown in Fig. 7. Values for thermopower are negative over the entire range, confirming the majority carriers are electrons. The maximum values for the 0 and 3 % Ho-doping are approximately 125 μV/K at 150 K, while the maximum for 1 % Ho is 145 μV/K at 100 K. The increase in the magnitude of the thermopower for 1 % Ho is most likely caused by a decrease in carrier concentration at low temperatures, even though the mobility is not increased in this range. For 3 % Ho, the carrier concentration is higher and the mobility is lower which should decrease the absolute value of $\alpha$. Since $\alpha$ is nearly unchanged, it is apparent that phonon drag has a direct impact on the value of the Seebeck coefficient which can be seen in the increase in $\rho$ due to phonon–electron interactions. The temperature at which there is a maximum for $\alpha$ in BiSb is dependent upon the concentration of Sb as well as $\rho$ [11]. The absolute values for the maxima presented in

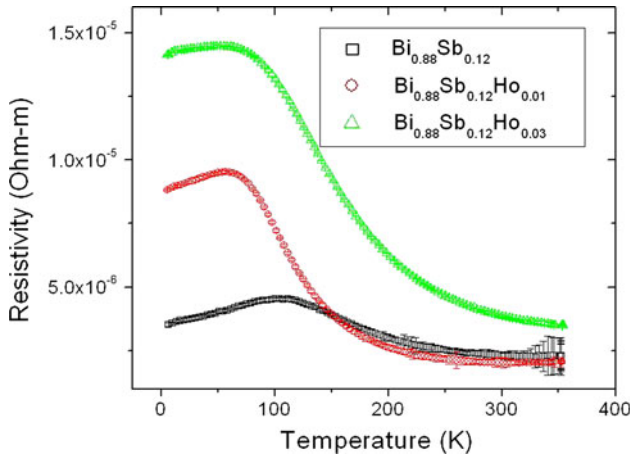


**Fig. 6** Temperature dependence of resistivity for $Bi_{0.88}Sb_{0.12}$ (*Black*), $Bi_{0.88}Sb_{0.12}Ho_{0.01}$ (*Red*), $Bi_{0.88}Sb_{0.12}Ho_{0.03}$ (*Green*) (Color figure online)

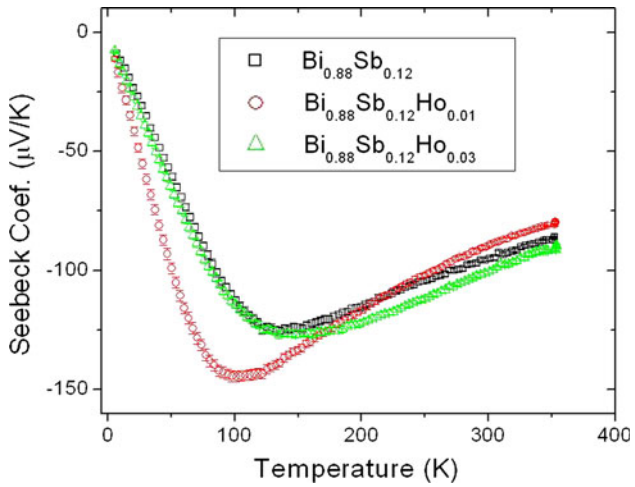


**Fig. 7** Temperature dependence of thermopower for $Bi_{0.88}Sb_{0.12}$ (*Black*), $Bi_{0.88}Sb_{0.12}Ho_{0.01}$ (*Red*), $Bi_{0.88}Sb_{0.12}Ho_{0.03}$ (*Green*) (Color figure online)

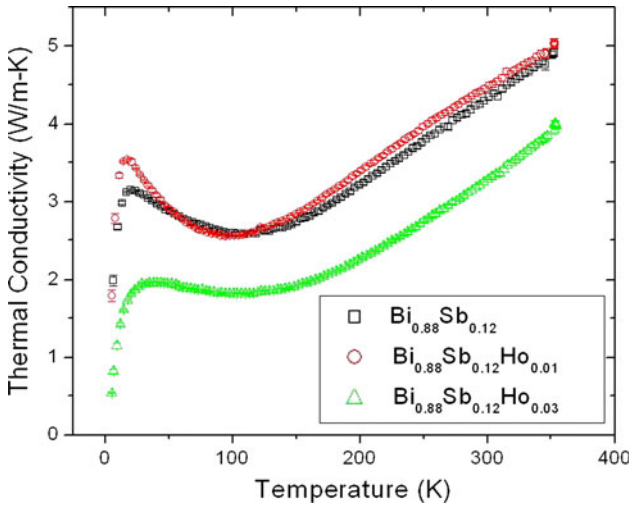


**Fig. 8** Temperature dependence of thermal conductivity for $Bi_{0.88}Sb_{0.12}$ (*Black*), $Bi_{0.88}Sb_{0.12}Ho_{0.01}$ (*Red*), $Bi_{0.88}Sb_{0.12}Ho_{0.03}$ (*Green*) (Color figure online)

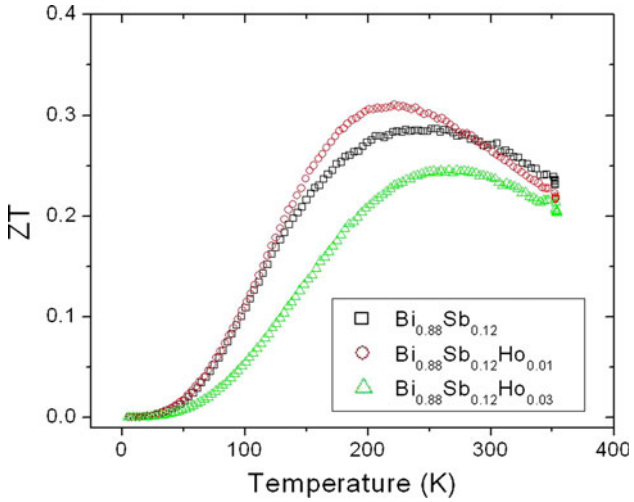


**Fig. 9** Temperature dependence of ZT for $Bi_{0.88}Sb_{0.12}$ (*Black*), $Bi_{0.88}Sb_{0.12}Ho_{0.01}$ (*Red*), $Bi_{0.88}Sb_{0.12}Ho_{0.03}$ (*Green*) (Color figure online)

Fig. 7 are consistent with the literature values for both polycrystal [16, 19, 35] and single crystal samples measured perpendicular to the trigonal axis [11], although the maxima occur at a slightly higher temperature.

The temperature dependence of the thermal conductivity is shown in Fig. 8 for all doping concentrations. We note that the thermal conductivity is drastically lowered, by more than four times, from that of single crystals [1, 11] and is lower from other reported polycrystals [23, 35]. Nanopolycrystalline samples prepared by cold-pressing rather than hot-pressing have a greater reduction in thermal conductivity, however $\rho$ is drastically increased [22]. This is a product of the ball milling and dc hot-pressing preparation methods, where the size of the particles is very small which increases phonon scattering as described by Goldsmid et al. [36]. This is the case for both the 0 and 1 % Ho samples. The thermal conductivity is further reduced in the 3 % Ho sample, where the lack of a peak at lower temperatures is evidence of structural disorder. The addition of 3 % Ho to the sample lowers the phonon mean free path by being a point defect scattering mechanism, which has also been seen in the literature [1, 4, 35–37]. Ho is perhaps a more effective scatterer since Ho (164 amu) has an atomic mass in between that of Bi (208 amu) and Sb (121 amu). The thermal conductivity in the 3 % sample is reduced due to additional Ho ions acting as scatterers, which has also been seen in other doped samples [35],

however the increase in resistivity leads to an overall decrease in ZT.

Figure 9 gives the value for the dimensionless figure of merit. There is an increase in the thermoelectric figure of merit due to 1 % Ho. The increase in ZT for the 1 % sample at 200 K is due to the enhanced Seebeck coefficient while maintaining a similar value for $\rho$ and $\kappa$ as that of $Bi_{0.88}Sb_{0.12}$ for temperatures greater than 150 K. In contrast, ZT decreases for 3 % Ho. Even though the thermal conductivity is decreased due to a shorter phonon mean free path, ZT is still lower due to additional point defect scatterers as well as phonon–electron interactions that affect the mobility of the charge carriers, increasing resistivity similar to results previously reported [17, 22]. The 1 % Ho sample presented here could be used with the p-type element of Hor et al. [35]; the benefits not only include improvement in the maximum value for ZT, by about 20 %, but also the temperature is the same at which both maxima occur, which is the ideal scenario of an optimized thermoelectric cooler or generator.

## Conclusion

The effects on the thermoelectric properties of $Bi_{0.88}Sb_{0.12}$ due to the addition of Ho impurities have been studied and an improvement to ZT is found by the addition of 1 % Ho. While improvements are found in thermoelectric properties in zero field, further changes may be found with the addition of magnetic field both parallel and perpendicular to the sample. Experiments on these samples, which will include the response of magnetic field on the unique magnetic properties of Ho, are underway.

**Acknowledgements** The authors gratefully acknowledge M. S. Dresselhaus, J. C. Lashley and P. S. Riseborough for their fruitful discussions and careful reading of the manuscript as well as G. McMahon for his assistance. This study is funded by the Air Force MURI program under contract FA9550-10-1-0533.

## References

1. Smith GE, Wolfe R (1962) J Appl Phys 33:841
2. Wolfe R, Smith GE (1962) Appl Phys Lett 1:5
3. Lenoir B, Demouge A, Perrin D, Scherrer H, Scherrer S, Cassart M, Michenaud JP (1995) J Phys Chem Solids 56:99
4. Yim WM, Amith A (1972) Solid-State Electron 15:1141
5. Ioffe AF (1957) Semiconductor thermoelements and thermoelectric cooling. Infosearch, London
6. Gopinathan KK, Goldsmid HJ, Matthews DN, Taylor KNR (1988) In: Proceedings of the 7th International Conference, Thermoelectric Energy Conversion 58
7. Dashevskii ZM, Sidorenko NA, Skipidarov SY, Tsvetkova NA, Mocolov AB (1991) In: Proceedings of the 10th International Conference, Thermoelectric Energy Conversion 142
8. Vedernikov MV, Kuznetsov VL, Ditman AV, Meleks BT, Burkov AT (1991) In: Proceedings of the 10th International Conference, Thermoelectric Energy Conversion 96
9. Fee MG (1993) Appl Phys Lett 62:1161
10. Jain AL (1959) Phys Rev 114:1518
11. Lenoir B, Cassart M, Michenaud JP, Scherrer H, Scherrer S (1996) J Phys Chem Solids 57:89
12. Ellet MR, Horst RB, Williams LR, Cuff KF (1966) J Phys Soc Jpn 21:666
13. Chao PW, Chu HT, Kao YH (1974) Phys Rev B 9:4030
14. Oelgart G, Schneider G, Kraak W, Herrmann R (1976) Phys Status Solidi (b) 74:K75
15. Kraak W, Oelgart G, Schneider G, Herrmann R (1978) Phys Status Solidi (b) 88:105
16. Kitagawa H, Noguchi H, Kiyabu T, Itoh M, Noda Y (2004) J Phys Chem Solids 65:1223
17. Devaux X, Brochin F, Martin-Lopez R, Scherrer H (2002) J Phys Chem Solids 63:119
18. Martin-Lopez R, Dauscher A, Scherrer H, Hejtmanek J, Kenzari H, Lenoir B (1999) Appl Phys A 68:597
19. Sharp JW, Volckmann EH, Goldsmid HJ (2001) Phys Status Solidi (a) 2:257
20. Belaya AD, Zayakin SA, Zemskov VS (1994) J Adv Mater 2:158
21. Ivanov GA, Kulikov VA, Naletov VL, Panarin AF, Regel AR (1973) Sov Phys Semicond 7:1134
22. Liu HJ, Li LF (2007) J Alloys Compd 433:279
23. Dutta S, Shubha V, Ramesh TG, D'Sa F (2009) J Alloys Compd 467:305
24. Schneider R, Chatterji T, Hoffmann JU, Hohlwein D (2000) Physica B 610:276
25. Snigirev OV, Tishin AM, Volkozub AV (1991) J Magn Magn Mater 94:342
26. Gebhardt JR, Baer RA, Ali N (1997) J Alloys Compd 250:655
27. Rosen M, Kalir D, Klimker H (1974) J Phys Chem Solids 35:1333
28. Jensen J, Mackintosh AR (1992) J Magn Magn Mater 1481:104
29. Poudel B, Hao Q, Ma Y, Lan YC, Minnich A, Yu B, Yan X, Wang DZ, Muto A, Vashaee D, Chen XY, Liu JM, Dresselhaus MS, Chen G, Ren ZF (2008) Science 320:634
30. Ma Y, Hao Q, Poudel B, Lan YC, Yu B, Wang DZ, Chen G, Ren ZF (2008) Nano Lett 8:2580
31. Zhu GH, Lan YC, Wang DZ, Vashaee D, Lee H, Wang XW, Joshi G, Yang J, Guilbert H, Pillitteri A, Dresselhaus MS, Chen G, Ren ZF (2009) Phys Rev Lett 102:196803
32. Yan X, Poudel B, Ma Y, Lan Y, Joshi G, Liu WS, Wang H, Wang DZ, Chen G, Ren ZF (2010) Nano Lett 10:3373
33. Zhitinskaya MK, Nemov SA, Ravich YI (1998) Phys Solid State 40(7):109
34. Hattori T (1970) J Phys Soc Jpn 29(5):1224
35. Hor YS, Cava RJ (2009) J Alloys Compd 479:368
36. Goldsmid HJ, Lyon HB, Volckmann EH (1995) In: Proceedings of XIV International Conference on Thermoelectrics. ZT Services Inc, Aubun, AI
37. Noguchi H, Kitagawa H, Kiyabu T, Hasezaki K, Noda Y (2007) J Phys Chem Solids 61:91

# Cerium Doped Bismuth Antimony

Kevin C. Lukas[1], Huaizhou Zhao[1], Ryan L. Stillwell[2], Zhifeng Ren[1], Cyril P. Opeil[1]

[1]Department of Physics, Boston College, Chestnut Hill, Massachusetts 02467, U.S.A.

[2]National High Magnetic Field Laboratory, Florida State University, Tallahassee, Florida 32306-4005, USA

## ABSTRACT

Bismuth-Antimony alloys have been shown to have high ZT values below room temperature, especially for single crystals. For polycrystalline samples, impurity doping and magnetic field have proven to be powerful tools in the search for understanding and improving thermoelectric performance. Nanopolycrystalline $Bi_{0.88}Sb_{0.12}$ doped with 0.05, 0.5 and 3 % Ce were prepared by ball milling and dc hot pressing techniques. Electrical resistivity, Seebeck coefficient, thermal conductivity, carrier concentration, mobility, and magnetization are measured in a temperature range of 5-350 K and in magnetic fields up to 9 Tesla. The effects of Ce doping on the thermoelectric properties of $Bi_{0.88}Sb_{0.12}$ in zero magnetic field are discussed.

## INTRODUCTION

Bismuth-Antimony alloys are known to have some of the best thermoelectric properties below room temperature, specifically single crystals [1-3]. The problem with single crystals is that they are difficult to fabricate and they are mechanically weak making them impractical for commercial use. Polycrystalline BiSb alloys have been fabricated via several different methods [4-7], however all polycrystalline samples have thermoelectric properties that are inferior to single crystal samples. In order to enhance the thermoelectric properties of polycrystalline BiSb, dopants can be added [8-10]. In our previous report, we demonstrated an increase in ZT for $Bi_{0.88}Sb_{0.12}$ doped with Holmium [11]. In this report we present the thermoelectric transport properties for $Bi_{0.88}Sb_{0.12}$ doped with 0.05, 0.5, and 3 % Cerium.

## EXPERIMENTAL DETAILS

The proper stoichiometric amounts of elemental Bismuth (Alfa Aesar 99.999%), Antimony (Alfa Aesar 99.999%) and Cerium (Alfa Aesar 99.99%) were melted in quartz tubes at 450 $^{o}$C for 3 hours then quenched in water. The ingot was then ball milled for five hours in a high energy ball mill from which the powder was taken and hot pressed at 200 $^{o}$C in a manner previously described [11]. XRD measurements were performed on as pressed samples using a Bruker AXS XRD to show the materials were single phase. The magnetic susceptibility ($\chi$) was measured using a Physical Properties Measurement System (PPMS) from Quantum Design. Samples were cut into 1 x 2 x 12 mm$^3$ dimensions to measure the Hall coefficient ($R_H$) and 2 x 2 x 4 mm$^3$ dimensions for measurements of electrical resistivity ($\rho$), thermal conductivity ($\kappa$), and the Seebeck Coefficient (S). All transport measurements were made perpendicular to the face of the disk, or pressing direction, using a PPMS.

## RESULTS AND DISCUSSION

Figure 1a shows XRD images of the 0, 0.05, 0.5, and 3 % Ce doped $Bi_{0.88}Sb_{0.12}$ samples. It can be seen that within the resolution of the machine, the samples are all single phase with no secondary impurities. Grain sizes of all samples are on average the same as seen in SEM images not shown here. Figure 1b shows the magnetic susceptibility plotted versus temperature. $Bi_{0.88}Sb_{0.12}$ is shifted up for clarity, though $\chi$ is positive showing that the material is paramagnetic over the entire temperature range. Single crystal Bismuth-Antimony alloys have been shown to be diamagnetic [12,13], however the samples in the present study have a larger carrier concentration than that of single crystals [14] due to the increased number of defects; it is known that excess free carriers can contribute to paramagnetism. From Figure 1b it can also be seen that the Ce did in fact assimilate into the sample based on the change in slope around 20 K; Ce has a ferromagnetic transition at 12 K [15]. As the concentration of Ce increases, the change in slope increases showing that the material is more magnetic, just as one would expect with an increasing magnetic dopant concentration. Because $1/\chi$ vs. T is not linear, a Curie-Weiss fit to extract any further information is not possible.

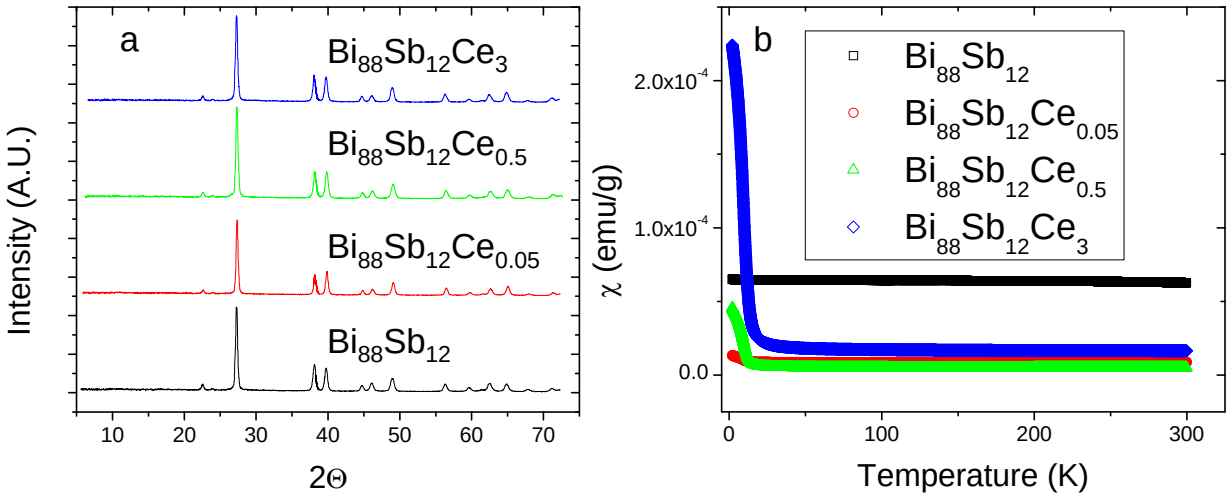


**Figure 1.** a) XRD images of all samples. b) Magnetic susceptibility plotted versus temperature for $Bi_{0.88}Sb_{0.12}$(black square), $Bi_{0.88}Sb_{0.12}Ce_{0.05}$(red circle), $Bi_{0.88}Sb_{0.12}Ce_{0.5}$ (green triangle)and $Bi_{0.88}Sb_{0.12}Ce_3$ (blue diamond).

The Hall coefficient is negative over the entire temperature range showing the majority carriers are electrons. Figure 2 shows the carrier mobility ($\mu_H$) plotted against temperature determined from

$$\mu_H = R_H/\rho \quad (1)$$

while Figure 3 shows the carrier concentration (n) given by

$$n = 1/(qR_H) \quad (2)$$

where q is the electronic charge. From Figure 2 it can be seen that the addition of 0.05 % Ce leads to a slight increase in the carrier mobility, while a further increase in the Ce concentration decreases the mobility. Oppositely in Figure 3b it is seen that the carrier concentration decreases with the addition of 0.05 % Ce, and then the carrier concentration increases with the increasing percentage of Ce. The dip in carrier concentration at the lowest Ce percentage is identical to what is seen in the Ho doped $Bi_{0.88}Sb_{0.12}$ [11].

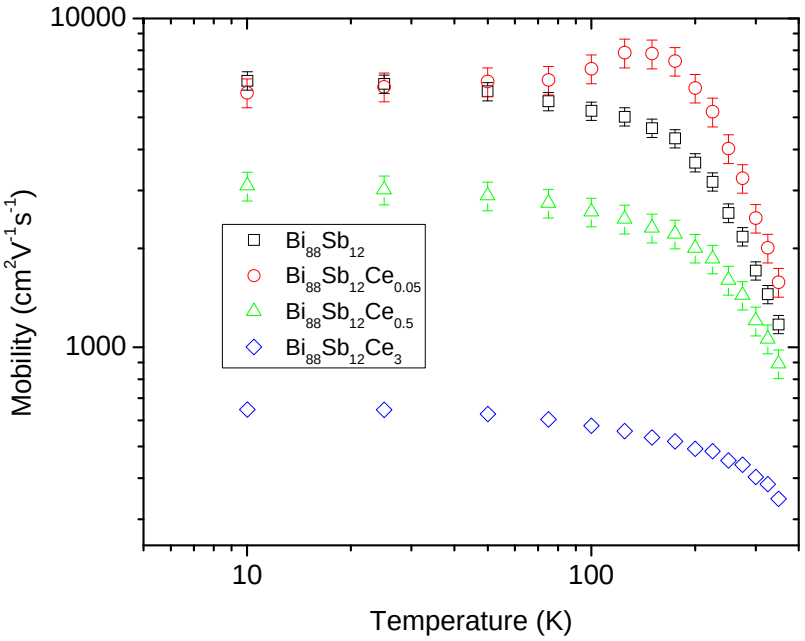


**Figure 2.** Carrier mobility plotted versus temperature for $Bi_{0.88}Sb_{0.12}$(black square), $Bi_{0.88}Sb_{0.12}Ce_{0.05}$(red circle), $Bi_{0.88}Sb_{0.12}Ce_{0.5}$ (green triangle)and $Bi_{0.88}Sb_{0.12}Ce_3$ (blue diamond).

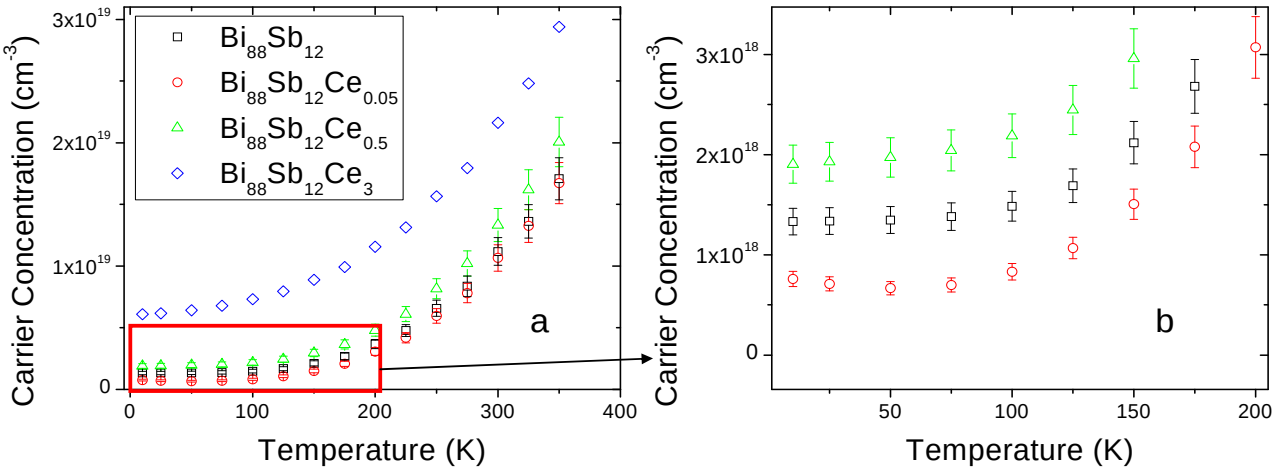

**Figure 3.** Carrier concentration plotted versus temperature for $Bi_{0.88}Sb_{0.12}$ (black square), $Bi_{0.88}Sb_{0.12}Ce_{0.05}$(red circle), $Bi_{0.88}Sb_{0.12}Ce_{0.5}$ (green triangle)and $Bi_{0.88}Sb_{0.12}Ce_3$ (blue diamond).

Figure 4 shows the electrical resistivity, thermal conductivity, Seebeck Coefficient, and ZT plotted with temperature where

$$ZT = [S^2/(\rho\kappa)]T \quad (3)$$

In Figure 4a the electrical resistivity exhibits typical semiconducting behavior as the stoichiometric composition $Bi_{0.88}Sb_{0.12}$ is known to be a semiconductor [3]. The inclusion of 0.05 % Ce causes a greater increase in ρ below 150 K, while above 150 K there is a decrease in the resistivity when compared to the parent sample. Electrical resistivity increases over the whole temperature range with the addition of 0.5 % Ce, and increases further when the Ce concentration is 3 %. Figure 4b shows the thermal conductivity where the upturn in κ at around 150 K is due to the bipolar contribution. The two samples containing the highest percentage of Ce suppress κ over the entire temperature range including the low temperature maxima, as is typical when the introduced dopant to the parent alloy acts as a scattering center. However at the lowest concentration of 0.05 % Ce, the low temperature peak is enhanced along with κ being slightly larger over the whole temperature range. The enhanced peak in κ at low temperatures along with the increased mobility could be a sign structural order in the 0.05 % Ce doped sample, however further structural analysis is required. The Seebeck Coefficient, Figure 4c, is negative over the entire temperature range confirming the majority carriers are electrons, and the maxima corresponds to the onset of the bipolar contribution as seen in the thermal conductivity. Adding 0.05 % Ce increases S at lower temperatures. The further addition of Ce decreases the values of S. As is typical, changes in S correspond to the changes in carrier concentration seen in Figure 3, as n increases S decreases. The dimensionless figure of merit, ZT, is plotted with temperature in Figure 4d. ZT is slightly enhanced with the addition of 0.05% Ce due to an increase in S as well as a decrease in ρ around 150 K. $Bi_{0.88}Sb_{0.12}$ samples doped with 0.5 and 3 % Ce show a decrease in ZT due to both an increase in ρ as well as a suppression of S caused by a strongly decreased mobility along with an increased carrier concentration. It is interesting to note that the Ce doped samples exhibit the same variations in their transport properties as the Ho doped $Bi_{0.88}Sb_{0.12}$ where the lowest Ho concentration showed an enhanced ZT due to an increased Seebeck Coefficient along with a slightly enhanced value for ρ [11]. Again these changes in the transport properties were due to a slightly enhanced mobility as well as a decrease in carrier concentration.

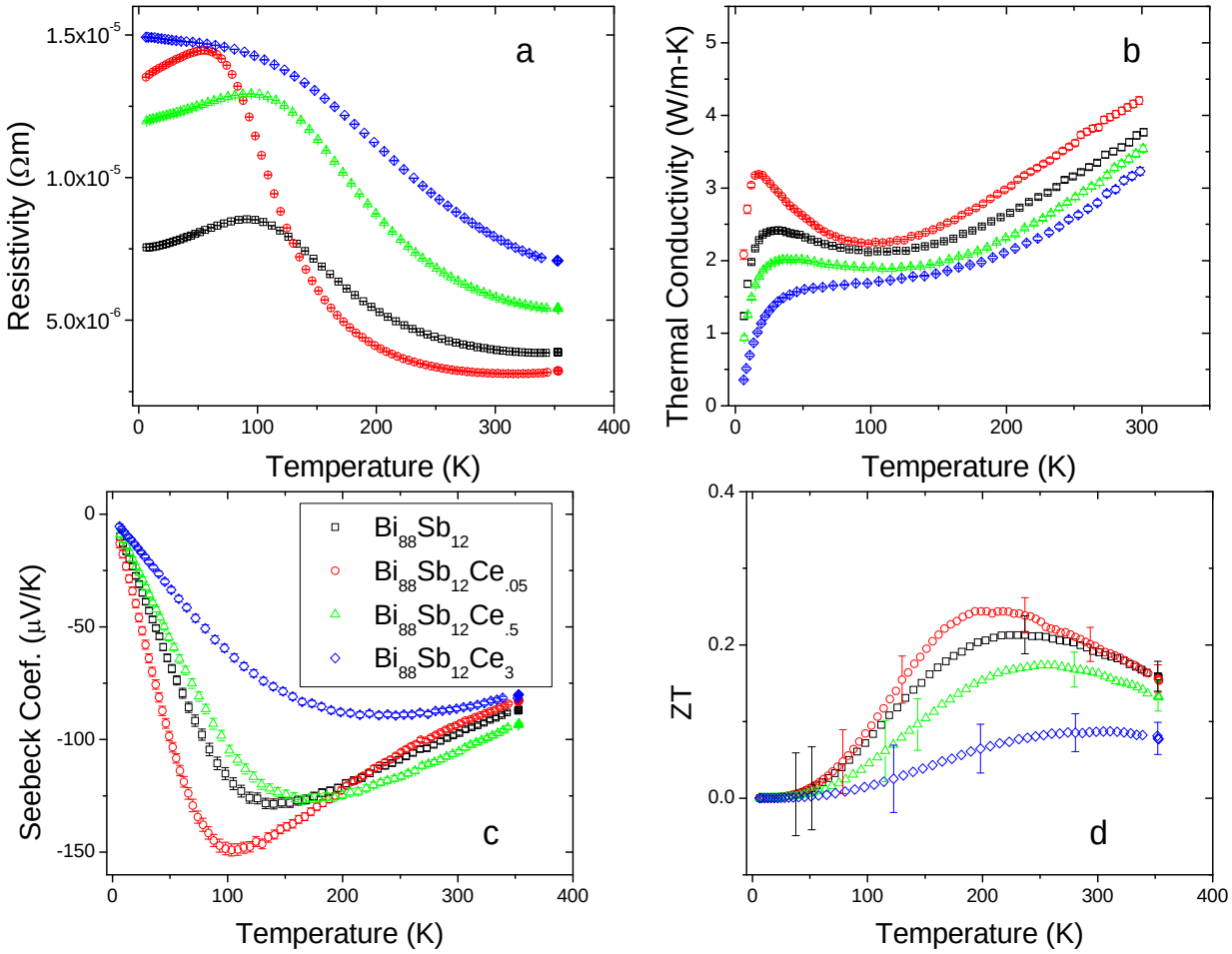


**Figure 4.** a) Electrical resistivity, b) thermal conductivity, c) Seebeck Coefficient, and d) ZT plotted versus temperature for $Bi_{0.88}Sb_{0.12}$(black square), $Bi_{0.88}Sb_{0.12}Ce_{0.05}$(red circle), $Bi_{0.88}Sb_{0.12}Ce_{0.5}$ (green triangle)and $Bi_{0.88}Sb_{0.12}Ce_3$ (blue diamond).

## CONCLUSION

$Bi_{0.88}Sb_{0.12}$ doped with 0, 0.05, 0.5, and 3 % Ce were prepared and their transport properties were measured. It is interesting to note that both Ce and Ho doped into $Bi_{0.88}Sb_{0.12}$ alter the transport properties in the same way. Further investigation is underway to understand why both Ce and Ho have similar affects on the transport properties of $Bi_{0.88}Sb_{0.12}$.

## ACKNOWLEDGMENTS

We (KL, ZR, CO) gratefully acknowledge funding for this work through the “Solid State Solar-Thermal energy conversion Center (S3TEC)”, an Energy Frontier research Center founded by the U.S. Department of Energy, Office of Basic Energy Science under award number: DE-SC0001299/DE-FG02-09ER46577. The authors (HZ, ZR, CO) also acknowledge funding by the Department of Defense, United States Air Force Office of Scientific Research, Multi-University Research Initiative (MURI) under Contract # FA9950-10-1-0533.

## REFERENCES


1. G.E. Smith, R. Wolfe, J. Appl. Phys. 33, 841, (1962).
2. R. Wolfe, G.E. Smith, Bell Tel. Laboratories 5, (1962).
3. B. Lenoir, A. Demouge, D. Perrin, H. Scherrer, S. Scherrer, M. Cassart, J.P. Michenaud, J. Phys. Chem. Solids 56, 99, (1995).
4. H. Kitagawa, H. Noguchi, T. Kiyabu, M. Itoh, Y.J. Noda, Phys. and Chem. of Solids 65, 1223, (2004).
5. X. Devaux, F. Brochin, R. Martin-Lopez, H. Scherrer, J. Phys. Chem. Solids 63, 119, (2002).
6. R. Martin-Lopez, A. Dauscher, H. Scherrer, J. Hejtmanek, H. Kenzari, B. Lenoir, Appl. Phys. A 68, 597, (1999).
7. J.W. Sharp, E.H. Volckmann, H.J. Goldsmid, Phys. Stat. Sol. (a) 185, 2, 257, (2001).
8. A.D. Belaya, S.A. Zayakin, V.S. Zemskov, J. Adv. Mater. 2, 158, (1994).
9. G.A. Ivanov, V.A. Kulikov, V.L. Naletov, A.F. Panarin, A.R. Regel, Sov. Phys. Semicond. 7, 1134, (1973).
10. Y.S. Hor, R.J. Cava, J. Alloys and Comp. 479, 368, (2009).
11. K.C. Lukas, H. Zhao, K. Modic, Z.F. Ren, C.P. Opeil, J. Materials Sci. DOI:10.1007/s10853-012-6463-6, (2012)
12. M. Sengupta, R. Bhattacharya, J. Phys Chem. Solids 46, 1, 9-16, (1985).
13. G.P. Mikitik, Y.V. Sharlai, Low Temp. Physics 26, 1, 39-46, (2000).
14. T.J. Hattori, J. Phys. Soc. Japan 29, 5, 1224, (1970).
15. T. Sakai, G. Adachi, J. Shiokawa, Mater. Research Bulletin 15, 7, 1001-1010, (1980).

# Role of phonon dispersion in studying phonon mean free paths in skutterudites

Mona Zebarjadi,[1] Jian Yang,[2] Kevin Lukas,[2] Boris Kozinsky,[3] Bo Yu,[2]
Mildred S. Dresselhaus,[4] Cyril Opeil,[2] Zhifeng Ren,[2] and Gang Chen[1]
[1]*Department of Mechanical Engineering, Massachusetts Institute of Technology, Cambridge, Massachusetts 02139, USA*
[2]*Department of Physics, Boston College, Chestnut Hill, Massachusetts 02467, USA*
[3]*Research and Technology Center, Robert Bosch LLC, Cambridge, Massachusett 02142, USA*
[4]*Department of Physics and Department of Electrical Engineering and Computer Science, Massachusetts Institute of Technology, Cambridge, Massachusetts 02139, USA*

(Received 24 April 2012; accepted 20 July 2012; published online 23 August 2012)

Experimental thermal conductivity of bulk materials are often modeled using Debye approximation together with functional forms of relaxation time with fitting parameters. While such models can fit the temperature dependence of thermal conductivity of bulk materials, the Debye approximation leads to large error in the actual phonon mean free path, and consequently, the predictions of the thermal conductivity of the nanostructured materials using the same relaxation time are not correct even after considering additional size effect on the mean free path. We investigate phonon mean free path distribution inside fully unfilled (Co4Sb12) and fully filled (LaFe4Sb12) bulk skutterudites by fitting their thermal conductivity to analytical models which employ different phonon dispersions. We show that theoretical thermal conductivity predictions of the nanostructured samples are in agreement with the experimental data obtained for samples of different grain sizes only when the full phonon dispersion is considered. © *2012 American Institute of Physics*. [http://dx.doi.org/10.1063/1.4747911]

## INTRODUCTION

Thermoelectric power generators can directly convert heat into electricity. The efficiency of a thermoelectric device is an increasing function of the material's figure-of-merit, $ZT = \sigma S^2 T/\kappa$, where $\sigma$ is the electrical conductivity, $S$ is the Seebeck coefficient; $T$ is the absolute temperature, and $\kappa$ is the thermal conductivity. A successful strategy in enhancing $ZT$ is through reducing the phonon thermal conductivity by alloying,[1] nanostructuring,[2] or introducing rattling atoms into materials with cage-like structures, such as skutterudites.[3] In all these cases, it has been shown that phonons could be scattered more significantly than electrons, leading to a higher $\sigma/\kappa$ ratio. While alloying affects low wavelength phonons of less than 1 nm, nanostructuring involves larger scales and can scatter mid to long wavelength phonons. Rattling atoms only scatter phonons which have frequencies close to those of the rattler's vibrations. To predict how nanostrcuturing affects the thermal conductivity, the knowledge of bulk phonon wavelengths and their mean free paths is required. Grain boundary interfaces can scatter phonons with mean free paths larger than the grain interface spacing, but they will not affect phonons with mean free paths much shorter than the interfacial separation distances. To find the phonon mean free path spectrum in a specific bulk material, it is very common to fit the thermal conductivity versus temperature by adjusting several parameters and then to back calculate the phonon mean free path spectrum. The thermal conductivity can be calculated knowing the dispersion relations and relaxation times for the relevant scattering processes. Phonon dispersion relations can be obtained accurately from first-principles calculations without involving much computation. The relaxation times are difficult to extract from first-principles calculations.[4] Recently there have been several valuable attempts to extract phonon-phonon scattering from first-principles,[5–9] but such computations are still time consuming and difficult to perform for each new material. Moreover, in practice, phonon-phonon scattering is not the only important scattering mechanism for nanocomposite thermoelectric materials. Often, there is a significant contribution to the total phonon scattering cross section from electrons, point defects, impurities, dangling bonds, random inhomogeneities, and boundary scatterings. For these scattering processes, only phenomenological models are applicable so far. Another difficulty is that there is a large uncertainty regarding the experimental density of the defects and what the grain boundaries look like. Therefore, fitting seems to be a reasonable approach for these cases.

The lattice thermal conductivity of bulk single crystals versus temperature ($\kappa_L$(T)) usually has a standard behavior. It starts from zero at zero temperature, increases to a peak value versus temperature, and then drops at high temperatures. This trend can be easily fitted using simple models and the simplest band dispersions such as the Debye dispersion. Three fitting parameters are often enough to get a perfect fit. Low temperature behavior can be fitted by adjusting the size scale of the sample boundaries, the middle range by the impurity density, and the high temperature range through adjusting the phonon-phonon coupling. However, depending on the dispersion used, different fitting parameters and different predicted phonon mean free path spectra could be

 © 2012 American Institute of Physics

Downloaded 24 Sep 2012 to 136.167.55.68. Redistribution subject to AIP license or copyright; see http://jap.aip.org/about/rights_and_permissions

obtained which then impose uncertainty on the design of the nanostructured materials.

Chen[10] compared several models to predict the lattice thermal conductivity of GaAs/AlAs superlattices. He proposed three models: the gray medium (constant mean free path model) without dispersion which is the simplest but least accurate model; the gray medium with dispersion (sine dispersion), and the non-gray medium with dispersion which is the most accurate one and its predictions are in agreement with the experimental data. They showed that both sine dispersion and model of Holland can fit the thermal conductivity of bulk GaAs with different sets of fitting parameters.[11]

Chung *et al.*[12] discussed the importance of the phonon dispersion in fitting the thermal conductivity data of germanium using the Holland model.[13] They observed a non-physical discontinuity in the transverse phonon relaxation times. However, they did not extend their analysis to find the differences in the phonon mean free paths. Baillis and Randrianalisoa[14] studied the effect of phonon dispersion to predict the in-plane and the out-of-plane thermal conductivity of silicon thin films and nanowires. They used the Holland dispersion and the Brillouin zone boundary condition dispersion models to fit the experimental data of bulk silicon and to predict the thermal conductivity of silicon nanostructures. They concluded that there is a significant discrepancy between the predictions of the two models, and that the Holland model overestimates the thermal conductivity of the nanostructures. A similar conclusion was also reached by Mingo[15] when comparing full phonon dispersion results with those of the Callaway model.[16]

In this paper, we compare the Debye dispersion results with those of the full phonon dispersion obtained from first-principles calculations and apply them specifically to the case of skutterudites. First, we show that there is a clear difference in the calculated phonon mean free path spectrum using the two different dispersion relations. Second, through a systematic experimental study, we quantify the effect of grain size on the lattice thermal conductivities. The experimental data will be compared to the theoretical predictions. Although both dispersion relations can lead to a good fit to the thermal conductivity of large grained bulk skutterudites, we show that it is only when considering the full dispersion (FD) that correct results are obtained in the predictions of the thermal conductivity of nanostructured unfilled skutterudites ($Co_4Sb_{12}$) and fully filled skutterudites ($LaFe_4Sb_{12}$).

The paper is organized as follows. First, we describe the experimental procedure of making and characterizing samples with different grain sizes. Then, we describe the modeling and apply it to pure skutterudites as well as to fully filled skutterudites. We fit the thermal conductivity of bulk $Co_4Sb_{12}$ and $LaFe_4Sb_{12}$ versus temperature using two different dispersions: a full dispersion obtained from first principles and a Debye dispersion. The phonon mean free path spectrum is then extracted from each model. Based on the obtained phonon mean free path spectrum, we predict the lattice thermal conductivity of the nanocomposites of different grain sizes and finally we compare the predictions with those of the experiments.

## EXPERIMENT

The polycrystalline $Co_4Sb_{12}$ and $LaFe_4Sb_{12}$ samples were made by following the method from Ref. 17. Polycrystalline samples were synthesized by melting stoichiometric amounts of high purity constituents in sealed carbon coated quartz tubes. The tubes were then loaded into a box furnace and heated to 600 °C at 1 °C/min and then to 1080 °C at 2 °C/min. After soaking at 1080 °C for 20 h, the quartz tubes containing the homogeneous molten liquid were then quenched in a water bath, followed by an annealing of 30 h at 700 °C. The as-prepared solids were then taken out from the tubes and cleaned with a wire brush before an additional ball milling process in high-energy ball mills with stainless grinding vial sets. The as-milled powders were finally consolidated into bulk pellets in a graphite die by a direct current-hot press method. Bar and disc-shaped samples were cut from those pellets for the characterization of the thermoelectric transport properties (bar shape for ZEM and PPMS setups and disk shape for the laser flash setup). The grain sizes were controlled by means of changing the ball milling time (from a few minutes to more than 10 h) and the pressing temperature (800–1000 K). We used a commercial four-probe system (ZEM-3, ULVAC-RIKO) to measure the electrical conductivity and a laser flash system (LFA 457, Netzsch), for thermal conductivity measurements, from 300 K to 700 K. A physical properties measurement system (PPMS) from Quantum Design was used for low temperature characterizations. The lattice thermal conductivity contribution was extracted using the Wiedemann–Franz law and a constant Lorenz number of $2.4 \times 10^{-8}$ W$\Omega$ K$^{-2}$. Here, we assume that the contribution from bipolar effects is small in the temperature region that we are studying.

## RESULTS AND DISCUSSION

### Pure skutterudites ($Co_4Sb_{12}$)

In what follows, we explain our methodology for extracting the thermal conductivity from the full dispersion and Debye models. First principles based phonon dispersion calculations of $Co_4Sb_{12}$ have been reported before in several published works.[18,19] Our dispersion (see Fig. 1) is in agreement with those of Feldman and Singh[18] and was reported elsewhere.[20] We obtain phonon frequencies ($\omega$) for each $q$ point in the first Brillouin zone and for each mode ($\lambda$). Having phonon dispersions, the group velocities ($\partial\omega_\lambda/\partial\vec{q}$) can be calculated for each mode and at each $q$ point in reciprocal space. The skutterudite crystal structure has a cubic symmetry, and therefore has isotropic thermal conductivities. The thermal conductivity for an isotropic structure can be written as

$$k = \frac{1}{3n_q\Omega}\sum_\lambda\sum_{q\in FBZ}\hbar\omega_\lambda(\vec{q})v_\lambda^2(\vec{q})\tau_\lambda(\vec{q})\frac{\partial n}{\partial T} \qquad (1)$$

where $\vec{q}$ is the wave vector, $\lambda$ is the mode index (branch index), $v_\lambda$ is the group velocity for the $\lambda$ mode, $n$ is the Bose-Einstein distribution function, $n_q$ is the number of q points sampling the first Brillouin zone, $\Omega$ denotes the primitive

Downloaded 24 Sep 2012 to 136.167.55.68. Redistribution subject to AIP license or copyright; see http://jap.aip.org/about/rights_and_permissions

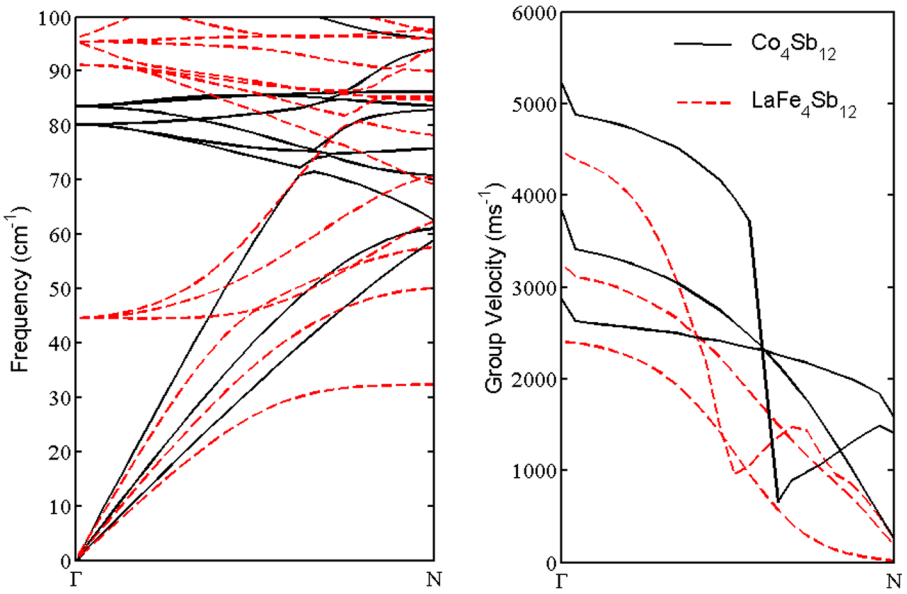


FIG. 1. Phonon dispersion (left) and group velocity amplitudes (right) along the ΓN [110] direction, calculated from first principles on a $50 \times 50 \times 50$ mesh. In the thermal conductivity calculations, we only included first 6 bands of each material. For clarity purposes, we only plotted the group velocities for the acoustic bands.

cell volume, and $\tau$ is the relaxation time. The dispersion and the group velocities along the ΓN [110] direction in the Brillouin Zone are shown in Fig. 1.

For the Debye formalism, we follow the modeling of Ref. 28. Equation (1) could be simplified by using the Debye dispersion. In this model, the group velocity is a constant number and is assumed to be independent of the modes and $\vec{q}$ points, namely the sound velocity of the material ($\omega = \upsilon_s q$). Converting the sum over the $\vec{q}$ points into an integral over the frequencies, we obtain the following expression for the thermal conductivity within the Debye model:

$$k = \int_0^{\omega_D} d\omega \; g(\omega)\hbar\omega\nu_s^2\tau(\omega)\frac{\partial n}{\partial T}, \tag{2}$$

$$\int_0^{\omega_D} d\omega \; g(\omega) = 3N, \tag{3}$$

where $\omega_D$ is the Debye frequency ($\hbar\omega_D = k_B\theta_D$), $\nu_s$ is the sound velocity, and $\theta_D$ is the Debye temperature. For $Co_4Sb_{12}$, $\theta_D = 307$ K and $\nu_s = 2.93 \times 10^5$ cm/s. These values are obtained from experimental measurements.[28] Following Ref. 28, three scattering mechanisms are included to calculate the frequency dependent relaxation times including phonon-phonon scattering ($\tau_{ph}$),[21] boundary scattering ($\tau_{BC}$), and isotope or mass fluctuation scattering ($\tau_{iso}$)[22]

$$\tau^{-1} = \tau_{BC}^{-1} + \tau_{iso}^{-1} + \tau_{ph}^{-1} = \frac{v}{l_g} + Ax^4T^4 + Bx^2T^3\exp\left(-\frac{\theta_D}{2T}\right);$$
$$x = \frac{\hbar\omega}{k_BT}, \tag{4}$$

where $l_g$ is the average grain size, $k_B$ is the Boltzmann constant, and A and B are fitting parameters representing the isotope scattering strength and the phonon-phonon coupling, respectively.

We use the same relaxation time model (Eq. (4)) and fit the experimental data of a sample with large grain size (representing a bulk sample) with the two dispersions described above. For the Debye model, we use the measured Debye temperature of 307 K, and for the full dispersion, we use the calculated Debye temperature based on first-principles calculations[18] (200 K). The average grain size ($l_g$) for our bulk sample is about 2 $\mu$m. Figure 2 shows the measured lattice thermal conductivity over a wide temperature range, measured for this sample, and our fits based on the two different dispersions. As indicated, both models can fit the experimental data. Note that above 600 K, we start to see a contribution from the bipolar effect as the thermal conductivity starts to increase with increasing the temperature. This effect is not considered in our model.

Table I summarizes the fitting parameter values used for each model. There are big differences in the obtained values

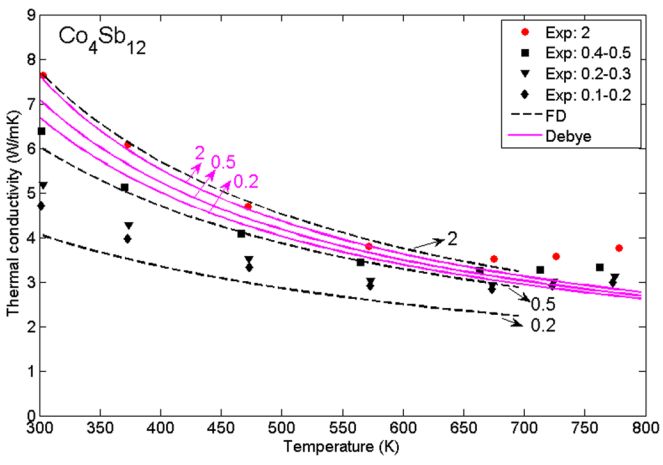


FIG. 2. Lattice thermal conductivity of $Co_4Sb_{12}$ versus temperature: Experimental data are labeled as Exp., the numbers in front of Exp. indicates the range of grain sizes in microns. Solid lines are calculated based on the Debye model and dashed lines are calculated based on the full dispersion model. In each case, the highest curve is fitted to the experimental data of the sample with an average grain size of 2 $\mu$m (red dots). The second curve is the model prediction for a sample with average grain size of 0.5 $\mu$m and the lowest curve is the model prediction for a sample with average grain size of 0.2 $\mu$m.

Downloaded 24 Sep 2012 to 136.167.55.68. Redistribution subject to AIP license or copyright; see http://jap.aip.org/about/rights_and_permissions

TABLE I. Fitting parameter values obtained from each model.

| Sample | Method | # of fitting parameters | A ($S^{-1}\,K^{-4}$) defect | B ($S^{-1}\,K^{-3}$) Umklapp | D ($10^{-15}$s) resonance | $\alpha$ ($10^{8}\,m^{-1}$) resonance | F ($10^{4}\,m^{-1}\,K^{-1}$) two-level tunneling | G ($K^{-2}$) two-level tunneling | A0 ($10^{32}\,S^{-3}\,K^{-2}$) resonance |
|---|---|---|---|---|---|---|---|---|---|
| $Co_4Sb_{12}$ | Debye | 2 | 116 | 99 500 | 0 | 0 | 0 | 0 | 0 |
| $Co_4Sb_{12}$ | Full dispersion | 2 | 380 | 18 426 | 0 | 0 | 0 | 0 | 0 |
| $LaFe_4Sb_{12}$ | Ref. 31 | 6 | 440 | 17 000 | 7 | 30 | 20 | 2 | 0 |
| $LaFe_4Sb_{12}$ | Debye + Einstein | 4 | 640 | 17 000 | 0 | 0 | 14 | 0 | 30.42 |
| $LaFe_4Sb_{12}$ | Full dispersion | 3 | 6000 | 60 000 | 0 | 0 | 15.5 | 0 | 0 |

for the different fitting parameters. Especially the impurity density is much weaker while the phonon-phonon coupling is much stronger in the Debye model compared to the full dispersion model. Therefore, we expect to find a large discrepancy in terms of the mean free path spectrum.

Figure 3 shows the cumulative thermal conductivity versus phonon mean free path at room temperature and shows the prediction of the two models for the mean free path spectrum and the contribution of each mean free path to the total thermal conductivity.[23] According to the Debye model, almost all of phonons contributing to the thermal conductivity have mean free paths below 200 nm and therefore are not affected much by grain sizes greater than 200 nm. This roughly means that a sample with an average grain size of 200 nm should have a similar thermal conductivity as that of the bulk sample at room temperature. The full dispersion, in contrast, predicts that there is a large contribution to the total thermal conductivity from phonons with mean free paths larger than 200 nm, and predicts a maximum reduction of about 60% when the grain size is reduced to about 200 nm.

Figure 2 shows experimental data of the measured thermal conductivity for samples of different grain sizes of $Co_4Sb_{12}$. These samples were prepared as we explained in the experimental section (See Fig. 4 for SEM images). Figure 2 indicates a reduction of 40% (from 7.6 to 4.7 $W\,m^{-1}\,K^{-1}$) in the thermal conductivity at room temperature, when the average grain size decreases from a couple of microns down to about 100 to 200 nm. As explained above, this observation is only consistent with the full dispersion model. To further illustrate this, we have also included in Fig. 2 the model predictions when the grain size is about 0.5 $\mu$m and 0.2 $\mu$m, respectively. Again the Debye model only shows a minor reduction, while the full dispersion model indicates a strong reduction in the thermal conductivity and is much closer to the experimental values. It should be noted that a direct comparison with the experiment is not possible since in the experiment there is a range of grain sizes and not a single size grains. We neither have a model to average over the different grain sizes nor do we have enough information on the exact experimental size distribution of the grains.

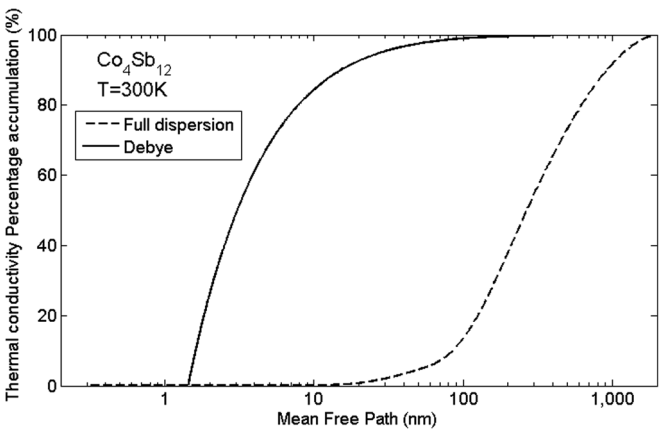


FIG. 3. Thermal conductivity percentage accumulation versus mean free path for $Co_4Sb_{12}$ at room temperature calculated using two different dispersions: Debye dispersion and FD calculated from first principles.

## Fully filled skutterudites ($LaFe_4Sb_{12}$)

In this section, we look at fully filled skutterudites. Unlike partially filled skutterudites which have randomness in their lattice structure, fully filled ones have periodic structures and therefore it is easier to investigate them theoretically.

Filled skutterudites are controversial in the literature. The rattling picture has been used widely for studying the thermal conductivity in these structures.[24,25] Based on this picture, skutterudites form relatively large cage-like structures. Filler atoms have weak bonds with the cage and therefore vibrate independently inside the host lattice. Large amplitude vibrations of the filler atoms in their cages have been confirmed experimentally,[26,27] but independent and incoherent vibrations have not. In terms of modeling, this means that in the presence of the filler atoms, one can approximate the phonon dispersion to be the same as that of the host matrix and only add flat optical bands to the dispersion to represent the filler atoms.[28] In a simplified model, known as the Debye + Einstein model, a Debye dispersion is taken for the phonon dispersion relation. Each optical band induced by the filler atoms is modeled only with a single frequency called the Einstein frequency. The phonons with frequencies close to the Einstein frequencies scatter largely from the filler atom vibrations (resonance scattering).[29] This phenomenological model has been quite successfully applied to different filled skutterudites where the experimental thermal conductivity data was fitted.[24,28,30]

We follow the same theoretical framework as we developed for pure skutterudites. The purpose is to look at the validity of the Debye + Einstein model for fully filled skutterudites. $LaFe_4Sb_{12}$ has been chosen because there are available experimental data and already developed phenomenological models for this material in the literature.[31] We follow the studying of Ref. 31, in which a fully filled $LaFe_4Sb_{12}$ bulk sample with large grain sizes (15 $\mu$m on the

Downloaded 24 Sep 2012 to 136.167.55.68. Redistribution subject to AIP license or copyright; see http://jap.aip.org/about/rights_and_permissions

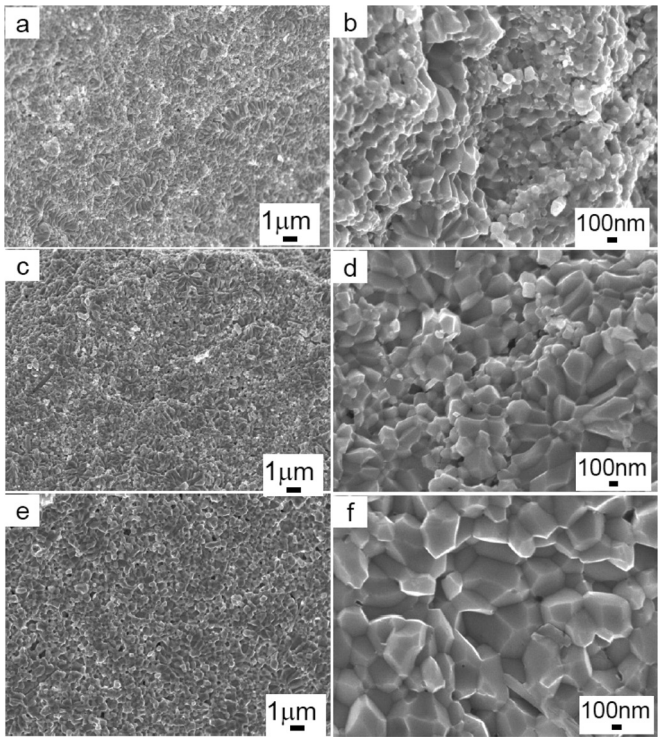


FIG. 4. Low- ((a), (c), and (e)) and high- ((b), (d), and (f)) magnification SEM images of the $Co_4Sb_{12}$ samples with different grain sizes: 100–200 nm ((a) and (b)), 200–300 nm ((c) and (d)), 400–500 nm ((e) and (f)).

average) was made and characterized at low temperatures. These samples were analyzed and their measured thermal conductivity data were fitted by using a Debye + Einstein model.[31] Here we first explain the model developed in Ref. 31 and reproduce their results. Then like before, we use first-principles calculations to obtain the full phonon dispersion and fit for the relaxation times. We compare the results of the phonon mean free path distribution with the two different approaches. Finally, we compare the predictions of the two models with the experimental data for samples of different grain sizes.

In Ref. 31, to explain the experimental data for the fully filled $LaFe_4Sb_{12}$, a Debye based model has been developed. The model is similar to what we explained in the previous section for pure skutterudites. However, two scattering rates are introduced in addition to those introduced in Eq. (4), two-level tunneling ($\tau_{TS}$) which is not the focus here and the resonance scattering ($\tau_{RS}$). Resonance scattering is introduced to take care of the Einstein frequencies introduced in the phonon dispersion as a result of introduced filler atoms

$$\tau^{-1} = \tau_{BC}^{-1} + \tau_{iso}^{-1} + \tau_{ph}^{-1} + \tau_{TS}^{-1} + \tau_{RS}^{-1}, \tag{5}$$

$$\tau_{TS}^{-1} = v\left[FTx\tanh\left(\frac{x}{2}\right) + \frac{1}{2}F\left(\frac{1}{Tx} + \frac{1}{GT^3}\right)^{-1}\right], \tag{6}$$

$$\tau_{RS}^{-1} = Df(\omega,T)g(\omega), \tag{7}$$

$$f(\omega,T) = \frac{(\omega_s-\omega)^2 e^{\frac{\hbar(\omega_s-\omega)}{k_BT}}\left(e^{\frac{\hbar\omega}{k_BT}}-1\right)}{\left(e^{\frac{\hbar\omega_s}{k_BT}}-1\right)\left(e^{\frac{\hbar(\omega_s-\omega)}{k_BT}}-1\right)},$$

$$g(\omega) = \left(1+4\frac{\alpha v}{\omega_s}\right)\ln\left[\frac{\omega}{\alpha v}\left(1-\frac{\omega}{\omega_s}\right)+1\right] - 4\frac{\omega}{\omega_s}\left(1-\frac{\omega}{\omega_s}\right),$$

$\omega_s$ is the Einstein frequency which can be related to the Einstein temperature $\theta_s$. For $LaFe_4Sb_{12}$, $\theta_D = 321$ K, $\theta_s = 88$ K, and $\nu_s = 3.078\times10^5$ cm/s which were measured experimentally.[31] The six parameters used to fit the data are A for defects, $B$ for phonon-phonon coupling (see Eq. (4)), $\alpha$ and $D$ for resonance, and $F$ and $G$ for two-level tunneling. The values of these parameters are reported in Table I after Ref. 31. Reproduced theoretical data and experimental data of Ref. 31 are plotted in Figure 6. We also tried a more simplified model for resonance scattering which is usually used in the literature,[28] and has only one fitting parameter ($A_0$) instead of two in the previous model ($\alpha$ and $D$)

$$\tau_{RS}^{-1} = \frac{A_0T^2\omega^2}{\left(\omega^2-\omega_s^2\right)^2}. \tag{8}$$

Also as an attempt to reduce the number of fitting parameters, we realized that the results are not sensitive to the $G$ parameter. Therefore, for our second fitting, we took the $G$ parameter out. In the figure legends and tables, we call this model Debye + Einstein model. But one should note that the Ref. 31 formalism is also a Debye + Einstein model and only uses a different expression for the resonance scattering. The results of our second fitting are reported in Table I and Fig. 5. Again we can fit the experimental data easily with this second Debye + Einstein model. Finally, we use the full dispersion model calculated from first principles and fit the relaxation times to obtain a third fit to the experimental data. This time, we do not include any resonance scattering term as it is unnecessary when the full band dispersion including

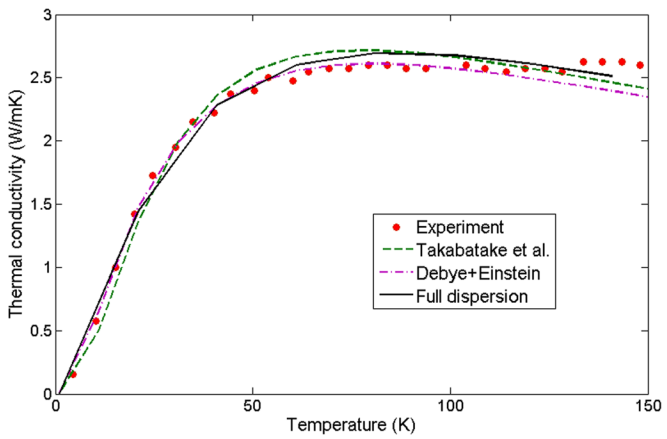


FIG. 5. Lattice thermal conductivity of $LaFe_4Sb_{12}$ plotted versus temperature. Experimental data are taken from Takabatake *et al.*[31] Three models based on relaxation times approximation are used to fit the experimental data. The first two models are Debye + Einstein models which are using Debye dispersion and adding a resonance scattering term for Einstein frequencies. These two models are using different expressions for resonance scattering (Eq. (7) is used by Takabatake *et al.* and Eq. (8) is used for the plot labeled as Debye + Einstein). The third model is based on full dispersion. All fitting parameters for this plot are listed in Table I.

Downloaded 24 Sep 2012 to 136.167.55.68. Redistribution subject to AIP license or copyright; see http://jap.aip.org/about/rights_and_permissions

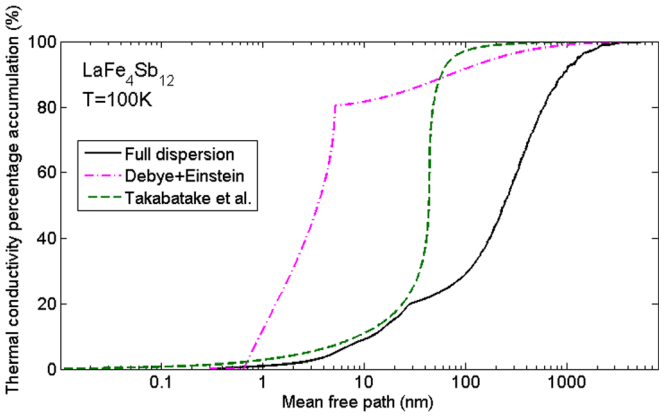


FIG. 6. Thermal conductivity percentage accumulation versus mean free path plotted at T = 100 K for the three different models described in the text as well as in the caption of Fig. 5.

optical phonons are explicitly taken into account. The effect of filler atoms is to introduce extra optical bands and also to reduce the group velocity of the acoustic phonons.[32] According to Table I, phonon-phonon coupling is much stronger in the presence of the filler atoms, if we compare the *B* parameter reported from the full dispersion model for unfilled and fully filled skutterudites. However, if we look at the predictions by the Debye model, phonon-phonon coupling is weaker in the presence of the filler atoms and most of the reduction in the thermal conductivity is a result of resonance scattering. Using first-principles calculations, Feldman *et al.*[33] showed that there is a strong hybridization between bare La vibrations and certain Sb-like phonon branches, suggesting anharmonic scattering by harmonic motions of rare earth elements as an important mechanism for the suppression of the thermal conductivity. This is in agreement with the strong phonon-phonon scattering that we observed with the full dispersion model in fully filled $LaFe_4Sb_{12}$.

Figure 5 indicates that all three models can provide a good fit to the experimental data of the thermal conductivity. However, the values reported in Table I are very different from one model to the other. Therefore, there should be a large difference in the distribution of phonon mean free paths, as shown in Fig. 6, where the accumulative thermal conductivity versus mean free path is plotted for the three models. Note that in these fittings we tried to stay close to the fitting of Ref. 31.

Again the Debye based models underestimate the phonon mean free path inside fully filled skutterudites. According to these models, unless we reduce the grain size to values below 100 nm, there should be no difference between the measured lattice thermal conductivities. However, in the full dispersion model, phonons with a mean free path longer than 100 nm make more than a 70% contribution to the total thermal conductivity and as we reduce the grain sizes to values below 1 $\mu$m, we should observe a large reduction in the lattice thermal conductivity.

Just like for the case of pure skutterudites, to confirm that nanostructuring is effective for $LaFe_4Sb_{12}$, we prepared samples of different grain sizes. High and low resolution SEM images are shown in Fig. 7 and the measured lattice

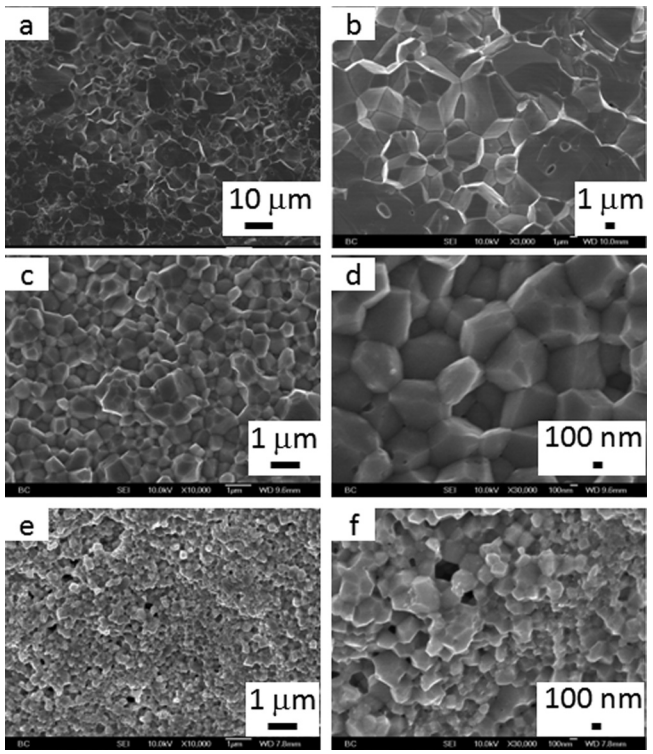


FIG. 7. Low- ((a)-(c) and (e)) and high- ((d) and (f)) magnification SEM images of the $LaFe_4Sb_{12}$ samples with different grain sizes: S1: 2–10 $\mu$m ((a) and (b)), S2: 0.5–1 $\mu$m ((c) and (d)), S3: 200–500 nm ((e) and (f)).

thermal conductivities are reported in Fig. 8. If we look at the measured data at T = 100 K, there is a clear difference in the measured thermal conductivities, despite the fact that the grain sizes are still larger than 100 nm for all samples. The only way to explain such a behavior is to rely on the predictions by full dispersions, not the Debye models. The predictions of the three models for samples of average grain size of

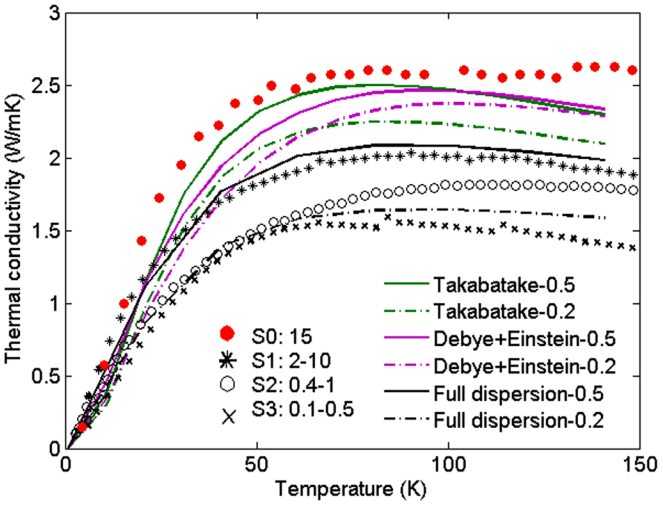


FIG. 8. Lattice thermal conductivity of $LaFe_4Sb_{12}$ samples of different grain sizes. The data of sample S0 are taken from Takabatake *et al.*[31] Samples S1-S3 are prepared in our lab and their SEM images are shown in Fig. 7. The numbers in front of sample numbers indicate the grain size range in microns for each sample. We have fitted the bulk sample data (red dots) with three different models explained in the text and the fits are reported in Fig. 5. Here the predictions of the models for samples with average grain sizes of 0.5 and 0.2 $\mu$m are reported.

Downloaded 24 Sep 2012 to 136.167.55.68. Redistribution subject to AIP license or copyright; see http://jap.aip.org/about/rights_and_permissions

500 nm and 200 nm are also shown in Fig. 8. Again it is not possible to directly compare the model with the experiment due to unknown size distribution of the grain sizes. However, clearly full dispersion predictions are closer to the experimental values of samples with similar grain sizes as those considered in the model.

## CONCLUSIONS

The thermal conductivity is an integrant over all phonon frequencies (only one number) and can be easily reproduced using simplified models with several fitting parameters. However, these simplified models do not necessarily result in correct distributions of the phonon mean free paths. Here, we showed that it is important to use the full dispersion and not the Debye model to get the correct mean free path spectrum. The Debye model underestimates the phonon mean free path both in the pure and fully filled skutterudites. Moreover, if we include resonance scattering combined with the Debye dispersion (Debye + Einstein model), the phonon-phonon scattering rate is underestimated. Experimental evidence shows that nanostructuring is an effective way to reduce the thermal conductivity of $Co_4Sb_{12}$ in the temperature range of 300–600 K and also that of the $LaFe_4Sb_{12}$ at low temperatures below 200 K, a result that is only consistent with the full dispersion predictions.

## ACKNOWLEDGMENTS

The study was supported by Bosch via the MIT Energy Initiative Program (G.C. and Z.F.R). K. L., C.O., and M.S.D. are partially supported by the MIT S3TEC, an Energy Frontier Research Center funded by the U.S. Department of Energy, Office of Science; Office of Basic Energy Sciences under Award No. DE-FG02-09ER46577 for basic research in thermoelectric transport and materials and solar thermoelectric prototypes.

[1]A. F. Ioffe, *Thermoelements and Thermoelectric Cooling* (Infosearch Limited, London, 1957).
[2]G. Chen, Phys. Rev. B **57**, 14958 (1998).
[3]G. A. Slack and V. G. Tsoukala, J. Appl. Phys. **76**, 1665 (1994).
[4]M. Zebarjadi, K. Esfarjani, M. S. Dresselhaus, Z. F. Ren, and G. Chen, Energy Environ. Sci. **5**, 5147–5162 (2012).
[5]D. A. Broido, M. Malorny, G. Birner, N. Mingo, and D. A. Stewart, Appl. Phys. Lett. **91**, 231922 (2007).
[6]A. Ward and D. A. Broido, Phys. Rev. B **81**, 085205 (2010).
[7]J. Garg, N. Bonini, B. Kozinsky, and N. Marzari, Phys. Rev. Lett. **106**, 045901 (2011).
[8]K. Esfarjani, G. Chen, and H. T. Stokes, Phys. Rev. B **84**, 085204 (2011).
[9]J. Shiomi, K. Esfarjani, and G. Chen, Phys. Rev. B **84**, 104302 (2011).
[10]G. Chen, J. Heat Transfer **119**, 220–229 (1997).
[11]G. Chen and C. L. Tien, ASME J. Heat Transfer **114**, 636–643 (1992).
[12]J. D. Chung, A. McGaughey, and M. Kaviany, J. Heat Transfer **126**, 376 (2004).
[13]M. G. Holland, Phys. Rev. **132**, 2461 (1963).
[14]D. Baillis and J. Randrianalisoa, Int. J. Heat Mass Transfer **52**, 2516 (2009).
[15]N. Mingo, Phys. Rev. B **68**, 113308 (2003).
[16]J. Callaway, Phys. Rev. **113**, 1046 (1959).
[17]B. C. Sales, D. Mandrus, B. C. Chakoumakos, V. Keppens, and J. R. Thompson, Phys. Rev. B **56**, 15081 (1997).
[18]J. L. Feldman and D. J. Singh, Phys. Rev. B **53**, 6273 (1996).
[19]P. Ghosez and M. Veithen, J. Phys.: Condens. Matter **19**, 096002 (2007).
[20]D. Wee, B. Kozinsky, N. Marzari, and M. Fornari, Phys. Rev. B **81**, 045204 (2010).
[21]C. T. Walker and R. O. Pohl, Phys. Rev. **131**, 1433 (1963).
[22]P. G. Klemens, in *Solid State Physics*, edited by F. Seitz and D. Turnbull (Academic, New York, 1958), Vol. 7, p. 1.
[23]C. Dames and G. Chen, *Thermal Conductivity of Nanostructured Thermoelectric Materials CRC Handbook*, edited by M. Rowe (Taylor & Francis, Boca Raton, 2006).
[24]B. C. Sales, D. Mandrus, B. C. Chakoumakos, V. Keppens, and J. R. Thompson, Phys. Rev. B **56**, 15081–15089 (1997).
[25]D. Cao, F. Bridges, P. Chesler, S. Bushart, E. D. Bauer, M. B. Maple, Phys. Rev. B **70**, 094109 (2004).
[26]V. Keppens, D. Mandrus, B. C. Sales, B. C. Chakoumakos, P. Dai, R. Coldea, M. B. Maple, D. A. Gajewski, E. J. Freeman, and S. Bennington, Nature **395**, 876–878 (1998).
[27]N. R. Dilley, E. D. Bauer, M. B. Maple, S. Dordevic, D. N. Basov, F. Freibert, T. W. Darling, A. Migliori, B. C. Chakoumakos, and B. C. Sales, Phys. Rev. B **61**, 4608 (2000).
[28]B. C. Sales, B. C. Chakoumakos, and D. Mandrus, Mater. Res. Soc. Symp. **626**, 2000.
[29]R. P. Hermann, F. Grandjean, and G. J. Long, Am. J. Phys. **73**, 110 (2005).
[30]G. S. Nolas, T. J. R. Weakley, J. L. Cohn, and R. Sharma, Phys. Rev. B **61**, 3845 (2000).
[31]T. Takabatake, E. Matsuoka, S. Narazu, K. Hayashi, S. Morimoto, T. Sasakawa, K. Umeo, and M. Sera, Physica B **383**, 93–102 (2006).
[32]M. Zebarjadi, K. Esfarjani, J. Yang, Z. F. Ren, and G. Chen, Phys. Rev. B **82**, 195207 (2010).
[33]J. L. Feldman, D. J. Singh, I. I. Mazin, D. Mandrus, and B. C. Sales, Phys. Rev. B **61**, R9209–R9212 (2000).

Downloaded 24 Sep 2012 to 136.167.55.68. Redistribution subject to AIP license or copyright; see http://jap.aip.org/about/rights_and_permissions

# Dramatic thermal conductivity reduction by nanostructures for large increase in thermoelectric figure-of-merit of $FeSb_2$

Huaizhou Zhao,[1] Mani Pokharel,[1] Gaohua Zhu,[1] Shuo Chen,[1] Kevin Lukas,[1] Qing Jie,[1] Cyril Opeil,[1] Gang Chen,[2] and Zhifeng Ren[1,a)]
[1]*Department of Physics, Boston College, Chestnut Hill, Massachusetts 02467, USA*
[2]*Department of Mechanical Engineering, Massachusetts Institute of Technology, Cambridge, Massachusetts 02139, USA*

(Received 12 August 2011; accepted 26 September 2011; published online 17 October 2011; corrected 14 November 2011)

In this report, thermal conductivity reduction by more than three orders of magnitude over its single crystal counterpart for the strongly correlated system $FeSb_2$ through a nanostructure approach was presented, leading to a significant increase of thermoelectric figure-of-merit (*ZT*). For the samples processed with the optimal parameters, the thermal conductivity reached 0.34 $Wm^{-1}$ $K^{-1}$ at 50 K, leading to a *ZT* peak of about 0.013, compared to 0.005 for single crystal $FeSb_2$, an increase of about 160%. This work suggests that nanostructure method is effective and can be possibly extended to other strongly correlated low temperature thermoelectric materials, paving the way for future cryogenic temperature cooling applications. © *2011 American Institute of Physics*. [doi:10.1063/1.3651757]

Of the several strongly correlated semiconductors including FeSi,[1] $Ce_3Bi_4Pt_3$,[2] and $FeGa_3$,[3] $FeSb_2$ has recently stimulated extensive research efforts due to its colossal thermopower (Seebeck coefficient, *S*) at 10 K.[4] The thermopower *S* of $FeSb_2$ single crystals is on the order of tens of mV $K^{-1}$ which contributes to the very large power factor (*PF*) of 0.23 $Wm^{-1}$ $K^{-2}$,[4,5] about 40 times of the best thermoelectric materials ($Bi_2Te_3$-based high-performance alloy ingots[6,7]). However, it is the figure of merit, $Z = S^2\sigma/\kappa$, where *S* is the Seebeck coefficient, $\sigma$ the electrical conductivity, and $\kappa$ the thermal conductivity, which determines the overall efficiency. To be practically useful, materials should have a dimensionless figure-of-merit (*ZT*) around 1. However, $FeSb_2$ single crystals have a peak *ZT* of around 0.005 at 12 K due to a large value of thermal conductivity of about 500 $Wm^{-1}$ $K^{-1}$.[5] In order for $FeSb_2$ to become a useful material for thermoelectric cooling, *ZT* must be increased to a meaningful value.

The large lattice thermal conductivity of strongly correlated materials such as $FeSb_2$ at low temperatures limits their *ZT*. Zhang *et al.*[8] predicted that phonon size effects in nanostructured strongly correlated materials can be exploited to reduce phonon thermal conductivity while maintaining electron transport due to the long phonon mean free path and short electron mean free path. For example, it was estimated that single crystal $FeSb_2$ has an electron mean free path of less than 10 nm at all temperatures with a phonon mean free path around 40 $\mu$m at 15 K.[9] This large difference of mean free paths allows the opportunity to tune the electrical and thermal properties almost independently by either doping[10,11] or nano-engineering the grain size.[11] In principle, thermal conductivity suppression can be realized through several different methods such as the introduction of impurities, defects, or grain boundaries. Although substantial thermal conductivity reduction was achieved by doping, no improvements in *ZT* were reported due to altered electron transport properties in $FeSb_2$.[10,11]

Nanostructure approach has proven to be a very efficient way to reduce the lattice contribution to the thermal conductivity in many thermoelectric material systems.[12–15] The lower limit of the lattice thermal conductivity in $FeSb_2$ has been calculated[16] to be as low as 0.3 $Wm^{-1}$ $K^{-1}$ at 50 K through the model proposed by Cahill *et al.*[17] It will be shown in this report that the thermal conductivity of nanostructured $FeSb_2$ is drastically decreased leading to an improvement in *ZT*.

The nanostructured $FeSb_2$ were synthesized by first ingot formation through melting and solidification, and then followed by ball milling and hot pressing with different processing parameters. Scanning electron microscopy (SEM, JEOL 6340F) was used to investigate the grain size distributions of the above processed samples. Transmission electron microscopy (TEM, JEOL 2010F) observation was performed on the representative sample S15hr-200C. The electrical resistivity ($\rho$), Seebeck Coefficient (*S*), thermal conductivity ($\kappa$), and Hall coefficient ($R_H$) were all measured on a physical property measurement system (PPMS) from Quantum Design. Within the one-band model, the charge-carrier concentration was determined by $n = 1/(e/R_H/)$. The Hall mobility was determined by $\mu_H = /R_H//\rho$.

SEM images in Fig. 1 show how the grain size changes as a function of ball milling time and hot pressing temperature. From the images, it can be seen that samples pressed from powders ball milled for shorter times (Fig. 1(a)) or at higher temperatures (Fig. 1(d)) have much larger grains than those from powders ball milled for longer time (Figs. 1(b) and 1(c)) and at lower temperatures (Figs. 1(e) and 1(f)). It is also noticed that S15hr-200 C was composed of particles in which there are many smaller grains, which are around $20 \pm 5$ nm estimated from SEM images (Fig. 1(f)). TEM images shown in Fig. 2 indicate that the particles in sample S15hr-200C were indeed composed of smaller crystalline grains with different orientations, consistent with the SEM image (Fig. 1(f)).

a)Author to whom correspondence should be addressed. Electronic mail: renzh@bc.edu.

 © 2011 American Institute of Physics

Downloaded 08 May 2012 to 136.167.55.37. Redistribution subject to AIP license or copyright; see http://apl.aip.org/about/rights_and_permissions

An enlarged area from Fig. 2(a) was shown in Fig. 2(b). It is clearly shown that the grains are well-crystallized with dimensions of $20 \times 15$ nm and a lattice spacing of 0.276 nm, which can be indexed to the (101) planes of orthorhombic *Pnnm* $FeSb_2$. The nano-sized grains and the boundaries between theses nano-sized crystals would contribute to the dramatic thermal conductivity reductions in the samples.

Figure 3(a) shows the temperature dependence of thermal conductivity for all samples and also the single crystals grown from vapor transport (VT) and self-flux (SF) methods.[5] A substantial decrease of thermal conductivity was found for all samples throughout the temperature range, decreasing as grain size decreases. The thermal conductivity of sample S15hr-600C is 17 $Wm^{-1}$ $K^{-1}$ at 40 K, compared with 0.34 $Wm^{-1}$ $K^{-1}$ for S15hr-200C at the same temperature due to a decrease in the lattice portion of the thermal conductivity. The peak positions of $\kappa$, which reveal the competition between the phonon-phonon (Umklapp) scattering or impurity scattering and the grain boundary scattering, shift to higher temperatures and nearly disappear on samples S15hr-200C and S15hr-room temperature. This demonstrates that grain boundary scattering is the dominant scattering mechanism in samples with smaller grain sizes. Moreover, fittings for all the curves below 100 K show a shift from $T^{2.04}$ to $T^{1.31}$ with the decreasing of grain sizes, as is also seen in nanocrystalline silicon[12] which indicates that other parameters besides $C_V$ such as porosity, phonon frequency ($\omega$), and the effective mean free path ($\Lambda_{eff}$) also play important roles in thermal conductivity reduction. When compared with single crystal $FeSb_2$, there is a reduction by more than three orders of magnitude in the thermal conductivity from

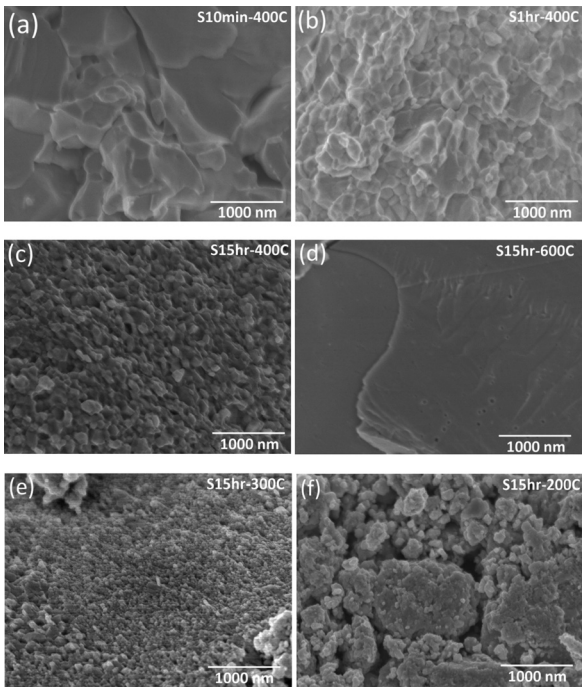


FIG. 1. SEM images for nanostructured samples that were prepared with different conditions. (a) hot pressed at 400 °C using powders ball milled for 10 min, (b) hot pressed at 400 °C using powders ball milled for 1 h, (c) hot pressed at 400 °C using powders ball milled for 15 h, (d) hot pressed at 600 °C using powders ball milled for 15 h, (e) hot pressed at 300 °C using powders ball milled for 15 h, and (f) hot pressed at 200 °C using powders ball milled for 15 h.

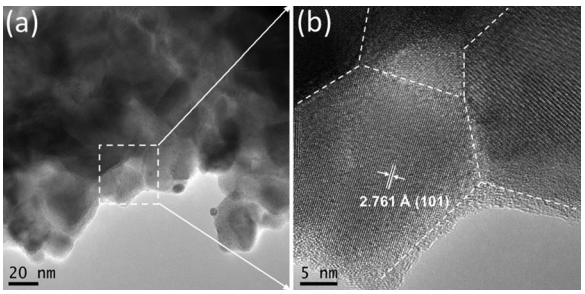


FIG. 2. TEM images for nanostructured sample S15hr-200C. (a) Lower magnification to show the average grain size and (b) higher magnification of the boxed area shown in (a) to show the crystalline orientation and defected boundaries.

500 $Wm^{-1}$ $K^{-1}$ down to around 0.1 $Wm^{-1}$ $K^{-1}$ at 20 K in the nanostructured sample S15hr-200C. Such a large thermal conductivity suppression by nanostructuring at low temperature is much larger than any other nanostructured thermoelectric materials at high temperatures. Nanostructured *p*-type BiSbTe bulk alloy achieved 83% thermal conductivity reduction compared with its ingot counterpart at 250 °C,[13] half-Heuslers achieved 33% in high temperature ranges,[15] and a 100% reduction for *p*-type silicon germanium alloy.[18]

Figure 3(b) shows the temperature dependence of electrical resistivity for all the samples. The data was fit using Arrhenius' law to find approximate energy gaps. Sample S15hrs-600C has two gaps of 28.2 meV and 4.2 meV. When the pressing temperature is lowered further, e.g., sample S15hrs-300C, only one gap appears with a value of 21 meV. The change in the band gaps corresponds to the increasing of crystal defects that are probably due to the decreased grain size and increased carrier concentration. It appears that the smaller energy gap located in the temperature range of 7-20 K was suppressed; and the larger band gap was decreased as can be seen in the sample pressed at room temperature whose band gap is reduced to 18 meV. Measurements of the carrier concentration, inset of Fig. 3(c) increased as well, confirming the narrowing of the energy gaps.

The temperature dependent Seebeck coefficients ($S$) are shown in Fig. 3(c). It shows that $S$ decreases as grain size is decreased, which could mean that carriers are generated. This is not the case for S10min-400C, which has smaller grains than S15hr-600C. From the relationship of the electrical property and the quality of crystal, it is believed that S10min-400C has fewer defects than that of S15hr-600C due to the longer ball milling time of the latter. Defects typically increase carrier concentration, which decreases the $S$. An increase in the carrier concentration will also lead to a decrease in the resistivity, which is the case as seen in Fig. 3(b). Mobility and carrier concentration measurements are shown for two samples in the inset of Fig. 3(c). Carrier concentration at 25 K is higher for the S15hr-300C sample with a value of $9.75 \times 10^{19}$ $cm^{-3}$ and while its mobility is lower at 4.52 $cm^2$ $V^{-1}s^{-1}$, when compared to S15hr-600C at 25 K, whose carrier concentration is decreased to $8.36 \times 10^{17}$ $cm^{-3}$ while its mobility is as high as 160 $cm^2$ $V^{-1}s^{-1}$. These properties directly correlate to the increase seen in the $S$. There is a cross over between the two samples in the Seebeck coefficient found at 65 K. This cross over is also seen in the measurements for carrier concentration at 65 K while the mobility remains relatively constant

Downloaded 08 May 2012 to 136.167.55.37. Redistribution subject to AIP license or copyright; see http://apl.aip.org/about/rights_and_permissions

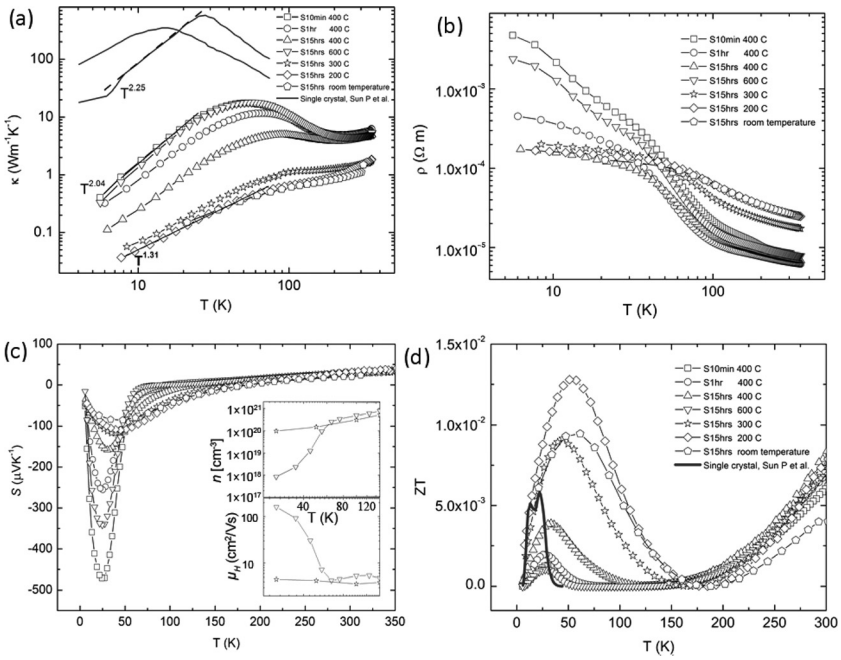


FIG. 3. Thermoelectric properties for nanostructured samples: (a) temperature dependence of thermal conductivity, fittings was applied to sample S10min-400C and S15hr-200C. Two solid curves correspond to thermal conductivity from single crystal samples (Ref. 5); (b) temperature dependence of resistivity; (c) temperature dependence of Seebeck coefficient, the insets indicate the temperature dependent carrier concentration and Hall mobility for S15hr-600C and S15hr-300C, respectively; (d) temperature dependence of *ZT*.

confirming both measurements. S15hr-600C has better crystallization and therefore a band gap of 4.2 meV in the temperature range 7-20 K, which is not seen in S15hr-300C and induces higher resistivity than that of S15hr-300C below 50 K. For the same reason, peak values of the Seebeck coefficient of S15hr-600C, which is 352 $\mu$V K$^{-1}$ at 20 K, is much larger than 117 $\mu$V K$^{-1}$ for S15hr-300C at 35 K. In $FeSb_2$ systems, the relation between carrier concentration and Seebeck coefficient has been intensively investigated recently by Sun *et al.*[9,11,19] It was found that an enhancement by a factor of 30 or larger could be applied to the calculated Seebeck coefficient based on the free-electron model. Due to this enhancement, it is quite likely that an increase in the Seebeck coefficient can be realized by tuning carrier concentration through doping or composition adjustment, providing the potential for much future work.

Figure 3(d) shows the temperature dependence of *ZT* for the nanostructured samples as well as those for single crystals. The *ZT* increases from 0.001 of sample S15hr-600C to 0.013 of S15hr-200C, which is an unambiguous indication of grain size effect. The optimal *ZT* value reaching 0.013 at 50 K in S15hr-200C is much higher than $ZT = 0.005$ at 10 K for single crystal samples. Though the power factor is much less than that of single crystal, the drastic reduction in thermal conductivity contributes to the increase in *ZT*. One feature worth pointing out is that the *ZT* curve in nanostructured $FeSb_2$ is broadened significantly over that of the single crystal counterpart, which is much more useful for applications between 10 and 150 K.

In conclusion, substantial thermal conductivity suppression for the strongly correlated system $FeSb_2$ through a nanostructure approach was reported in this letter. Thermal conductivity was reduced by more than three orders of magnitude over its single crystal counterpart. As grain size decreases from tens of microns to around 20 nm, the corresponding thermal conductivity decreases by 50 times, reaching 0.34 Wm$^{-1}$ K$^{-1}$ at 50 K. *ZT* was found to be 0.013, compared to 0.005 for single crystal $FeSb_2$, an increase of 160%. Although this is still far from the state-of-art requirement of $ZT = 1$, nanostructure to reduce thermal conductivity in $FeSb_2$ is clearly the right way, and a combination with other methods of *ZT* enhancement including doping or composition adjustment is expected to further increase the *ZT*.

The work is sponsored by Air Force MURI program under Contract FA9550-10-1-0533.

[1]B. C. Sales, E. C. Jones, B. C. Chakoumakos, J. A. Fernandez-Baca, H. E. Harmon, J. W. Sharp, and E. H Volckmann, Phys. Rev. B: Condens. Matter. **50**(12), 8207 (1994).
[2]M. F. Hundley, P. C. Canfield, J. D. Thompson, and Z. Fisk, Phys. Rev. B **50**(24), 18142 (1994).
[3]Y. Hadano, S. Narazu, M. A. Avila, T. Onimaru, and T. Takabatake, J. Phys. Soc. Jpn. **78**(1), 013702 (2009).
[4]A. Bentien, S. Johnsen, G. K. H. Madsen, B. B. Iversen, and F. Steglich, Europhys. Lett. **80**, 17008 (2007).
[5]P. Sun, N. Oeschler, S. Johnsen, B. B. Iversen, and F. Steglich, J. Phys.: Conf. Ser. **150**, 012049 (2009).
[6]O. Yamashita, S. Tomiyoshi, and K. Makita, J. Appl. Phys. **93**, 368 (2003).
[7]S. Paschen, in *Thermoelectric Handbook*, edited by D. M. Rowe (CRC Press, Taylor & Francis Group, Boca Raton, 2006), Chap. 15.
[8]Y. Q. Zhang, M. S. Dresselhaus, Y. Shi, Z. F. Ren, and G. Chen, Nano Lett. **11**(3), 1166 (2011).
[9]P. Sun, N. Oeschler, S. Johnsen, B. B. Iversen, and F. Steglich, Phys. Rev. B **79**(15), 153308 (2009).
[10]A. Bentien, G. K. H. Madsen, S. Johnson, and B. B. Iversen, Phys. Rev. B **74**(20), 205105 (2006).
[11]P. Sun, M. Søndergaard, Y. Sun, S. Johnsen, B. B. Iversen, and F. Steglich, Appl. Phys. Lett. **98**, 072105 (2011).
[12]Z. Wang, J. E. Alaniz, W. Jang, J. E. Garay, and C. Dames, Nano Lett. **11**(6), 2206 (2011).
[13]B. Poudel, Q. Hao, Y. Ma, Y. Lan, A. Minnich, B. Yu, X. Yan, D. Wang, A. Muto, D. Vashaee, X. Chen, J. Liu, M. S. Dresselhaus, G. Chen, and Z. F. Ren, Science **320**(5876), 634 (2008).
[14]Y. C. Lan, A. J. Minnich, G. Chen, and Z. F. Ren, Adv. Funct. Mater. **20**, 357 (2010).
[15]X. Yan, G. Joshi, W. S. Liu, Y. C. Lan, H. Wang, S. Lee, J. W. Simonson, S. J. Poon, T. M. Tritt, G. Chen, and Z. F. Ren, Nano Lett. **11**, 556 (2011).
[16]S. Zhu, W. Xie, D. Thompson, T. Holgate, M. Zhou, Y. Yan, and T. M. Tritt, J. Mater. Res. **26**(15), 1894 (2011).
[17]D. G. Cahill, S. K. Watson, and R. O. Pohl, Phys. Rev. B **46**(10), 6131 (1992).
[18]G. Joshi, H. Lee, Y. Lan, X. Wang, G. Zhu, D. Wang, R. W. Gould, D. C. Cuff, M. Y. Tang, M. S. Dresselhaus, G. Chen, and Z. F. Ren, Nano Lett. **8**(12), 4670 (2008).
[19]P. Sun, N. Oeschler, S. Johnsen, B. B. Iversen, and F. Steglich, Dalton Trans. **39**, 1012 (2010).

Downloaded 08 May 2012 to 136.167.55.37. Redistribution subject to AIP license or copyright; see http://apl.aip.org/about/rights_and_permissions

Energy & Environmental Science

RSC Publishing

PAPER

View Article Online
View Journal | View Issue

# Studies on the $Bi_2Te_3$–$Bi_2Se_3$–$Bi_2S_3$ system for mid-temperature thermoelectric energy conversion

Cite this: *Energy Environ. Sci.*, 2013, **6**, 552

Weishu Liu,[a] Kevin C. Lukas,[a] Kenneth McEnaney,[b] Sangyeop Lee,[b] Qian Zhang,[a] Cyril P. Opeil,[a] Gang Chen*[b] and Zhifeng Ren*[a]

Received 19th September 2012
Accepted 21st November 2012

DOI: 10.1039/c2ee23549h

www.rsc.org/ees

Bismuth telluride ($Bi_2Te_3$) and its alloys have been widely investigated as thermoelectric materials for cooling applications at around room temperature. We report a systematic study on many compounds in the $Bi_2Te_3$–$Bi_2Se_3$–$Bi_2S_3$ system. All the samples were fabricated by high energy ball milling followed by hot pressing. Among the investigated compounds, $Bi_2Te_2S_1$ shows a peak $ZT$ ~0.8 at 300 °C and $Bi_2Se_1S_2$ ~0.8 at 500 °C. The results show that these compounds can be used for mid-temperature power generation applications. The leg efficiency of thermoelectric conversion for segmented elements based on these n-type materials could potentially reach 12.5% with a cold side at 25 °C and a hot side at 500 °C if appropriate p-type legs are paired, which could compete well with the state-of-the-art n-type materials within the same temperature range, including lead tellurides, lead selenides, lead sulfides, filled-skutterudites, and half Heuslers.

Published on 22 November 2012 on http://pubs.rsc.org | doi:10.1039/C2EE23549H
Downloaded by Boston College on 28 January 2013

**Broader context**

Thermoelectric converters have provided a new class of green energy from solar heat, terrestrial heat, and waste heat from both automobile vehicles and industrial operations. $Bi_2Te_3$-based materials have distinguished themselves in low-temperature power generation applications. For these applications, the hot side temperature is typically limited to less than 250 °C due to the declining $ZT$ value. For the mid-temperature range, PbTe and skutterudite materials were being considered as the candidates. However, the toxicity or thermal stability issue is still the most worrying part for these materials. In this work, we proposed an alternative by using a segmented leg made from $Bi_2(Te, Se, S)_3$-based materials, which shows a potential leg efficiency of 12.5% with a cold side of 25 °C and a hot side of 500 °C. It competes well with the state-of-the-art n-type materials within the same temperature range. Specifically, two new compounds, *i.e.*, $Bi_2Te_2S_1$ and $Bi_2Se_1S_2$, have been identified as the promising materials for the mid-temperature applications.

## 1 Introduction

Bismuth telluride ($Bi_2Te_3$) crystallizes in a rhombohedral lattice ($R\bar{3}m$), and shows a lamella structure with a five atomic layer block in the sequence of Te(1)–Bi–Te(2)–Bi–Te(1).[1] $Bi_2Te_3$ is a good thermoelectric material near room temperature,[2] and has dominated the thermoelectric cooling application. The thermoelectric performance of a material is based on a dimensionless figure of merit, $ZT$, which is defined as $ZT = (S^2\sigma/\kappa)T$, where $S$, $\sigma$, $\kappa$, and $T$ are the Seebeck coefficient, electrical conductivity, thermal conductivity, and absolute temperature, respectively. Recently, $Bi_2Te_3$-based nanocomposites synthesized from powder metallurgy methods have drawn much attention as a result of their better thermoelectric and mechanical properties.[3–12] $Bi_2Te_3$-based materials are also used in low-temperature (RT-300 °C) heat to electricity conversion applications, including solar to electrical generation.[13,14] For these applications, the hot side temperature is typically less than 250 °C due to the $ZT$ value drop and materials' instability above 300 °C. For the mid-temperature range between 200 and 600 °C, other materials such as PbTe, skutterudites, and half Heuslers are being studied. The primary motivation of this work is to explore some new compositions within the $Bi_2Te_3$–$Bi_2Se_3$–$Bi_2S_3$ system to achieve higher $ZT$ values in the mid-temperature range.

Historically, partial substitution of tellurium in $Bi_2Te_3$ by selenium (Se) or sulfur (S) was used to reduce the lattice thermal conductivity thereby raising the $ZT$ value in n-type $Bi_2Te_3$-based thermoelectric materials.[2,15–18] $Bi_2Se_3$ and $Bi_2S_3$ were much less studied as thermoelectric materials than $Bi_2Te_3$.[19–22] Recently, Biswas *et al.* reported that a $ZT$ value of 0.6 at 487 °C was obtained in an n-type $Bi_2S_3$ ingot doped with $BiCl_3$.[23] The peak $ZT$ value of such Te-free thermoelectric material is still low when compared with $Bi_2Te_3$. However, $Bi_2Te_3$ is not stable above 300 °C. In this report, we investigated the thermoelectric properties of some new compositions in the $Bi_2Te_3$–$Bi_2Se_3$–$Bi_2S_3$ system to see whether these materials can be used at temperatures higher than 300 °C. According to our study, the peak $ZT$ of $Bi_2Te_{2.7}Se_{0.3}$ shifted from 125 °C to 200 °C by partially

[a]Department of Physics, Boston College, Chestnut Hill, Massachusetts 02467, USA. E-mail: renzh@bc.edu; Fax: +1-617-552-8478; Tel: +1-617-552-2832

[b]Department of Mechanical Engineering, Massachusetts Institute of Technology, Cambridge, Massachusetts 02139, USA. E-mail: gchen2@mit.edu; Fax: +1-617-324-5519; Tel: +1-617-253-0006



This journal is © The Royal Society of Chemistry 2013

Published on 22 November 2012 on http://pubs.rsc.org | doi:10.1039/C2EE23549H
Downloaded by Boston College on 28 January 2013

substituting Te with S, also a peak *ZT* of ~0.8 at 300 °C could be obtained in $Bi_2Te_2S_1$ and ~0.8 at 500 °C in $Bi_2Se_1S_2$ by carrier concentration optimization. These results place such materials as promising candidates for intermediate temperature (300–500 °C) thermoelectric applications.

## 2 Experimental details

### Synthesis

The fabrication process is similar to that of our previous reports.[11,12] Bismuth chunks (Bi, 99.999%, Alfa Aesar), tellurium chunks (Te, 99.999%, Alfa Aesar), selenium shots (Se, 99.999%, Alfa Aesar), and sulfur powders (S, 99.99%, Alfa Aesar) were weighted according to the stoichiometry $Bi_2(Te, Se, S)_3$, specified in each section, plus a very small amount of copper for either process repeatability control or carrier concentration adjustment (the exact amount for each composition will be described in the appropriate places). The elements were then subjected to ball milling for 20 hours. The ball milled powders were then loaded into a graphite die with an inner diameter of 12.7 mm and sintered by direct current induced hot pressing (dc-HP) at 500 °C for 2 minutes into a rod with a height of 12–13 mm. These dimensions allow us to carry out the thermal and electrical conductivity measurements along the same direction (all the data reported in this paper are from the same direction).

### Crystalline structure

X-ray diffraction measurements were conducted on a PANalytical multipurpose diffractometer with an X'celerator detector (PANalytical X'Pert Pro). The lattice parameters and atomic sites of each element in the $Bi_2(Te, Se, S)_3$ phase were calculated by the Rietveld refinement method, which was performed using commercial software (X'Pert High Score Plus, X'Pert Pro).

### Thermoelectric transport properties

The electrical resistivity was measured by a reversed dc-current four-point method, while the Seebeck coefficient was determined by the slope of the voltage difference *versus* temperature difference curve based on a static temperature difference method. The simultaneous measurement of electrical resistivity and Seebeck coefficient was conducted on a commercial system (ZEM-3, ULVAC). The thermal conductivity was calculated from the relationship $\kappa = DC_pd$, where $D$, $C_p$, and $d$ are the thermal diffusivity, specific heat, and volumetric density, respectively. The thermal diffusivity was measured by the laser flash method with a commercial system (LFA447 for the $D$ from 25 to 250 °C, LFA457 for the $D$ from 250 to 500 °C, Netzsch). The specific heat capacity was determined using two differential scanning calorimeters (DSC200-F3 for the $C_p$ from 25 to 250 °C, DSC404-C for the $C_p$ from 250 to 500 °C, Netzsch). The volumetric density (listed in Table 1) was measured by the Archimedes method. The Hall coefficient, $R_H$, measurement was carried out on two commercial systems (PPMS, Quantum Design; Electromagnet7600, LakeShore), with a magnetic field of up to 9 T and an electrical current of 10–20 mA.

## 3 Results and discussion

### 3.1 $Bi_2Te_3$–$Bi_2Se_3$–$Bi_2S_3$

Fig. 1 shows the phase diagram for the $Bi_2Te_3$–$Bi_2Se_3$–$Bi_2S_3$ system, which includes more than ten nominal compositions studied. Three regions could be identified: a rhombohedral region ($Bi_2Te_3$, $Bi_2Te_2Se_1$, $Bi_2Te_1Se_2$, $Bi_2Se_3$, $Bi_2Te_2S_1$, and $Bi_2Te_{1.8}Se_{0.6}S_{0.6}$, filled circles), an orthorhombic region ($Bi_2S_3$, $Bi_2Se_1S_2$, and $Bi_2Se_2S$, open circles), and a mixture region ($Bi_2Te_1S_2$, $Bi_2Te_1Se_1S_1$, $Bi_2Te_{0.6}Se_{1.8}S_{0.6}$, and $Bi_2Te_{0.6}Se_{0.6}S_{1.8}$, half-filled circles). In the $Bi_2Te_3$–$Bi_2Se_3$ system, the interphases $Bi_2Te_2Se_1$ (named as Kawazulite) and $Bi_2Te_1Se_2$ (named as Skippenite) have been previously identified in natural minerals,[24] but were less intentionally studied when compared with $Bi_2Te_3$ and $Bi_2Se_3$. The varying lattice parameters ($a$, $b$ and $c$) from $Bi_2Te_3$ to $Bi_2Se_3$ follow the Vegard's law, which indicates a linear structure shrinkage. The detailed lattice parameters and atomic sites are given in Table 1. Liu *et al.* reported a miscibility gap between the rhombohedral phase $Bi_2Se_3$ and orthorhombic phase $Bi_2Se_2S_1$ in the $Bi_2Se_3$–$Bi_2S_3$ system.[25] A similar miscibility gap has also been observed in our work. The sulfur-rich phases $Bi_2Se_1S_2$ and $Bi_2Te_1S_2$ were not well studied in the literature. According to our study, $Bi_2Se_1S_2$ is a single phase and shares a similar crystalline structure with $Bi_2S_3$. In the crystalline structure of $Bi_2S_3$, sulfur has three equivalent sites S(1) (0.6154, 0.75, 0.0576), S(2) (0.7148, 0.25, 0.3055), and S(3) (0.4505, 0.75, 0.3609). The crystalline structure information of $Bi_2S_3$ was used as the starting value for the Rietveld refinement of the $Bi_2Se_1S_2$ XRD pattern. All three possible substitutions of sulfur with selenium have been investigated. Se atoms in the $Bi_2Se_1S_2$ compound are most likely in the S(2)-site of the $Bi_2S_3$-type lattice structure, as shown in Table 1. $Bi_2Te_1S_2$ is a mixture of a rhombohedral phase (63.2 mol%) and an orthorhombic phase (36.8 mol%), which indicates another miscibility gap between $Bi_2S_3$ and $Bi_2Te_2S_1$. Additionally, the nominal compositions $Bi_2Te_1Se_1S_1$, $Bi_2Te_{0.6}Se_{1.8}S_{0.6}$, and $Bi_2Te_{0.6}Se_{0.6}S_{1.8}$ are also a mixture of the rhombohedral and orthorhombic phases. The predicted mixture region, presented in Fig. 1 by the shaded region, is useful for design of new nanostructures to achieve a reduced lattice thermal conductivity by controlling the size, morphology, and concentration of the precipitation phase.[26,27]

Fig. 2 shows the temperature dependent thermoelectric properties of the $Bi_2Te_3$–$Bi_2Se_3$ system. In order to achieve good process repeatability, 1 at.% copper (Cu) was used.[12] Fig. 2(a) demonstrates a continuous decrease in electrical resistivity with increasing Se content from $Bi_2Te_3$ to $Bi_2Se_3$. The negative sign of the Seebeck coefficient for all these samples indicates n-type carriers, as shown in Fig. 2(b). The Seebeck coefficient at room temperature dramatically decreases from −241 to −131, −59 and −37 μV $K^{-1}$ for the samples of $Bi_2Te_3$, $Bi_2Te_2Se_1$, $Bi_2Te_1Se_2$, and $Bi_2Se_3$, respectively, which is in agreement with the trend observed in electrical resistivity. The considerable changes in both the electrical resistivity and Seebeck coefficient suggest a rising carrier concentration or band structure change with the increased Se in the $Bi_2Te_{3-x}Se_x$ system. A possible explanation is that Se has a higher evaporation pressure than Te and hence easily forms donor-like vacancies in the $Bi_2Te_3$-type lattice.[28]

Published on 22 November 2012 on http://pubs.rsc.org | doi:10.1039/C2EE23549H
Downloaded by Boston College on 28 January 2013

**Table 1** Volumetric density, crystalline structure, lattice parameters, and atomic sites of some compounds in the $Bi_2Te_3$–$Bi_2Se_3$–$Bi_2S_3$ system

| Compounds | Density (g cm$^{-3}$) | Structure | Lattice parameter | | Atomic site | | | | |
|---|---|---|---|---|---|---|---|---|---|
| **Rhombohedral phases** | | | | | | | | | |
| $Bi_2Te_3$ | 7.75 | $R\bar{3}m$ no. 166 | Axis | (Å) | | Bi(1) | Te(1) | Te(2) | |
| | | | *A* | 4.3856 | *x* | 0 | 0 | 0 | |
| | | | *B* | 4.3856 | *y* | 0 | 0 | 0 | |
| | | | *C* | 30.503 | *z* | 0.4005 | 0.2097 | 0 | |
| $Bi_2Te_2Se_1$ | 7.63 | $R\bar{3}m$ no. 166 | Axis | (Å) | | Bi(1) | Te(1) | Se(1) | |
| | | | *A* | 4.3001 | *x* | 0 | 0 | 0 | |
| | | | *B* | 4.3001 | *y* | 0 | 0 | 0 | |
| | | | *C* | 30.000 | *z* | 0.3920 | 0.2160 | 0 | |
| $Bi_2Te_1Se_2$ | 7.49 | $R\bar{3}m$ no. 166 | Axis | (Å) | | Bi(1) | Se(1) | Te(1) | |
| | | | *A* | 4.2178 | *x* | 0 | 0 | 0 | |
| | | | *B* | 4.2178 | *y* | 0 | 0 | 0 | |
| | | | *C* | 29.458 | *z* | 0.3989 | 0.2120 | 0 | |
| $Bi_2Se_3$ | 7.47 | $R\bar{3}m$ no. 166 | Axis | (Å) | | Bi(1) | Se(1) | Te(1) | |
| | | | *A* | 4.1396 | *x* | 0 | 0 | 0 | |
| | | | *B* | 4.1396 | *y* | 0 | 0 | 0 | |
| | | | *C* | 28.634 | *z* | 0.4012 | 0.2121 | 0 | |
| $Bi_2Te_2S_1$ | 7.49 | $R\bar{3}m$ no. 166 | Axis | (Å) | | Bi(1) | Se(1) | Te(1) | |
| | | | *A* | 4.2535 | *x* | 0 | 0 | 0 | |
| | | | *B* | 4.2535 | *y* | 0 | 0 | 0 | |
| | | | *C* | 29.608 | *z* | 0.3928 | 0.2143 | 0 | |
| **Orthorhombic phases** | | | | | | | | | |
| $Bi_2Se_2S_1$ | 7.36 | *Pnma* no. 62 | axis | (Å) | | Bi(1) | Bi(2) | Se(1) | S(1) | Se(2) |
| | | | *a* | 11.66327 | *x* | 0.51805 | 0.6542 | 0.6239 | 0.7115 | 0.4252 |
| | | | *b* | 4.068393 | *y* | 0.25 | 0.75 | 0.75 | 0.25 | 0.75 |
| | | | *c* | 11.44897 | *z* | 0.1689 | 0.4643 | 0.0697 | 0.2978 | 0.3687 |
| $Bi_2Se_1S_2$ | 7.05 | *Pnma* no. 62 | axis | (Å) | | Bi(1) | Bi(2) | S(1) | Se(1) | S(2) |
| | | | *a* | 11.5044 | *x* | 0.5164 | 0.6587 | 0.6164 | 0.7288 | 0.4630 |
| | | | *b* | 4.0254 | *y* | 0.25 | 0.75 | 0.75 | 0.25 | 0.75 |
| | | | *c* | 11.2959 | *z* | 0.1712 | 0.4633 | 0.0532 | 0.2986 | 0.3816 |
| $Bi_2S_3$ | 6.73 | *Pnma* no. 62 | axis | (Å) | | Bi(1) | Bi(2) | S(1) | S(2) | S(3) |
| | | | *a* | 11.2867 | *x* | 0.5174 | 0.6592 | 0.6154 | 0.7148 | 0.4505 |
| | | | *b* | 3.9816 | *y* | 0.25 | 0.75 | 0.75 | 0.25 | 0.75 |
| | | | *c* | 11.1421 | *z* | 0.1727 | 0.4663 | 0.0576 | 0.3055 | 0.3609 |

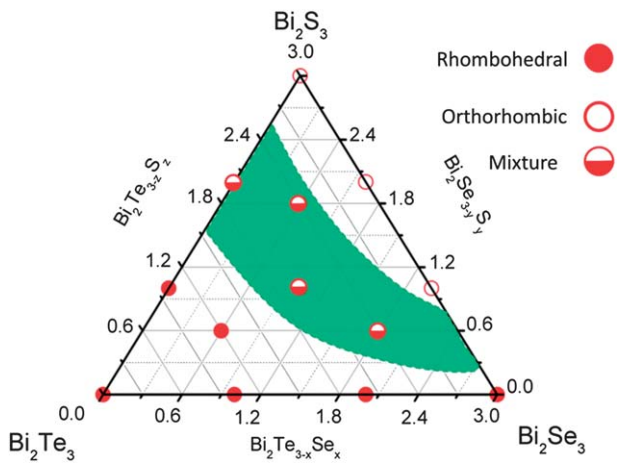


**Fig. 1** Phase diagram of the $Bi_2Te_3$–$Bi_2Se_3$–$Bi_2S_3$ system.

Owing to the large difference in Seebeck coefficient, the $Bi_2Se_3$ sample has a much lower power factor (330 μW m$^{-1}$ K$^{-2}$) than the $Bi_2Te_3$ sample (2920 μW m$^{-1}$ K$^{-2}$), as shown in Fig. 2(c). Fig. 2(d) shows the measured specific heat for these samples, which are 2–8% higher than the theoretical value from the Dulong–Petit law, depending on the temperature. The inset of Fig. 2(d) compares the difference in specific heat for the $Bi_2Te_{3-x}Se_x$ system between measured values and theoretical values at room temperature. The thermal conductivities are plotted in Fig. 2(e), from which we can see that $Bi_2Se_3$ has the highest thermal conductivity associated with the large contribution from the electrons. In order to confirm the impact of the alloying effect on the phonon transport, the lattice thermal conductivities at room temperature are estimated from $\kappa_{lat} = \kappa_{tot} - L\sigma T$, where the Lorenz numbers ($L$) are calculated by using the Fermi energies derived from Seebeck coefficients.[12] The lattice thermal conductivities of the $Bi_2Te_{3-x}Se_x$ system are 1.18, 0.73, 0.60, 0.47, and 0.66 W m$^{-1}$ K$^{-1}$, for $x = 0$, 0.3, 1, 2 and 3, respectively. A valley in the lattice thermal conductivity was clearly seen in the $Bi_2Te_3$–$Bi_2Se_3$ system. This phenomenon could be understood through the effect of imperfections on the heat transport by lattice in a solid solution. The mass fluctuation and chemical bond changing were believed to generate strong scattering of the transport of phonons.[29,30] Due to the high power factor and low thermal conductivity, the classic

 This journal is © The Royal Society of Chemistry 2013

Published on 22 November 2012 on http://pubs.rsc.org | doi:10.1039/C2EE23549H
Downloaded by Boston College on 28 January 2013

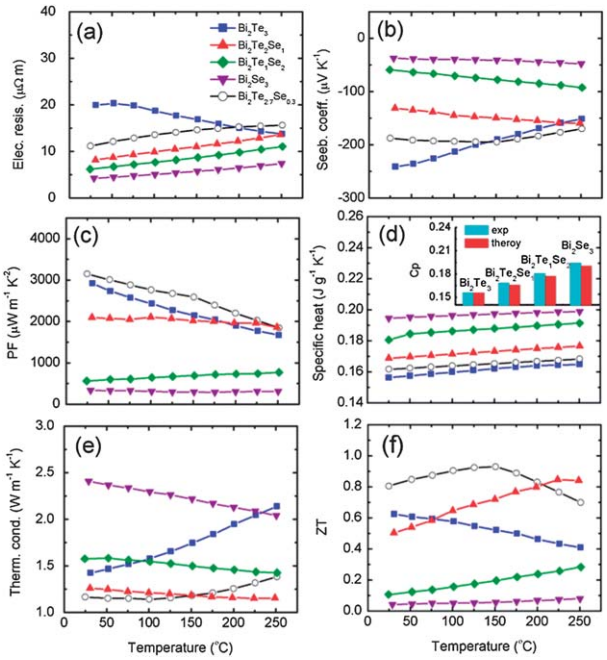


**Fig. 2** Temperature dependent thermoelectric properties of the $Bi_2Te_3$–$Bi_2Se_3$ system, (a) electrical resistivity, (b) Seebeck coefficient, (c) power factor, (d) specific heat, (e) thermal conductivity, and (f) figure of merit *ZT*. The inset of figure (d) shows the comparison of specific heat at room temperature between the experimentally measured value and theoretically calculated value.

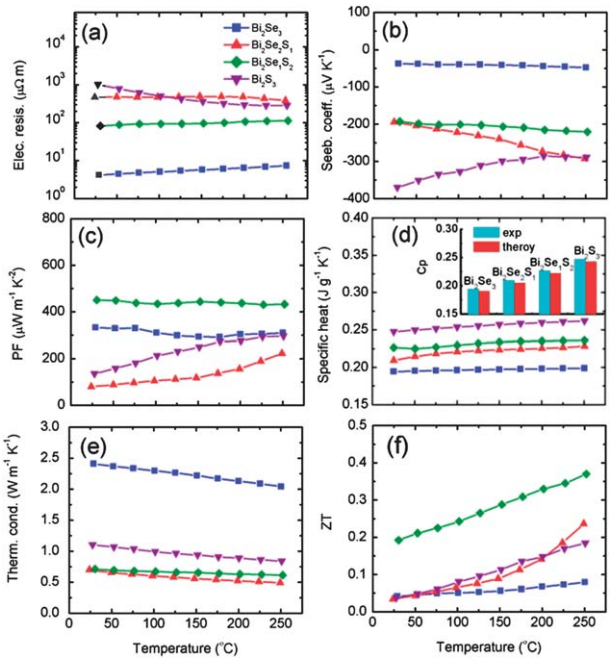


**Fig. 3** Temperature dependent thermoelectric properties of the $Bi_2Se_3$–$Bi_2S_3$ system, (a) electrical resistivity, (b) Seebeck coefficient, (c) power factor, (d) specific heat, (e) thermal conductivity, and (f) figure of merit *ZT*. The inset of figure (d) shows the comparison of specific heat at room temperature between the experimentally measured value and theoretically calculated value.

composition $Bi_2Te_{2.7}Se_{0.3}$ shows the highest peak *ZT* value, *i.e.*, ~0.9 at 150 °C. Additionally, the $Bi_2Te_2Se_1$ sample shows a *ZT* value of ~0.8 at 250 °C, which is good for thermoelectric applications at temperatures higher than 200 °C.

In contrast to the $Bi_2Te_3$–$Bi_2Se_3$ system, the $Bi_2Se_3$–$Bi_2S_3$ system shows a totally different picture owing to the lattice structure difference between $Bi_2Se_3$ and other S-containing $Bi_2Se_{3-y}S_y$ compounds, as indicated in Fig. 3. Here, a similar amount of Cu (1 at.%) was used for achieving good process repeatability. The rhombohedral phase ($Bi_2Se_3$) shows a heavily doped n-type semiconducting behavior, *i.e.*, low electrical resistivity (4.2 μΩ m at 25 °C) and Seebeck coefficient (−37 μV $K^{-1}$ at 25 °C). However, all the investigated orthorhombic phases show very poor electrical conductivity, resulting from the lower carrier concentration as compared with $Bi_2Se_3$. From the electrical resistivity and Seebeck coefficient plotted in Fig. 3(a) and (b), no obvious trend connected with the sulfur content can be identified within the orthorhombic phase region. Among the three orthorhombic phases, the power factor 430 μW $m^{-1}$ $K^{-2}$ of $Bi_2Se_1S_2$ is slightly higher than 295 μW $m^{-1}$ $K^{-2}$ of $Bi_2S_3$ and 220 μW $m^{-1}$ $K^{-2}$ of $Bi_2Se_2S_1$ at 250 °C, as shown in Fig. 3(c). The power factor of the as-pressed $Bi_2S_3$ is slightly higher than that of $Bi_2S_{3-\delta}$ made by a similar powder metallurgy process.[20] The thermal conductivities, calculated by using the measured specific heat and diffusivity coefficient, are plotted in Fig. 3(e). All the samples show almost a linear decrease with increasing temperature, without notable bipolar effect. Because of the low power factor, the *ZT* values of $Bi_2Se_3$ and $Bi_2S_3$ are only 0.05 near room temperature and 0.1–0.2 at 250 °C. However, the *ZT* values of both $Bi_2Se_1S_2$ and $Bi_2Se_2S_1$ rise with temperature, demonstrating the potential for high temperature application (the high temperature, up to 500 °C, thermoelectric properties of $Bi_2Se_1S_2$ are also measured and shown in Fig. 7).

Fig. 4 shows the thermoelectric properties of the $Bi_2Te_3$–$Bi_2S_3$ system with 1 at.% Cu for achieving good process repeatability. In contrast to $Bi_2Se_{3-y}S_y$, the solubility of sulfur in $Bi_2Te_{3-z}S_z$ is much higher. In the rhombohedral phase region, both the electrical resistivity and Seebeck coefficient of $Bi_2Te_{3-z}S_z$ decrease significantly with the increasing sulfur content, as shown in Fig. 4(a) and (b). Here, sulfur behaves as a strong donor in $Bi_2Te_{3-z}S_z$, which is similar to the effect of Se in $Bi_2Te_{3-x}Se_x$. A similar donor behavior for sulfur was also identified in $Bi_2Te_{3-z}S_z$ ingot.[31] The calculated lattice thermal conductivities near room temperature are 1.18, 0.89, 0.97, and 1.10 W $m^{-1}$ $K^{-1}$ for $Bi_2Te_3$, $Bi_2Te_2S_1$, $Bi_2Te_1S_2$, and $Bi_2S_3$, respectively. Due to the narrow band gap, the *ZT* value of $Bi_2Te_3$ shows a large decrease from 0.62 to 0.41 with increasing temperature from 25 to 250 °C. In contrast, $Bi_2Te_2S_1$ shows a continuous rise from 0.2 to 0.45, suggesting that $Bi_2Te_2S_1$ could be a new candidate for higher temperature application after further carrier optimization.

In order to fully show the $Bi_2Te_3$–$Bi_2Se_3$–$Bi_2S_3$ system, contouring diagrams are plotted in Fig. 5 according to the Hall carrier concentration, weighted mobility, and lattice thermal conductivity at room temperature. Here, the Hall carrier concentration is calculated by using the relationship of $n_H = 1/(eR_H)$, where e and $R_H$ are free charge and Hall coefficient, respectively, as shown in Fig. 5(a). At first glance, a mountain of carrier concentration $n_H$ is shown near the center of the $Bi_2Te_3$–$Bi_2Se_3$–$Bi_2S_3$ diagram. It is consistent with our observation that

Published on 22 November 2012 on http://pubs.rsc.org | doi:10.1039/C2EE23549H
Downloaded by Boston College on 28 January 2013

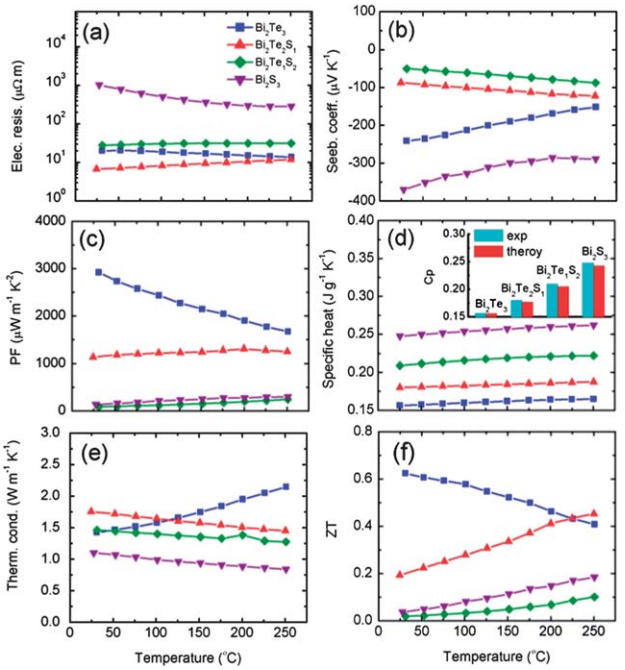


**Fig. 4** Temperature dependent thermoelectric properties of the $Bi_2Te_3$–$Bi_2S_3$ system, (a) electrical resistivity, (b) Seebeck coefficient, (c) power factor, (d) specific heat, (e) thermal conductivity, and (f) figure of merit *ZT*. The inset of figure (d) shows the comparison of specific heat at room temperature between the experimentally measured value and theoretically calculated value.

$Bi_2Te_1Se_1S_1$ has a very low electrical resistivity (6.2 μΩ m at 25 °C) and Seebeck coefficient (−31.5 μV $K^{-1}$ at 25 °C). Another feature is that the carrier concentration of the composition at the edge is higher than that of the compositions at the corners (*i.e.*, $Bi_2Te_3$, $Bi_2Se_3$, and $Bi_2S_3$). Generally, the increased carrier concentration with the substitution of Te in $Bi_2Te_3$ by Se or S results from the increased vacancy at the Te-site of the $Bi_2Te_3$ lattice. Fig. 5(a) shows a similar trend at the $Bi_2Te_3$-rich end. The measured electrical resistivity and Seebeck coefficient, plotted in Fig. 2 and 4, also demonstrate a similar trend. The $n_H$ of $Bi_2Se_3$ is much higher than that of $Bi_2Te_3$, and slightly lower than those of $Bi_2Te_2Se_1$ and $Bi_2TeSe_2$.

According to previous theoretical studies,[32,33] the combination of the carrier mobility and effective mass, *i.e.*, $\mu(m^*/m_0)^{3/2}$, can be an index to determine whether a material is good for the thermoelectric purpose. According to Slack's definition,[34] the parameter $\mu(m^*/m_0)^{3/2}$ is named the weighted carrier mobility $U$, where $\mu$, $m^*$, and $m_0$ are the carrier mobility, the density of states effective mass for the conduction band (or valence band), and the free electron mass, respectively. Generally, a material with heavy $m^*$ usually has low $\mu$. A high value of $U$ usually means a high power factor PF (PF = $S^2\sigma$) at an optimized carrier concentration. Fig. 5(b) plots the weighted carrier mobility for the $Bi_2Te_3$–$Bi_2Se_3$–$Bi_2S_3$ system. Here, the values of $U$ were deduced from the measured Seebeck coefficient and electrical conductivity according to the following equations,[35]

$$S = -\frac{k_B}{e}\left(\frac{(r+5/2)F_{r+3/2}(\xi)}{(r+3/2)F_{r+1/2}(\xi)} - \xi\right), \quad (1)$$

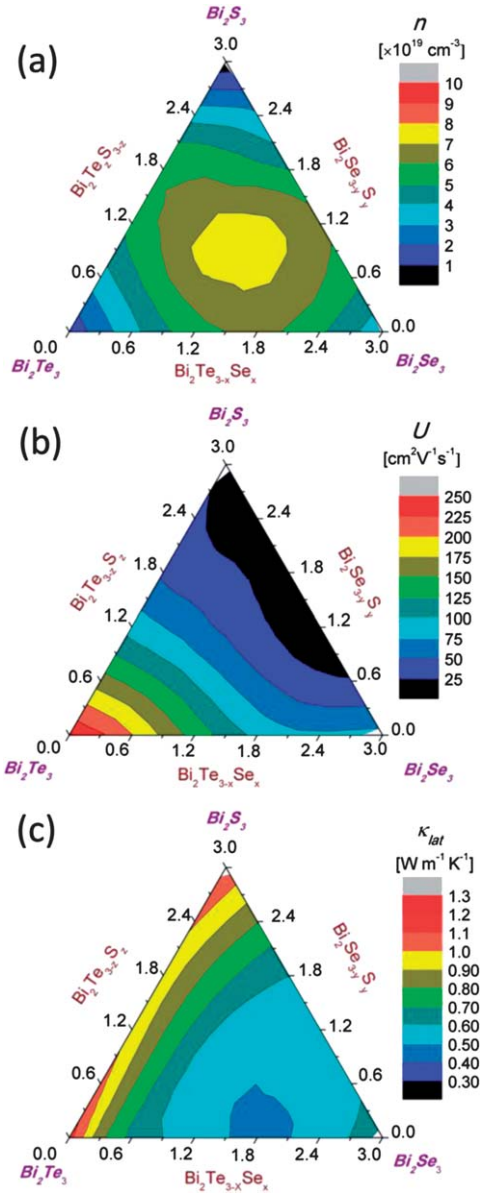


**Fig. 5** (a) Hall carrier concentration, (b) weighted mobility, and (c) lattice thermal conductivity of the $Bi_2Te_3$–$Bi_2Se_3$–$Bi_2S_3$ system.

$$\sigma = 2e\left(\frac{2\pi m_0 k_B T}{h^2}\right)^{3/2}(m^*/m_0)^{3/2}\mu F_{r+1/2}(\xi), \quad (2)$$

$$F_n(\xi) = \int_0^\infty \frac{x^n}{1+e^{(x-\xi)}}\,dx, \quad (3)$$

where the $e$, $r$, $k_B$, and $h$ are the free electron charge, scattering parameter, Boltzmann constant, and Plank constant, respectively. The numerical calculation process of $U$ is to get the reduced Fermi energy $\xi$ from eqn (1), and then to insert $\xi$ into eqn (2) to get $\mu(m^*/m_0)^{3/2}$, with the measured $S$ and $\sigma$, and assumption of acoustic phonon scattering ($r = -1/2$). From Fig. 5(b), it is clearly shown that $Bi_2Te_3$ has the highest weighted

 This journal is © The Royal Society of Chemistry 2013

Published on 22 November 2012 on http://pubs.rsc.org | doi:10.1039/C2EE23549H
Downloaded by Boston College on 28 January 2013

mobility, while the substitutions of Te with Se or S yield a significant decrease in weighted carrier mobility. This phenomenon is in good agreement with the normal observations that $Bi_2Te_3$ has a higher power factor than $Bi_2Se_3$ and $Bi_2S_3$. Polycrystalline samples made by ball milling and hot pressing could have power factors over 3000 $\mu W\ m^{-1}\ K^{-2}$, about ten times higher than that of $Bi_2S_3$ even at an optimized carrier concentration.

Fig. 5(c) shows the lattice thermal conductivity for the $Bi_2Te_3$–$Bi_2Se_3$–$Bi_2S_3$ system. Firstly, the decreased lattice thermal conductivities associated with the alloying effect are seen in all the three subsystems, the valley of the lattice thermal conductivity is located at the mixture region of the rhombohedral and orthorhombic phase for both the $Bi_2Te_3$–$Bi_2S_3$ and $Bi_2Se_3$–$Bi_2S_3$ subsystems. In the $Bi_2Te_3$–$Bi_2Se_3$ system, the minimum value is very close to $Bi_2Te_{1.2}Se_{1.8}$. Secondly, the minimum lattice thermal conductivity value in the $Bi_2Se_3$–$Bi_2S_3$ system is higher than that in the $Bi_2Te_3$–$Bi_2Se_3$ system.

### 3.2 $Bi_2Te_{2.7-x}Se_{0.3}S_x$

Since $Bi_2Te_3$ has high lattice thermal conductivity, partial substitution of Te by Se to form a $Bi_2Te_{3-x}Se_x$ alloy is essential to optimize the *ZT* value. $Bi_2Te_{2.7}Se_{0.3}$ is the classic composition for thermoelectric applications near room temperature. However, the *ZT* value of $Bi_2Te_{2.7}Se_{0.3}$ drops quickly as the temperature becomes higher than 200 °C. We studied the effect of partial replacement of Te with S in the classic composition $Bi_2Te_{2.7}Se_{0.3}$. In these samples, a 0.5 at.% Cu was used to achieve good process repeatability. Fig. 6(a)–(e) show the temperature dependent thermoelectric properties of as-pressed $Bi_2Te_{2.7-x}Se_{0.3}S_x$ with different sulfur doping concentrations ($x = 0$, 0.2, and 0.4). The Seebeck coefficient of $Bi_2Te_{2.7-x}Se_{0.3}S_x$ roughly decreases with increasing sulfur content at room temperature, demonstrating a donor behavior. The possible reason would be the reduced formation energy of Te-site vacancies as sulfur partially substitutes for tellurium of the $Bi_2Te_3$-type crystalline structure. Another notable character of the temperature dependent electrical resistivity and Seebeck coefficient, plotted in Fig. 6(a) and (b), is the peak value ($\rho_{max}$ and $S_{max}$) shift towards higher temperatures. This change is a typical behavior of a suppressed bipolar effect due to the increase of the extrinsic carrier.[36] Owing to the decreasing weighted mobility with the addition of sulfur, a large decrease of power factor was seen near room temperature in $Bi_2Te_{2.7-x}Se_{0.3}S_x$: from 2401 to 1773, and 1255 $\mu W\ m^{-1}\ K^{-2}$ for $x = 0$, 0.2, and 0.4, respectively. Fig. 6(d) is the temperature dependent thermal conductivity of the as-pressed $Bi_2Te_{2.7-x}Se_{0.3}S_x$. Most noticeable is the less bipolar contribution to the thermal conductivity with increasing sulfur content. It is shown that $Bi_2Te_{2.7}Se_{0.3}$ has a quickly rising thermal conductivity as temperature is increased above 150 °C, in contrast, $Bi_2Te_{2.3}Se_{0.3}S_{0.4}$ has a quite slow rise in the whole temperature range from room temperature to 325 °C. As a result, the temperature for the peak *ZT* shifted from 125 °C for $Bi_2Te_{2.7}Se_{0.3}$ ($ZT_{max} \sim 0.8$) to 200 °C for $Bi_2Te_{2.3}Se_{0.3}S_{0.4}$ ($ZT_{max} \sim 0.7$), see Fig. 6(e).

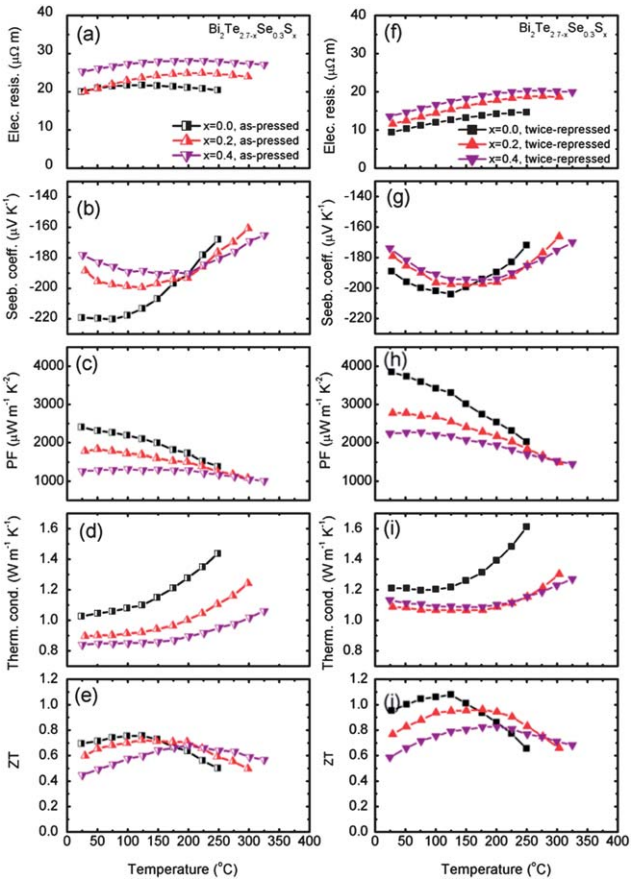


**Fig. 6** Temperature dependent thermoelectric properties of the as-pressed and twice-repressed $Bi_2Te_{2.7-x}Se_{0.3}S_x$ with different sulfur contents ($x = 0$, 0.2, and 0.4).

It was reported that re-orientation of randomly distributed grains helps to achieve a *ZT* enhancement of n-type $Bi_2Te_3$-based thermoelectric materials.[9,11] Here, a twice-repressing process was used to get stronger (00*l*)-texture, in contrast to the previous once-repressing process, and finally higher *ZT* along the direction perpendicular to the press direction. Fig. 6(f)–(j) show the temperature dependent thermoelectric properties of the twice-repressed $Bi_2Te_{2.7-x}Se_{0.3}S_x$ with different amounts of sulfur ($x = 0$, 0.2, and 0.4). When compared with the as-pressed sample, the twice-repressed sample shows a considerable reduction in electrical resistivity due to texturing. Additionally, a slight decrease in the Seebeck coefficient is observed, which is related to the increase of Te vacancies owing to the mechanical deformation during the hot pressing process.[12,37] Benefiting from the enhanced texture, the power factors show significant improvement: from 2401 to 3845 $\mu W\ m^{-1}\ K^{-2}$ for $Bi_2Te_{2.7}Se_{0.3}$ (~60% enhancement) and from 1255 to 2234 $\mu W\ m^{-1}\ K^{-2}$ for $Bi_2Te_{2.3}Se_{0.3}S_{0.4}$ (~78% enhancement). It is worth pointing out that the highest power factor we obtained previously by only once-repressing is about 3390 $\mu W\ m^{-1}\ K^{-2}$. The thermal conductivity of the twice-repressed sample is obviously higher than the as-pressed sample because of the larger contribution from the carriers, as shown in Fig. 6(d) and (i). Even with the higher thermal conductivity, the *ZT* values of all the

Published on 22 November 2012 on http://pubs.rsc.org | doi:10.1039/C2EE23549H
Downloaded by Boston College on 28 January 2013

twice-repressed $Bi_2Te_{2.7-x}Se_{0.3}S_x$ samples are still much higher than those of the as-pressed samples. As an example, the enhancement of the peak $ZT$ value for $Bi_2Te_{2.3}Se_{0.3}S_{0.4}$ is ~14% from ~0.7 (as-pressed) to ~0.8 (twice-repressed). Similarly, $Bi_2Te_{2.7}Se_{0.3}$ shows an even larger enhancement of ~38% from ~0.8 (as-pressed) to ~1.1 (twice-repressed). Furthermore, the temperature dependent $ZT$ curve for $Bi_2Te_{2.3}Se_{0.3}S_{0.4}$ in the range of 200 to 325 °C is quite flat with an average value larger than 0.7, which could be a candidate to push the hot side temperature of the current STEG from ~200 °C to ~325 °C.

### 3.3 $Bi_2Se_1S_2$ and $Bi_2Te_2S_1$

Goldsmid has developed a simple formula to estimate the band gap of a semiconductor from the peak Seebeck coefficient and corresponding temperature, *i.e.*, $E_G = 2eS_{max}T$.[38] This simple relationship is applied to the $Bi_2Te_3$–$Bi_2Se_3$–$Bi_2S_3$ system. Band-gap ($E_G$) enlargement was observed from $Bi_2Te_3$ to $Bi_2Se_3$, and to $Bi_2S_3$. $Bi_2Te_2S_1$ ($E_G = 0.20$ eV) and $Bi_2Se_1S_2$ ($E_G = 0.34$ eV) show promising thermoelectric applications at temperatures up to 300–500 °C.

Fig. 7 shows the temperature dependent thermoelectric properties of these two new compounds: $Bi_2Se_1S_2$ and $Bi_2Te_2S_1$. Here 0.05–3 at.% Cu is used to optimize the carrier concentration. For $Bi_2Se_1S_2$, the increased electrical resistivity and Seebeck coefficient with temperature suggest a behavior of heavily doped semiconductor. Furthermore, a power factor of 603 μW m$^{-1}$ K$^{-2}$ at 500 °C is obtained in $Bi_2Se_1S_2$, which nearly is double when compared with the optimized $Bi_2S_3$ made by a similar powder metallurgy method. The thermal conductivity of $Bi_2Se_1S_2$ continuously decreases with increasing temperature without any notable bipolar effect. The larger band gap of $Bi_2Se_1S_2$, when compared with $Bi_2Te_3$, is the direct reason for the negligible bipolar thermal conductivity. Benefited from the enlarged band gap, the heavily doped $Bi_2Se_1S_2$ shows a continuous increase in $ZT$ value with increasing temperature from room temperature to 500 °C. A value of ~0.8 at 500 °C is obtained in this Te-free $Bi_2Se_1S_2$ sample, which corresponds to ~33% enhancement over a reported $Bi_2S_3$ ingot.[23] This value makes $Bi_2Se_1S_2$ competitive with PbS[39] and half-Heusler.[40] Another compound, $Bi_2Te_2S_1$, has a much higher power factor than that of $Bi_2Se_1S_2$ because of its higher weighted mobility (as shown in Fig. 5(b)). $Bi_2Te_2S_1$ shows a peak $ZT \sim 0.8$ near 300 °C, which indicates its promise to fill the temperature gap for power generation between $Bi_2Te_3$ and $Bi_2Se_1S_2$.

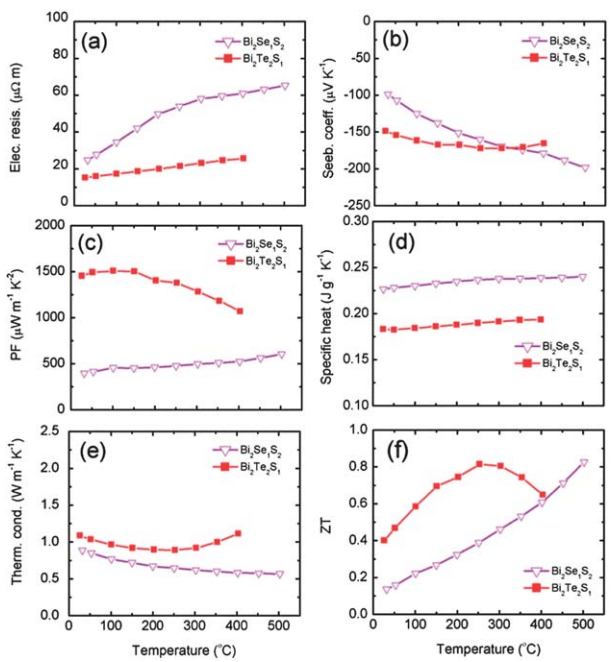


**Fig. 7** Temperature dependent thermoelectric properties of the $Bi_2Se_1S_2$ and $Bi_2Te_2S_1$.

### 3.4 Power generation efficiency of segmented legs

For an ideal thermoelectric converter with constant material properties, the leg efficiency from thermal to electric power ($\eta_{te}$) is governed by the Carnot efficiency and a $ZT$ related factor through a relationship,[38]

$$\eta_{te} = \frac{T_h - T_c}{T_h}\left(\frac{\sqrt{1+Z\bar{T}}-1}{\sqrt{1+Z\bar{T}}+\frac{T_c}{T_h}}\right), \quad (4)$$

where $T_h$ and $T_c$ are the temperatures of hot side and cold side, respectively, $\bar{T}$ is the average temperature between $T_h$ and $T_c$. When the temperature-dependent properties are considered, $Z\bar{T}$ in eqn (4) can be replaced by the average $ZT$ over the whole temperature range from $T_c$ to $T_h$ to provide an estimate of the leg efficiency. Two more accurate methods for calculating the efficiency of a leg with temperature-dependent material properties have been described by Snyder and Ursell,[41] and by Mahan.[42] In this study the discretization method of Mahan is used. The heat flow in the leg is assumed to be one-dimensional, and losses from the sidewalls of the leg are neglected such that Mahan's discretization equations are used, as well as the corresponding discretization for the voltage in the leg:

$$\frac{dT}{dx} = \frac{JST - q}{k}, \quad (5)$$

$$\frac{dq}{dx} = \rho J^2 + JS\frac{dT}{dx}, \quad (6)$$

$$\frac{dV}{dx} = -\rho J - S\frac{dT}{dx}, \quad (7)$$

where $J$ is the current density, $q$ is the heat flux density, $\rho$ is the electrical resistivity, and $V$ is the voltage, $S$ is the Seebeck coefficient, and $T$ is the temperature. These equations are solved iteratively to match the temperature boundary conditions at a given current density, $J$. The efficiency is calculated as the electrical power out divided by the heat flux into the leg:

$$\eta_{leg} = \frac{J(V_c - V_h)}{q_h}. \quad (8)$$

The current density is then optimized to maximize the efficiency of the leg.

 This journal is © The Royal Society of Chemistry 2013

Published on 22 November 2012 on http://pubs.rsc.org | doi:10.1039/C2EE23549H
Downloaded by Boston College on 28 January 2013

The best material presented in this paper for high-temperature applications is $Bi_2Se_1S_2$. When the performance of this leg between two heat reservoirs at 500 °C and 25 °C is calculated (*via* Mahan's method), the efficiency is 7.1%. One of the reasons for the low efficiency is the low *ZT* at lower temperatures. However, other materials in this paper have *ZT*s greater than that of $Bi_2Se_1S_2$ over various portions of the aforementioned temperature range. Therefore an interesting solution would be to use a segmented leg. The segmented leg, shown in Fig. 8(a), comprises the following segments: $Bi_2Te_{2.7}Se_{0.3}$ for 25–175 °C, $Bi_2Te_{2.5}Se_{0.3}S_{0.2}$ for 175–250 °C, $Bi_2Te_2S_1$ for 250–400 °C, and $Bi_2Se_1S_2$ for 400–500 °C. When such segments are used, the efficiency of the leg is 12.5%. The wide variety of material properties that exist within the $Bi_2Te_3$–$Bi_2Se_3$–$Bi_2S_3$ system provide opportunities for high-efficiency thermoelectric energy conversion.

For comparison, the *ZT* values of the state-of-the-art (SOA) thermoelectric materials are also plotted in Fig. 8(b), which include PbTe:La,[43] PbSe:Al,[44] PbS:Cl,[39] filled-skutterudites,[45] and half Heuslers.[40] The 12.5% efficiency of the segmented leg based on $Bi_2Te_3$–$Bi_2Se_3$–$Bi_2S_3$ materials compares well with those of other thermoelectric materials over the same temperature range: PbTe:La (6.7%), PbSe:Al (9.4%), PbS:Cl (4.6%), filled skutterudites (13.1%), and half-Heuslers (8.4%), as shown in Fig. 8(c). It is worth pointing out that the peak *ZT* of our segmented leg is only ~1.1 at 125 °C, while PbTe:La and filled skutterudites have much higher *ZT* values of ~1.6 at 500 °C (ref. 43) and ~1.7 at 580 °C,[45] respectively. Our study further demonstrates that achieving a high *ZT* across the entire temperature range is as important for efficiency as achieving a high peak *ZT*. Since thermoelectric devices must contain both n-type and p-type legs, a p-type leg with comparable efficiency is needed in order to achieve a device efficiency of 12.5%. Exploring the corresponding p-type $(Bi, Sb)_2(Te, Se, S)_3$-based legs could result in a lead-free substitute for p-type PbTe-based materials.[46–48]

Our study already clearly shows the promise to replace some toxic lead-containing materials by $Bi_2Te_3$–$Bi_2Se_3$–$Bi_2S_3$ based materials for medium temperature applications. However, it is worth pointing out that the metallization and thermal stability of these compositions need to be investigated before considering them for real industrial applications. Although the repeated measurement of the same sample shows good thermal stability for all the samples, the long-time thermal stability especially under a large temperature gradient has to be to studied.

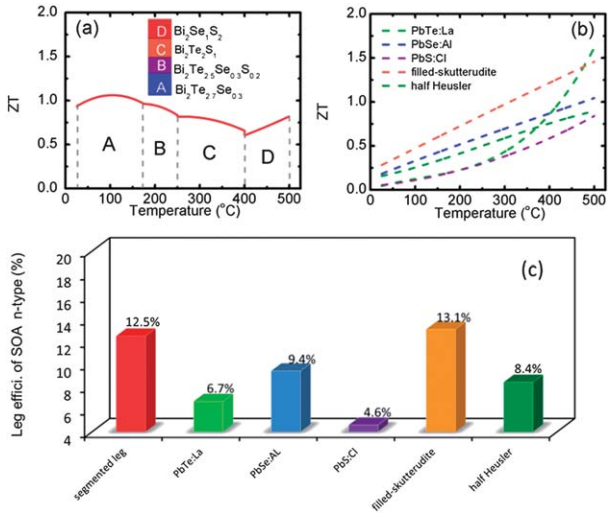


**Fig. 8** (a) Temperature dependent *ZT* value of the segmented leg made from the $Bi_2(Te, Se, S)_3$-based materials, (b) temperature dependent *ZT* of the single leg made of the state-of-the-art (SOA) thermoelectric materials, (c) comparison of leg efficiency between the $Bi_2(Te, Se, S)_3$-based segmented leg with a SOA single leg at $T_c = 25$ °C and $T_h = 500$ °C.

## 4 Conclusions

A systematic study has been conducted on the $Bi_2Te_3$–$Bi_2Se_3$–$Bi_2S_3$ system. $Bi_2Te_3$ has the highest weighted mobility among all compositions, which corresponds to a high power factor. The lattice thermal conductivity map shows a minimum near $Bi_2Te_{1.2}Se_{1.8}$, owing to the strong alloy scattering of the phonon transport. The peak *ZT* of the classic n-type composition $Bi_2Te_{2.7}Se_{0.3}$ could be shifted from 125 to 275 °C by partially substituting Te with S. The temperature dependent *ZT* curve for $Bi_2Te_{2.3}Se_{0.3}S_{0.4}$ in the range of 200 to 325 °C is quite flat with an average value larger than 0.7. Additionally, two compounds, *i.e.*, $Bi_2Te_2S_1$ (*ZT* ~ 0.8 at 300 °C) and $Bi_2Se_1S_2$ (*ZT* ~ 0.8 at 500 °C), are promising for medium temperature power generation application. A segmented leg based on $Bi_2Te_{2.7}Se_{0.3}$ for 25–175 °C, $Bi_2Te_{2.5}Se_{0.3}S_{0.2}$ for 175–250 °C, $Bi_2Te_2S_1$ for 250–400 °C, and $Bi_2Se_1S_2$ for 400–500 °C has shown a leg efficiency of 12.5% when the appropriate p-type leg is paired, which competes well with the state-of-the-art thermoelectric materials in the same temperature range, such as PbTe, PbSe, PbS, filled-skutterudite, and half Heusler, for application in solar-thermal to electrical power generation.

## Acknowledgements

This work is supported by "Solid State Solar-Thermal Energy Conversion Center ($S^3$TEC)", an Energy Frontier Research Center funded by the U.S. Department of Energy, Office of Science, Office of Basic Energy Science under award number DE-SC0001299/DE-FG02-09ER46577 (GC and ZFR).

## References

1 J. R. Drabble and C. H. L. Goodman, *J. Phys. Chem. Solids*, 1958, **5**, 142–144.
2 H. J. Goldsmid, *J. Appl. Phys.*, 1961, **32**, 2198–2202.
3 J. Jiang, L. D. Chen, S. Q. Bai, Q. Yao and Q. Wang, *Scr. Mater.*, 2005, **52**, 347–351.
4 X. B. Zhao, X. H. Ji, Y. H. Zhang, T. J. Zhu, J. P. Tu and X. B. Zhang, *Appl. Phys. Lett.*, 2005, **86**, 062111.
5 J. L. Cui, H. F. Xue, W. J. Xiu, L. Jiang and P. Z. Ying, *Solid State Sci.*, 2006, **179**, 3751–3755.
6 L. D. Zhao, B. P. Zhang, J. F. Li, H. L. Zhang and W. S. Liu, *Solid State Sci.*, 2008, **10**, 651–658.

Published on 22 November 2012 on http://pubs.rsc.org | doi:10.1039/C2EE23549H
Downloaded by Boston College on 28 January 2013

7 B. Poudel, Q. Hao, Y. Ma, Y. C. Lan, A. Minnich, B. Yu, X. Yan, D. Z. Wang, A. Muto, D. Vashaee, X. Y. Chen, J. M. Liu, M. S. Dresselhaus, G. Chen and Z. F. Ren, *Science*, 2008, **320**, 634–638.
8 Y. Ma, Q. Hao, B. Poudel, Y. C. Lan, B. Yu, D. Z. Wang, G. Chen and Z. F. Ren, *Nano Lett.*, 2008, **8**, 2580–2584.
9 L. D. Zhao, B. P. Zhang, W. S. Liu and J. F. Li, *J. Appl. Phys.*, 2009, **105**, 023704–023706.
10 W. J. Xie, J. He, H. J. Kang, X. F. Tang, S. Zhu, M. Laver, S. Y. Wang, J. R. D. Copley, C. M. Brown, Q. J. Zhang and T. M. Tritt, *Nano Lett.*, 2010, **10**, 3283–3289.
11 X. Yan, B. Poudel, Y. Ma, W. S. Liu, G. Joshi, H. Wang, Y. C. Lan, D. Z. Wang, G. Chen and Z. F. Ren, *Nano Lett.*, 2010, **10**, 3373–3378.
12 W. S. Liu, Q. Y. Zhang, Y. C. Lan, S. Chen, X. Yan, Q. Zhang, H. Wang, D. Z. Wang, G. Chen and Z. F. Ren, *Adv. Energy Mater.*, 2011, **1**, 577–587.
13 K. McEnaney, D. Kraemer, Z. F. Ren and G. Chen, *J. Appl. Phys.*, 2011, **110**, 074502–074506.
14 D. Kraemer, B. Poudel, H. P. Feng, J. C. Caylor, B. Yu, X. Yan, Y. Ma, X. W. Wang, D. Z. Wang, A. Muto, K. McEnaney, M. Chiesa, Z. F. Ren and G. Chen, *Nat. Mater.*, 2012, **10**, 532–538.
15 N. K. Stark, T. E. Svechnikov and S. N. Chizhevskaya, *Inorg. Mater.*, 1985, **21**, 328–331.
16 H. Sherrer and S. Scherrer, Bismuth telluride, antimony telluride, and their solid solutions, in *CRC Thermoelectric Handbook*, ed. D. M. Rowe, CRC Press, Boca Raton, 1995.
17 T. S. Oh, D. B. Hyun and N. V. Kolomoets, *Scr. Mater.*, 2000, **42**, 849–854.
18 L. V. Prokofieva, D. A. Pshenay-Severin, P. P. Konstantinov and A. A. Shabaldin, *Semiconductors*, 2009, **43**, 937–976.
19 A. Saji, S. Ampili, S. H. Yang, K. J. Ku and M. Elizabeth, *J. Phys.: Condens. Matter*, 2005, **17**, 2873–2888.
20 L. D. Zhao, B. P. Zhang, W. S. Liu, H. L. Zhang and J. F. Li, *J. Solid State Chem.*, 2008, **181**, 3278–3282.
21 Z. H. Ge, B. P. Zhang, Z. X. Yu and J. F. Li, *J. Mater. Res.*, 2011, **26**, 2711–2718.
22 Z. H. Ge, B. P. Zhang, Y. Liu and J. F. Li, *Phys. Chem. Chem. Phys.*, 2012, **14**, 4475–4481.
23 K. Biswas, L. D. Zhao and M. G. Kanatzidis, *Adv. Energy Mater.*, 2012, **2**, 634–638.
24 N. J. Cook, C. L. Ciobanu, T. Wagner and C. J. Stanley, *Can. Mineral.*, 2007, **45**, 665–708.
25 H. F. Liu, C. R. Knowles and L. L. Y. Chang, *Can. Mineral.*, 1995, **33**, 115–128.
26 J. F. Li, W. S. Liu, L. D. Zhao and M. Zhou, *NPG Asia Mater.*, 2010, **2**, 152–158.
27 W. S. Liu, X. Yan, G. Chen and Z. F. Ren, *Nano Energy*, 2012, **1**, 42–56.
28 J. Horák, J. Navrátil and Z. Starý, *J. Phys. Chem. Solids*, 1992, **53**, 1067–1072.
29 J. Callaway and H. C. von Baeyer, *Phys. Rev.*, 1960, **120**, 1149–1154.
30 B. Abeles, *Phys. Rev.*, 1963, **131**, 1906–1911.
31 W. Wong-Ng, H. Joress, J. Martin, P. Y. Zavalij, Y. Yan and J. Yang, *Appl. Phys. Lett.*, 2012, **100**, 082107.
32 H. J. Goldsmid, *Electronic Refrigeration*, Pion Ltd, London, 1986.
33 G. D. Mahan, *J. Appl. Phys.*, 1989, **65**, 1578–1583.
34 G. A. Slack, New materials and performance limits for thermoelectric cooling, in *CRC Thermoelectric Handbook*, ed. D. M. Rowe, CRC Press, Boca Raton, 1995.
35 W. S. Liu, B. P. Zhang, L. D. Zhao and J. F. Li, *Chem. Mater.*, 2008, **20**, 7526–7531.
36 W. S. Liu, B. P. Zhang, J. F. Li, H. L. Zhang and L. D. Zhao, *J. Appl. Phys.*, 2007, **102**, 103717.
37 J. M. Schultz, J. P. McHugh and W. A. Tiller, *J. Appl. Phys.*, 1962, **33**, 2443–2450.
38 H. J. Goldsmid, *Introduction to thermoelectricity*, Springer-Verlag, Berlin Heidelberg, 2010.
39 L. D. Zhao, S. H. Lo, J. Q. He, H. Li, K. Biswas, J. Androulakis, C. I. Wu, T. P. Hogan, D. Y. Chung, V. P. Dravid and M. G. Kanatzidis, *J. Am. Chem. Soc.*, 2011, **133**, 20476–20487.
40 G. Joshi, X. Yan, H. Z. Wang, W. S. Liu, G. Chen and Z. F. Ren, *Adv. Energy Mater.*, 2011, **1**, 643–647.
41 G. J. Snyder and T. S. Ursell, *Phys. Rev. Lett.*, 2003, **91**, 148021–148024.
42 G. D. Mahan, *J. Appl. Phys.*, 1991, **70**, 4551–4554.
43 Y. Z. Pei, J. Lensch-Falk, E. S. Toberer, D. L. Medlin and G. J. Snyder, *Adv. Funct. Mater.*, 2011, **21**, 241–249.
44 Q. Y. Zhang, H. Wang, W. S. Liu, H. Z. Wang, B. Yu, Q. Zhang, Z. T. Tian, G. Ni, S. Lee, K. Esfarjani, G. Chen and Z. F. Ren, *Energy Environ. Sci.*, 2012, **5**, 5246–5251.
45 X. Shi, J. Yang, J. R. Salvador, M. F. Chi, J. Y. Cho, H. Wang, S. Q. Bai, J. H. Yang, W. Q. Zhang and L. D. Chen, *J. Am. Chem. Soc.*, 2011, **133**, 7837–7846.
46 Y. Z. Pei, X. Y. Shi, A. LaLonde, H. Wang, L. D. Chen and G. J. Snyder, *Nature*, 2011, **473**, 66–69.
47 Q. Zhang, F. Cao, W. S. Liu, K. Lukas, B. Yu, S. Chen, C. Opeil, D. Broido, G. Chen and Z. F. Ren, *J. Am. Chem. Soc.*, 2012, **134**, 10031–10038.
48 K. Biswas, J. Q. He, Q. C. Zhang, G. Y. Wang, C. Uher, V. P. Dravid and M. G. Kanatzidis, *Nat. Chem.*, 2011, **3**, 160–166.

 This journal is © The Royal Society of Chemistry 2013

NANO LETTERS

Letter

pubs.acs.org/NanoLett

# Enhancement of Thermoelectric Properties by Modulation-Doping in Silicon Germanium Alloy Nanocomposites

Bo Yu,[†,∥] Mona Zebarjadi,[‡,∥] Hui Wang,[†] Kevin Lukas,[†] Hengzhi Wang,[†] Dezhi Wang,[†] Cyril Opeil,[†] Mildred Dresselhaus,[§] Gang Chen,*[,‡] and Zhifeng Ren*[,†]

[†]Department of Physics, Boston College, Chestnut Hill, Massachusetts 02467, United States

[‡]Department of Mechanical Engineering and [§]Department of Electrical Engineering and Computer Science, Massachusetts Institute of Technology, Cambridge, Massachusetts 02139, United States

**ABSTRACT:** Modulation-doping was theoretically proposed and experimentally proved to be effective in increasing the power factor of nanocomposites $(Si_{80}Ge_{20})_{70}(Si_{100}B_5)_{30}$ by increasing the carrier mobility but not the figure-of-merit (ZT) due to the increased thermal conductivity. Here we report an alternative materials design, using alloy $Si_{70}Ge_{30}$ instead of Si as the nanoparticles and $Si_{95}Ge_5$ as the matrix, to increase the power factor but not the thermal conductivity, leading to a ZT of 1.3 ± 0.1 at 900 °C.

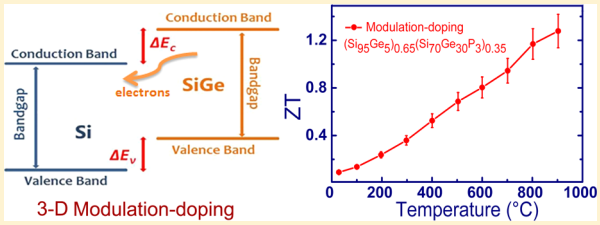


**KEYWORDS:** *Modulation-doping, thermoelectrics, nanocomposite, silicon germanium (SiGe), dimensionless figure-of-merit*

The performance of thermoelectric materials depends on their dimensionless thermoelectric figure-of-merit ZT = $(S^2\sigma/\kappa)T$, where $S$ is the Seebeck coefficient, $\sigma$ the electrical conductivity, $\kappa$ the thermal conductivity, and $T$ the absolute temperature at which the properties are measured. The numerator $S^2\sigma$ is called the power factor.[1] It is generally recognized that for the next generation of thermoelectric materials, strategies to enhance the power factor[2−4] are essential in addition to those to decrease the thermal conductivity.

Silicon germanium (SiGe) alloys are suitable candidates for high-temperature thermoelectric applications because of their reasonably good thermoelectric properties and superior long-term reliability at elevated temperatures. Consequently, SiGe thermoelectric modules with a material ZT of 0.5 (p-type) and 0.9 (n-type) have been used in space radioisotope thermoelectric generators (RTGs) by United States NASA since 1976.[1] New applications, especially heat conversion at high temperatures, demand higher ZTs for such material applications. Recently, a good enhancement in ZT values has been demonstrated for both n- and p-type SiGe alloys by using a nanocomposite approach.[5−8] The lattice thermal conductivity of the nanocomposite samples is much lower compared to that of their equivalent large crystalline bulk materials because of the much increased grain boundaries of the numerous nanograins that effectively scatter long wavelength phonons. Using this approach, the peak ZT value of p-type nanostructured $Si_{80}Ge_{20}B_5$ samples was improved from 0.5 to 0.95,[5] and that of n-type $Si_{80}Ge_{20}P_2$ from 0.93 to around 1.3.[6] However, these materials contain a fairly high concentration of Ge that is about a hundred times more expensive than Si. In 2009, Zhu et al. reported[7] that by using the nanocomposite approach, only a 5% Ge replacement of Si is sufficient to further reduce the thermal conductivity of n-type nano-Si by a factor of 2, resulting in a ZT peak value of 0.94 in $Si_{95}Ge_5$ doped with GaP and P at ∼900 °C, and this result is significant since a much smaller amount of expensive Ge is used. Furthermore, if Ge is entirely eliminated, the ZT peak of pure nano-Si would drop to about 0.7 at around 1000 °C.[9] Clearly there is a trade-off between the cost and the performance of $Si_{1-x}Ge_x$ alloys.

Recently, we introduced a three-dimensional (3-D) modulation-doping approach[10] to improve the power factor of thermoelectric nanocomposites by mainly increasing the mobility. Modulation-doping has been widely used in thin-film semiconductors that separate the charge carriers from the ionized dopants to reduce the charge scattering and to increase the carrier mobility, thus increasing the electrical conductivity as a consequence.[11−13] The proposed modulation-doped sample is a two-phase nanocomposite made out of two different types of nanograins. Rather than uniformly doping the sample, dopants are incorporated into only one type of nanograins. Charge carriers spill over from the doped nanograins to the undoped or lightly doped matrix phase, leaving behind ionized nanograins. Instead of the usually heavy uniform doping in thermoelectric materials, causing strong ionized impurity scattering of charges, ionized nanoparticles can be spatially placed much further apart in the modulation-doping scheme, leading to reduced electron scattering for higher mobility. Traditionally, molecular beam epitaxy (MBE) was used to grow these thin layers, consisting of an undoped conducting layer (channel), a doped layer that donates carriers, and an undoped spacer layer separating the ionized dopants from the conducting channel. Adapting such a concept, our study[10] theoretically and experimentally demonstrated that

**Received:** January 24, 2012
**Revised:** March 6, 2012
**Published:** March 21, 2012

 © 2012 American Chemical Society  dx.doi.org/10.1021/nl3003045 | *Nano Lett.* 2012, 12, 2077−2082

modulation-doping is also effective in 3-D bulk nanocomposite systems by improving the mobility, thus the power factor. The power factor of the p-type $Si_{86}Ge_{14}B_{1.5}$ uniform sample was improved by 40% using the modulation-doping approach achieved by using a 30% fraction of $Si_{100}B_5$ nanograins in the intrinsic $Si_{80}Ge_{20}$ matrix to make a modulation-doped sample: $(Si_{80}Ge_{20})_{0.7}(Si_{100}B_5)_{0.3}$.[10] A smaller improvement of about 20% was observed in the power factor of a n-type sample $(Si_{80}Ge_{20})_{0.8}(Si_{100}P_3)_{0.2}$ compared to its equivalent uniform nanocomposite $Si_{84}Ge_{16}P_{0.6}$.[10] However, the ZTs were not increased due to the high thermal conductivities of the pure Si nanoparticles.

The modulation-doping scheme produced enhancement in electrical conductivity, leading to the increase in the electronic part of the thermal conductivity. Such an increase in the electronic part is inevitable because charge carriers are also heat carriers. At the same time, the increase in the lattice part is also unavoidable since the nanoparticles Si have a much higher thermal conductivity. Ideally, we want to maintain the low thermal conductivity of the nanostructured materials. Therefore modulation-doping scheme should be also focused on strategies to reduce the lattice part of the thermal conductivity. Here, we report our success on simultaneously improving the power factor and reducing the lattice part of the thermal conductivity by a new materials design and band alignment in the scheme of modulation-doping by using $Si_{95}Ge_5$ as the matrix (instead of $Si_{80}Ge_{20}$, lower Ge concentration not only increase the mobility but also reduce the cost) and $Si_{70}Ge_{30}P_3$ as the nanoparticles that have a much lower thermal conductivity, to eventually enhance the ZT.

Ideally, for modulation-doping in bulk nanocomposites, one wants to choose nanoparticles with a low density of states compared to the matrix. The nanoparticles should also form proper band alignments with the matrix to promote the flow of carriers from the nanoparticles into the matrix.[14] In this study, we have chosen $Si_{70}Ge_{30}P_3$ as the doped nanoparticle for two reasons: good band alignment and low thermal conductivity. It is known that SiGe and Si can form either type I or type II band alignment in thin-film heterostructures (Figure 1).[13,15] In

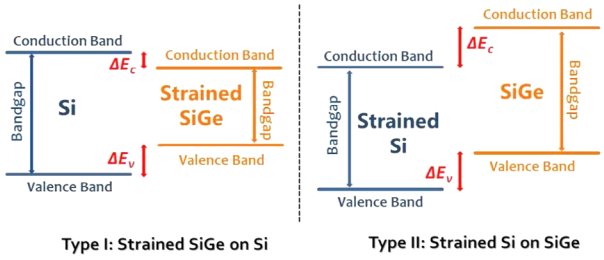


**Figure 1.** Type I (strained SiGe on Si) and type II (strained Si on SiGe) band alignments.

nanocomposites, it is difficult to determine the band alignment because such composites are obtained by consolidating two types of crystal grains into a bulk 3-D material instead of growing atomic layers one by one. Both types of grains might be under tension, and the possible dangling bonds, impurities, and trapped charges at the interfaces might all affect the final band alignment. For n-type materials, the nanoparticles should have relatively higher conduction band edges compared to the matrix grains, forcing the carriers to flow into the matrix. For our materials design, we accept type II band alignment, which is the case for the Si/Ge interface,[16] and therefore we chose nanoparticle grains containing more Ge compared to the matrix. From our experimental observations, which will be shown later, one can conclude that the band discontinuity in our case is type II and is large enough for the purpose of modulation-doping. Moreover, a larger density of states effective mass (mainly due to the larger valley degeneracy of Si compared to Ge) in the Si-rich matrix ($Si_{95}Ge_5$) compared to the selected nanoparticles leads to more available energy states for the carriers to fill.

For the consideration of the thermal conductivity, $Si_{70}Ge_{30}$ has the lowest thermal conductivity among $Si_{1-x}Ge_x$ alloys.[17] Using $Si_{70}Ge_{30}P_3$ composition as the nanoparticles then has clearly a big advantage in our experiment; as we increase the nanoparticle molar fraction, the thermal conductivity decreases and the electrical conductivity increases simultaneously.

The alloyed $Si_{1-x}Ge_x$ nanopowders were prepared by ball milling pure elements of Si, Ge, and P for about 10 h in a high-energy ball mill and then mixed in the container according to the designed molar ratio for a very short time (several minutes). Finally the powder mixtures were consolidated rapidly into 12.7 mm disks in a graphite die by a dc hot press method. The sample density was measured by the Archimedean method, and all samples reported here have densities close to the theoretical values (Table 1). We measured the electrical conductivity and the Seebeck coefficient using a commercial four-probe system (ULVAC, ZEM-3) and using 2 × 2 × 12 mm bars cut from the disks. The thermal diffusivity was measured directly on these disks by laser flash (NETZSCH LFA 457), and the specific heat was measured by differential scanning calorimetry (DSC, NETZSCH 404C). All experiments were repeated a few times, and the data are within the measurement errors (3% for electrical conductivity, thermal diffusivity, and specific heat, 4% for thermal conductivity, and 5% for Seebeck coefficient, resulting in an uncertainty of 11% for the ZT values). Room temperature Hall measurements were performed on polished thin bulk samples using a physical properties measurement system (PPMS) from Quantum Design with typical sample dimensions of 0.5 × 2 × 11 mm. The hot-pressed samples were also cut, polished, and then ion milled for microstructure study using transmission electron microscope (TEM, JEOL JSM2010F) techniques.

We study the thermoelectric properties of the proposed modulation-doped $(Si_{95}Ge_5)_{1-x}(Si_{70}Ge_{30}P_3)_x$ as a function of nanoparticle molar fraction, $x$. For comparison purposes, we also prepared composition equivalent uniform samples as

**Table 1. Theoretical and Measured Densities of As-Prepared Silicon Germanium Nanocomposite Samples**

| | modulation doped (NPs molar fraction) | | | | | equivalent uniform | | | | | uniform |
|---|---|---|---|---|---|---|---|---|---|---|---|
| sample type | 5% | 15% | 25% | 35% | 45% | 5% | 15% | 25% | 35% | 45% | $Si_{95}Ge_5P_2$ |
| theoretical (g cm$^{-3}$) | 2.517 | 2.592 | 2.666 | 2.741 | 2.816 | 2.517 | 2.592 | 2.666 | 2.741 | 2.816 | 2.480 |
| measured (g cm$^{-3}$) | 2.505 | 2.596 | 2.662 | 2.731 | 2.813 | 2.511 | 2.590 | 2.671 | 2.728 | 2.815 | 2.482 |
| percentage (%) | 99.5 | 100.2 | 99.8 | 99.6 | 99.9 | 99.8 | 99.9 | 100.2 | 99.5 | 100.0 | 100.1 |


dx.doi.org/10.1021/nl3003045 | Nano Lett. 2012, 12, 2077−2082

references: $Si_{93.75}Ge_{6.25}P_{0.15}$, $Si_{91.25}Ge_{8.75}P_{0.45}$, $Si_{88.75}Ge_{11.25}P_{0.75}$, $Si_{86.25}Ge_{13.75}P_{1.05}$, and $Si_{83.75}Ge_{16.25}P_{1.35}$. Figure 2a shows the

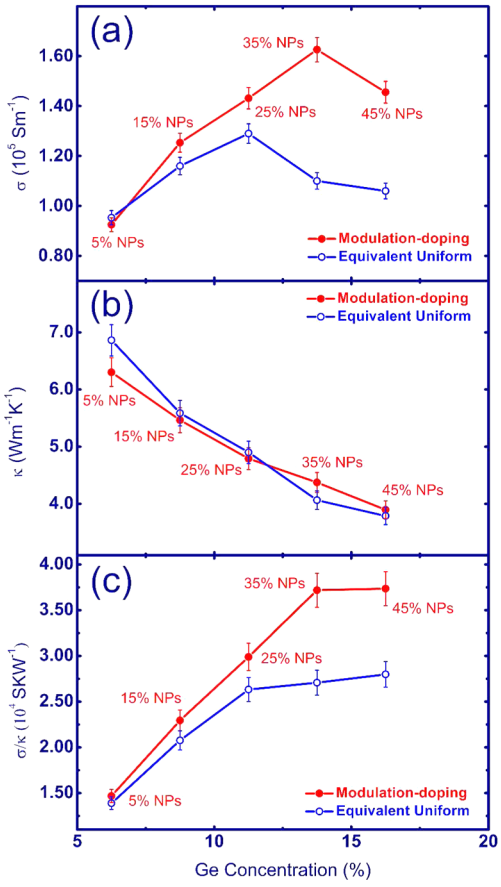


**Figure 2.** (a) Electrical conductivity $\sigma$, (b) thermal conductivity $\kappa$, and (c) $\sigma/\kappa$ ratio of modulation-doped $Si_{1-x}Ge_x$ nanocomposite samples as a function of Ge concentration, in comparison with those of equivalent uniform compositions.

electrical conductivity at room temperature as a function of Ge concentration. In modulation-doped samples, a fairly good electrical conductivity $\sigma$ of $9.25 \times 10^4$ S m$^{-1}$ is achieved with even only 5% nanoparticles and $\sigma$ continues to rise with increasing nanoparticle ratio. When we increase the molar fraction of nanoparticles, more carriers are introduced into the matrix to increase the electrical conductivity through modulation-doping. However, at the same time, these nanoparticles also introduce excessive interfaces and a larger static potential barrier (when compared to ionized impurity atoms) to scatter the electrons, which negatively affect the electrical conductivity. So when the nanoparticle molar fraction increases to more than 35%, the electrical conductivity starts to decrease, as shown in Figure 2a. Similar trends are observed in the equivalent samples. However, for the equivalent samples, the electrical conductivity starts to decrease at lower Ge molar fractions, and the peak value of the electrical conductivity in this series of samples is much lower than that of the modulation-doped samples. When the nanoparticle molar fraction is 35%, the electrical conductivity of the modulation-doped sample has the highest value of $1.63 \times 10^5$ S m$^{-1}$ (54% higher compared to the corresponding equivalent uniform composition $Si_{86.25}Ge_{13.75}P_{1.05}$). This electrical conductivity value is also much higher than that of our previously reported data[10] with a similar composition, indicating that the current materials design is more favorable for n-type $Si_{1-x}Ge_x$ samples. We should point out that the mobility of our best sample with 35% nanoparticles at room temperature is 36.42 cm$^2$ V$^{-1}$ s$^{-1}$, which is much higher compared to its uniform counterpart $Si_{86.25}Ge_{13.75}P_{1.05}$ with a mobility of 24.26 cm$^2$ V$^{-1}$ s$^{-1}$, while the carrier concentration stays almost the same at around $2.78 \times 10^{20}$ cm$^{-3}$ in both samples. Surprisingly, the mobility of the modulation-doped samples is also higher than that (29.21 cm$^2$ V$^{-1}$ s$^{-1}$) of the uniform nanocomposite $Si_{95}Ge_5P_2$ (optimally doped matrix) that has much less Ge, further proving the advantage of our current materials designing approach.

For the thermal conductivity $\kappa$ (Figure 2b), unlike our previous study[10] in which the thermal conductivity increased largely with the addition of nanoparticles (pure Si was used), here it is natural that $\kappa$ rapidly goes down as the ratio of nanoparticles increases, since the doped nanoparticles are less thermally conductive than the matrix. The lowest room temperature thermal conductivity reaches about 3.90 W m$^{-1}$ K$^{-1}$ at the highest nanoparticle molar ratio (45%), equivalent to a composition of $Si_{83.75}Ge_{16.25}P_{1.35}$. Comparing to the equivalent uniform sample, modulation-doped samples have higher electronic thermal conductivities because of their higher electrical conductivities. For example, for the 45% volume fraction of nanoparticles, the electronic part of the thermal conductivity is around 1 W m$^{-1}$ K$^{-1}$ using the Wiedemann–Franz law assuming a Lorenz number of $2.44 \times 10^{-8}$ W Ω K$^{-2}$, while that of the equivalent sample is only 0.7 W m$^{-1}$ K$^{-1}$. In this study, we were able to maintain the total thermal conductivity of the modulation-doped sample as low as those of the single-phase equivalent samples, which means that the lattice part of the thermal conductivity in our modulation-doped nanocomposite sample is lower than its equivalent single-phase sample.

Figure 2c shows the ratio $\sigma/\kappa$ (at room temperature) dependence of the Ge concentration. It is clearly shown that the $\sigma/\kappa$ ratio of the modulation-doped samples increases much faster than those of the equivalent uniform samples with increasing Ge content. In fact, most of the rapid increase in $\sigma/\kappa$ is from the rapid increase in the electrical conductivity (Figure 2a), while the values of the thermal conductivities (Figure 2b) are comparable, which is very different from the situation when pure Si was used as the nanoparticle material. The highest $\sigma/\kappa$ value for our modulation-doped samples happens at 35% nanoparticles, or 13.75% Ge equivalently, which is 54% higher than the $\sigma/\kappa$ of its equivalent uniform nanocomposite $Si_{86.25}Ge_{13.75}P_{1.05}$.

Figure 3 shows the temperature dependence of the thermoelectric properties of modulation-doped samples. This figure shows that the increase of the electrical conductivity (Figure 3a) decreases the Seebeck coefficient (Figure 3b) due to the usual interdependence of the transport parameters.[18−20] The obvious trend of the lower thermal diffusivity and thermal conductivity (Figure 3c,e, respectively) is caused by the interface phonon scattering due to the presence of more nanoparticles. The low thermal conductivity also benefits from the low specific heat (Figure 3d) of the nanoparticles. With 35% nanoparticles, our modulation-doped sample has the biggest advantage on the $\sigma/\kappa$ value over its equivalent uniform sample (Figure 2c), and the highest ZT value reaches 1.3 at 900 °C (Figure 3f), about the same as that of the best uniform nanocomposite $Si_{80}Ge_{20}P_2$ reported for $Si_{1-x}Ge_x$ so far,[6] but


dx.doi.org/10.1021/nl3003045 | Nano Lett. 2012, 12, 2077−2082

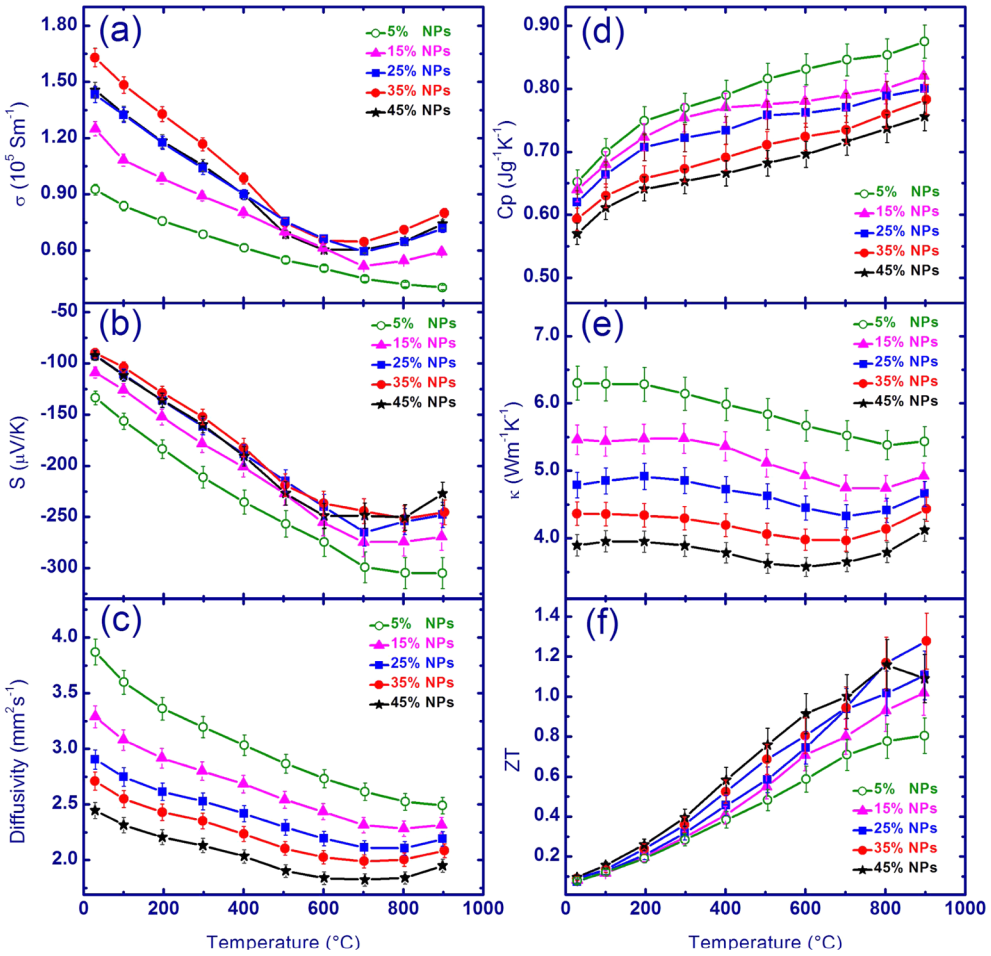


**Figure 3.** Temperature dependence of (a) electrical conductivity $\sigma$, (b) Seebeck coefficient $S$, (c) diffusivity, (d) specific heat $C_p$, (e) thermal conductivity $\kappa$, and (f) ZT of modulation-doped $Si_{1-x}Ge_x$ nanocomposite samples with different nanoparticle molar fractions.

less Ge is used in the modulation-doped samples, meaning lower cost.

Figure 4 shows the comparison for each individual property between the best modulation-doped sample $(Si_{95}Ge_5)_{0.65}(Si_{70}Ge_{30}P_3)_{0.35}$ and its equivalent uniform sample $Si_{86.25}Ge_{13.75}P_{1.05}$. To compare the modulation-doping with uniform impurity doping, we also include the data for the optimally doped matrix, $Si_{95}Ge_5P_2$. As one could see, over the whole temperature range, the modulation-doped sample has a higher electrical conductivity due to higher carrier mobility than the equivalent uniform sample (Figure 4a). The difference is pretty large at low temperature but gets smaller as the temperature increases, since electron−phonon scattering increases with temperature and starts to dominate at high temperatures.[1] Another possibility is that the interfaces may also have a larger impact on carrier transport at high temperatures. Compared to the modulation-doped sample, the uniform $Si_{95}Ge_5P_2$ sample has a much higher carrier concentration of $4.01 \times 10^{20}$ $cm^{-3}$ at room temperature due to its higher P concentration, which should be the reason for its higher electrical conductivity even though its carrier mobility is lower. The modulation-doped sample has a similar thermal diffusivity (Figure 4d) and a similar specific heat ($C_p$) values (Figure 4e) compared to the equivalent uniform sample. As a result, the thermal conductivity (Figure 4f) of the modulation-doped sample is similar to that of the equivalent uniform sample. However the temperature dependence of $\sigma/\kappa$ (Figure 4g), clearly shows that the modulation-doped sample has an advantage over the whole temperature range. It is important to note that the Seebeck coefficient of any modulation-doped sample in our study is similar to that of its corresponding equivalent uniform sample, similar to our observations in the previous report.[10] For example in Figure 4b, considering the 5% experimental error bar, the values for Seebeck coefficient are very close over the whole temperature range. Overall, our modulation-doping approach has improved the value of $\sigma/\kappa$ but has left the Seebeck coefficient almost untouched. With higher electrical conductivity and a similar Seebeck coefficient, the modulation-doped sample shows an improved power factor compared to its equivalent uniform sample, leading to the fact that the modulation-doped sample shows better ZT values (Figure 4h) than the equivalent uniform sample. Because the absolute ZT value at low temperature is small, one may find the difference at low temperature insignificant. Actually, the improvement at room temperature is 23%. At 900 °C, the peak value is close to 1.3, about 30% higher than the equivalent uniform sample (ZT ∼ 1.0) and 36% higher than the optimally doped matrix (ZT ∼ 0.9). Comparing to the previously reported best n-type alloy $Si_{80}Ge_{20}P_2$,[6] the peak ZTs are basically the same, but the modulation-doped samples contain much less Ge, equivalent to $Si_{86.25}Ge_{13.75}P_{1.05}$, meaning a much lower fabrication cost.

Since the matrix and nanoparticles have different Si to Ge ratios, they may diffuse into each other during the hot-pressing


dx.doi.org/10.1021/nl3003045 | Nano Lett. 2012, 12, 2077−2082

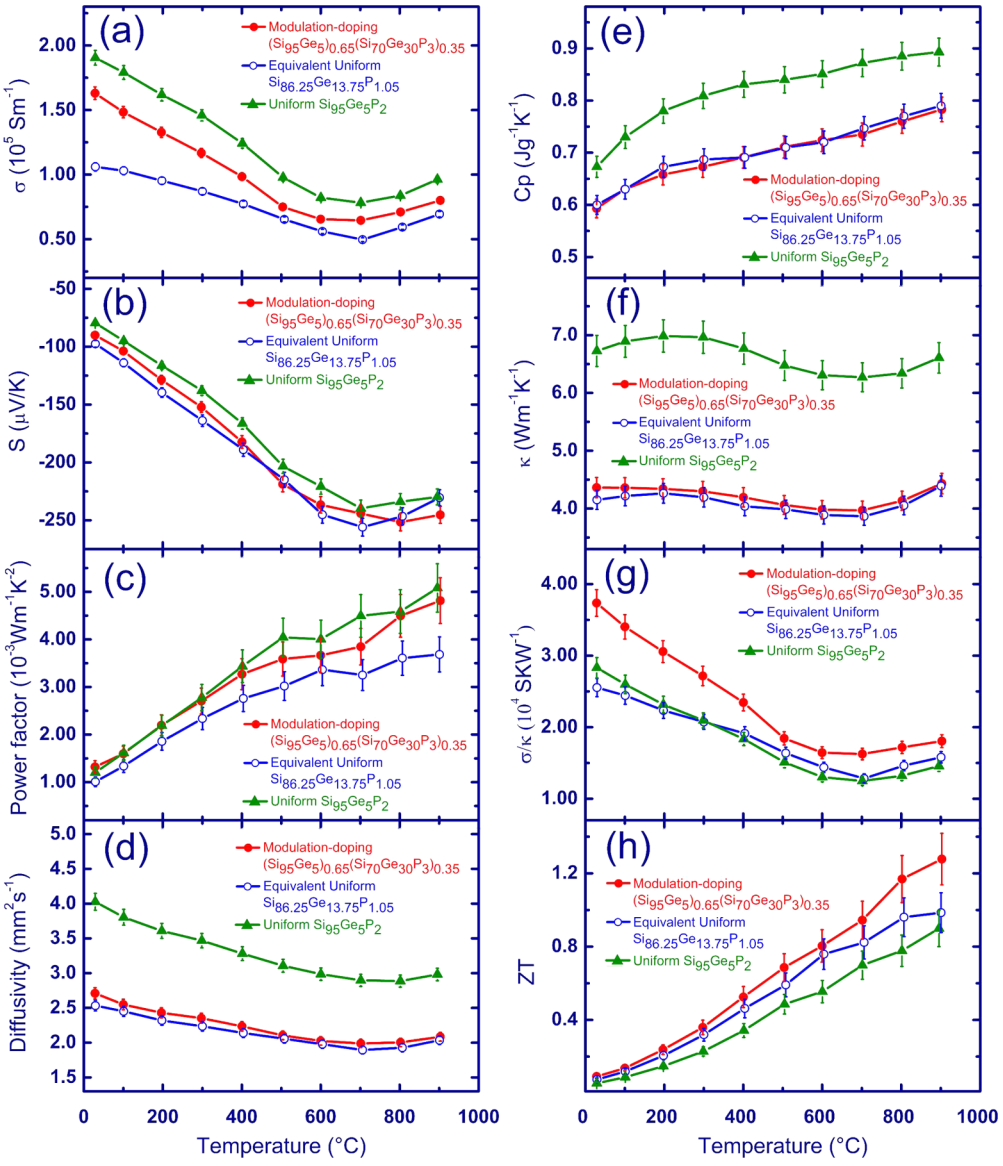


**Figure 4.** Temperature-dependent (a) electrical conductivity $\sigma$, (b) Seebeck coefficient $S$, (c) power factor, (d) diffusivity, (e) specific heat $C_p$, (f) thermal conductivity $\kappa$, (g) $\sigma/\kappa$ ratio, and (h) ZT of modulation-doped $Si_{1-x}Ge_x$ nanocomposite sample with a 35% nanoparticle molar fraction, in comparison with those of equivalent uniform $Si_{86.25}Ge_{13.75}P_{1.05}$ and optimally doped $Si_{95}Ge_5P_2$ uniform samples.

process. To prove whether such diffusion has really happened, we performed an energy dispersive spectroscopy (EDS) study on our hot-pressed modulation-doped samples using a TEM. For reference purposes, $Si_{95}Ge_5$ nanopowders were measured first. The EDS data repeatedly showed that the average atomic ratio between Si and Ge is 94.3:5.7, which is very close to the as-prepared composition (95:5). After the validation step, we then measured the best modulation-doped samples with a 35% nanoparticle molar fraction. At low magnifications (30 000–100 000) with the incident beam spread over a larger sample area, EDS results showed that the average chemical composition of the area is $Si_{86}Ge_{14}$, consistent with the designed equivalent composition $Si_{86.25}Ge_{13.75}$. At higher magnification (Figure 5a,b), we found that there are two typical domains with different compositions. The ones with more Si (Figure 5a), with the measured Si:Ge at five positions to be 89.1:10.9 (A), 89.3:10.7 (B), 89.4:10.6 (C), 89.3:10.7 (D), and 90.9:9.1 (E), give an average value of 89.6:10.4, which indicates 5% diffusion of Ge from nanoparticles into the matrix

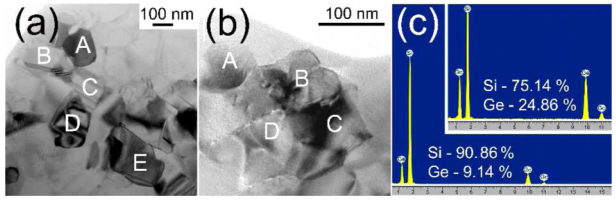


**Figure 5.** (a-b) TEM images and (c) EDS spectra [the spectrum in (c) is for the grain E in (a), the inset in (c) is for the grain A in (b)] of modulation-doped sample with a 35% nanoparticle molar fraction.

when compared to the original matrix composition of 95:5. The other domains turn out to have higher Ge (Figure 5b): 73.1:26.9 (A), 69.3:30.7 (B), 75.1:24.9 (C), and 75.1:24.9 (D), giving an averaging 73.1:26.9, little bit higher Si than that of the nanoparticles $Si_{70}Ge_{30}P_3$, a result of the minor diffusion. Typical EDS spectra for each case are given in Figure 5c. From these results, we could say that even though there might be some diffusion between the matrix and the nanoparticles, the two


dx.doi.org/10.1021/nl3003045 | Nano Lett. 2012, 12, 2077–2082

components still keep apart from each other. Compared to a thin-film configuration of modulation-doped structures, a better design will be to have a spacer layer. The spacer would have a dual role. First it will prevent grain growth, and second, it will separate the carriers from their parent atoms. The spacer itself should not react with either the host or the nanoparticles. In n-type configuration, the case of this study, the spacer band should align below the nanoparticles band and above the host matrix, so that the carriers can fall from the nanoparticles to the spacer and then to the matrix. However, how to make those spacer layers turns out to be extremely challenging in nanocomposites. Nevertheless, modulation-doping behavior is successfully demonstrated in this work.

In conclusion, we designed a new materials approach to unambiguously demonstrate the effectiveness of modulation-doping in thermoelectric nanocomposites. The electrical conductivity of a $Si_{86.25}Ge_{13.75}P_{1.05}$ sample was improved by 54% using the modulation-doping approach in $(Si_{95}Ge_5)_{0.65}(Si_{70}Ge_{30}P_3)_{0.35}$ that has the same overall composition. The enhancement was due to the 50% enhancement of the carrier mobility by spatially separating carriers from their parent atoms. More importantly, the thermal conductivity was kept low due to the low thermal conductivity of the nanoparticles. In fact the two-phase composite has a lower lattice thermal conductivity compared to its equivalent single-phase nanocomposite. At the same time, the Seebeck coefficient was not deteriorated. The unaffected Seebeck coefficient, combining with the enhanced electrical conductivity and the lower thermal conductivity produces a peak ZT of ~1.3 at 900 °C. The resulted ZT is about 30−40% higher than the equivalent uniform sample and the optimally doped matrix and could already compete with the state-of-the-art n-type $Si_{80}Ge_{20}P_2$ thermoelectric bulk materials with a much lower materials cost. To further improve the modulation-doping approach, using a thin spacer layer to minimize the diffusion would be expected to further improve the measured performance.

## AUTHOR INFORMATION


### Corresponding Author

*E-mail: gchen2@mit.edu; renzh@bc.edu

### Author Contributions

‖These authors contributed equally.


### Notes

The authors declare no competing financial interest.

## ACKNOWLEDGMENTS

We would like to acknowledge Dr. Gaohua Zhu, Dr. Weishu Liu, Dr. Xiaowei Wang, and Dr. Giri Joshi for their extensive input to this work. This project is funded by the "Solid State Solar-Thermal Energy Conversion Center ($S^3$TEC)", an Energy Frontier Research Center funded by the U.S. Department of Energy, Office of Science, and Office of Basic Energy Science under award number DE-SC0001299/DE-FG02-09ER46577.

## REFERENCES


(1) Rowe, D. M. *CRC Handbook of Thermoelectrics*; CRC Press: Boca Raton, FL, 1995.

(2) Mahan, G. D.; Sofo, J. O. *Proc. Natl. Acad. Sci. U.S.A.* **1996**, *93*, 7436.

(3) Heremans, J. P.; Thrush, C. M.; Morelli, D. T.; Wu, M. C. *Phys. Rev. Lett.* **2002**, *88*, 216801.

(4) Zebarjadi, M.; Esfarjani, K.; Bian, Z. X.; Shakouri, A. *Nano Lett.* **2011**, *11*, 225.

(5) Joshi, G.; Lee, H.; Lan, Y. C.; Wang, X. W.; Zhu, G. H.; Wang, D. Z.; Muto, A. J.; Tang, M. Y.; Song, J. K. S.; Dresselhaus, M. S.; Chen, G.; Ren, Z. F. *Nano Lett.* **2008**, *8*, 4670.

(6) Wang, X. W.; Lee, H.; Lan, Y. C.; Zhu, G. H.; Joshi, G.; Wang, D. Z.; Yang, J.; Muto, A. J.; Tang, M. Y.; Song, J. K. S.; Dresselhaus, M. S.; Chen, G.; Ren, Z. F. *Appl. Phys. Lett.* **2008**, *93*, 193121.

(7) Zhu, G. H.; Lee, H.; Lan, Y. C.; Wang, X. W.; Joshi, G.; Wang, D. Z.; Yang, J.; Vashaee, D.; Guilbert, H.; Pillitteri, A.; Dresselhaus, M. S.; Chen, G.; Ren, Z. F. *Phys. Rev. Lett.* **2009**, *102*, 196803.

(8) Lan, Y. C.; Minnich, A. J.; Chen, G.; Ren, Z. F. *Adv. Funct. Mater.* **2010**, *20*, 357.

(9) Bux, S. K.; Blair, R. G.; Gogna, P. K.; Lee, H.; Chen, G.; Dresselhaus, M. S.; Kaner, R. B.; Fleurial, J. -P. *Adv. Funct. Mater.* **2009**, *19*, 2445.

(10) Zebarjadi, M; Joshi, G.; Zhu, G. H.; Yu, B.; Minnich, A. J.; Lan, Y. C.; Wang, X. W.; Dresselhaus, M. S.; Ren, Z. F.; Chen, G. *Nano Lett.* **2011**, *11*, 2225.

(11) Dingle, R.; Störmer, H. L.; Gossard, A. C.; Wiegmann, W. *Appl. Phys. Lett.* **1978**, *33*, 665.

(12) Daembkes, H. *Modulation-doped Field-effect Transistors: Principles, Design, and Technology*, 2nd ed.; IEEE Press: New York, 1991.

(13) Schäffler, F. *Semicond. Sci. Technol.* **1997**, *12*, 1515.

(14) Zebarjadi, M.; Esfarjani, K.; Dresselhaus, M. S.; Ren, Z. F.; Chen, G. *Energy Environ. Sci.* **2012**, *5*, 5147.

(15) Yang, L. F.; Watling, J. R.; Wilkins, R. C. W.; Boriçi, M.; Barker, J. R.; Asenov, A.; Roy, S. *Semicond. Sci. Technol.* **2004**, *19*, 1174.

(16) Van de Walle, C. G.; Martin, R. M. *Phys. Rev. B.* **1986**, *34*, 5621.

(17) Stohr, J.; Klemm, W. *Z. Anorg. Allg. Chem.* **1954**, *241*, 305.

(18) Snyder, G. J.; Toberer, E. S. *Nat. Mater.* **2008**, *7*, 105.

(19) Dresselhaus, M. S.; Chen, G.; Tang, M. Y.; Yang, R. G.; Lee, H.; Wang, D. Z.; Ren, Z. F.; Fleurial, J. -P.; Gogna, P. *Adv. Mater.* **2007**, *19*, 1043.

(20) Minnich, A. J.; Dresselhaus, M. S.; Ren, Z. F.; Chen, G. *Energy Environ. Sci.* **2009**, *2*, 466.

Nano Energy (2012) 1, 183–189

Available online at www.sciencedirect.com

SciVerse ScienceDirect

journal homepage: www.elsevier.com/locate/nanoenergy

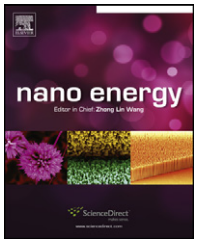


RAPID COMMUNICATION

# Suppression of grain growth by additive in nanostructured p-type bismuth antimony tellurides

Qian Zhang[a], Qinyong Zhang[a,b], Shuo Chen[a], Weishu Liu[a], Kevin Lukas[a], Xiao Yan[a], Hengzhi Wang[a], Dezhi Wang[a], Cyril Opeil[a], Gang Chen[c,*], Zhifeng Ren[a,**]

[a]*Department of Physics, Boston College, Chestnut Hill, MA 02467, USA*
[b]*School of Material Science and Engineering, Xihua University, Chengdu, Sichuan 610039, P. R. China*
[c]*Department of Mechanical Engineering, Massachusetts Institute of Technology, Cambridge, MA 02139, USA*

Received 26 September 2011; accepted 31 October 2011
Available online 15 November 2011

**KEYWORDS**
Thermoelectrics;
Bismuth antimony tellurides;
Nanostructure;
Ball milling;
Hot pressing;
Surface energy

**Abstract**
Grain growth is a major issue in the preparation of nanostructured bismuth-antimony-tellurides during hot pressing the nanopowders into dense bulk samples. To prevent grain agglomeration during ball milling and growth during hot pressing, organic agent (Oleic Acid, OA) as additive was added into the materials at the beginning of the ball milling process. With different concentrations of OA (0.5, 1.0, 1.5, 2.0, and 2.5 wt%), grains with different sizes are obtained. Structural analysis clearly shows that it is the particle size of the nanopowders that determines the final grain size in the densely compacted bulk samples. A combination of small grains ~200-500 nm and nanopores leads to effective phonon scattering, which results in the decrease of lattice thermal conductivity, and ZT of ~1.3 at 373 K for the sample with 2.0 wt% OA.
© 2011 Elsevier Ltd. All rights reserved.

## Introduction

Thermoelectric (TE) devices that convert energy between heat and electricity have been a focused research field recently [1–3]. The energy conversion efficiency increases with a dimensionless thermoelectric figure-of-merit ($ZT$), defined as $(S^2\sigma/\kappa)T$, where $Z$ is the figure-of-merit, $T$ the absolute temperature, $S$ the Seebeck coefficient, $\sigma$ the electrical conductivity, and $\kappa$ the total thermal conductivity with contributions from the lattice ($\kappa_L$) and the charge carriers ($\kappa_e$). The materials with high electrical conductivity, high Seebeck coefficient and low thermal conductivity are needed to achieve good $ZT$ values. $Bi_2Te_3$-based materials are the best TE materials commercially used around room temperature (200–400 K). Great efforts have been devoted to improve this class of materials [4–7]. Recent research

*Corresponding author. Tel.: +1 617 253 0006; fax: +1 617 324 5519.
**Corresponding author. Tel.: +1 617 552 2832; fax: +1 617 552 8478.
*E-mail addresses:* gchen2@mit.edu (G. Chen), renzh@bc.edu (Z. Ren).

2211-2855/$ - see front matter © 2011 Elsevier Ltd. All rights reserved.
doi:10.1016/j.nanoen.2011.10.006

**Table 1** Volumetric density, carrier concentration, and Hall mobility at room temperature of the as-prepared $Bi_{0.4}Sb_{1.6}Te_3/x$ with $x$=0, 0.5, 1.0, 1.5, 2.0, and 2.5 wt%.

| $Bi_{0.4}Sb_{1.6}Te_3/x$ ($x$ in wt%) | $x$=0 | $x$=0.5 | $x$=1.0 | $x$=1.5 | $x$=2.0 | $x$=2.5 |
|---|---|---|---|---|---|---|
| Volumetric density (g cm$^{-3}$) | 6.65 | 6.40 | 6.00 | 5.92 | 6.01 | 5.90 |
| Carr. conc. ($\times 10^{19}$, cm$^{-3}$) | 4.29 | 4.27 | 2.94 | 2.96 | 3.09 | 3.22 |
| Hall mobility (cm$^2$ V$^{-1}$ s$^{-1}$) | 163 | 162 | 179 | 172 | 179 | 147 |

shows that nanostructures in bulk materials can significantly enhance the $ZT$ value by reducing the thermal conductivity via effective phonon scattering without too much affecting the power factor ($S^2\sigma$) [8,9]. Bulk materials with different nanostructures embedded in the $Bi_xSb_{2-x}Te_3$ matrix are achieved by hot pressing nanopowders prepared by various methods, such as hydrothermal technique [10], ball milling [4,11], and melt spinning [12]. Hetero nanopowders such as fullerene, nano-SiC, nano-ZnAlO, etc., are also embedded in the $Bi_xSb_{2-x}Te_3$ matrix to act as phonon scattering centers to enhance $ZT$ [13-15].

To effectively scatter phonons, it is desired to preserve nanostructures in bulk materials. Usually, the spark plasma sintering (SPS) technique is employed with a relatively short sintering time, which can suppress the grain growth to some extent [12,16,17]. However, in spite of the controllable particle size that has been obtained in the starting nanopowders, the grain growth during the sintering process is still a big issue [16,18,19], where the grains easily grow to micron-size, which degrades the nano-effect. For example, by ball milling the commercial ingots or elemental chunks and following with hot pressing, $ZT$ values of ~1.4 or ~1.3 at about 373 K have been achieved, respectively [4,11]. Nanograins in the bulk materials are considered beneficial to decreasing the thermal conductivity. However, there are still substantial amount of grains larger than 1 μm [19]. We postulate that the large surface energy possessed by the ultrafine ball milled nanopowders results in grain aggregation to form much larger particles, and that it is these large particles that form the final grain size during the hot pressing causing grain growth. In the present work, small amount of well-chosen surfactant as additive is added into the samples while ball milling to lower the surface energy and get uniform smaller grains after hot pressing, leading to the decreased lattice thermal conductivity and subsequently a peak $ZT$~1.3 at 373 K. It is worth to point out that such $ZT$ values is about the best we have achieved before without the additives because of a degraded power factor when additive is used in the current study.

## Experimental procedure

Stoichiometric Bi (99.999%), Sb (99.999%), and Te (99.999%) were weighted and melted to form ingot $Bi_{0.4}Sb_{1.6}Te_3$. With different concentrations of the additive agent (Oleic Acid, OA, 99%, Alfa Aesar) ($x$=0, 0.5, 1.0, 1.5, 2.0, and 2.5 wt%), the ingots of $Bi_{0.4}Sb_{1.6}Te_3/x$ were ball milled for 4 h. The ball milled powders were then loaded into a graphite die with an inner diameter of 12.7 mm and hot-pressed by direct current (dc-HP) press, first at 360 °C for 2 min to evaporate the OA, then at 450 °C for 2 min to produce the final disks for the measurements. X-ray diffraction analysis was conducted on a PANalytical multipurpose diffractometer with an X'celerator detector (PANalytical X'Pert Pro). The microstructures were investigated by a scanning electron microscope (SEM, JEOL 6340 F) and a high resolution transmission electron microscope (HRTEM, JEOL 2010 F). For HRTEM observations of the as-prepared powders, the samples were dispersed ultrasonically in ethanol for 5 min. A few droplets of the dispersion was placed on holy carbon coated copper grids and dried in air. The electrical resistivity ($\rho$) and the Seebeck coefficient were simultaneously measured on a commercial system (ULVAC ZEM-3) using the four-point dc current-switching method and the static temperature difference method. The thermal diffusivity ($\alpha$) and the specific heat ($C_p$) were measured on a laser flash apparatus (Netzsch LFA 447) and a thermal analyzer (Netzsch DSC200-F3), respectively. The volumetric density ($D$) was quantified by an Archimedes method and listed in Table 1. The thermal conductivity $\kappa$ was calculated from the relationship $\kappa = D\alpha C_p$. The Hall Coefficient $R_H$ was measured using the PPMS (Physical Properties Measurement System, Quantum Design) at room temperature. The carrier concentration $n$ and Hall mobility $\mu_H$ were calculated using the relations $n = 1/(eR_H)$ and $\mu_H = \sigma R_H$, respectively.

## Results and discussions

XRD shows that single phase is obtained for all ingots by melting. The $Bi_{0.4}Sb_{1.6}Te_3$ ingots were then ball milled with different concentrations of additive OA and followed with hot pressing. Fig. 1 shows the XRD patterns of the as-prepared disk samples. There is no difference of peak positions in all the samples. All the peaks can be indexed to the hexagonal structure (space group R3m). The SEM, TEM, and HRTEM images of the ball milled nanopowders without OA are shown in Fig. 2(a)-(c). Although ball milling can decrease individual grains efficiently down to ~10 nm (Fig. 2(c)), which is consistent with the previous reports [4,11], the surface energy increases correspondingly and makes it easy to form lots of micron-size aggregated particles, as shown in Fig. 2(a) and (b). It is very likely that after hot pressing, the majority of the aggregated particles grow to micron size grains, as presented in Fig. 3(a).

In order to reduce the surface energy, several kinds of additives are tried. The best results so far are from samples with a 2 wt% Oleic Acid (OA). Fig. 2(d)-(e) are the SEM, TEM, and HRTEM images of the ball milled nanopowder with 2 wt% OA, respectively. We noticed that even with the lubrication from OA coating during ball milling, which may reduce the

energy transfer from the balls to the ingots, the ball milling is still powerful enough to break the ingots to ~10 nm fine grains. With OA, the particle size before hot pressing is obviously smaller because of the less agglomeration, which is shown in Fig. 2(d) and (e). Correspondingly, the grain size in the final disk samples is obviously decreased after hot pressing. The SEM images from the freshly fractured surface of the bulk samples with different concentrations of OA are shown in Fig. 3(b)–(f). With increase in concentration of OA, the grain size decreases to ~200–500 nm. The grain size is uniform when $x$ is more than 2.0 wt%. Furthermore, the additive begins to evaporate when the temperature is higher than the boiling point of OA (360 °C) during hot pressing, leaving lots of nanopores inside the samples, which is reflected in the reduced relative densities to ~90–95% of the theoretical density.

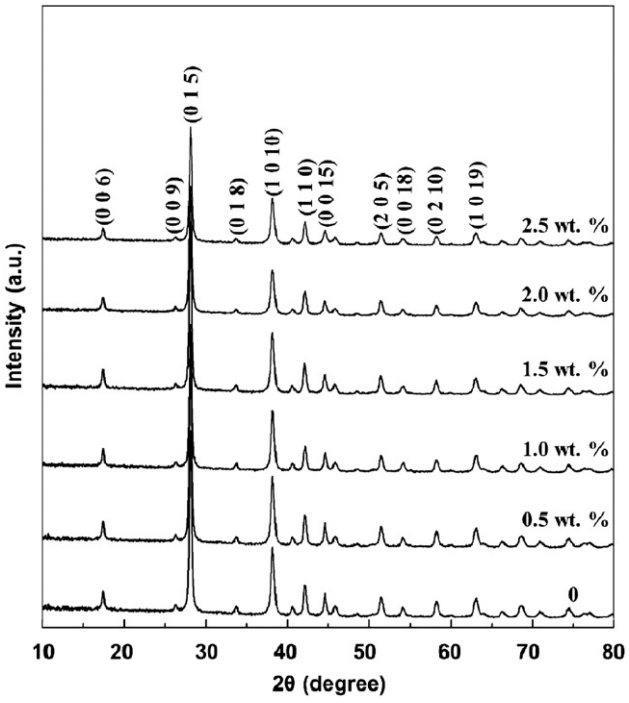


**Figure 1** XRD patterns of the as-prepared bulk $Bi_{0.4}Sb_{1.6}Te_3/x$ with different concentrations of OA ($x$=0, 0.5, 1.0, 1.5, 2.0, and 2.5 wt%).

We measured the TE properties parallel and perpendicular to the press directions. The nonflake structure and the random distribution create no anisotropy in all the samples. The temperature dependences of the electrical conductivity and Seebeck coefficient of the as-prepared $Bi_{0.4}Sb_{1.6}Te_3/x$ with $x$=0, 0.5, 1.0, 1.5, 2.0, and 2.5 wt% are presented in Fig. 4(a) and (b). The electrical conductivity is decreased with the increase of OA, likely due to the small amount of the organic agent left as well as the nanopores created when OA evaporates. The Hall measurements in Table 1 show the results of the carrier concentration ($n$) and the mobility ($\mu$) at room temperature, which affect the electrical conductivity ($\sigma$) by the relationship $\sigma=ne\mu$. The decrease in the electrical conductivity is obviously connected with the decrease in the carrier concentration. We consider that the coated OA during the ball milling process depresses the creation of defects, such as the Te vacancy and the $Sb_{Te}$ anti-site deficiency, which decreases the concentration of the holes. However, the mobility is maintained in spite of the

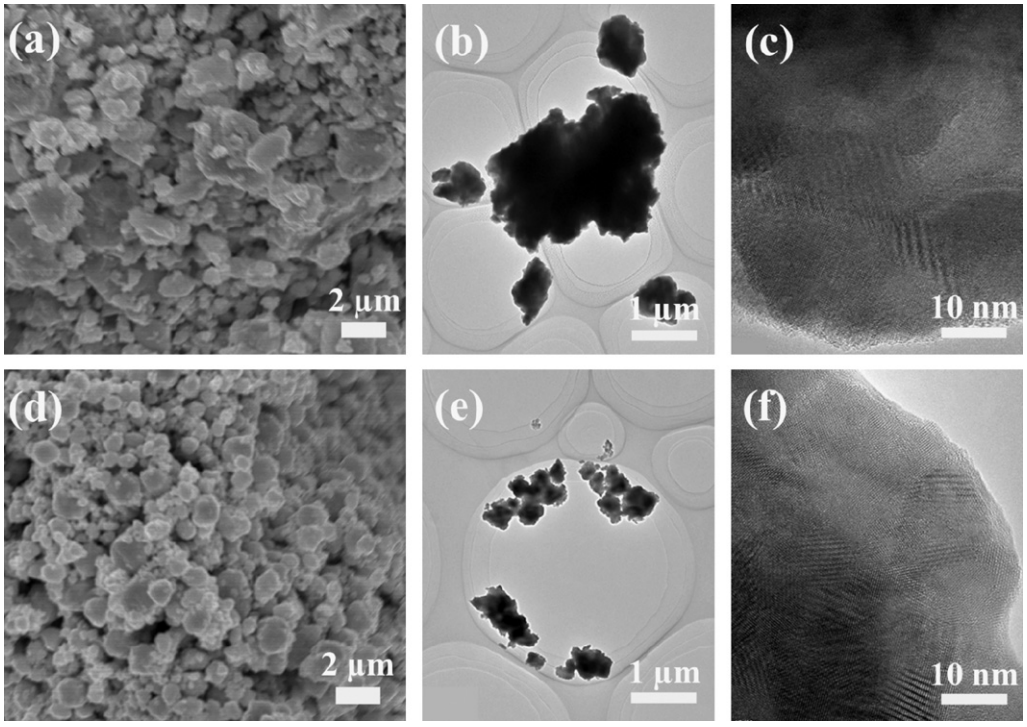


**Figure 2** SEM images of the ball-milled $Bi_{0.4}Sb_{1.6}Te_3$ powder without additive OA (a) and with 2.0 wt% additive OA (d). TEM images of the ball-milled $Bi_{0.4}Sb_{1.6}Te_3$ powder without additive OA (b) and with 2.0 wt% additive OA (e). HRTEM images of the ball-milled $Bi_{0.4}Sb_{1.6}Te_3$ powder without additive OA (c) and with 2.0 wt% additive OA (f).

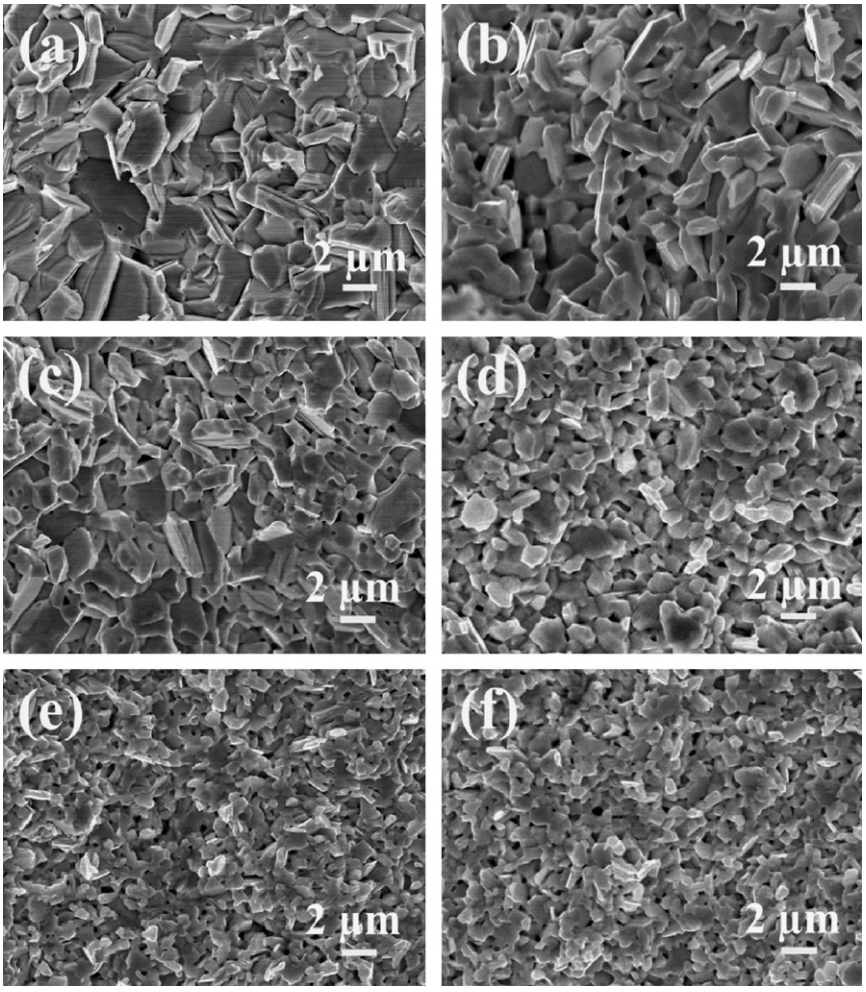


**Figure 3** SEM images of the as-prepared bulk samples $Bi_{0.4}Sb_{1.6}Te_3/x$ with different concentrations of additive OA $x$=0, 0.5, 1.0, 1.5, 2.0, and 2.5 wt% for (a), (b), (c), (d), (e), and (f), respectively.

increased grain boundaries and the dispersed nanoholes, which are beneficial for the decrease of the thermal conductivity.

Fig. 4(c) and (d) presents the total thermal conductivity and the lattice thermal conductivity of the ball milled samples with different concentrations of OA, respectively. The total thermal conductivity $\kappa$ is the sum of the carrier thermal conductivity $\kappa_e$ and the lattice thermal conductivity $\kappa_L$. We estimate $\kappa_e$ from the Wiedemann-Franz relation, $\kappa_e = L\sigma T$, with the Lorenz number $L$ taken as $1.6 \times 10^{-8}$ $V^2K^{-2}$ based on a previous calculation [20]. Although ball milling produces nanograins and interfaces that reduce lattice thermal conductivity [4,11], there are still larger-sized grains caused by non-uniform ball milling, agglomeration and the grain growth during the hot-pressing. With an increase of OA, the grain size is decreased and becomes more uniform. Both the decreased grain size and the nanopores created in the sample preparation scatter phonons, leading to a large reduction in the lattice thermal conductivity. With a 2.5 wt% OA, the lattice thermal conductivity decreases by 30%. The highest $ZT$ value reaches 1.3 at by 373 K for samples with $x$=2.0 and 2.5 wt% (Fig. 4(f)). We also present the temperature dependence of the thermal diffusivity and specific heat of all the samples in Fig. 4(g) and (h), respectively. The increase on the specific heat is likely due to the remaining carbon. The organic residue and the relative low density may also deteriorate the electrical properties, which may be solved by purifying the powder before hot pressing.

Even though we decreased the grain size by using additives during balling milling for having achieved lower thermal conductivity, we did not achieve improvement in $ZT$ values due to the fact that the additives have also decreased the power factor, shown in Fig. 4(e). Nevertheless, the grain size suppression is a good start to further improve the $ZT$ values when a way to preserve the power factor is accomplished.

## Conclusions

In summary, p-type $Bi_{0.4}Sb_{1.6}Te_3$ thermoelectric bulk materials were prepared by ball milling the ingot with oleic acid and followed by hot pressing. The agglomeration of the nanopowders is alleviated by the introduction of the functional surfactant additive (oleic acid) during ball milling. The growth of the grains during hot pressing is

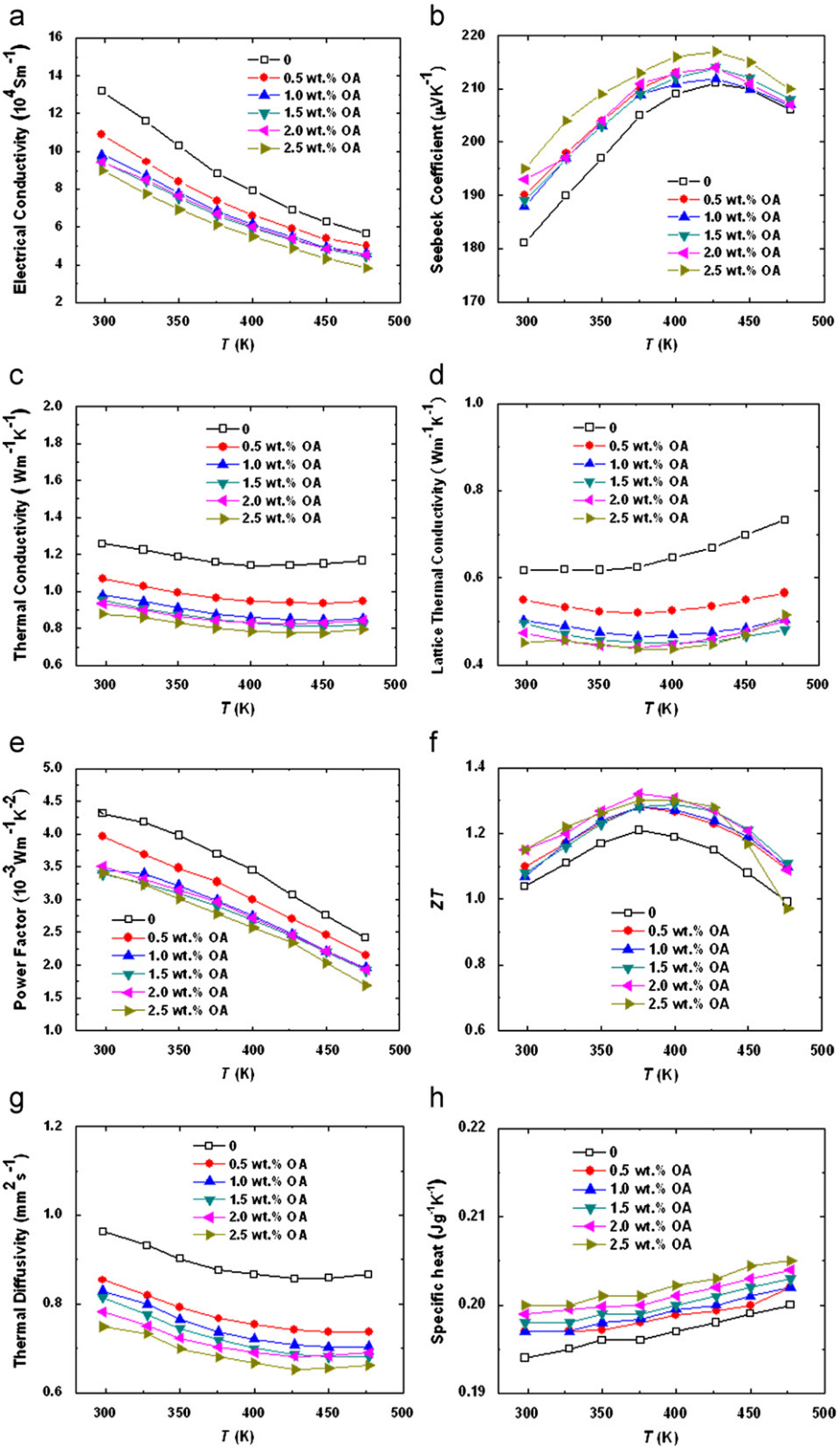


**Figure 4** Temperature dependence of the electrical conductivity (a), Seebeck coefficient (b), total thermal conductivity (c), lattice thermal conductivity (d), power factor (e), *ZT* (f), thermal diffusivity (g), and specific heat (h) of the as-prepared $Bi_{0.4}Sb_{1.6}Te_3/x$ with different concentrations of OA ($x$=0, 0.5, 1.0, 1.5, 2.0, and 2.5 wt%).

suppressed, which leads to increased phonon scattering for the decreased lattice thermal conductivity. However, power factor was also decreased, leading to a *ZT* value of ~1.3 at 373 K, which is about the same as reported before. Higher *ZT* values are expected when a way to preserve the power factor is accomplished.

## Acknowledgment

This work is supported by "Solid State Solar–Thermal Energy Conversion Center ($S^3$TEC)", an Energy Frontier Research Center funded by the U.S. Department of Energy, Office of Science, Office of Basic Energy Science under award number DE-SC0001299 (G.C. and Z.F.R.).

## References

[1] B.C. Sales, Science 295 (2002) 1248.
[2] A. Majumdar, Science 303 (2004) 777.
[3] R. Venkatasubramanian, E. Siivola, T. Colpitts, B. O'Quinn, Nature 413 (2001) 597.
[4] B. Poudel, Q. Hao, Y. Ma, Y.C. Lan, A. Minnich, B. Yu, X. Yan, D.Z. Wang, A. Muto, D. Vashaee, X. Chen, J. Liu, D.S. Dresselhaus, G. Chen, Z.F. Ren, Science 320 (2008) 634.
[5] C.M. Jaworski, V. Kulbachinskii, J.P. Heremans, Physical Review B 80 (2009) 233201.
[6] J. Shen, T. Zhu, X. Zhao, S. Zhang, S. Yang, Z. Yin, Energy and Environmental Science 3 (2010) 1519.
[7] X. Yan, B. Poudel, Y. Ma, W.S. Liu, G. Joshi, H. Wang, Y.C. Lan, D.Z. Wang, G. Chen, Z.F. Ren, Nano Letters 10 (2010) 3373.
[8] M.S. Dresselhaus, G. Chen, M.Y. Tang, R.G. Yang, H. Lee, D.Z. Wang, Z.F. Ren, J.P. Fleurial, P. Gogna, Advanced Materials (Weinheim, Germany) 19 (2007) 1043.
[9] J.R. Szczech, J.M. Higgins, S. Jin, Journal of Materials Chemistry 21 (2011) 4037.
[10] Y.Q. Cao, X.B. Zhao, T.J. Zhu, X.B. Zhang, J.P. Tu, Applied Physics Letters 92 (2008) 143106.
[11] Y. Ma, Q. Hao, B. Poudel, Y.C. Lan, B. Yu, D.Z. Wang, G. Chen, Z.F. Ren, Nano Letters 8 (2008) 2580.
[12] W. Xie, X. Tang, Y. Yan, Q. Zhang, T.M. Tritt, Applied Physics Letters 94 (2009) 102111.
[13] N. Gothard, J.E. Spowart, T.M. Tritt, Physica Status Solidi A 207 (2010) 157.
[14] L.D. Zhao, B.P. Zhang, J.F. Li, M. Zhou, W.S. Liu, J.J. Liu, Journal of Alloys and Compounds 455 (2008) 259.
[15] T. Zhang, Q. Zhang, J. Jiang, Z. Xiong, J. Chen, Y. Zhang, W. Li, G. Xu, Applied Physics Letters 98 (2011) 022104.
[16] M. Scheele, N. Oeschler, K. Meier, A. Kornowski, C. Klinke, H. Weller, Advanced Functional Materials 19 (2009) 3476.
[17] C. Liao, L. Wu, Applied Physics Letters 95 (2009) 052112.
[18] S. Wang, W. Xie, H. Li, X. Tang, Journal of Physics D: Applied Physics 43 (2010) 335404.
[19] Y.C. Lan, B. Poudel, Y. Ma, D.Z. Wang, M.S. Dresselhaus, G. Chen, Z.F. Ren, Nano Letters 9 (2009) 1419.
[20] W.S. Liu, Q.Y. Zhang, Y.C. Lan, S. Chen, X. Yan, Q. Zhang, H. Wang, D.Z. Wang, G. Chen, Z.F. Ren, Advanced Energy Materials 1 (2011) 577.

**Qian Zhang**, Ph.D., is currently a postdoctoral fellow in Department of Physics at Boston College, USA. She received her Ph.D. degree in Materials Science and Engineering from Zhejiang University, China. She completed her doctoral thesis as a member of Prof. Xinbing Zhao's group from 2006 to 2009 for the research of $Mg_2(Si,Sn)$ based thermoelectric materials. In 2009, she spent a year as postdoctoral fellow in Chemistry at National University of Singapore focusing on the chemical synthesis of lead chalcogenide nanoparticles and their related thermoelectric applications. Her current research is mainly on optimization and characterization of bismuth telluride and lead chalcogenide thermoelectric materials.

**Qinyong Zhang**, Ph.D., is currently an associate professor at Xihua University and was a postdoctoral fellow in Department of Physics at Boston College, USA. He received his Ph.D. degree in Materials Physics and Chemistry from the University of Electronic Science and Technology, Chengdu, China. His current research is focused mainly on fabrication and characterization of lead chalcogenide thermoelectric materials and clean energy applications.

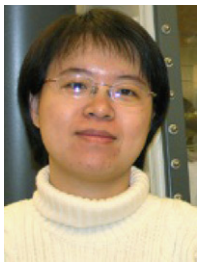

**Shuo Chen**, Ph.D., currently a research assistant professor in the Department of Physics at Boston College, USA. She earned her B.S. degree in Physics at Peking University, China and a Ph.D. degree in Physics Boston College, USA. Her research interests include synthesis and understanding materials and devices for energy applications and in-situ transmission electron microscopy. Currently she is working on half-Heuslers thermoelectric materials.

**Weishu Liu**, Ph.D., is currently a postdoctoral fellow in Department of Physics at Boston College, USA. He received his Ph.D. degree in Materials Science from the University of Science and Technology Beijing, China. He completed his doctoral thesis as a member of Prof. Jing-Feng Li's Group from 2003 to 2008 in Tsinghua University. In 2009, he spent a year as a postdoctoral research associate at the University of Washington, and then moved to Boston College. His current research is focused mainly on the design, fabrication, and tailoring of nanocomposite for solid state solar thermoelectric power generation, and waste heat harvesting.

**Kevin Lukas**, Ph.D. candidate at Boston College 2008-present. Kevin received his B.A. from Saint Anselm College in Applied Physics in 2006 and M.S. from Central Connecticut State University in 2008. Research focuses predominantly on transport measurements in thermoelectric materials.

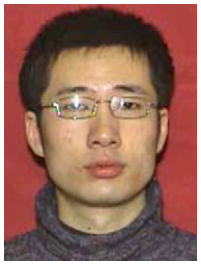

**Xiao Yan**, Ph.D., is a postdoctoral fellow in the Department of Physics at Boston College, USA. He received his B.S. degree in the Department of Physics from the Nanjing University, China and a Ph.D. degree in the same field from Boston College, USA. His main research interests focus on the synthesis and characterization of nanostructured thermoelectric materials, such as $Bi_2Te_3$, skutterudites, and half-Heuslers.

**Dr. Hengzhi Wang** is a researcher at Boston College, Ph.D. in Materials Science and Engineering in 2002 from Nanjing University of Science and Technology; a specialist on microscopy and microanalysis of nanoscaled materials (TEM/SEM/EDS/XRD).

**Dr. Dezhi Wang**, electron microscope facility manager and research assistant professor in Boston College. He received his bachelor degree in 1984 and master degree in 1987 from Huazhong University of Science and Technology in materials science and engineering. He obtained his Ph.D. in 2007 from Boston College in Physics. His research focuses on nanostructure synthesis and characterizations.

**Dr. Cyril Opeil, S.J.** Professor at Boston College. Received his B.S. in Electronics Engineering from the University of Scranton, and his Ph.D. in Experimental Physics at Boston College. He was a Post Doctoral Research Assistant at Los Alamos National Laboratory. Research interests include martensitic materials, thermoelectric materials, photoemission spectroscopy, and meteorite formation.

**Dr. Gang Chen** is currently the Carl Richard Soderberg Professor of Power Engineering at Massachusetts Institute of Technology. He obtained his Ph.D. degree from UC Berkeley in 1993 working under then Chancellor Chang-Lin Tien, master and bachelor degrees from Huazhong University of Science and Technology, China. He was a faculty member at Duke University (1993–1997), University of California at Los Angeles (1997–2001), before joining MIT in 2001. He is a member of national Academy of Engineering. He is a recipient of the NSF Young Investigator Award, the ASME Heat Transfer Memorial Award, and the R&D100 Award. He is a member of the US National Academy of Engineering, a Guggenheim Fellow, an AAAS Fellow, and an ASME Fellow. He has published extensively in the area of nanoscale energy transport and conversion and nanoscale heat transfer. He is the director of Solid-State Solar-Thermal Energy Conversion Center funded by the US DOE's Energy Frontier Research Centers program.

**Dr. Zhifeng Ren** is currently a professor of physics at Boston College. He obtained his Ph.D. degree from the Institute of Physics Chinese Academy of Sciences in 1990, master degree from Huazhong University of Science and Technology in 1987, and bachelor degree from Sichuan Institute of Technology in 1984. He was a postdoc and research faculty at SUNY Buffalo (1990–1999) before joining BC in 1999. He specializes in thermoelectric materials, solar thermoelectric devices & systems, photovoltaic materials & systems, carbon nanotubes & semiconducting nanostructures, nanocomposites, bio agent delivery & bio sensors, and superconductors. He is a fellow of APS and AAAs, a recipient of R&D 100 award. He has published extensively, and was ranked as the 49th of the top 100 Materials Scientists worldwide. He has co-founded companies in the field of carbon nanotubes, thermoelectric materials, and photovoltaics.

PHYSICAL REVIEW B **86**, 100401(R) (2012)

# Spin ordering and electronic texture in the bilayer iridate $Sr_3Ir_2O_7$

Chetan Dhital,[1] Sovit Khadka,[1] Z. Yamani,[2] Clarina de la Cruz,[3] T. C. Hogan,[1] S. M. Disseler,[1] Mani Pokharel,[1] K. C. Lukas,[1] Wei Tian,[3] C. P. Opeil,[1] Ziqiang Wang,[1] and Stephen D. Wilson[1,*]

[1]*Department of Physics, Boston College, Chestnut Hill, Massachusetts 02467, USA*

[2]*Chalk River Laboratories, Canadian Neutron Beam Centre, National Research Council, Chalk River, Ontario, Canada K0J 1P0*

[3]*Neutron Scattering Science Division, Oak Ridge National Laboratory, Oak Ridge, Tennessee 37831-6393, USA*

(Received 7 June 2012; published 7 September 2012)

Through a neutron scattering, charge transport, and magnetization study, the correlated ground state in the bilayer iridium oxide $Sr_3Ir_2O_7$ is explored. Our combined results resolve scattering consistent with a high temperature magnetic phase that persists above 600 K, reorients at the previously defined $T_{AF} = 280$ K, and coexists with an electronic ground state whose phase behavior suggests the formation of a fluctuating charge or orbital phase that freezes below $T^* \approx 70$ K. Our study provides a window into the emergence of multiple electronic order parameters near the boundary of the metal to insulator phase transition of the $5d$ $J_{\text{eff}} = 1/2$ Mott phase.

DOI: 10.1103/PhysRevB.86.100401 PACS number(s): 75.25.Dk, 75.50.Ee, 72.20.Ht

There has been considerable interest recently in studying the phase behavior of correlated $5d$-electron transition metal oxides due to the potential of realizing electronic phenomena possible only when electron hopping, spin-orbit coupling, and Coulomb interaction energy scales are almost equivalent.[1–3] Of particular focus has been members of the iridium oxide Ruddelsden-Popper (RP) series $Sr_{n+1}Ir_nO_{3n+1}$, where an experimental picture of a spin-orbit induced $J_{\text{eff}} = 1/2$ Mott insulating state has been proposed.[4,5] Upon increasing the dimensionality of the iridate RP series to higher $n$, optical[6] and transport measurements[7,8] have shown that the effective bandwidth increases and the system transitions from a quasi-two-dimensional insulating state to a metallic phase in the three-dimensional limit.

Specifically, the reported optical gap in the $n = 2$ member $Sr_3Ir_2O_7$ (Sr-327) shifts considerably downward relative to the $n = 1$ $Sr_2IrO_4$ system into what should be a weakly insulating phase,[6] demonstrating that Sr-327 occupies a unique position in the iridate RP phase diagram near the boundary of the metal to insulator phase transition in the RP series. Given this framework, $Sr_3Ir_2O_7$ exhibits a number of anomalous features in its magnetic properties: Bulk magnetization measurements of Sr-327 reveal a rich behavior possessing three distinct energy scales,[8,9] and recent muon spin rotation ($\mu$SR) measurements have revealed the presence of highly disordered local spin behavior,[10] both supporting the notion of multiple coexisting or competing magnetic phases. However, the details of how spin order evolves in this material and interfaces with the energy scales identified in both transport and bulk susceptibility measurements remains largely unexplored.

In this Rapid Communication, we utilize neutron scattering, bulk magnetization, and transport techniques to explore the phase behavior in $Sr_3Ir_2O_7$ (Sr-327). At high temperatures, a phase appears with $T_{\text{onset}} > 600$ K followed by a second magnetic transition at $T_{AF} = 280$ K. Scattering from this high temperature phase is consistent with a magnetic origin, provides an explanation for the absence of Curie-Weiss paramagnetism in this material above 280 K,[11] and also suggests an origin for the recently reported anomalous 93 meV magnon gap.[12] At low temperatures, the spin order is decoupled within resolution from a second upturn in the bulk spin susceptibility at $T_O = 220$ K, suggestive of the formation of an electronic glass that freezes below $T^* \approx 70$ K. Below this freezing energy scale, charge transport demonstrates a localized ground state that can be biased into a regime of field enhanced conductivity (FEC) consistent with collective transport above a threshold electric field. Our combined results demonstrate the coexistence of spin order with an unconventional, electronically textured, phase in an inhomogeneous ground state near the boundary but on the insulating side of the $J_{\text{eff}} = 1/2$ Mott transition.

Single crystals of $Sr_3Ir_2O_7$ (Sr-327) were grown via flux techniques similar to earlier reports.[13,14] The resulting Sr:Ir ratio was confirmed to be 3:2 via energy dispersive spectroscopy (EDS) measurements, and a number of Sr-327 crystals were also ground into a powder and checked via x-ray diffraction in a Bruker D2 Phaser system. No coexisting $Sr_2IrO_4$ phase was observed and the resulting pattern was refined to the originally reported $I4/mmm$ structure—we note, however, that, due to the small scattering signal from oxygen, we are unable to distinguish between this and the various reported orthorhombic symmetries.[8,11,13] For the remainder of this Rapid Communication, we will index the unit cell using the pseudotetragonal unit cell with $a = b = 5.50$ Å, $c = 20.86$ Å.

Neutron measurements were performed on the HB-1A triple-axis spectrometer at the High Flux Isotope Reactor (HFIR) at Oak Ridge National Laboratory and on the C5 spectrometer at the Canadian Neutron Beam Centre at Chalk River Laboratories. Experiments on C5 were performed with a vertically focusing pyrolitic graphite (PG-002) monochromator and analyzer, an $E_f = 14.5$ meV, two PG filters after the sample, and collimations of 33′-48′-51′-144′ before the monochromator, sample, analyzer, and detector, respectively. On HB-1A, a double bounce PG monochromator was utilized with fixed $E_i = 14.7$ meV, two PG filters before the sample, and collimations of 48′-48′-40′-68′. Magnetization measurements were performed on a Quantum Design MPMS-XL system and resistivity data was collected in a series of four-wire setups: (1) Zero field resistance from 300 to 12 K was collected

 ©2012 American Physical Society

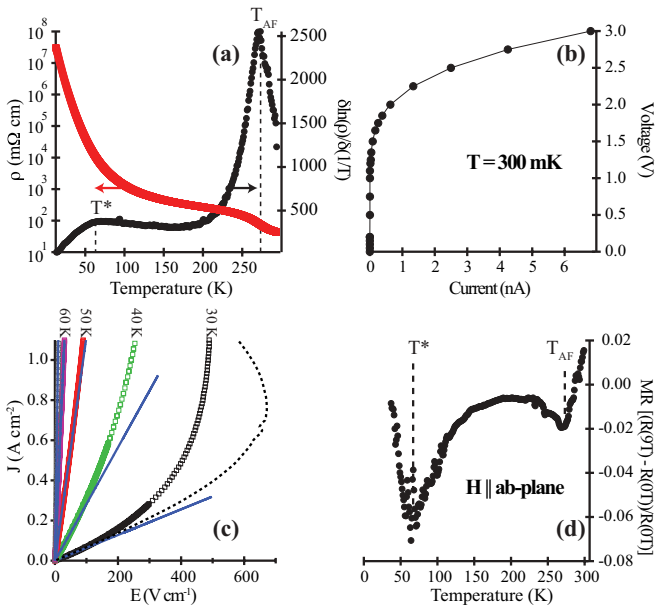


FIG. 1. (Color online) (a) Temperature dependence of the *ab*-plane resistivity for Sr-327. Also plotted is the $\frac{\partial \ln \rho}{\partial (1/T)}$ vs $T$ showing two peaks at $T_{AF}$ and $T^*$. (b) $I$-$V$ curve of *ab*-plane transport at 300 mK showing voltage biasing into a FEC regime. (c) Current driven, pulsed, $I$-$V$ measurements as a function of temperature. Solid lines show linear fits to the Ohmic regime at each temperature. The dashed line is a Joule heating model at 30 K as described in the text. (d) Magnetoresistance (MR) ratio as described in the text plotted as a function of temperature showing two well defined minima at the $T^*$ and $T_{AF}$ transitions.

with a Keithley 2182A voltmeter, (2) data from 12 to 0.3 K was collected in a $^3$He absorption refrigerator with an Keithley Model 617 electrometer, and (3) magnetoresistance data was collected in a 9 T Quantum Design PPMS.

Looking first at the results of our *ab*-plane transport measurements under low (1 $\mu$A) current, Fig. 1(a) shows the zero field resistivity as a function of temperature. The sample's resistivity increases from several m$\Omega$ cm at room temperature to beyond 10 M$\Omega$ cm below 20 K, and begins to show saturation behavior below 2 K.[14] There is no substantial interval of constant activation energy, as illustrated by the overplot of $\frac{\partial \ln \rho}{\partial (1/T)}$ versus $T$ in this same panel. Instead, $\frac{\partial \ln \rho}{\partial (1/T)}$ shows two peaks suggestive of two phase transitions coupling to charge carriers: the first near the known magnetic phase transition at $T_{AF} = 280$ K (Ref. 8) and the second indicating a lower temperature phase formation at $T^* \approx 70$ K.

In order to investigate further the transport properties of this lower temperature, $T^*$ phase, the charge transport was characterized via a voltage driven $I$-$V$ sweep at 300 mK shown in Fig. 1(b). A pronounced nonlinearity appears, where with increasing field strength the system switches from a linear, Ohmic regime with near zero conductance into a highly non-Ohmic FEC regime. To determine the temperature evolution of this FEC feature, a separate sample was mounted and probed with 600 $\mu$s current pulses to minimize heating effects [Fig. 1(c)]. While it is difficult to completely preclude all heating effects within the rise and sample time of the pulse, these pulsed measurements show that the nonlinear bend in the $I$-$V$ curve persists and eventually vanishes below resolution at $T \approx 60$ K.

A separate (rough) check for discriminating the nonlinear conduction from simple Joule heating can be performed by looking at the 30 K data in Fig. 1(c). The Ohmic regime $R(30\text{ K}) = 42$ k$\Omega$ and the maximum pulsed current (2 mA) during the 600 $\mu$s pulse delivers a maximum $\Delta Q = 10.1 \times 10^{-5}$ J. While low temperature heat capacity data are needed for Sr-327, as a lower estimate, the heat capacity of $Sr_2IrO_4$ at 30 K can be used ($\approx$14 J/K),[15] giving a maximum $\Delta T = 5.5$ K (for a $1.32 \times 10^{-6}$ mol sample). In carrying out a similar analysis for each current value pulsed at 30 K and assuming *perfect* thermal isolation, the measured Ohmic $R(T)$ can be used to determine the lowest fields possible due to pure Joule heating as a function of the pulsed current density. This limiting case is plotted as a dashed line in Fig. 1(c), demonstrating that the nonlinear feature at 30 K is intrinsic.[16]

In looking at the magnetoresistance of the same sample plotted in the Fig. 1(d), the MR $= [R(9\text{ T}) - R(0\text{ T})]/R(0\text{ T})$ ratio is negative and shows two minima at $T^* \approx 70$ K and $T_{AF} = 280$ K. The lower minimum appears approximately at the temperature where the onset of FEC emerges and coincides with the low-$T$ peak in $\frac{\partial \ln \rho}{\partial 1/T}$. The origin of the negative magnetoresistance is likely the removal of spin disorder scattering due to biased magnetic domain populations which will be discussed later, and the inflection below $T^*$ supports the idea of a field coupled order parameter freezing below 70 K. The suppression of enhanced fluctuations originating from an additional electronic instability, however, may also account for the overall negative MR.

Magnetization data shown in Fig. 2(a) supports the idea of a bulk phase transition below 70 K where a downturn in the dc susceptibility originally reported by Cao *et al.*[8] begins, suggestive of a glassy freezing process. Consistent with earlier reports,[8,9] three energy scales are apparent in the field cooled magnetization data: a canted AF phase transition at $T_{AF} = 280$ K, a sharp upturn at $T_O = 220$ K, and an eventual decrease in susceptibility below $T^* = 70$ K. Both field cooled (FC) and zero field cooled (ZFC) data show similar downturns near $T^*$ and an irreversibility temperature near $T_O$. At 300 K, however,

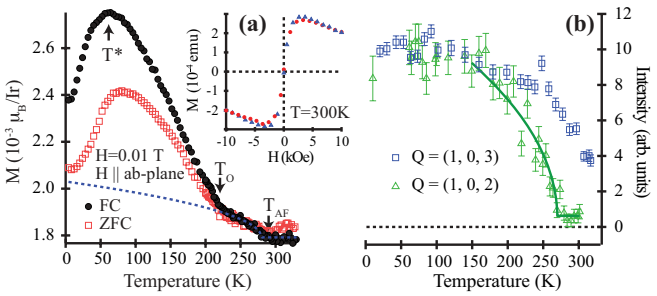


FIG. 2. (Color online) (a) dc-magnetization data for Sr-327 with $H = 0.01$ T aligned parallel to the *ab* plane for both FC (solid symbols) and ZFC temperature sweeps (open symbols). The dashed line shows the mean-field order parameter fit to the net moment from the 280 K transition. The inset shows $M$ vs $H$ sweep at 300 K. (b) Temperature dependence of the peak intensities at (1,0,3) and (1,0,2) magnetic reflections. The solid line is a power law fit to the (1,0,2) order parameter.

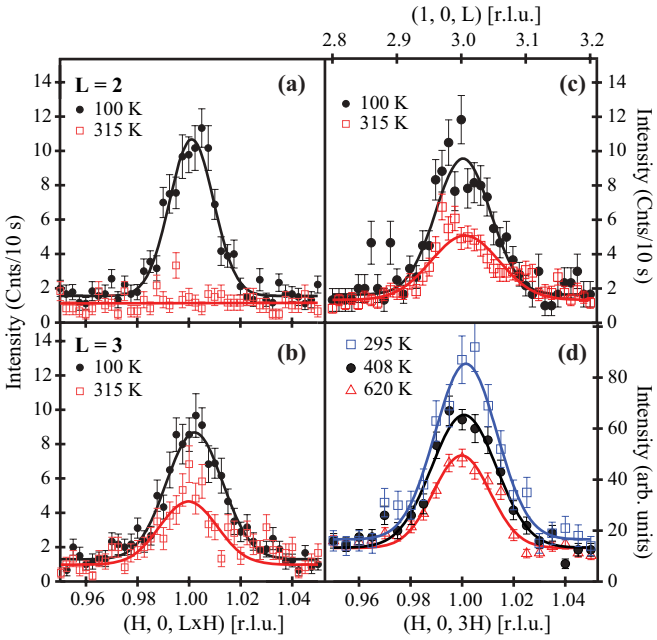


FIG. 3. (Color online) Radial **Q** scans at 100 and 315 K through the (a) **Q** = (1,0,2) and (b) **Q** = (1,0,3) reflections. Solid lines are Gaussian fits to the data. (c) *L* scans across the (1,0,3) peak position showing three-dimensional (3D) superlattice peaks at 100 and 315 K. (d) **Q** scans showing the temperature dependence of the (1,0,3) peak.

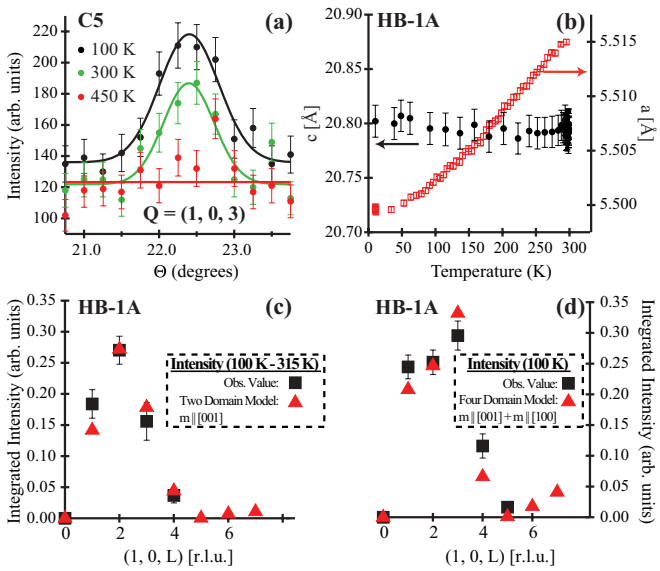


FIG. 4. (Color online) (a) Rocking scans on a separate crystal showing the temperature dependence of the (1,0,3) peak above 300 K. (b) Temperature dependence of the *a*- and *c*-axis lattice parameters measured at the (2,0,0) and (0,0,4) reflections. Integrated intensities plotted as (c) 100 K with 315 K data subtracted and (d) the total scattering data at 100 K. Data is compared with two simple collinear spin models described in the text.

field sweeps plotted in the inset of Fig. 2(a) reveal a rapid saturation of the spin response, suggesting the persistence of magnetic correlations above $T_{AF}$.

In order to further investigate the spin order, neutron diffraction measurements were performed on a 7 mg single crystal Sr-327 sample with the results plotted in Figs. 3 and 4. $[H,0,L]$, $[H,K,0]$, and $[H,H,L]$ zones were explored and magnetic reflections were observed only at the $(1,0,L)$ positions for $L = 1,2,3,4,5$. The correlated order is three dimensional with $\xi_L = \sqrt{2\ln(2)} \times 1/w = 147 \pm 10$ Å, where $w(\text{Å}^{-1})$ is the peak's Gaussian width [Fig. 3(c)]. The appearance of both $L =$ even and $L =$ odd reflections in a simple collinear picture of the spin structure is therefore consistent with recent x-ray results resolving the presence of two magnetic domains.[9] attributable to in-plane structural twinning in an orthorhombic symmetry.

Looking at the order parameters for both the $L = 3$ and $L = 2$ reflections in Fig. 2(b), the magnetic intensities show that the $L = 2$ peak disappears at $T_{AF}$ while substantial intensity remains at 280 K in the $L = 3$ reflection. **Q** scans plotted in Fig. 3(b) demonstrate this more explicitly. The peak remaining above 280 K is long-range ordered with a minimum correlation length of $93 \pm 18$ Å, comparable to the correlation length observed at 10 K ($97 \pm 5$ Å). Due to the rather coarse collimations used, both these values and those of all magnetic Bragg reflections are resolution limited. At 300 K peaks remain at the $(1,0,L)$ $L = 1,3,4$ positions, all forbidden in the reported structural space groups to date. This same crystal was then loaded into a furnace and measured at higher temperatures, where, upon warming, the remnant peaks continue to decrease in intensity as illustrated in Fig. 3(d); however, they notably remain present beyond 600 K. The continued temperature dependence of these peaks above 300 K and the absence of peaks at higher order *L* and *H* strongly imply that this remnant scattering is magnetic and that an additional magnetic phase persists beyond 280 K.

In order to verify this in a second sample, a 2 mg crystal from a separate batch was explored on the C5 spectrometer with the results plotted in Fig. 4(a). Again, a clear temperature dependence above 300 K was observed with the remnant (1,0,3) peak vanishing within the error of the measurement by 450 K. The earlier disappearance of this high temperature AF peak is likely due to the poorer statistics in the measurement of this second sample; however, variable oxygen stoichiometry between samples may also play a role in diminishing the effective transition temperature.

Due to the presence of two magnetic domains[9] and the rapid attenuation due to the Ir magnetic form factor, it is difficult to uniquely determine a model of the spin structure in both the high and low temperature magnetic phases. If we assume that the scattering seen at 315 K is a separate, saturated, order parameter, then the additional intensity due to the 280 K transition is plotted in Fig. 4(c). The rapid disappearance of magnetic peaks for $L > 5$ suggests a sizable component of the moment directed along the *c* axis, and the best symmetry bound two-domain model matching the data is a *G*-type arrangement of AF-coupled bilayers with moments directed along the (0,0,1) axis, consistent with a recent x-ray report.[14,17] The ordered moment using this model is $\mu = 0.52 \pm 0.08 \mu_B$.

Looking instead at the total scattering observed at 100 K in Fig. 4(d), no simple collinear model captures all of the major reflections well. Nevertheless, if we again use a twinned *G*-type spin structure, a model comprising four magnetic domains with

two different moment orientations can be constructed. If the two twin domains added to the previous model have moments directed along the (1,0,0) axis, this four domain model roughly fits the data.[14] This added domain would comprise the high temperature phase in a two domain picture, however, future polarized measurements are required to differentiate between this multidomain picture, a potential noncollinear spin structure with an accompanying spin reorientation at 280 K, and to confirm the magnetic nature of the high temperature phase.

Our combined data demonstrate the presence of canted 3D antiferromagnetic domains whose phase evolution is decoupled within resolution from the fluctuation and freezing behavior at $T^*$ and $T_O$ [Fig. 2(b)], precluding any additional major spin reorientations at these temperatures. This suggests that there remain additional moments weakly coupling[8,9] to fluctuations below $T_O$ and eventually freezing below $T^*$. Our measurements in their entirety therefore suggest a picture of three distinct order parameters driving the phase behavior of Sr-327: (1) a high temperature phase (of likely magnetic origin) with $T_{onset} > 620$ K, (2) a canted AF magnetic transition at 280 K, followed by (3) the freezing of the $T^*$ phase into an electronically textured ground state.

The $T^*$ transition is nominally suggestive of a charge density wave (CDW) or collective transport mechanism which becomes depinned above a threshold field, leading to an avalanche process in the carrier number. The structural lattice parameters [Fig. 4(b)], however, evolve smoothly as the system is cooled from 315 to 10 K and, to date, no structural distortion associated with a conventional CDW formation has been observed below 300 K,[11,18] although, high temperature structural measurements are a promising avenue for future studies. An alternative scenario of exchange coupled metallic islands condensing below $T^*$ with a substantial Coulomb barrier for tunneling may also address the transport mechanism below $T^*$.[19,20] Similar non-Ohmic behavior has also been reported in other correlated iridates,[21,22] suggesting an electronic inhomogeneity intrinsic to these 5*d*-correlated materials.

Curiously, X-ray measurements on a Sr-327 sample with a qualitatively similar bulk spin susceptibility have reported the onset of AF order at $T_O$.[9] This resonant x-ray scattering (RXS) study speculated about the presence of short-range order setting in at $T_{AF}$ and diverging at $T_O$ as the reason for the discrepancy,[9] however, our measurements reveal no appreciable change in the correlation length upon cooling through $T_O$. Given that more recent RXS measurements show the onset of magnetism at the expected $T_{AF} = 285$ K,[17] variation in sample quality is likely the cause for the variance reported between these two RXS studies.

To summarize, our studies have illustrated a complex electronic ground state in the $Sr_3Ir_2O_7$ system with multiple electronic order parameters. Our observation of scattering consistent with an AF phase extending beyond 600 K is supported by the absence of Curie-Weiss behavior above the previously identified $T_{AF}$ (Ref. 11) and also by the rapid field-induced saturation of the magnetization at 300 K. The system then transitions through a magnetic transition at $T_{AF} =$ 280 K, and exhibits multiple magnetic domains or alternatively noncollinear spin order in its ground state. The spin order appears decoupled from two additional energy scales appearing in transport and bulk susceptibility measurements, suggesting a fluctuating charge/orbital state that freezes into an inhomogeneous electronic ground state where tunneling and sliding effects manifest under increasing electric field strength.

S.D.W. acknowledges helpful discussions with Ying Ran and Stefano Boseggia, and Michael Graf for use of a $^3$He refrigerator. The work at BC was supported by NSF Award DMR-1056625 and DOE DE-SC0002554. Part of this work was performed at ORNL's HFIR, sponsored by the Scientific User Facilities Division, Office of Basic Energy Sciences, US DOE.

*stephen.wilson@bc.edu

[1] B.-J. Yang and Y. B. Kim, Phys. Rev. B **82**, 085111 (2010).
[2] D. A. Pesin and L. Balents, Nat. Phys. **6**, 376 (2010).
[3] F. Wang and T. Senthil, Phys. Rev. Lett. **106**, 136402 (2011).
[4] B. J. Kim *et al.*, Phys. Rev. Lett. **101**, 076402 (2008).
[5] B. J. Kim *et al.*, Science **323**, 1329 (2009).
[6] S. J. Moon *et al.*, Phys. Rev. Lett. **101**, 226402 (2008).
[7] J. M. Longo, J. A. Kafalas, and R. J. Arnott, J. Solid State Chem. **3**, 174 (1971).
[8] G. Cao, Y. Xin, C. S. Alexander, J. E. Crow, P. Schlottmann, M. K. Crawford, R. L. Harlow, and W. Marshall, Phys. Rev. B **66**, 214412 (2002).
[9] S. Boseggia, R. Springell, H. C. Walker, A. T. Boothroyd, D. Prabhakaran, D. Wermeille, L. Bouchenoire, S. P. Collins, and D. F. McMorrow, Phys. Rev. B **85**, 184432 (2012).
[10] I. Franke, P. J. Baker, S. J. Blundell, T. Lancaster, W. Hayes, F. L. Pratt, and G. Cao, Phys. Rev. B **83**, 094416 (2011).
[11] I. Nagai *et al.*, J. Phys.: Condens. Matter **19**, 136214 (2007).
[12] J. Kim *et al.*, arXiv:1205.5337.
[13] M. A. Subramarian, M. K. Crawford, and R. L. Harlow, Mater. Res. Bull. **29**, 645 (1994).
[14] See Supplemental Material at http://link.aps.org/supplemental/10.1103/PhysRevB.86.100401 for additional details.
[15] N. S. Kini *et al.*, J. Phys.: Condens. Matter **18**, 8205 (2006).
[16] Both higher field pulsed measurements and dc measurements show pronounced regions of negative differential resistance; however, for the purpose of this Rapid Communication, we limit our discussion to only measurements where the effect of Joule heating has been minimized.
[17] J. W. Kim, Y. Choi, J. Kim, J. F. Mitchell, G. Jackeli, M. Daghofer, J. van den Brink, G. Khaliullin, and B. J. Kim, Phys. Rev. Lett. **109**, 037204 (2012).
[18] H. Matsuhata *et al.*, J. Solid State Chem. **177**, 3776 (2004).
[19] D. P. Arovas, F. Guinea, C. P. Herrero, and P. San Jose, Phys. Rev. B **68**, 085306 (2003).
[20] P. San-Jose, C. P. Herrero, F. Guinea, and D. P. Arovas, Eur. Phys. B **54**, 309 (2006).
[21] G. Cao, J. Bolivar, S. McCall, J. E. Crow, and R. P. Guertin, Phys. Rev. B **57**, R11039 (1998).
[22] G. Cao *et al.*, Solid State Commun. **113**, 657 (2000).

JACS
JOURNAL OF THE AMERICAN CHEMICAL SOCIETY

Article

pubs.acs.org/JACS

# Heavy Doping and Band Engineering by Potassium to Improve the Thermoelectric Figure of Merit in p-Type PbTe, PbSe, and $PbTe_{1-y}Se_y$

Qian Zhang,[†] Feng Cao,[†] Weishu Liu,[†] Kevin Lukas,[†] Bo Yu,[†] Shuo Chen,[†] Cyril Opeil,[†] David Broido,[†] Gang Chen,*[,‡] and Zhifeng Ren*[,†]

[†]Department of Physics, Boston College, Chestnut Hill, Massachusetts 02467, United States

[‡]Department of Mechanical Engineering, Massachusetts Institute of Technology, Cambridge, Massachusetts 02139, United States

Supporting Information

**ABSTRACT:** We present detailed studies of potassium doping in $PbTe_{1-y}Se_y$ ($y$ = 0, 0.15, 0.25, 0.75, 0.85, 0.95, and 1). It was found that Se increases the doping concentration of K in PbTe as a result of the balance of electronegativity and also lowers the lattice thermal conductivity because of the increased number of point defects. Tuning the composition and carrier concentration to increase the density of states around the Fermi level results in higher Seebeck coefficients for the two valence bands of $PbTe_{1-y}Se_y$. Peak thermoelectric figure of merit ($ZT$) values of ~1.6 and ~1.7 were obtained for Te-rich $K_{0.02}Pb_{0.98}Te_{0.75}Se_{0.25}$ at 773 K and Se-rich $K_{0.02}Pb_{0.98}Te_{0.15}Se_{0.85}$ at 873 K, respectively. However, the average $ZT$ was higher in Te-rich compositions than in Se-rich compositions, with the best found in $K_{0.02}Pb_{0.98}Te_{0.75}Se_{0.25}$. Such a result is due to the improved electron transport afforded by heavy K doping with the assistance of Se.

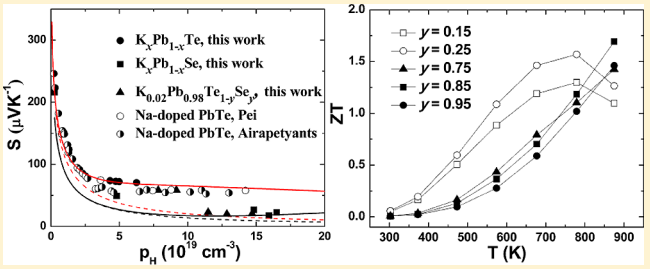


## INTRODUCTION

Intensive attention has recently been paid to energy conversion using thermoelectric principles, which can directly convert both waste heat and solar energy into electricity.[1−3] Large-scale applications call for thermoelectric materials with high values of the dimensionless figure of merit $ZT = [S^2\sigma/(\kappa_L + \kappa_e)]T$, where $S$ is the Seebeck coefficient, $\sigma$ is the electrical conductivity, $\kappa_L$ is the lattice thermal conductivity, $\kappa_e$ is the charge-carrier thermal conductivity, and $T$ is the absolute temperature.[4−7] Accordingly, a combination of a high Seebeck coefficient with high electrical conductivity and low thermal conductivity is desired and has been pursued. However, it is difficult to optimize one parameter without deteriorating the others. Complex crystals are normally considered to have the advantage of decoupling the three interrelated quantities with the concept of "electron−crystal phonon−glass".[8−10] Nanostructuring is the major approach for $ZT$ enhancement, since it allows independent tuning of all of the parameters.[11−17]

Lead telluride (PbTe) with the simple face-centered-cubic (fcc) rock salt structure is one of the most studied thermoelectric materials suitable for the intermediate temperature range (600−800 K).[18−21] Its cheaper sister compound lead selenide (PbSe) also has a decent value of $ZT$.[22−24] Excellent progress has recently been made through band engineering, such as resonant states[18,19,23] and band convergence,[20,22,25,26] leading to improvements in both the electrical conductivity and Seebeck coefficient simultaneously without affecting the thermal conductivity too much.[27] Good results were reported for Tl-doped PbTe, which pushed the $ZT$ value to ~1.5 at 773 K by creating resonant states near the Fermi energy.[18] Recently, Al doping was reported to result in n-type resonant doping in PbSe with a peak $ZT$ value of ~1.3.[23] A great deal of theoretical work has been performed to find possible new resonant dopants in PbTe and PbSe.[28−30] It was predicted that the alkali metals K, Rb, and Cs can create resonant density of states (DOSs) distortion in PbTe, whereas Na cannot because it does not change the DOS near the top of the valence band.[28] However, PbTe doped heavily with Na still exhibits high $ZT$ values, which are believed to be the result of the coexistence of light-hole (L) and heavy-hole (Σ) valence bands in PbTe.[31] Effective doping of Na moves the Fermi level close to the Σ band, which has a much larger DOS, helping increase the Seebeck coefficient.[20,32−34] A $ZT$ value of ~1.4 at 750 K in Na-doped PbTe with a Hall carrier concentration ($p_H$) greater than $\sim 7.5 \times 10^{19}$ cm$^{-3}$ has been obtained.[20] A similar effect has been shown theoretically and experimentally in PbSe, which has a flat, high-mass, high-DOS band 0.35−0.4 eV below the valence-band maximum.[35] $ZT$ values reaching 1.2−1.3 at 850 K have been reported for Na-doped PbSe with a Hall carrier concentration of $(9-15) \times 10^{19}$ cm$^{-3}$.[22] Furthermore, a $ZT$ value of ~1.8 at ~850 K was reported for $Na_{0.02}Pb_{0.98}Te_{0.85}Se_{0.15}$ as a result of alloying with Se.[25] Regardless of whether the increase in the electronic power factor ($\sigma S^2$) is due to resonant levels or the Σ band, it is obvious that band engineering can enhance the carrier (electron/hole) transport. Indeed, both resonant states and band convergence contribute to the high $ZT$ value in Tl-doped

**Received:** February 7, 2012
**Published:** May 24, 2012

 © 2012 American Chemical Society 

Table 1. Theoretical Densities ($D_T$), Measured Volumetric Densities ($D$), Relative Densities ($D_R$), and Electrical Conductivity Power Law Exponents ($\delta$) for $K_xPb_{1-x}Te$, $K_xPb_{1-x}Se$, and $K_{0.02}Pb_{0.98}Te_{1-y}Se_y$

| | $K_xPb_{1-x}Te$ | | | | $K_xPb_{1-x}Se$ | | | $K_{0.02}Pb_{0.98}Te_{1-y}Se_y$ | | | | |
|---|---|---|---|---|---|---|---|---|---|---|---|---|
| | 0.01 | 0.0125 | 0.015 | 0.02 | 0.01 | 0.0125 | 0.015 | 0.15 | 0.25 | 0.75 | 0.85 | 0.95 |
| $D_T$ ($gcm^{-3}$) | 8.18 | 8.18 | 8.17 | 8.14 | 8.19 | 8.18 | 8.18 | 8.09 | 8.10 | 8.13 | 8.13 | 8.14 |
| $D$ ($g\ cm^{-3}$) | 8.06 | 8.02 | 8.02 | 8.01 | 7.84 | 7.9 | 7.92 | 7.97 | 7.99 | 7.97 | 7.91 | 8.02 |
| $D_R$ | 99% | 98% | 98% | 98% | 96% | 97% | 97% | 99% | 99% | 98% | 97% | 99% |
| $\delta$ | 3.11 | 2.95 | 3 | 2.94 | 3.17 | 2.8 | 2.99 | 2.34 | 2.4 | 2.58 | 2.9 | 2.87 |

PbTe.[26] However, it is desired to avoid Tl for practical applications because of its toxicity. Motivated by recent calculations,[28] we chose to study K doping to make $K_xPb_{1-x}Te_{1-y}Se_y$ because of the smaller ionic radius of $K^+$ compared with $Rb^+$ and $Cs^+$. Normally, it is believed that K has a limited solubility in PbTe,[26,36] which limits the Hall carrier concentration to less than $6 \times 10^{19}$ $cm^{-3}$. Thus, reports on K doping in PbTe have been very limited, in contrast to Na doping in PbTe, which can produce much higher carrier concentrations. In this work, we were able to increase the Hall carrier concentration to $(8-15) \times 10^{19}$ $cm^{-3}$ in PbTe by K doping with the help of Se through the balance of electronegativity. It is shown that band engineering works well in $K_xPb_{1-x}Te_{1-y}Se_y$, giving a higher Seebeck coefficient. Peak $ZT$ values of ~1.6 and ~1.7 were obtained in Te-rich $K_{0.02}Pb_{0.98}Te_{0.75}Se_{0.25}$ and Se-rich $K_{0.02}Pb_{0.98}Te_{0.15}Se_{0.85}$, respectively. However the average $ZT$ of the Te-rich compositions was higher, making this material more favorable for practical applications.

## EXPERIMENTAL SECTION

**Synthesis.** Ingots with nominal compositions $K_xPb_{1-x}Te$ ($x$ = 0.01, 0.0125, 0.015, and 0.02), $K_xPb_{1-x}Se$ ($x$ = 0, 0.005, 0.01, 0.0125, and 0.025), and $K_{0.02}Pb_{0.98}Te_{1-y}Se_y$ ($y$ = 0.15, 0.25, 0.75, 0.85, and 0.95; other compositions such as $y$ = 0.4 and 0.5 were also studied, but those results have not been shown here to increase the readability of the figures) were prepared in a quartz tube with carbon coating. The raw materials inside the quartz tube were slowly raised to 1000−1100 °C and kept there for 6 h, then slowly cooled to 650 °C and maintained at that temperature for 50 h, and finally slowly cooled to room temperature. The obtained ingots were cleaned and hand-milled in a glovebox. The sieved (325 mesh) powder was loaded into a half-inch die and hot-pressed at 500−600 °C for 2 min. The hot-pressed pellets were sealed in a quartz tube for further annealing at 600 °C for 4 h to make the sample stable during the measurements at temperatures up to 600 °C.

**Characterizations.** X-ray diffraction (XRD) analysis was conducted on a PANalytical multipurpose diffractometer with an X'celerator detector (PANalytical X'Pert Pro). The electrical resistivity ($\rho$) and the Seebeck coefficient were measured using a four-point direct-current switching method and the static temperature difference method, respectively, both of which were conducted on a commercial system (ULVAC ZEM-3). The thermal diffusivity ($\alpha$) was measured on a laser flash apparatus (Netzsch LFA 447), and the specific heat ($C_p$) was measured on a differential scanning calorimetry thermal analyzer (Netzsch DSC200-F3). The volumetric density ($D$) was measured by the Archimedes method and is shown in Table 1 along with the theoretical density ($D_T$). The thermal conductivity ($\kappa$) was calculated as $\kappa = D\alpha C_p$. The Hall coefficient ($R_H$) at room temperature was measured using a Quantum Design Physical Properties Measurement System. The Hall carrier concentration ($n_H$) and Hall mobility ($\mu_H$) were calculated as $n_H = (eR_H)^{-1}$ and $\mu_H = \sigma R_H$. It is understood that there is a 3% error in the electrical conductivity, 5% error in the Seebeck coefficient, and 4% error in the thermal conductivity, resulting in errors of 10% for the power factor and 11% for $ZT$. For better readability of the figures, we have deliberately plotted the curves without the error bars.

## RESULTS AND DISCUSSION

On the basis of the ionic radii of Pb, Na, and K (Table 2), $K^+$ is closer to $Pb^{2+}$ but a little bigger. For samples $K_xPb_{1-x}Te$ ($x$ = 0.01, 0.0125, 0.015, and 0.02), the electrical conductivity, Seebeck coefficient, power factor, thermal diffusivity, specific heat, lattice thermal conductivity, and total thermal conductivity were measured, and the results are presented in Figure 1a−f, respectively. The electrical conductivity at room temperature increased a little bit with increasing K concentration, but no change was seen at high temperature, where all of the samples showed a decrease with temperature (Figure 1a). The Seebeck coefficients of all of the samples (Figure 1b) changed only slightly, likely as a result of contributions from both the light and heavy holes with the high carrier concentration.[26] The power factor increased with increasing K concentration and peaked at ~500 K (Figure 1c). The thermal diffusivity was basically the same for all of the samples (Figure 1d), consistent with the microstructures (see the Supporting Information). The specific heats of the samples were similar (Figure 1e), indicating good repeatability of the measurements. Combining the thermal diffusivities, specific heats, and volumetric densities gave the thermal conductivities (Figure 1f), which were very close to each other.

Table 2. Ionic Radii ($r$) and Pauling Electronegativities (PE) of K, Na, Pb, Te, and Se

| | K | Na | Pb | Te | Se |
|---|---|---|---|---|---|
| $r$ (Å) | 1.33 | 0.97 | 1.20 | 2.11 | 1.91 |
| PE | 0.82 | 0.93 | 2.33 | 2.10 | 2.55 |

To provide a better understanding of the band structure of $K_xPb_{1-x}Te$, a Pisarenko plot (Seebeck coefficient vs Hall carrier concentration) at room temperature was made (Figure 2, solid circles) and compared with reported results for Na-doped PbTe (open and half-open circles).[20,32] The Hall carrier concentration of our K-doped PbTe samples ($<6.3 \times 10^{19}$ $cm^{-3}$) was lower than that in Na-doped PbTe, which could be as high as $14 \times 10^{19}$ $cm^{-3}$. The flattening of the Seebeck coefficient with increasing carrier concentration indicates a contribution from the second valence band. This behavior has been explained previously using a multiband model with a nonparabolic L band described by a Kane model and a parabolic Σ band,[25,26,37] and we employed a similar model here.

The Seebeck coefficient $S_L$ and carrier concentration $p_L$ for a single nonparabolic light-hole band at the L point are given by

$$S_L = \pm\frac{k_B}{e}\left[\frac{{}^1F^1_{-2}(\eta,\beta)}{{}^0F^1_{-2}(\eta,\beta)} - \eta\right] \quad (1)$$


dx.doi.org/10.1021/ja301245b | J. Am. Chem. Soc. 2012, 134, 10031−10038

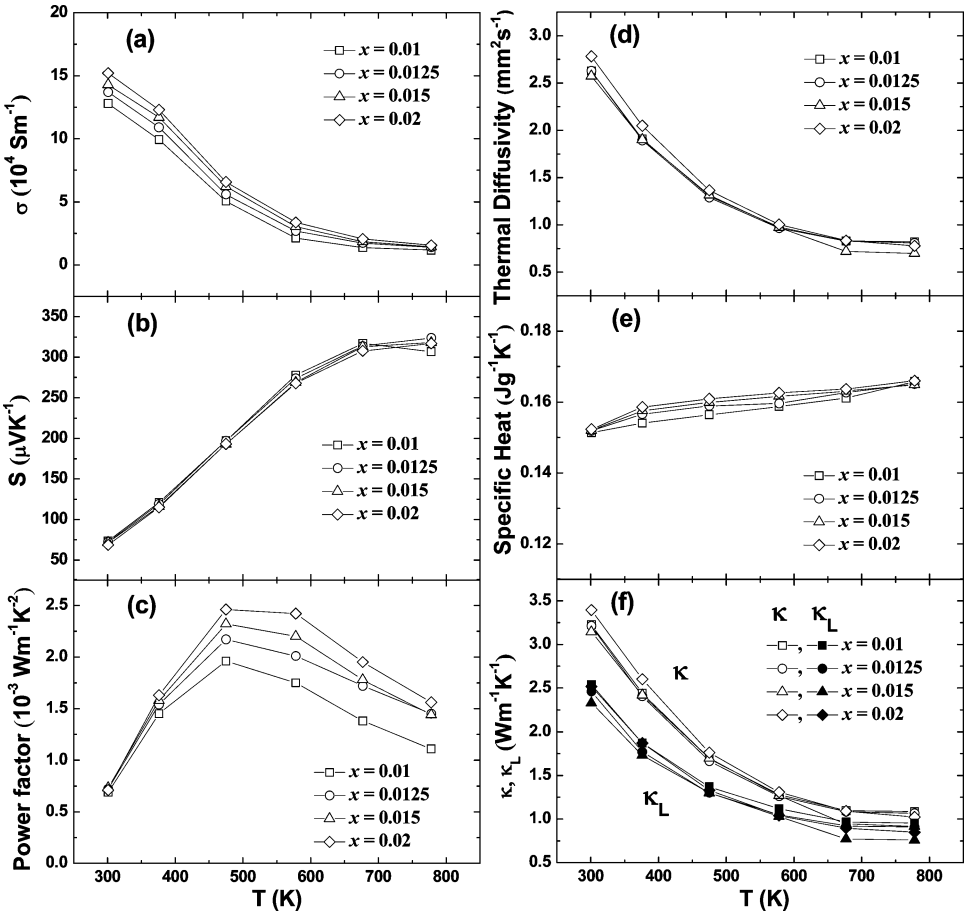


**Figure 1.** Temperature dependences of (a) electrical conductivity, (b) Seebeck coefficient, (c) power factor, (d) thermal diffusivity, (e) specific heat, and (f) total and lattice thermal conductivities for $K_xPb_{1-x}Te$ ($x$ = 0.01, 0.0125, 0.015, and 0.02).

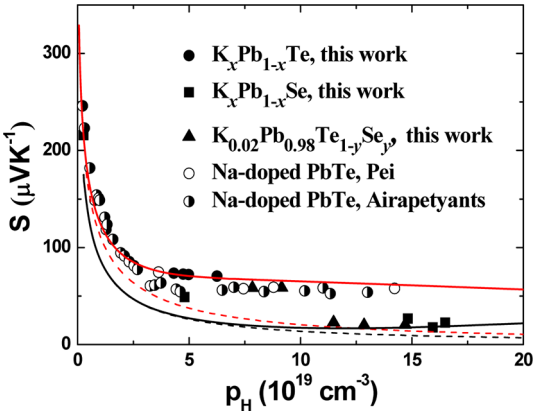


**Figure 2.** Room-temperature Pisarenko plots for (●) $K_xPb_{1-x}Te$ ($x$ = 0.01, 0.0125, 0.015, and 0.02), (■) $K_xPb_{1-x}Se$ ($x$ = 0, 0.005, 0.010, 0.0125, and 0.015), and (▲) $K_{0.02}Pb_{0.98}Te_{1-y}Se_y$ ($y$ = 0.15, 0.25, 0.75, 0.85, and 0.95). For comparison, data for Na-doped PbTe reported by (○) Pei et al.[20] and (◑) Airapetyants et al.[32] are also shown. The dashed black curve is based on a model employing a single nonparabolic band with a PbSe light-hole effective mass of $m^*/m_e$ = 0.28. The solid black curve is based on a two-band model (nonparabolic L band and parabolic Σ band) with a PbSe heavy-hole effective mass of $m^*/m_e$ = 2.5. The dashed red curve is based on a model employing a single nonparabolic band with a PbTe light-hole effective mass of $m^*/m_e$ = 0.36. The solid red curve is based on a two-band model (nonparabolic L band and parabolic Σ band) with a PbTe heavy-hole effective mass of $m^*/m_e$ = 2.

$$p_L = \frac{1}{3\pi^2}\left(\frac{2m_L^* k_B T}{h^2}\right)^{3/2} {}^0F_0^{3/2}(\eta, \beta) \tag{2}$$

where $k_B$ is Boltzmann's constant, $e$ is the electron charge, ${}^nF_k^m$ is the generalized Fermi function,[37] $\eta$ is the reduced Fermi level, $h$ is Planck's constant, and $m_L^*$ is the light-hole DOS effective mass, taken as $m_L^*/m_e$ = 0.36.[37] The nonparabolicity parameter, $\beta$, is given by $\beta = k_BT/E_g$, where $E_g$ is the L-point band gap. We assumed that deformation potential scattering by acoustic phonons dominates.[20,25,37] We also did the calculation including ionized impurity scattering for the nonparabolic L band. The relaxation time for ionized impurities, $\tau_I$, is much larger than that for deformation potential scattering, $\tau_D$. When the relaxation times were combined using Matheiessen's rule ($1/\tau = 1/\tau_I + 1/\tau_D$), there was almost no difference in $S_L$ relative to the result when only $\tau_D$ was included. For the heavy-hole band, taken along the Σ direction in the Brillouin zone,[37] the Seebeck coefficient $S_\Sigma$ and carrier concentration $p_\Sigma$ are given by

$$S_\Sigma = \frac{k_B}{e}\left[\frac{{}^1F_{-2}^1(\eta_\Sigma, 0)}{{}^0F_{-2}^1(\eta_\Sigma, 0)} - \eta_\Sigma\right] \tag{3}$$

$$p_\Sigma = \frac{1}{3\pi^2}\left(\frac{2m_\Sigma^* k_B T}{h^2}\right)^{3/2} {}^0F_0^{3/2}(\eta_\Sigma, 0) \tag{4}$$


dx.doi.org/10.1021/ja301245b | J. Am. Chem. Soc. 2012, 134, 10031−10038

where $m_\Sigma^*$ is the heavy-hole DOS effective mass, taken as $m_\Sigma^*/m_e = 2$,[38] and $\eta_\Sigma = \eta - \Delta E/k_BT$, where $\Delta E$ is the energy difference between the light-hole and heavy-hole band maxima, whose value is discussed below. It should be noted that for this parabolic band, $\beta = 0$. The total Seebeck coefficient from both hole bands, $S_{total}$, is taken to be:

$$S_{total} = \frac{\sigma_L S_L + \sigma_\Sigma S_\Sigma}{\sigma_L + \sigma_\Sigma} \quad (5)$$

where $\sigma_L$ and $\sigma_\Sigma$ are the electrical conductivities of the L and Σ bands, respectively.[37]

The total Hall carrier concentration for a two-band system, $p_H$, is related to the carrier concentrations in the two bands, $p_L$ and $p_\Sigma$, as described previously in refs 25 and 37 (this expression is provided in the Supporting Information and in refs 25 and 37). In Figure 2, the solid red line shows the calculated $S_{total}$ as a function of $p_H$ for PbTe. It can be seen that the data (solid circles) falls nicely on the flat part of the solid red line at $S \approx 75\ \mu V\ K^{-1}$, indicating a clear contribution from two bands as a result of K doping. Alternatively, Kanatzidis et al.[26] obtained a plateau at $S \approx 56\ \mu V\ K^{-1}$ using a light-hole effective mass of $\sim 0.2m_e$, which can explain Na-doped PbTe pretty well. The magnitude of the heavy-hole contribution was highlighted by examining a one-band light-hole model obtained by removing the contribution from the Σ band. This case gave the dashed red line shown in Figure 2, which falls well below the measured data at high carrier concentrations.

As the temperature increased, the Seebeck coefficient increased dramatically to $\sim 320\ \mu V\ K^{-1}$ at 775 K, a value much higher even than that for Na-doped PbTe ($\sim 260\ \mu V\ K^{-1}$ at 775 K), which is believed to be due to the two-band contribution.[20] In view of the fact that first-principles calculations predicted possible resonant states introduced by K doping,[28] it is likely that resonant doping may also play a minor role here in addition to the two-band contribution. However, we do not have enough evidence to support this because the Seebeck coefficient is not high enough. The limited carrier concentration of $< 6 \times 10^{19}\ cm^{-3}$ resulting from K doping restrains the increase in the electrical conductivity (shown in Figure 1 a), which is the determining factor when the $S$ flattens. Furthermore, the decrease in electrical conductivity with temperature is faster in K-doped samples, as exhibited by the values of $\delta$, the exponents in the power law for the electrical conductivity ($\sigma \approx T^{-\delta}$), presented in Table 1.

Generally speaking, the total thermal conductivity $\kappa$ is the sum of the charge-carrier thermal conductivity $\kappa_e$ and the lattice thermal conductivity $\kappa_L$. The value of $\kappa_e$ can be calculated via the Wiedemann–Franz relation, $\kappa_e = L\sigma T$, in which the Lorenz number $L$ is the same for the electrons and holes; $\kappa_L$ is then derived by subtracting $\kappa_e$ from $\kappa$. Values of $\kappa$ and $\kappa_L$ are presented in Figure 1f. Again, a multiband model was employed for the accurate estimation of $L$. This model gives the following expressions:[37]

$$L_L = \left(\frac{k_B}{e}\right)^2 \left\{ \frac{{}^2F_{-2}^1(\eta, \beta)}{{}^0F_{-2}^1(\eta, \beta)} - \left[\frac{{}^1F_{-2}^1(\eta, \beta)}{{}^0F_{-2}^1(\eta, \beta)}\right]^2 \right\} \quad (6)$$

$$L_\Sigma = \left(\frac{k_B}{e}\right)^2 \left\{ \frac{{}^2F_{-2}^1(\eta_\Sigma, 0)}{{}^0F_{-2}^1(\eta_\Sigma, 0)} - \frac{{}^1F_{-2}^1(\eta_\Sigma, 0)}{{}^0F_{-2}^1(\eta_\Sigma, 0)} \right\} \quad (7)$$

$$L_{total} = \frac{\sigma_L L_L + \sigma_\Sigma L_\Sigma}{\sigma_L + \sigma_\Sigma} \quad (8)$$

where $L_L$, $L_\Sigma$, and $L_{total}$ are the Lorenz numbers for the L band, the Σ band, and both bands, respectively. Because of the low electrical conductivity, the carrier thermal conductivity is also low. With almost the same lattice thermal conductivity (the same lattice scattering), we achieved a total thermal conductivity lower than that of Na-doped PbTe.[20] The highest $ZT$ value was ~1.3 at ~673 K for $K_{0.015}Pb_{0.985}Te$ (Figure 3), which is comparable with that of Na-doped PbTe at the same temperature.[20]

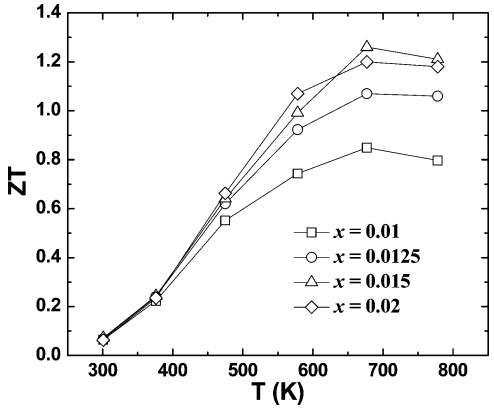


**Figure 3.** Temperature dependence of $ZT$ for $K_xPb_{1-x}Te$ ($x$ = 0.01, 0.0125, 0.015, and 0.02).

In both the PbTe and PbSe systems, $K^+$ and $Na^+$ dopants substitute for $Pb^{2+}$, and both K and Na have lower Pauling electronegativities (PE) than Pb (Table 2). In spite of their comparable ionic radii, the solubilities of K and Na are determined by the difference in the electronegativities of the average anion ($Te^{2-}$ or $Se^{2-}$) and cation ($Pb^{2+}$ together with $K^+$ or $Na^+$) after doping. Typically, a larger difference results in higher solubility. Since K has a lower electronegativity than Na, the average cation electronegativity after doping is lower in the case of K substitution. For PbTe, a lower average cation electronegativity reduces the electronegativity difference relative to the difference for $Te^{2-}$ and $Pb^{2+}$ without doping, so K has less solubility than Na in PbTe. For PbSe, the situation is opposite (a lower average cation electronegativity enlarges the electronegativity difference relative to $Se^{2-}$ and $Pb^{2+}$ without doping), so K has a higher solubility than Na in PbSe.

Samples of $K_xPb_{1-x}Se$ with different K concentrations ($x$ = 0, 0.005, 0.010, 0.0125, and 0.015) were prepared and measured. The electrical conductivity, Seebeck coefficient, power factor, thermal diffusivity, specific heat, and thermal conductivity are shown in Figure 4a–f, respectively. It is clear that for $x \geq 0.01$, the electrical conductivity increased dramatically. The room-temperature Hall carrier concentration increased to $\sim 1.6 \times 10^{20}\ cm^{-3}$ (Figure 2, solid squares). Again we constructed the room-temperature Pisarenko plots for the single nonparabolic band model (dashed black line) and the two-band model (solid black line). For PbSe, we used $m_L^*/m_e = 0.28$ for the light-hole effective mass[23] and $m_\Sigma^*/m_e = 2.5$ for the heavy-hole effective mass, which was obtained from a first-principles calculation.[39] There was not much difference between the two models, suggesting that most of the contribution comes from the L band at room temperature, which agrees well with the previous


dx.doi.org/10.1021/ja301245b | J. Am. Chem. Soc. 2012, 134, 10031–10038

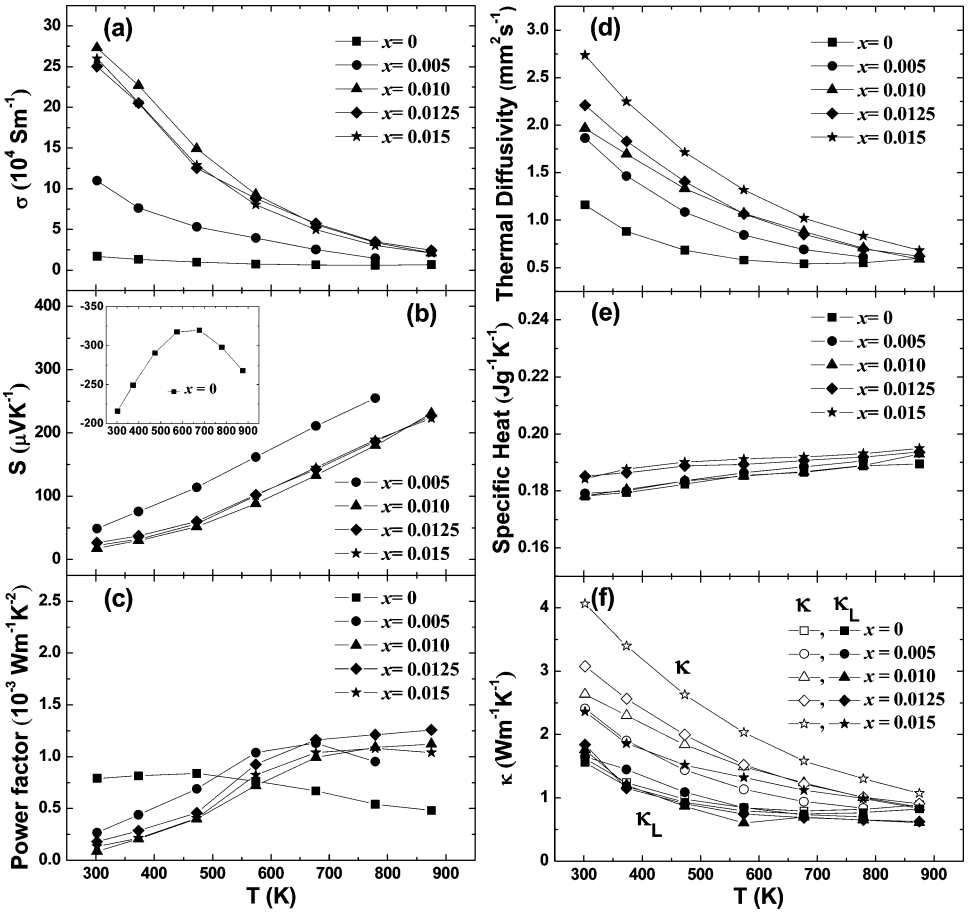


**Figure 4.** Temperature dependences of (a) electrical conductivity, (b) Seebeck coefficient, (c) power factor, (d) thermal diffusivity, (e) specific heat, and (f) total and lattice thermal conductivities for $K_xPb_{1-x}Se$ ($x$ = 0, 0.005, 0.010, 0.0125, and 0.015).

results.[22] The pinning of the Fermi level by the heavy band happens only at high temperatures when the offset value of the two bands is small enough. A high Seebeck coefficient of ~210 $\mu$V $K^{-1}$ at 875 K was obtained with the contribution from both bands. Since the band gap of PbSe increases with temperature (~0.43 eV at 850 K vs ~0.28 eV at 300 K), the Seebeck coefficient goes up all the way with increasing temperature without any sign of the bipolar effect. Low lattice thermal conductivities of ~1.7 W $m^{-1}$ $K^{-1}$ at 300 K and ~0.6 W $m^{-1}$ $K^{-1}$ at high temperature, similar to the previously reported values,[22] were calculated here for K-doped PbSe using $L$ obtained from eqs 6−8. We noticed that the electrical conductivity decreased rapidly with increasing temperature, as indicated by the $\delta$ values shown in Table 1. However, with the high starting point of the electrical conductivity and the high Seebeck coefficient, the maximum $ZT$ value reached was ~1.2 at 873 K (Figure 5), although the average $ZT$ was clearly lower than that for K-doped $K_xPb_{1-x}Te$. Both the maximum $ZT$ and the average $ZT$ were comparable to those for Na-doped PbSe.

After studying K doping in PbTe and PbSe independently, we turned our attention to studying K doping in $PbTe_{1-y}Se_y$, with the aim of simultaneously increasing the power factor and further reducing the thermal conductivity to achieve higher $ZT$ values. We fixed the K concentration in the Pb sites at 2% on the basis of the results for K in PbTe and PbSe, and we examined different Se concentrations in $K_{0.02}Pb_{0.98}Te_{1-y}Se_y$: $y$ = 0.15, 0.25, 0.75, 0.85, and 0.95. All of the the XRD patterns (Figure 6) showed a single phase with the fcc rock salt

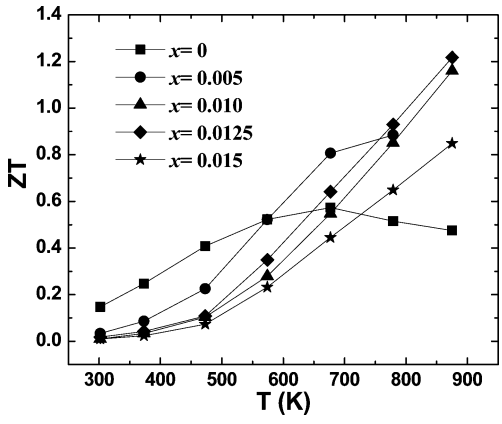


**Figure 5.** Temperature dependence of $ZT$ for $K_xPb_{1-x}Se$ ($x$ = 0, 0.005, 0.010, 0.0125, and 0.015).

structure. The peaks shifted to higher $2\theta$ with increasing Se concentration because of the smaller lattice parameters. The good solid solution formation was confirmed by the good fit to Vegard's law (Figure 6 inset).

Figure 7 shows the room-temperature Hall carrier concentration as a function of (a) K and (b) Se concentration. With the help of Se, the Hall carrier concentration was effectively increased from $<6 \times 10^{19}$ $cm^{-3}$ in PbTe to the optimized concentration of $(8-15) \times 10^{19}$ $cm^{-3}$ for $PbTe_{1-y}Se_y$, consistent with the values observed in the previous reports.[20,22] The room-temperature Pisarenko plot for the


dx.doi.org/10.1021/ja301245b | J. Am. Chem. Soc. 2012, 134, 10031−10038

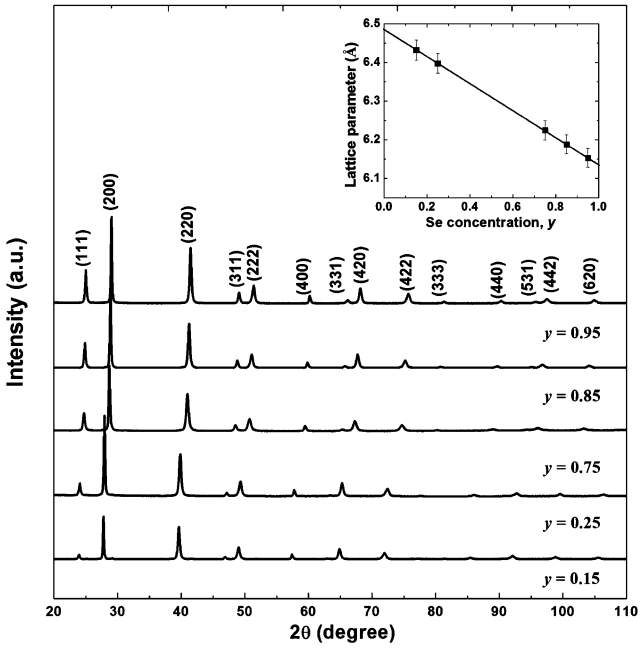


**Figure 6.** XRD patterns for $K_{0.02}Pb_{0.98}Te_{1-y}Se_y$ ($y$ = 0.15, 0.25, 0.75, 0.85, and 0.95). The inset shows the lattice parameter relation with increasing Se concentration in $K_{0.02}Pb_{0.98}Te_{1-y}Se_y$.

$K_{0.02}Pb_{0.98}Te_{1-y}Se_y$ solid solution samples is shown in Figure 2 (solid triangles). The noticeable deviation of the Seebeck coefficient from the single-band model (dashed red line) for $K_{0.02}Pb_{0.98}Te_{1-y}Se_y$ ($y$ = 0.15 and 0.25) supports the effects of heavy-hole bands. Because of the relatively low effective mass and larger energy difference between heavy-hole and light-hole band edges, $\Delta E$, in PbSe, the Seebeck coefficients are lower than those of K-doped PbTe (solid circles). For $K_{0.02}Pb_{0.98}Te_{1-y}Se_y$ ($y$ = 0.75, 0.85, and 0.95), more features come from K-doped PbSe. As the temperature increases, the two bands start to converge. We obtained good fits to the data using the energy differences between the conduction (C) band edge and the L and Σ band edges:

$$\Delta E_{C-L} = 0.18 + (4T/10000) - 0.04y$$
$$\Delta E_{C-\Sigma} = 0.42 + 0.10y \quad (9)$$

where $y$ is the concentration of Se.[37,40] It has been concluded that the convergence of the electronic bands can provide more benefit for the enhancement of the Seebeck coefficient by multiple bands.[25] However, when $y$ = 0 (PbTe), the L band will gradually move below the Σ band at a certain temperature and depart from the convergence. Thus, using Se to increase the convergence temperature ($T_{cvg}$) gives the most optimized Seebeck coefficient at high temperature (Figure 8 b). With

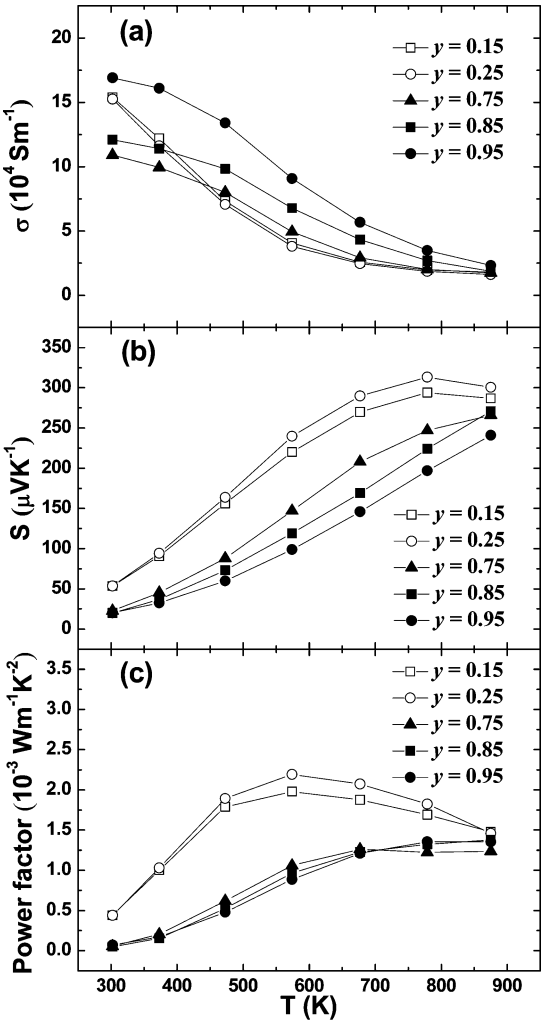


**Figure 8.** Temperature dependences of (a) electrical conductivity, (b) Seebeck coefficient, and (c) power factor for $K_{0.02}Pb_{0.98}Te_{1-y}Se_y$ ($y$ = 0.15, 0.25, 0.75, 0.85, and 0.95).

increasing Se concentration, the temperature for the highest Seebeck coefficient increased. The highest Seebeck coefficient was ~320 $\mu$V K$^{-1}$ at 775 K, which is much higher than the value of ~220 $\mu$V K$^{-1}$ for Na-doped $PbTe_{1-y}Se_y$ at 775 K. The

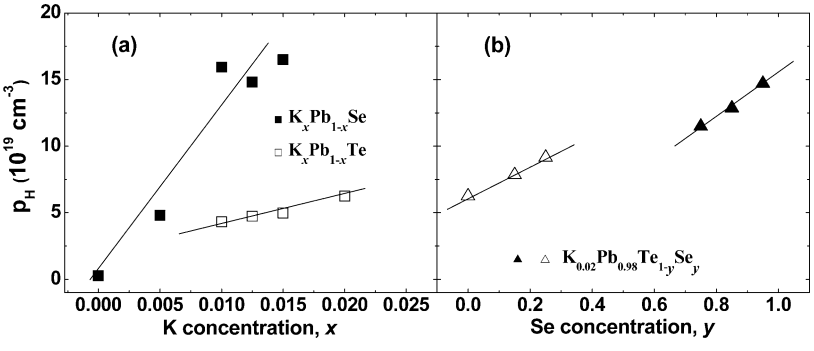


**Figure 7.** Hall carrier concentration at room temperature as a function of (a) K and (b) Se concentration.


dx.doi.org/10.1021/ja301245b | J. Am. Chem. Soc. 2012, 134, 10031−10038

successfully improved carrier concentration compensates for the loss in the carrier mobility resulting from the increased scattering of the electrons, which keeps the electrical conductivity the same at low temperature (Figure 8a). Fortunately, the decrease in the electrical conductivity is slowed with temperature, giving a smaller $\delta$ (Table 1). As a result, the power factor is enhanced at high temperature (Figure 8c).

The other obvious but very important role that Se plays is to decrease the lattice thermal conductivity by alloying scattering when it is used together with Te. The thermal diffusivity, specific heat, and total and lattice thermal conductivities for $K_{0.02}Pb_{0.98}Te_{1-y}Se_y$ ($y$ = 0.15, 0.25, 0.75, 0.85, and 0.95) are shown in Figure 9a–c, respectively. The increased lattice

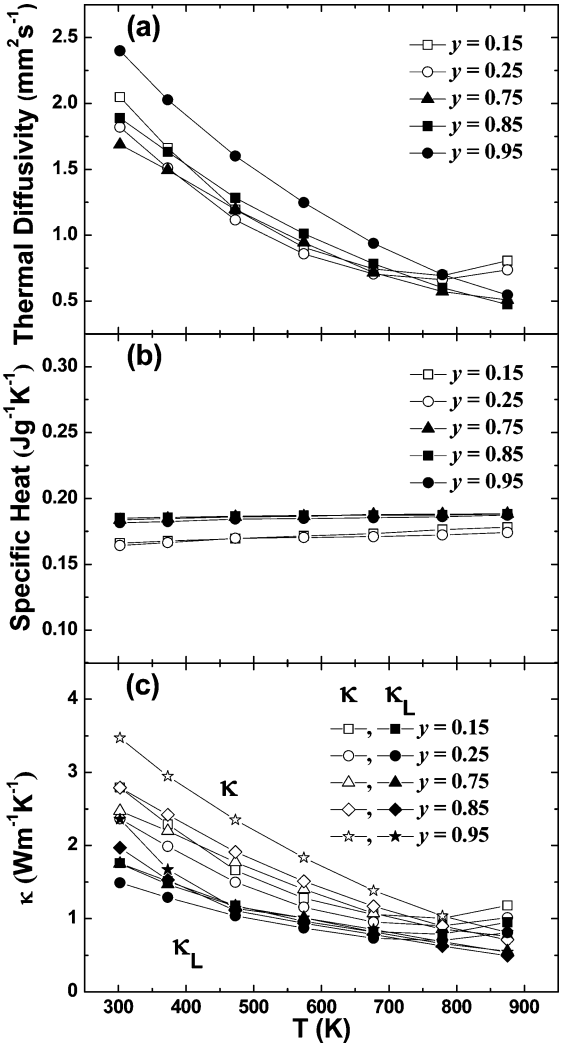


**Figure 9.** Temperature dependences of (a) thermal diffusivity, (b) specific heat, and (c) total and lattice thermal conductivities for $K_{0.02}Pb_{0.98}Te_{1-y}Se_y$ ($y$ = 0.15, 0.25, 0.75, 0.85, and 0.95).

thermal conductivities at 800 K (Figure 9 c) may come from the error in the calculated values of $L$ without considering the contribution from conduction band. It seems that increasing the Se concentration ($K_{0.02}Pb_{0.98}Te_{0.15}Se_{0.85}$) can increase the peak $ZT$ to ~1.7 at ~873 K in comparison with the value of ~1.6 in $K_{0.02}Pb_{0.98}Te_{0.75}Se_{0.25}$ at ~773 K (Figure 10), but the Te-rich composition is clearly more promising for any applications below 873 K since the average $ZT$ values are much higher.

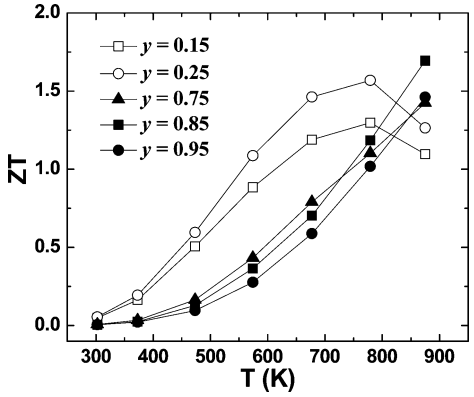


**Figure 10.** Temperature dependence of $ZT$ for $K_{0.02}Pb_{0.98}Te_{1-y}Se_y$ ($y$ = 0.15, 0.25, 0.75, 0.85, and 0.95).

Up to now, only Tl has been shown to induce resonant states in p-type PbTe, resulting in an extraordinary increase in the Seebeck coefficient.[18] However, with the help of a second valence band in PbTe, high $ZT$ values can also be obtained by heavy doping with Na, K, and Mg, especially when combined with the alloy scattering introduced by PbSe or PbS.[20,25,26,41,42] Additionally, typical nanostructures have been created in the PbTe matrix to lower the lattice thermal conductivity by addition of a second phase and ball milling.[43,44] Other group IIIA elements (Al, Ga, and In),[45−47] group VIIA elements,[21] and some rare-earth elements[48] have proved to be good n-type dopants. A $ZT$ value of >1.5 at 775 K was reached in La-doped PbTe with $Ag_2Te$ nanoscale precipitates.[48] With decent $ZT$s in both p-type and n-type doping, PbTe is a promising candidate for thermoelectric applications in the near future.

## CONCLUDING REMARKS

Potassium, an acceptor dopant in $K_xPb_{1-x}Te_{1-y}Se_y$, can strongly enhance the Seebeck coefficient by activating the heavy-hole band via heavy doping, which increases the DOS near the Fermi level. Combined with a lower lattice thermal conductivity due to increased point defects and the increased electrical conductivity at high temperature, higher peak $ZT$ values of ~1.6 and ~1.7 were obtained in Te-rich samples $K_{0.02}Pb_{0.98}Te_{0.75}Se_{0.25}$ at 773 K and Se-rich samples $K_{0.02}Pb_{0.98}Te_{0.15}Se_{0.85}$ at 873 K, respectively, but the average $ZT$ of the Te-rich samples was much higher than those of the Se-rich samples. Since Te is more expensive than Se, however, a trade-off between cost and performance needs to be considered for practical applications.

## ASSOCIATED CONTENT

### Supporting Information

Microstructures and chemical compositions for some samples; room-temperature Pisarenko plots for $K_xPb_{1-x}Te$ ($x$ = 0.01, 0.0125, 0.015, and 0.02), $K_xPb_{1-x}Se$ ($x$ = 0, 0.005, 0.010, 0.0125, and 0.015), and $K_{0.02}Pb_{0.98}Te_{1-y}Se_y$ ($y$ = 0.15, 0.25, 0.75, 0.85, and 0.95) with the fitting line based on $\Delta E_{C-\Sigma}$ = 0.36 eV (see ref 40); and the relationship between carrier concentration and Hall carrier concentration for PbTe and PbSe. This material is available free of charge via the Internet at http://pubs.acs.org.

## AUTHOR INFORMATION


### Corresponding Author

gchen2@mit.edu; renzh@bc.edu


### Notes

The authors declare no competing financial interest.

## ACKNOWLEDGMENTS

This work was supported by "Solid State Solar-Thermal Energy Conversion Center ($S^3$TEC)", an Energy Frontier Research Center funded by the U.S. Department of Energy, Office of Science, Office of Basic Energy Sciences under Award DE-SC0001299 (G.C. and Z.R.), and National Science Foundation under grant No. 1066634 (D.B.).

## REFERENCES


(1) Rowe, D. M. *CRC Handbook of Thermoelectrics*; CRC Press: Boca Raton, FL, 1995.

(2) Disalvo, F. J. *Science* **1999**, *285*, 703.

(3) Kraemer, D.; Poudel, B.; Feng, H. P.; Cavlor, J. C.; Yu, B.; Yan, X.; Ma, Y.; Wang, X. W.; Wang, D. Z.; Muto, A.; McEnaney, K.; Chiesa, M.; Ren, Z. F.; Chen, G. *Nat. Mater.* **2011**, *10*, 532.

(4) Harman, T. C.; Taylor, P. J.; Walsh, M. P.; LaForge, B. E. *Science* **2002**, *297*, 2229.

(5) Yan, X.; Joshi, G.; Liu, W. S.; Lan, Y. C.; Wang, H.; Lee, S.; Simonson, J. M.; Poon, S. J.; Tritt, T. M.; Chen, G.; Ren, Z. F. *Nano Lett.* **2011**, *11*, 556.

(6) Zhang, Q.; He, J.; Zhu, T. J.; Zhang, S. N.; Zhao, X. B.; Tritt, T. M. *Appl. Phys. Lett.* **2008**, *93*, No. 102109.

(7) Poudel, B.; Hao, Q.; Ma, Y.; Lan, Y. C.; Minnich, A.; Yu, B.; Yan, X.; Wang, D. Z.; Muto, A.; Vashaee, D.; Chen, X.; Liu, J.; Dresselhaus, D. S.; Chen, G.; Ren, Z. F. *Science* **2008**, *320*, 634.

(8) Sales, B. C.; Mandrus, D.; Williams, R. K. *Science* **1996**, *272*, 1325.

(9) Yu, C.; Zhu, T. J.; Zhang, S. N.; Zhao, X. B.; He, J.; Su, Z.; Tritt, T. M. *J. Appl. Phys.* **2008**, *104*, No. 013705.

(10) Kleinke, H. *Chem. Mater.* **2010**, *22*, 604.

(11) Dresselhaus, M. S.; Chen, G.; Tang, M. Y.; Yang, R. G.; Lee, H.; Wang, D. Z.; Ren, Z. F.; Fleurial, J. P.; Gogna, P. *Adv. Mater.* **2007**, *19*, 1043.

(12) Liu, W. S.; Yan, X.; Chen, G.; Ren, Z. F. *Nano Energy* **2012**, *1*, 42.

(13) Martin, J.; Wang, L.; Chen, L. D.; Nolas, G. S. *Phys. Rev. B* **2009**, *79*, No. 115311.

(14) Faleev, S. V.; Leonard, F. *Phys. Rev. B* **2008**, *77*, No. 214304.

(15) Zhang, Q.; Zhang, Q. Y.; Chen, S.; Liu, W. S.; Lukas, K.; Yan, X.; Wang, H. Z.; Wang, D. Z.; Opeil, C.; Chen, G.; Ren, Z. F. *Nano Energy* **2012**, *1*, 183.

(16) Scheele, M.; Oeschler, N.; Meier, K.; Kornowski, A.; Linke, C.; Weller, H. *Adv. Funct. Mater.* **2009**, *19*, 1.

(17) Zhang, Q.; Sun, T.; Cao, F.; Li, M.; Hong, M. H.; Yuan, J. K.; Yan, Q. Y.; Hng, H. H.; Wu, N. Q.; Liu, X. G. *Nanoscale* **2010**, *2*, 1256.

(18) Heremans, J. P.; Jovovic, V.; Toberer, E. S.; Samarat, A.; Kurosaki, K.; Charoenphakdee, A.; Yamanaka, S.; Snyder, G. J. *Science* **2008**, *321*, 554.

(19) Yu, B.; Zhang, Q. Y.; Wang, H.; Wang, X. W.; Wang, H. Z.; Wang, D. Z.; Snyder, G. J.; Chen, G.; Ren, Z. F. *J. Appl. Phys.* **2010**, *108*, No. 016104.

(20) Pei, Y.; LaLonde, A.; Iwanaga, S.; Snyder, G. J. *Energy Environ. Sci.* **2011**, *4*, 2085.

(21) LaLonde, A. D.; Pei, Y. Z.; Snyder, G. J. *Energy Environ. Sci.* **2011**, *4*, 2090.

(22) Wang, H.; Pei, Y.; LaLonde, A. D.; Snyder, G. J. *Adv. Mater.* **2011**, *23*, 1366.

(23) Zhang, Q. Y.; Wang, H.; Liu, W. S.; Wang, H. Z.; Yu, B.; Zhang, Q.; Tian, Z. T.; Ni, G.; Lee, S.; Esfarjani, K.; Chen, G.; Ren, Z. F. *Energy Environ. Sci.* **2012**, *5*, 5246.

(24) Androulakis, J.; Lee, Y.; Todorov, I.; Chung, D. Y.; Kanatzidis, M. *Phys. Rev. B* **2011**, *83*, No. 195209.

(25) Pei, Y.; Shi, X.; LaLonde, A.; Wang, H.; Chen, L.; Snyder, G. J. *Nature* **2011**, *473*, 66.

(26) Androulakis, J.; Todorov, I.; Chung, D.-Y.; Ballikaya, S.; Wang, G.; Uher, C.; Kanatzidis, M. *Phys. Rev. B* **2010**, *82*, No. 115209.

(27) Delaire, O.; Ma, J.; Marty, K.; May, A. F.; McGuire, M. A.; Du, M. H.; Singh, D. J.; Podlesnyak, A.; Ehlers, G.; Lumsden, M. D.; Sales, B. C. *Nat. Mater.* **2011**, *10*, 614.

(28) Ahmad, S.; Mahanti, S. D.; Hoang, K.; Kanatzidis, M. G. *Phys. Rev. B* **2006**, *74*, No. 155205.

(29) Xiong, K.; Lee, G.; Gupta, R. P.; Wang, W.; Gnade, B. E.; Cho, K. *J. Phys. D: Appl. Phys.* **2010**, *43*, No. 405403.

(30) Ahmad, S.; Hoang, K.; Mahanti, S. D. *Phys. Rev. Lett.* **2006**, *96*, No. 056403.

(31) Singh, D. J. *Phys. Rev. B* **2010**, *81*, No. 195217.

(32) Airapetyants, S. V.; Vinogradova, M. N.; Dubrovskaya, I. N.; Kolomoets, N. V.; Rudnik, I. M. *Sov. Phys. Solid State* **1966**, *8*, 1069.

(33) Khokhlov, D. *Lead Chalcogenides: Physics and Applications*; Taylor & Francis; New York, 2003.

(34) Allgaier, R. S. *J. Appl. Phys.* **1961**, *32*, 2185.

(35) Parker, D.; Singh, D. J. *Phys. Rev. B* **2010**, *82*, No. 035204.

(36) Noda, Y.; Orihashi, M.; Nishida, I. A. *Mater. Trans., JIM* **1998**, *39*, 602.

(37) Ravich, Y. I.; Efimova, B. A.; Smirnov, I. A. *Semiconducting Lead Chalcogenides*; Plenum Press: New York, 1970.

(38) Crocker, A. J.; Rogers, L. M. *Br. J. Appl. Phys.* **1967**, *18*, 563.

(39) Svane, A.; Christensen, N. E.; Cardona, M.; Chantis, A. N.; van Schilfgaarde, M.; Kotani, T. *Phys. Rev. B* **2010**, *81*, No. 245120.

(40) It should be noted that the gap between conduction and heavy-hole bands in PbTe is typically taken to be $\Delta E_{C-\Sigma} = 0.36$ eV. As shown in the Supporting Information, we found a poorer fit to the data using this value of $\Delta E_{C-\Sigma}$ in comparison with the value of 0.42 eV given in eq 9.

(41) Jaworski, C. M.; Wiendlocha, B.; Jovovic, V.; Heremans, J. P. *Energy Environ. Sci.* **2011**, *4*, 4155.

(42) Pei, Y. Z.; LaLonde, A. D.; Heinz, N. A.; Shi, X. Y.; Lwanaga, S.; Wang, H.; Chen, L. D.; Snyder, G. J. *Adv. Mater.* **2011**, *23*, 5674.

(43) Biswas, K.; He, J. Q.; Zhang, Q. C.; Wang, G. Y.; Uher, C.; Dravid, V. P.; Kanatzidis, M. G. *Nat. Chem.* **2011**, *3*, 160.

(44) Zhang, Q. Y.; Wang, H. Z.; Zhang, Q.; Liu, W. S.; Yu, B; Wang, H.; Wang, D. Z.; Ni, G.; Chen, G.; Ren, Z. F. *Nano Lett.* **2012**, *12*, 2324.

(45) Jaworski, C. M.; Heremans, J. P. *Phys. Rev. B* **2012**, *85*, No. 033204.

(46) Volkov, B. A.; Ryabova, L. I.; Khokhlov, D. R. *Phys. Usp.* **2002**, *45*, 819.

(47) Jovovic, V.; Thiagarajan, S. J.; Heremans, J. P.; Komissarova, T.; Khokhlov, D.; Nicorici, A. *J. Appl. Phys.* **2008**, *103*, No. 053710.

(48) Pei, Y. Z.; Lensch-Falk, J.; Toberer, E. S.; Medlin, D. L.; Snyder, G. J. *Adv. Funct. Mater.* **2011**, *21*, 241.

Nanotechnology **23** (2012) 505402 (7pp) doi:10.1088/0957-4484/23/50/505402

# Figure-of-merit enhancement in nanostructured $FeSb_{2-x}Ag_x$ with $Ag_{1-y}Sb_y$ nanoinclusions

**Huaizhou Zhao[1,3], Mani Pokharel[1,3], Shuo Chen[1], Bolin Liao[2], Kevin Lukas[1], Cyril Opeil[1], Gang Chen[2] and Zhifeng Ren[1]**

[1] Department of Physics, Boston College, Chestnut Hill, MA 02467, USA
[2] Department of Mechanical Engineering, Massachusetts Institute of Technology, Cambridge, MA 02139, USA

E-mail: zhifeng.ren@bc.edu

Received 27 August 2012, in final form 28 October 2012
Published 29 November 2012
Online at stacks.iop.org/Nano/23/505402

**Abstract**

We present the figure-of-merit ($ZT$) improvement in nanostructured $FeSb_{2-x}Ag_x$ with $Ag_{1-y}Sb_y$ nanoinclusions through a metal/semiconductor interface engineering approach. Owing to the interfaces between $FeSb_{2-x}Ag_x$ and $Ag_{1-y}Sb_y$ phases, as well as the identical work functions, both thermal conductivity and electrical resistivity of the nanocomposites were significantly reduced in the lower temperature regime compared with pure $FeSb_2$. Overall, an improvement of 70% in $ZT$ was achieved for the optimized nanocomposite $FeSb_{1.975}Ag_{0.025}/Ag_{0.77}Sb_{0.23}$ sample, in which $Ag_{0.77}Sb_{0.23}$ is about 10% by molar ratio. The results of this approach clearly demonstrated the metal/semiconductor interface concept and confirmed the potential of strongly correlated material systems as promising thermoelectric materials.

(Some figures may appear in colour only in the online journal)

## 1. Introduction

As one of the promising technologies in waste-heat recovery and cooling applications, solid-state conversion between heat and electrical power using thermoelectric materials has stimulated enormous efforts and enthusiasm in the last decade. The figure of merit ($ZT$) of thermoelectric materials, determining the conversion efficiency, has almost been doubled in the last couple of years in a few traditional materials. It is well known that $ZT = (s^2\sigma/\kappa)T$, where $S, \sigma, \kappa$, and $T$ are the Seebeck coefficient, electrical conductivity, thermal conductivity, and absolute temperature, respectively. The competitive nature of these components makes it difficult to enhance the $ZT$ by adjusting any of the individual properties without affecting others. The currently developed approaches, such as nanostructures reducing lattice thermal conductivity [1–4], resonant doping [5–7], band engineering [8, 9] at the Fermi level, as well as modulation doping providing additional electrical conductivity channels [10, 11], have been proved to be efficient in a few material systems. In the literature, the metal/semiconductor interface concept was proposed theoretically and testified experimentally in a few cases for their potential application in thermoelectric materials [12–17]. Indeed, modeling shows that, by introducing uniformly distributed metal nanoparticles to the three-dimensional semiconductor structure, either electronic ($\kappa_e$) or phononic ($\kappa_{ph}$) thermal conductivity, and thus $\kappa_{total} = \kappa_e + \kappa_{ph}$, can be suppressed dramatically [14]. Furthermore, due to the energy barrier ($V_B$) built between metal nanoparticles and the host semiconductor at the interfaces, the lower energy carrier could be scattered, which would result in a reduced electrical conductivity but an enhanced Seebeck coefficient. As a result, the power factor ($PF = s^2\sigma$) could be enhanced and an enhanced $ZT$ could be expected. However, for a phononic ($\kappa_{ph}$) thermal conductivity dominated system, the modeling showed that a much smaller $V_B$ than 0.03 eV is preferred to secure an even slightly enhanced $PF$ [14], and zero energy barriers at the interface would be expected in the real case

[3] These authors contributed equally to this work.

 © 2012 IOP Publishing Ltd Printed in the UK & the USA

even though there is no net gain on *PF*. Overall, for a phononic ($\kappa_{ph}$) thermal conductivity dominated system, the enhanced *ZT* could be expected solely from the reduced thermal conductivity through the metal/semiconductor nanocomposite approach. In reality, due to the difficulty matching the semiconductor with the right metals, there has been no convincing demonstration of this concept.

Low temperature thermoelectric materials are usually semimetals or narrow bandgap semiconductors [18]. Correlated material and Kondo systems, such as $CeB_6$ [19], $YbAl_3$ [20], FeSi [21], and $FeSb_2$ [22–28], are promising thermoelectric materials for cryogenic cooling applications, although their *ZT* values are still too low to be considered for real use at this point. Among them, $FeSb_2$ shows extraordinary large *S* and *PF* despite the variations in its magnitude reported and the arguments of the physical origin of such a high *S* [22, 26, 28]. Doping and nanostructures have been adopted in efforts to reduce its phonon dominated thermal conductivity while trying to maintain the high *S* [4, 24, 25]. Although improvements have been achieved in $FeSb_2$ nanocomposite and Te-doped single crystals, further progress seems elusive because of the extreme sensitivity of the Seebeck coefficient to its electron carrier concentrations and the difficulty in further suppressing the thermal conductivity.

In this report, based on the identical work functions at certain crystal faces for $FeSb_2$ and Ag, we have found that Ag might be the matched metal phase to fabricate the metal/semiconductor interface for $FeSb_2$. We designed three-dimensional metal/semiconductor interfaces by adding Ag nanoparticles to form $Ag_{1-y}Sb_y$ nanoparticles in nanostructured $FeSb_{2-x}Ag_x$. Resulting from the chemical reaction between Ag and Sb, a nanocomposite of $FeSb_{1.975}Ag_{0.025}$ with 10% $Ag_{0.77}Sb_{0.23}$ by molar ratio was created and demonstrated to have much enhanced *ZT*, a 70% improvement, in comparison with the pure nanostructured $FeSb_2$. This result exemplified the possible demonstration of the concept of a metal/semiconductor interface in thermoelectric material systems. The same approach can also be extended to other strongly correlated materials or Kondo systems for thermoelectric properties enhancement.

## 2. Experiments and methods

The $FeSb_{2-x}Ag_x/Ag_{1-y}Sb_y$ nanocomposites were synthesized by the following procedure. First, $FeSb_2$ nanopowder was synthesized through high temperature melting and quenching, followed by 12 h ball milling as we reported before [4]. Then various numbers of Ag nanoparticles (NPs) (100 nm, Aldrich) were added to the synthesized $FeSb_2$ powders with the targeted final nominal composition $FeSb_2Ag_m$ with $m = 0.028, 0.056, 0.11, 0.22$, and 0.33. Together with the $FeSb_2$ nanopowder, each individual composition having the weight of 5 g was further mixed via ball milling for 3 h. The direct current (dc) hot pressing method was used to prepare disk samples from the final powders with different compositions. All disk samples were pressed at 200 °C and 80 MPa for 2 min, resulting densities in the range of 5.91–6.01 g $cm^{-3}$, about 76.8%–78.1% of the theoretical densities of 7.70 g $cm^{-3}$.

The final hot pressed products were characterized by x-ray diffraction (XRD, Bruker AXS) for phase identification, scanning electron microscopy (SEM, JEOL 6340F) for texturing and grain size distributions, and transmission electron microscopy (TEM) and scanning transmission electron microscopy (STEM) (JEOL 2010F, which is equipped with both TEM and STEM mode) for detailed structures of the optimized nanocomposite sample with nominal composition $FeSb_2Ag_{0.11}$. The STEM samples were prepared as follows: a small piece of disk sample was gently hand ground, and the obtained suspension was dipped onto a typical carbon-coated Cu grid, which can be used for STEM observation after drying. The edge area of the grains was selected for observations.

The temperature dependent electrical resistivity ($\rho$), Seebeck coefficient (*S*), thermal conductivity ($\kappa$), and Hall coefficient ($R_H$) were measured on a Physical Property Measurement System (PPMS) from Quantum Design using the thermal transport option (TTO). Gold leads were soldered onto samples with dimensions $3 \times 3 \times 5$ $mm^3$. The Seebeck coefficient, thermal conductivity and electrical resistivity were measured on a bar sample of dimensions $3 \times 3 \times 5$ $mm^3$. The normal two-point TTO option of the PPMS was used. As a check, the thermal and electrical conductivities for the sample $FeSb_2$ were measured in both two-point and four-point configurations. The values from the two configurations agreed well within the experimental error, showing negligible effect of the contact resistances. A piece with dimensions $1 \times 3 \times 10$ $mm^3$ was cut out of the same disk for Hall coefficient measurement. All the properties were measured in the direction perpendicular to the hot pressing direction.

The Hall coefficient $R_H(T)$ was determined under a magnetic field 9 T and a current of 20 mA. Five platinum wires were spark welded onto the Hall sample, and for the four-point resistivity measurement one of the wires was left unconnected. Within the one-band model, the charge carrier concentration was determined by $n = 1/(e|R_H|)$. The Hall mobility was determined by $\mu_H = |R_H|/\rho$. The Hall effect $R_H(T)$ measurements were performed on all samples.

To investigate the property of the metal/semiconductor interfaces between $FeSb_{2-x}Ag_x$ and $Ag_{1-y}Sb_y$ nanoparticles, it is necessary to know the work functions of both materials. Since it is not trivial to extract the work function value of $FeSb_2$ experimentally, here we adopt an alternative approach to roughly estimate the work function of $FeSb_2$ via first-principles calculation based on the density functional theory (DFT). A standard 'slab-supercell method' is used [29]. Slab-supercells are constructed by stacking layers of atoms for (001), (010), and (100) planes with 16 Å vacuum between each two slabs. The DFT calculation is implemented using the Quantum ESPRESSO package [30]. The Perdew–Zunger pseudopotentials with the local density approximation (LDA) are used, which we believe is sufficient to give a reasonable estimation. The plane wave cut-off energy is chosen as 80 Ryd to guarantee the convergence of the total energy and charge density distribution, and the convergence with the *k*-mesh

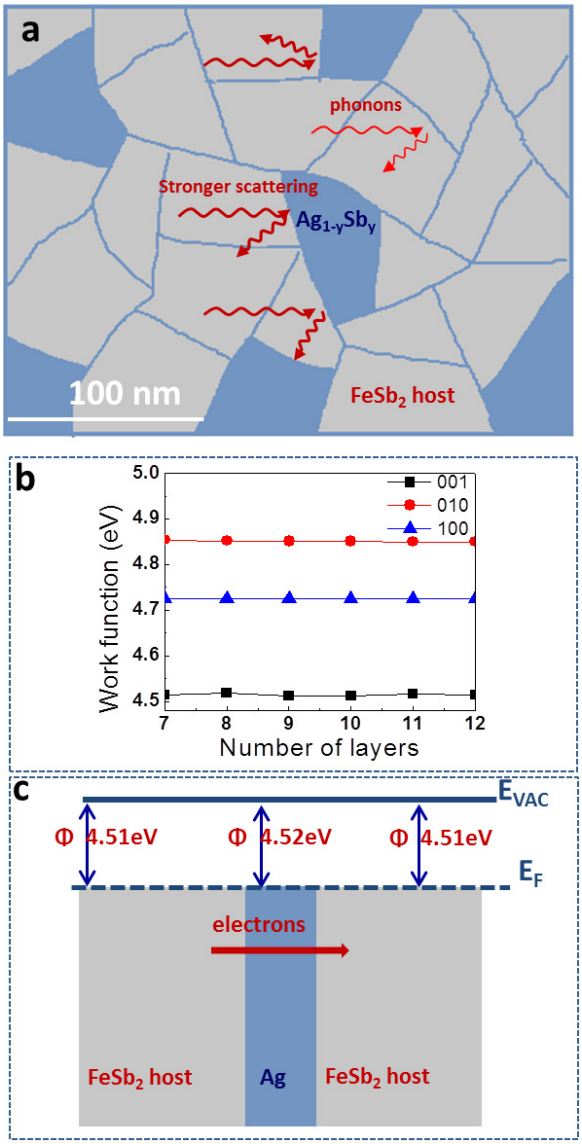


**Figure 1.** Schematics of the phonon scattering (a), DFT convergence plot on work function for $FeSb_2$ (b), band alignment and electron diffusion (c) at the interface between $FeSb_2$ and Ag in the nanocomposites; the scale bar indicates that the grains inside the sample are around 30 nm on average.

density is also checked. The work functions are calculated as the difference between the vacuum level and the Fermi level inside the slab.

## 3. Results and discussion

The schematic diagrams of the phonon scattering, the calculated work functions for $FeSb_2$, and the band alignment and electron transport between Ag and $FeSb_2$ in the nanocomposite are shown in figures 1(a)–(c), respectively. In addition to the phonon scattering by nanograins as we have reported [4], the interface shown in figure 1(a) between $FeSb_{2-x}Ag_x$ and $Ag_{1-y}Sb_y$ can also scatter the medium to long wavelength phonons as predicted by theory [13, 14]. The work function of $FeSb_2$ can be simply calculated by subtracting the Fermi level from the vacuum energy level. The

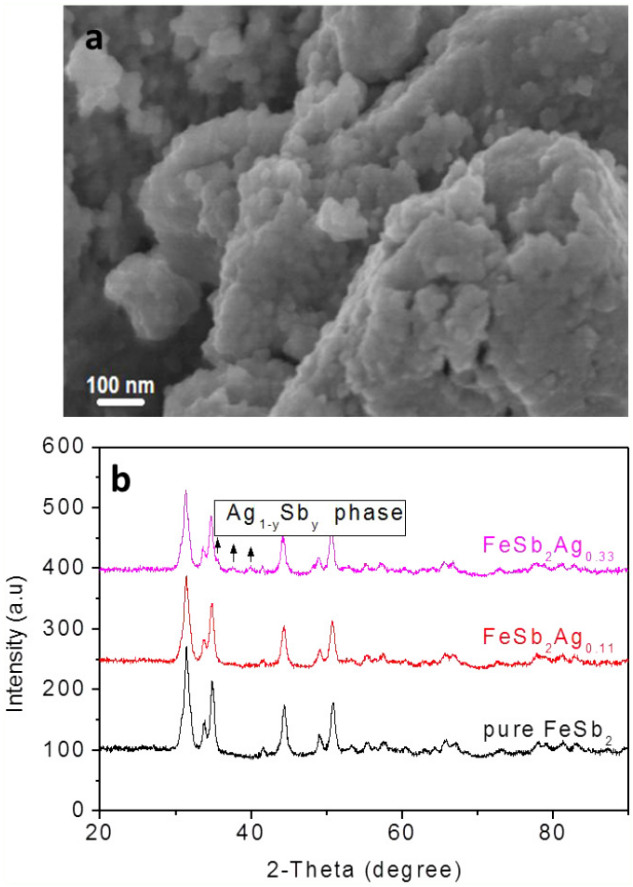


**Figure 2.** SEM image (a) for $FeSb_2Ag_{0.11}$ nanocomposite, and XRD patterns (b) for pure $FeSb_2$ and nanocomposites $FeSb_2Ag_{0.11}$ and $FeSb_2Ag_{0.33}$.

work functions of $FeSb_2$ were calculated to be 4.514 eV for the (001) plane, 4.852 eV for the (010) plane, and 4.723 eV for the (100) plane (as shown in figure 1(b)). Meanwhile, the reported work functions of silver are 4.52 eV for the (110) plane and 4.74 eV for (111) plane [31]. It is noticed that Ag and $FeSb_2$ have rather close work functions in at least two crystal planes. Therefore, as representative of the band alignment at the interface between Ag and $FeSb_2$ in the designed nanocomposite, figure 1(c) shows the band alignment and the electron transport between the (110) plane of silver and (001) plane of $FeSb_2$. Due to the roughly identical work functions between Ag and $FeSb_2$ in these planes, band alignment showed there is no energy barrier at the interface. Based on the model [13], it is reasonable to speculate that the electron transported from $FeSb_2$ to Ag will not be scattered, and enhanced $ZT$ can be expected solely from thermal conductivity reduction in the nanocomposite.

Because the densities 6.23 g $cm^{-3}$ (about 77% of the theoretical value 8.09 g $cm^{-3}$) and grain sizes (~30 nm) of all six samples are very similar, only an SEM image for sample $FeSb_2Ag_{0.11}$ is shown in figure 2(a). It can be seen that the sample is composed of micro-sized aggregates consisting of much smaller grains of ~30 nm on average, which is consistent with the TEM observation in figure 3(a). The porous structure is also a typical feature of the low-density sample and is consistent with our previous report on

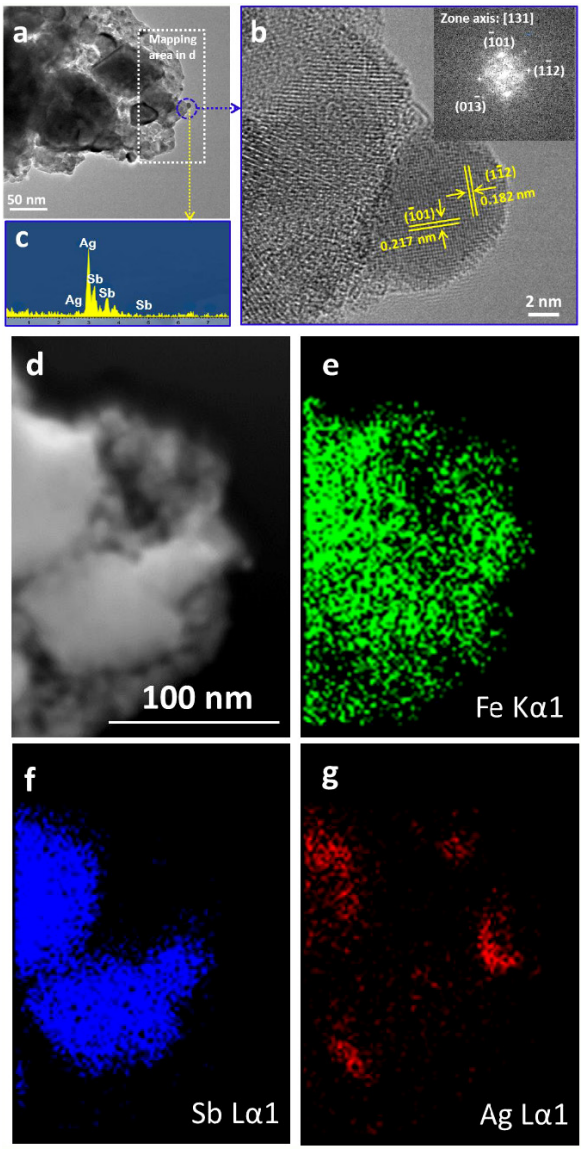


**Figure 3.** TEM images and STEM mappings of the selected area of $FeSb_2Ag_{0.11}$ nanocomposite: (a) low magnification TEM image of a typical area of the sample; (b) expanded view of a selected area shown in (a), with the IFFT for the nanoinclusion as the inset; (c) EDX showing the targeted nanoparticle in (b) is composed of Ag and Sb with the chemical formula of $Ag_{0.77}Sb_{0.23}$; (d) image of the STEM mapping area selected from (a); (e) mapping of Fe $K_{\alpha_1}$; (f) mapping of Sb $L_{\alpha_1}$; (g) mapping of Ag $L_{\alpha_1}$.

$FeSb_2$ [4]. The small grain size and porous structure in the samples lead to a significant thermal conductivity reduction and enhanced figure of merit $ZT$ in $FeSb_2$ nanocomposite. XRD patterns in figure 2(b) show that, with the addition of Ag NPs, a second phase becomes visible when Ag NPs are higher than a certain amount and can be indexed to allargentum, $Ag_{1-y}Sb_y$ ($P63/mmc$) [32]. Allargentum, $Ag_{1-y}Sb_y$ (with $y = 0.009$–$0.16$), is a metallic compound, which formed by the reaction between Ag and $FeSb_2$ during the ball milling and hot pressing process. Increasing the hot pressing temperature of the composite would lead to the formation of another impurity phase, $Ag_3Sb$ [33].

Figure 3 shows the STEM results on the composition and structures of the optimized nanocomposite sample with nominal composition $FeSb_2Ag_{0.11}$. The low magnification image in figure 3(a) shows nanograins with abundant grain boundaries, and the grain size varies from ∼10 to ∼100 nm, favorable for phonon scattering. The enlarged image (figure 3(b)) of the selected small area shown in figure 3(a) reveals an impurity phase; combined with its composition ($Ag_{0.77}Sb_{0.23}$) shown in figure 3(c), the impurity phase can be indexed to allargentum $Ag_{1-y}Sb_y$ ($P63/mmc$) structure by indexing its two lattice faces to (1$\bar{1}$2) and ($\bar{1}$01), which are parallel to the zone axis [131] as shown by the inverse Fast Fourier transform (IFFT) as the inset of figure 3(b). The phase indexing is consistent with our XRD results. Figure 3(d) is the expanded image of the dotted box area shown in figure 3(a). Figures 3(e)–(g) show the elemental mapping results for the selected area in figure 3(d). The total Ag content in the area of figure 3(d) is 3.2% by weight, compared with 3.8% of the initial nominal composition. It is noted that Ag is not uniform, suggesting that Ag is in the form of $Ag_{1-x}Sb_x$ as a second phase in the composite. This is very different from the scenario that Ag alloyed into the $FeSb_2$ lattice forming uniform Ag distribution in the mapping, although there could be a minor concentration in the lattice as we discussed in the following. The second phase as nanoinclusions can be indexed to allargentum $Ag_{0.77}Sb_{0.23}$. The size of each $Ag_{0.77}Sb_{0.23}$ grain is less than 100 nm, which is smaller than the initial 100 nm Ag NPs. Those $Ag_{0.77}Sb_{0.23}$ nanoinclusions in the nanocomposite with nominal composition $FeSb_2Ag_{0.11}$ will behave as phonon scattering centers to reduce thermal conductivity. Here we notice that a possible Ag doping in $FeSb_2$ might happen while Ag reacted with $FeSb_2$ to form $Ag_{0.77}Sb_{0.23}$. A solid chemical reaction can be depicted as the following: $FeSb_2 + 0.11Ag \rightarrow FeSb_{2-x}Ag_x + zAg_{0.77}Sb_{0.23}$. Based on the phase diagram, $x$ is 0.025, and $z$ is 0.11. Thus, the host $FeSb_2$ could be $FeSb_{1.975}Ag_{0.025}$. To be accurate, the as-formed nanocomposite for nominal composition $FeSb_2Ag_{0.11}$ can be presented as $FeSb_{1.975}Ag_{0.025}/Ag_{0.77}Sb_{0.23}$ with $Ag_{0.77}Sb_{0.23}$ of ∼10% in molar ratio.

The measured TE properties are shown in figure 4. We observed a significant thermal conductivity reduction for all $FeSb_2Ag_m$ composites as shown in figure 4(a). The inset in figure 4(a) shows the thermal conductivity versus Ag content for all samples measured at 50 K. It can be seen that, with the increase of Ag content, thermal conductivity first decreased to a minimum of 0.24 W $m^{-1}$ $K^{-1}$ for nanocomposite $FeSb_2Ag_{0.028}$ from 0.38 W $m^{-1}$ $K^{-1}$ for pure nanostructured $FeSb_2$. The TEM and EDX investigations for all $FeSb_2Ag_m$ samples revealed uniformly distributed $Ag_{1-y}Sb_y$ nanoparticles in these nanocomposites with an average size of 20 nm. With the increase of Ag content, allargentum, $Ag_{1-y}Sb_y$, emerged as a significant phase in $FeSb_2Ag_m$ nanocomposite. Owing to the high thermal conductivity of $Ag_{1-y}Sb_y$ metal phase, the total thermal conductivity in the nanocomposite increases with the increase of Ag content, and reaches a maximum at 0.29 W $m^{-1}$ $K^{-1}$ for $FeSb_2Ag_{0.22}$. Meanwhile, with the increase of Ag, the

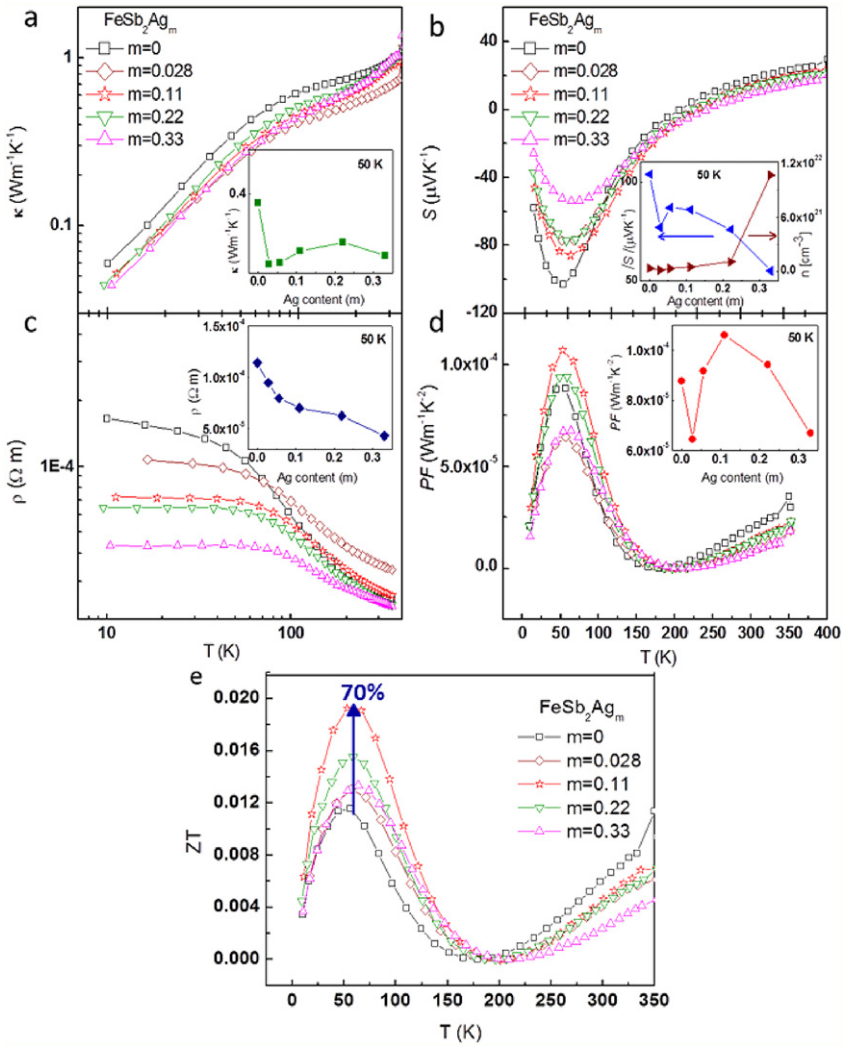


**Figure 4.** Thermoelectric properties of $FeSb_2Ag_m$ ($m = 0, 0.028, 0.11, 0.22$, and 0.33) samples: (a) temperature dependence of thermal conductivity (the inset shows the measured thermal conductivity at 50 K versus Ag content); (b) temperature dependence of Seebeck Coefficients (the inset shows the measured electron carrier concentrations versus Ag content, as well as the peak Seebeck coefficient at 50 K versus Ag content); (c) temperature dependence of electrical resistivity; (d) temperature dependence of power factor (the inset shows the peak value of power factor at 50 K versus Ag content); (e) temperature dependence of $ZT$ for $FeSb_2$ and $FeSb_{2-x}Ag_x/Ag_{1-y}Sb_y$ nanocomposites.

phonon scattering from the interfaces between $FeSb_{2-x}Ag_x$ and $Ag_{1-y}Sb_y$ became dominant and eventually outweighed the contribution of the $Ag_{1-y}Sb_y$ metal phase, and the total thermal conductivity decreased to another low level at 0.26 W $m^{-1}$ $K^{-1}$ for $FeSb_2Ag_{0.33}$ nanocomposite.

An ideal metal/semiconductor interface in three-dimensional structures has been theoretically predicted to scatter phonons for reducing thermal conductivity [14]. $FeSb_2$ has a very large lattice thermal conductivity in the total thermal conductivity: 99.9% below 75 K [25], and ∼80% at room temperature. Data in figure 4(a) shows the reduced thermal conductivity for all $FeSb_2Ag_m$ composites compared to pure $FeSb_2$ in the whole temperature range. Considering the very low electrical conductivity shown in figure 4(c), the lattice thermal conductivity in the nanocomposite $FeSb_2Ag_m$ is still dominant.

Figure 4(b) indicates the temperature dependence of the Seebeck coefficient. Overall, the peak values are all significantly reduced in comparison with that of single crystals [23, 25, 26], and also lower than those of samples with larger grain sizes [4]. We have ascribed this to the increased carrier concentrations due to defects in $FeSb_2$ nanocomposites [4]. The inset in figure 4(b) indicates the Ag content dependent Seebeck coefficient and carrier concentration for all samples at 50 K. A deep valley of Seebeck coefficient at $-77$ μV $K^{-1}$ was first observed for $FeSb_2Ag_{0.028}$. With the emergence and increase of allargentum ($Ag_{1-y}Sb_y$) phase, the Seebeck coefficient at 50 K became higher for $FeSb_2Ag_{0.056}$ and then decreased to $-55$ μV $K^{-1}$ for nanocomposite $FeSb_2Ag_{0.33}$. Meanwhile, we observed that, with the increase of Ag content, the electron carrier concentration at 50 K rose from $0.36 \times 10^{21}$ $cm^{-3}$ for pure $FeSb_2$ to $10.6 \times 10^{21}$ $cm^{-3}$ for $FeSb_2Ag_{0.33}$. However, the Seebeck coefficients for the corresponding temperature upon Ag addition in those nanocomposites did not decrease as much as expected, even though they did decrease to some

extent. Based on the parabolic band approximation, $S(T)$ of a degenerate electron system with dominant scattering by acoustic phonons is given by $S(T) = \frac{2m^*Tk_B^2\pi^2}{3eh^2}(\frac{8\pi}{3n})^{\frac{2}{3}}$. By assuming $m^* = m_0$, the free electron mass, the above equation has to be multiplied by a factor of 5.5 in order to reproduce the peak $S$ value for the $FeSb_2Ag_{0.33}$ nanocomposite. This enhancement has been observed in Te-doped $FeSb_2$ single crystal samples reported by Sun *et al* [26], wherein they proposed an enhancement factor of 10–30.

The electrical resistivity shown in figure 4(c) has a similar feature as that of the Te-doped $FeSb_2$ single crystal [26]. Above 100 K, the electrical conductivity is dominated by holes, which means that increasing the electron carrier concentration through n-type Te doping or electron diffusions in our $FeSb_2Ag_m$ composites would not lead to significant improvement in the electrical conductivity. However, below 100 K, the contributions of added electrons from Ag addition and non-scattering transport for electrons between Ag and $FeSb_2$ nanograins became significant. As can be seen in figure 4(c), the electrical conductivity was improved in a linear relationship with the Ag content (inset in figure 4(c)), as happened in Te-doped $FeSb_2$. It is noted that the p-type doping can also increase the electrical conductivity in poly-crystal $FeSb_2$ but with a different mechanism [22]. Upon Sn doping, $FeSb_2$ behaved like a fermion metal and the system became hole dominated, and with the increase of Sn, the electrical resistivity in the whole temperature range decreased dramatically. However, a large reduction on the Seebeck coefficient through Sn doping caused no gain in the power factor of the materials. Certainly, increasing the Seebeck coefficient of $FeSb_2$ nanocomposite by reducing the electron carrier concentration seems very attractive. However, the high sensitivity of the Seebeck coefficient in $FeSb_2$ to doping makes this elusive so far.

The power factor (PF) in figure 4(d) shows a trade-off between Seebeck coefficient and electrical resistivity. The inset in figure 4(d) indicates there is a maximum value at the composition of $FeSb_2Ag_{0.11}$ among all the samples at 50 K. Moreover, a similar valley as that for Seebeck coefficient for the sample $FeSb_2Ag_{0.028}$ is also observed. By taking advantage of the greatly reduced thermal conductivity for all $FeSb_2Ag_m$ nanocomposites, we enhanced the peak $ZT$ to ~0.02, which is four times higher than the single crystal value [23], and ~70% improvement over the best $FeSb_2$ nanocomposite in our previous report [4].

Enhancement of $ZT$ of semiconductor thermoelectric materials through the metal/semiconductor interface approach has been theoretically investigated and predicted by the Léonard group [14]. Typically, for either a $\kappa_e$ or $\kappa_{ph}$ dominated system, as a sum, the electron and phonon scatterings at the metal/semiconductor interface would lead to concrete thermal conductivity reductions. In a phonon thermal conductivity dominated system, the thermal conductivity reduction in $FeSb_2Ag_m$ nanocomposites is not too surprising. However, inspired by the model proposed by Léonard [14], the band bending and Fermi level alignment at the interface of $FeSb_2$ and Ag showed there is no significant potential barriers. Reasonably, the electron configuration at the $FeSb_2$/Ag interfaces can be extended to all $FeSb_2Ag_m$ nanocomposites. Under this situation, electrons can transport into the lightly doped $FeSb_{2-x}Ag_x$ and $Ag_{1-y}Sb_y$ without any need to overcome energy barriers, leading to increased electrical conductivity for the composites.

We believe that further $ZT$ enhancement can be realized through tuning the nature of metal phase, size, and distribution of the grains in the nanocomposite. The results also provide inspiring hints for the application of metal/semiconductor interface in other strongly correlated materials or Kondo systems for possible enhancement in $ZT$.

## 4. Conclusion

In summary, we present the substantial figure-of-merit $ZT$ improvement in $FeSb_{2-x}Ag_x/Ag_{1-y}Sb_y$ nanocomposite through a metal/semiconductor interface engineering approach by mixing nanopowders of $FeSb_2$ and Ag using ball milling, followed by a dc hot pressing process. Owing to the interfaces between $FeSb_{2-x}Ag_x$ and $Ag_{1-y}Sb_y$ phases, as well as the roughly identical work functions among them, both thermal conductivity and electrical resistivity of the nanocomposite were reduced significantly in the lower temperature regime compared with the pure $FeSb_2$ nanocomposite. Overall, an improvement of 70% in $ZT$ for the optimized sample $FeSb_{1.975}Ag_{0.025}/Ag_{0.77}Sb_{0.23}$ (10% in molar ratio) nanocomposite was achieved. It seems we have evidence to show the metal/semiconductor interface does provide benefits to thermoelectric materials, which may potentially be useful for other strongly correlated material systems.

## Acknowledgments

The work is sponsored by the Air Force MURI program under contract FA9550-10-1-0533. The authors would like to thank Dr Mona Zebarjadi for insightful discussion.

## References

[1] Hsu K F, Loo S, Guo F, Chen W, Dyck J S, Uher C, Hogan T, Polychroniadis E K and Kanatzidis M G 2004 *Science* **303** 818–21
[2] Poudel B *et al* 2008 *Science* **320** 634–8
[3] Yan X *et al* 2011 *Nano Lett.* **11** 556–60
[4] Zhao H Z, Pokharel M, Zhu G H, Chen S, Lukas K, Jie Q, Opeil C, Chen G and Ren Z F 2011 *Appl. Phys. Lett.* **99** 163101
[5] Heremans J P, Jovovic V, Toberer E S, Saramat A, Kurosaki K, Charoenphakdee A, Yamanaka S and Snyder G J 2008 *Science* **321** 554–8
[6] Zhang Q Y *et al* 2012 *Energy Environ. Sci.* **5** 5246–51
[7] Heremans J P, Wiendlocha B and Chamoire A M 2012 *Energy Environ. Sci.* **5** 5510–30
[8] Pei Y Z, Shi X Y, LaLonde A, Wang H, Chen L D and Snyder G J 2011 *Nature* **473** 66–9
[9] Zhang Q, Cao F, Liu W S, Lukas K, Yu B, Chen S, Opeil C, Broido D, Chen G and Ren Z F 2012 *J. Am. Chem. Soc.* **134** 10031–8
[10] Zebarjadi M, Joshi G, Zhu G H, Yu B, Minnich A, Lan Y C, Wang X W, Dresselhaus M, Ren Z F and Chen G 2011 *Nano Lett.* **11** 2225–30

[11] Yu B, Zebarjadi M, Wang H, Lukas K, Wang H Z, Wang D Z, Opeil C, Dresselhaus M, Chen G and Ren Z F 2012 *Nano Lett.* **12** 2077–82
[12] Heremans J P, Thrush C M and Morelli D T 2005 *J. Appl. Phys.* **98** 063703
[13] Kim W, Zide J, Gossard A, Klenov D, Stemmer S, Shakouri A and Majumdar A 2006 *Phys. Rev. Lett.* **96** 045901
[14] Faleev S V and Léonard F 2008 *Phys. Rev.* B **77** 214304
[15] Zebarjadi M, Esfarjani K, Shakouri A, Bahk J-H and Bian Z X 2009 *Appl. Phys. Lett.* **94** 202105
[16] Sumithra S, Takas N J, Misra D K, Nolting W M, Poudeu P F P and Stokes K L 2011 *Adv. Energy Mater.* **1** 1141–7
[17] Ko D K, Kang Y J and Murray C B 2011 *Nano Lett.* **11** 2841–4
[18] Smith G E and Wolfe R 1962 *J. Appl. Phys.* **33** 841–6
[19] Harutyunyan S R, Vardanyan V H, Kuzanyan A S, Nikoghosyan V R, Kunii S, Wood K S and Gulian A M 2003 *Appl. Phys. Lett.* **83** 2142
[20] Rowe D M, Gao M and Kuznestsov V L 1998 *Phil. Mag. Lett.* **77** 105–8
[21] Sales B C, Delaire O, McGuire M A and May A F 2011 *Phys. Rev.* B **83** 125209
[22] Bentien A, Madsen G K H, Johnson S and Iversen B B 2006 *Phys. Rev.* B **74** 205105
[23] Bentien A, Johnsen S, Madsen G K H, Iversen B B and Steglich F 2007 *Europhys. Lett.* **80** 17008
[24] Sun P, Oeschler N, Johnsen S, Iversen B B and Steglich F 2009 *Phys. Rev.* B **79** 153308
[25] Sun P, Oeschler N, Johnsen S, Iversen B B and Steglich F 2010 *Dalton Trans.* **39** 1012–9
[26] Sun P, Søndergaard M, Sun Y, Johnsen S, Iversen B B and Steglich F 2011 *Appl. Phys. Lett.* **98** 072105
[27] Diakhate M S, Hermann R P, Möchel A, Sergueev I, Søndergaard M, Christensen M and Verstraete M J 2011 *Phys. Rev.* B **84** 125210
[28] Mani A, Janaki J, Satya A T, Kumary T G and Bharathi A 2012 *J. Phys.: Condens. Matter* **24** 075601
[29] Singh-Miller N E and Marzari N 2009 *Phys. Rev.* B **80** 235407
[30] Giannozzi P *et al* 2009 *J. Phys.: Condens. Matter* **21** 395502
[31] *CRC Handbook of Chemistry and Physics* 2008 89th edn, (Boca Raton, FL: CRC Press) pp 12–114
[32] Petruk W, Cabri L J, Harris D C, Stewart J M and Clark L A 1970 *Can. Mineral.* **10** 163–72
[33] Scott J D 1976 *Can. Mineral.* **14** 139–42

JACS
JOURNAL OF THE AMERICAN CHEMICAL SOCIETY
Article
pubs.acs.org/JACS

# Study of the Thermoelectric Properties of Lead Selenide Doped with Boron, Gallium, Indium, or Thallium

Qian Zhang,[†] Feng Cao,[†] Kevin Lukas,[†] Weishu Liu,[†] Keivan Esfarjani,[‡] Cyril Opeil,[†] David Broido,[†] David Parker,[§] David J. Singh,[§] Gang Chen,*[,‡] and Zhifeng Ren*[,†]

[†]Department of Physics, Boston College, Chestnut Hill, Massachusetts 02467, United States
[‡]Department of Mechanical Engineering, Massachusetts Institute of Technology, Cambridge, Massachusetts 02139, United States
[§]Materials Science and Technology Division, Oak Ridge National Laboratory, Oak Ridge, Tennessee 37831-6056, United States

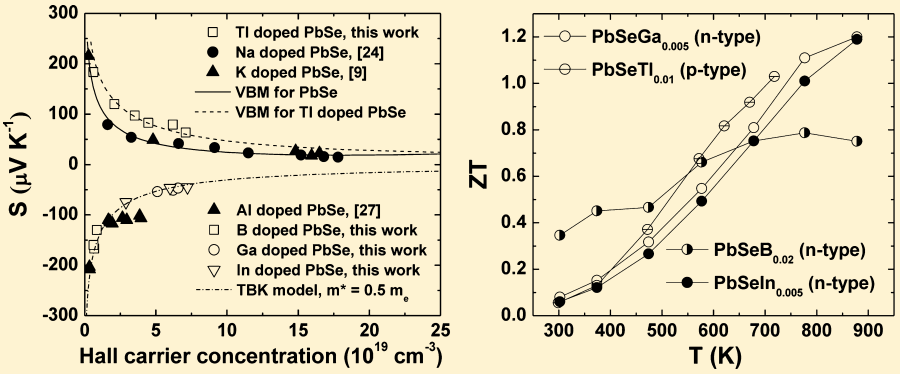


**ABSTRACT:** Group IIIA elements (B, Ga, In, and Tl) have been doped into PbSe for enhancement of thermoelectric properties. The electrical conductivity, Seebeck coefficient, and thermal conductivity were systematically studied. Room-temperature Hall measurements showed an effective increase in the electron concentration upon both Ga and In doping and the hole concentration upon Tl doping to ~$7 \times 10^{19}$ cm$^{-3}$. No resonant doping phenomenon was observed when PbSe was doped with B, Ga, or In. The highest room-temperature power factor ~$2.5 \times 10^{-3}$ W m$^{-1}$ K$^{-2}$ was obtained for PbSe doped with 2 atom % B. However, the power factor in B-doped samples decreased with increasing temperature, opposite to the trend for the other dopants. A figure of merit ($ZT$) of ~1.2 at ~873 K was achieved in PbSe doped with 0.5 atom % Ga or In. With Tl doping, modification of the band structure around the Fermi level helped to increase the Seebeck coefficient, and the lattice thermal conductivity decreased, probably as a result of effective phonon scattering by both the heavy $Tl^{3+}$ ions and the increased grain boundary density after ball milling. The highest p-type $ZT$ value was ~1.0 at ~723 K.

## INTRODUCTION

Thermoelectric (TE) materials need high $ZT$ values to be useful for applications. Here $ZT = [S^2\sigma/(\kappa_L+\kappa_e)]T$, and $S$ is the Seebeck coefficient, $\sigma$ the electrical conductivity, $\kappa_L$ the lattice thermal conductivity, $\kappa_e$ the electronic thermal conductivity, and $T$ the absolute temperature.[1−3] With good $ZT$ values found in both n- and p-type PbTe recently, PbTe is viewed as one of the best TE materials at mid-temperature range (400−800 K).[4−10] Most of the possible dopants have been studied for enhancement of $ZT$ in PbTe by calculations or experiments.[11−17] Group IIIA elements have been found to be effective for controlling both the carrier concentration and the carrier type in this material.[11,18−22] It was found that group IIIA elements can be either acceptors[11,21] or donors.[18,19,22] Different models have been proposed to explain this amphoteric behavior.[20] Interestingly, In and Tl doping has been reported to induce resonant states in n- and p-type PbTe, respectively, which helps increase the Seebeck coefficient without correspondingly diminishing the electrical conductivity, therefore enhancing the $ZT$ value.[11,19,21]

Another IV−VI narrow band gap semiconductor, PbSe, has drawn much attention because of several advantages.[23−27] Most of all, it also has decent doping optimized $ZT$.[24,27] Parker and Singh predict $ZT$ as high as 2 at 1000 K if heavily doped with holes. A band flattening ~0.35−0.4 eV below the valence band edge helps the enhancement of the Seebeck coefficient,[23] and the increased band gap postpones the saturation of the Seebeck coefficient with increasing temperature. Na, K, and Ag are subsequently confirmed as good dopants offering high hole concentration and high $ZT > 1$.[9,24,28] For n-type PbSe, the conventional electron impurity Cl and I that work well in PbTe can also work in PbSe.[8,26,29] Additionally, the impact of Bi,[30] rare-earth elements (Ce, Pr, Nd, Eu, Gd, and Yb),[31] Pb and Se defects,[32] codopants of Na and Cd, and Mn have all been studied.[29] However, it is still interesting and perhaps controversial to consider group IIIA elements in PbSe.[25,27,33−36] Encouragingly, Al was found as an effective n-

**Received:** August 8, 2012
**Published:** October 1, 2012


© 2012 American Chemical Society

dx.doi.org/10.1021/ja307910u | J. Am. Chem. Soc. 2012, 134, 17731−17738

Table 1. Theoretical Density $D_T$, Measured Volumetric Density $D$, and Relative Density $D_R$ for $PbSeB_x$, $PbSeGa_x$, $PbSeIn_x$, and $PbSeTl_x$

| | $PbSeB_x$ | | | $PbSeGa_x$ | | | $PbSeIn_x$ | | | $PbSeTl_x$ | | |
|---|---|---|---|---|---|---|---|---|---|---|---|---|
| comp. | 0.01 | 0.02 | 0.03 | 0.003 | 0.005 | 0.007 | 0.003 | 0.005 | 0.007 | 0.005 | 0.010 | 0.020 |
| $D_T$ (g cm$^{-3}$) | 8.19 | 8.14 | 8.08 | 8.24 | 8.23 | 8.22 | 8.24 | 8.24 | 8.23 | 8.25 | 8.25 | 8.24 |
| $D$ (g cm$^{-3}$) | 7.85 | 7.87 | 7.87 | 7.98 | 7.94 | 8.00 | 8.00 | 7.9 | 7.92 | 7.73 | 7.68 | 7.56 |
| $D_R$ | 96% | 97% | 97% | 97% | 96% | 97% | 97% | 96% | 96% | 94% | 93% | 92% |

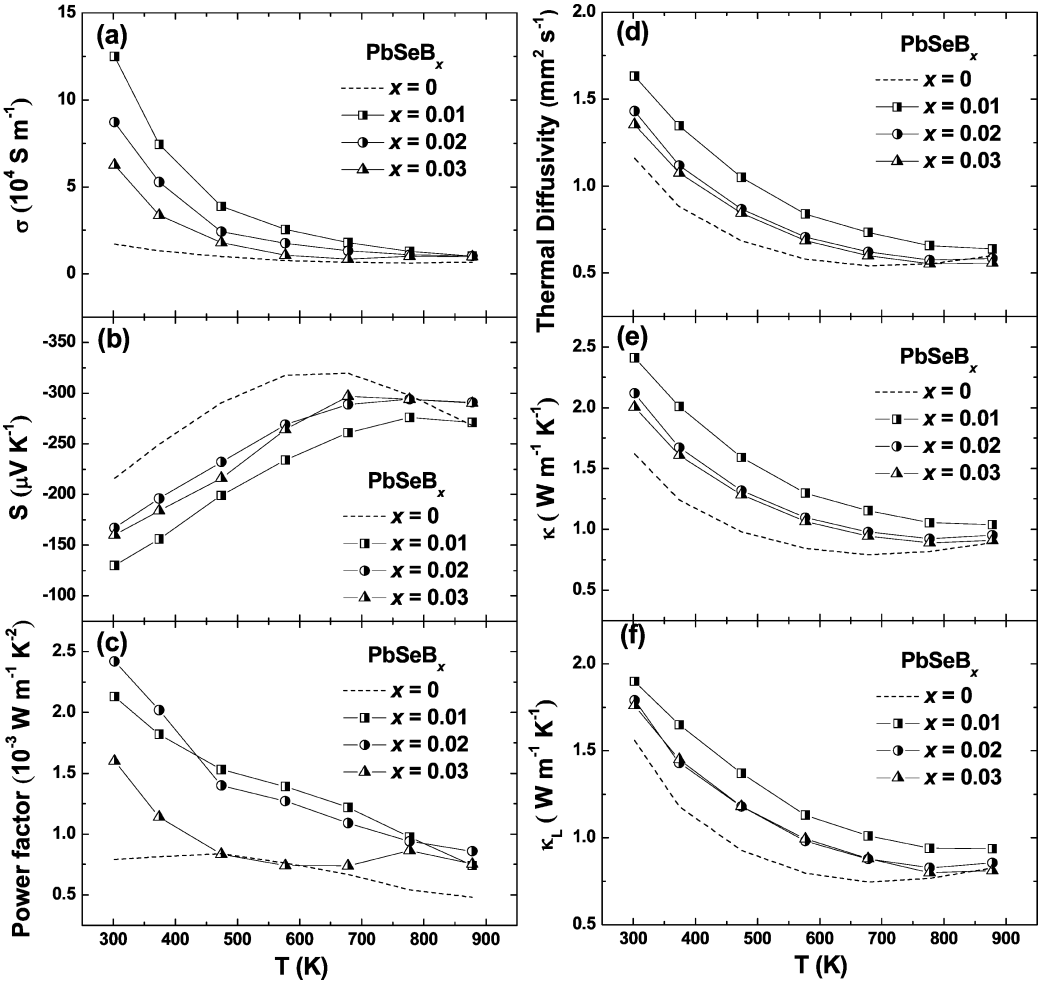


Figure 1. Temperature dependence of (a) electrical conductivity, (b) Seebeck coefficient, (c) power factor, (d) thermal diffusivity, (e) total thermal conductivity, and (f) lattice thermal conductivity for $PbSeB_x$ ($x$ = 0, 0.01, 0.02, and 0.03).

type dopant in PbSe, which can create resonant states for the enhancement of $ZT$,[27] like Tl in p-type PbTe.[11,21,37,38] It was also suggested that In and Tl create resonant levels in PbSe without strong experimental evidence.[33−35] Recent results by the first-principles calculations concluded that the resonant states in Tl- and In-doped PbSe extend largely into the band gap and even the conduction band, respectively, which degrades the TE properties.[36] In this paper, we report systematic experimental study on the doping effect of group IIIA elements (B, Ga, In, and Tl) on thermoelectric properties of PbSe. The electrical conductivity, Seebeck coefficient, and thermal conductivity of samples with different doping concentrations are investigated. The comparison of all group IIIA elements doping in PbSe is presented. In spite of the absence of resonant states, $ZT$ of ∼1.2 is obtained in both 0.5 at % Ga-doped n-type PbSe and 0.5 at % In-doped n-type PbSe at ∼873 K. The band structure modification around Fermi level and reduced lattice thermal conductivity help the $ZT$ reach ∼1.0 at about 723 K for Tl-doped p-type PbSe.

## EXPERIMENTAL SECTION

**Synthesis.** Samples with nominal compositions $PbSeB_x$ (boron powder 99.99%, $x$ = 0.01, 0.02, and 0.03), $PbSeGa_x$ (gallium ingots 99.99%, $x$ = 0.003, 0.005, and 0.007), $PbSeIn_x$ (indium powder 99.99%, $x$ = 0.003, 0.005, and 0.007), and $PbSeTl_x$ (thallium granules 99.99%, $x$ = 0.00125, 0.0025, 0.005, 0.01, 0.015, and 0.02) were prepared by melting the materials inside a quartz tube with carbon coating. The detailed procedure can be found in our previous report.[9] The same compositions of $PbSeTl_x$ ($x$ = 0, 0.00125, 0.0025, 0.005, 0.01, 0.015, and 0.02) were also prepared by mechanical alloying due to the difficulty of doping Tl into the PbSe lattice by a melting method. In the case of ball milling, the raw materials Tl (granules, 99.99%), Pb (granules, 99.99%), and Se (granules, 99.99%) were sealed directly in the stainless steel jar inside an argon-filled glovebox and ball milled by a high-energy ball mill SPEX 8000D (SPEX Sample


dx.doi.org/10.1021/ja307910u | J. Am. Chem. Soc. 2012, 134, 17731−17738

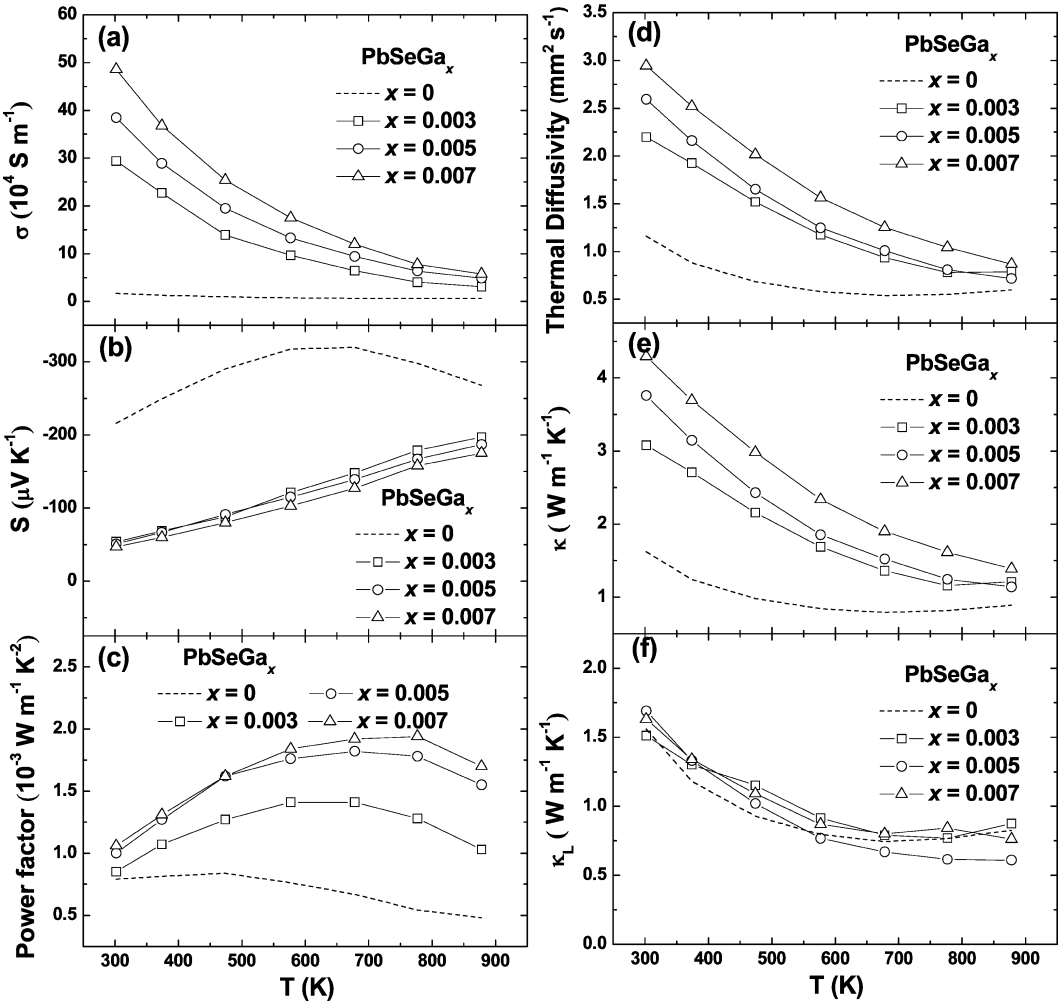


**Figure 2.** Temperature dependence of (a) electrical conductivity, (b) Seebeck coefficient, (c) power factor, (d) thermal diffusivity, (e) total thermal conductivity, and (f) lattice thermal conductivity for $PbSeGa_x$ ($x$ = 0, 0.003, 0.005, and 0.007).

Prep.). The obtained powder was loaded into the graphite die and consolidated by direct current (dc)-induced hot pressing.

**Characterizations.** X-ray diffraction spectra analysis was conducted on a PANalytical multipurpose diffractometer with an X'celerator detector (PANalytical X'Pert Pro). All samples are confirmed in a single phase. The microstructures were investigated by a scanning electron microscope (SEM, JEOL 6340F). The electrical resistivity ($\rho$) and Seebeck coefficient ($S$) were simultaneously measured on a commercial system (ULVAC ZEM-3). The thermal conductivity $\kappa$ was calculated using $\kappa = D\alpha C_p$, where $D$ is volumetric density determined by the Archimedes method and shown in Table 1 compared with the theoretical density $D_T$, $\alpha$ the thermal diffusivity obtained on a laser flash apparatus (Netzsch LFA 457), and $C_p$ the specific heat measured on a differential scanning calorimetry thermal analyzer (Netzsch DSC 404 C). The Hall Coefficient $R_H$ at room temperature was measured using the Physical Properties Measurement System (PPMS, Quantum Design). The Hall carrier concentration $n_H$ and mobility $\mu_H$ were calculated using $n_H = 1/(eR_H)$ and $\mu_H = \sigma R_H$, respectively. The uncertainty for the electrical conductivity is 3%, the Seebeck coefficient 5%, and the thermal conductivity 4%, so the combined uncertainty for the power factor is 10% and that for the $ZT$ value is 11%.[39] Error bars were not used in the figures to increase the readability of the curves.

## RESULTS AND DISCUSSION

Different compositions are prepared for optimization of the TE properties. Figures 1, 2, and 3 present the (a) electrical conductivity, (b) Seebeck coefficient, (c) power factor, (d) thermal diffusivity, (e) total thermal conductivity, and (f) lattice thermal conductivity of three samples for each kind of doping, $PbSeB_x$ ($x$ = 0, 0.01, 0.02, and 0.03), $PbSeGa_x$ ($x$ = 0, 0.003, 0.005, and 0.007), and $PbSeIn_x$ ($x$ = 0, 0.003, 0.005, and 0.007), respectively. The properties of undoped PbSe were reported in the previous work.[9] All compositions are nominal, but the real composition is very close to the nominal since there was no noticeable mass loss during the sample preparation process. All doping can increase the electrical conductivity. With increasing temperature, the electrical conductivity decreases, and the Seebeck coefficient increases. The Seebeck coefficient increases without a sign of bipolar effect with Ga or In doping. However, the Seebeck coefficient saturates at ~400−500 °C in B-doped PbSe with lower carrier concentration. All three dopings are n-type with a negative Seebeck coefficient. The highest power factor is ~2.5 × 10$^{-3}$ W m$^{-1}$ K$^{-2}$ at room temperature for the 2 at % B-doped PbSe, ~2.0 × 10$^{-3}$ W m$^{-1}$ K$^{-2}$ at 500 °C for 0.7 at % Ga-doped PbSe. In a conservative way, the $C_p$ of $PbSeB_{0.03}$, $PbSeGa_{0.007}$, $PbSeIn_{0.007}$, and $PbSeTl_{0.02}$ is used for the calculation of the total thermal conductivity of each kind of doping, shown in Figure 4. All the total thermal conductivities decrease with increasing temperature. By subtracting the electronic thermal conductivity from the total thermal conductivity ($\kappa_L = \kappa_{total} - \kappa_e = \kappa_{total} - L\sigma T$, where $L$ is the


dx.doi.org/10.1021/ja307910u | J. Am. Chem. Soc. 2012, 134, 17731−17738

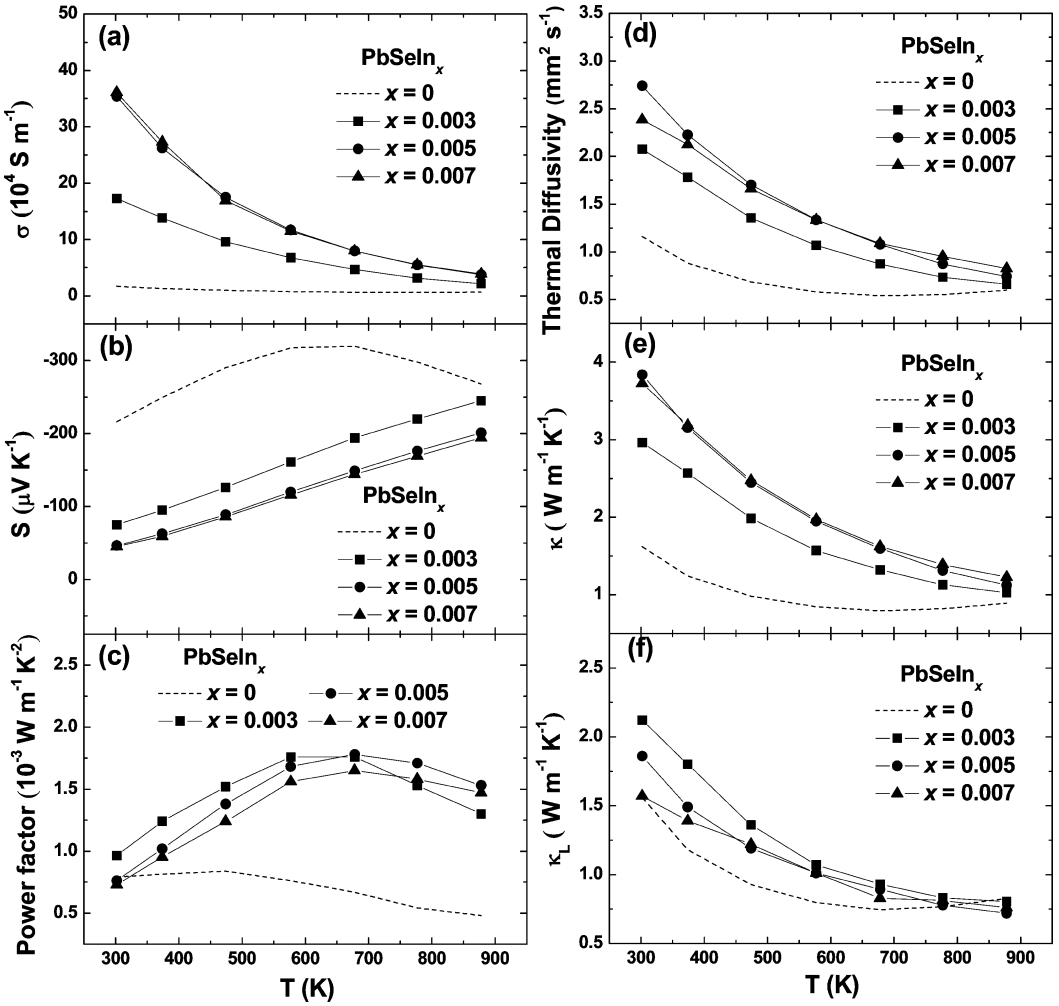


**Figure 3.** Temperature dependence of (a) electrical conductivity, (b) Seebeck coefficient, (c) power factor, (d) thermal diffusivity, (e) total thermal conductivity, and (f) lattice thermal conductivity for $PbSeIn_x$ ($x$ = 0, 0.003, 0.005, and 0.007).

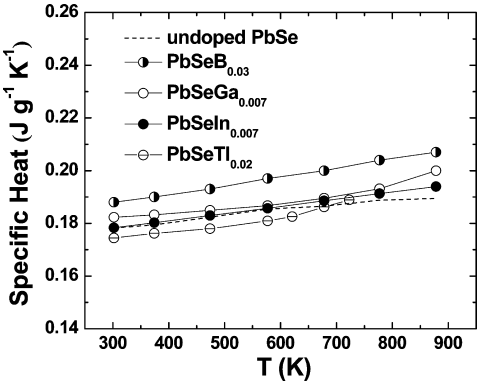


**Figure 4.** Temperature dependence of specific heat for $PbSeB_{0.03}$, $PbSeGa_{0.007}$, $PbSeIn_{0.007}$, $PbSeTl_{0.02}$, and undoped PbSe.

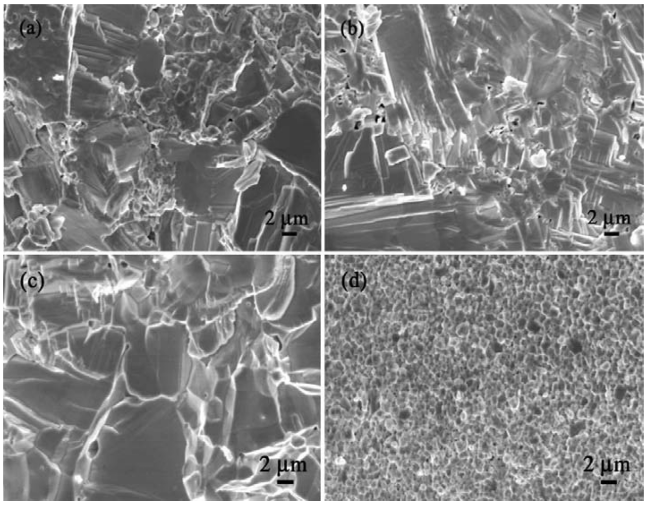


**Figure 5.** Representative SEM images of hot pressed (a) $PbSeB_{0.02}$, (b) $PbSeGa_{0.005}$, (c) $PbSeIn_{0.005}$, and (d) $PbSeTl_{0.01}$.

Lorenz number calculated using a two-band model),[9,40] the lattice thermal conductivity is obtained. In spite of the lowest total thermal conductivity, B-doped PbSe has the highest lattice thermal conductivity because of the weakest phonon scattering by the lightest $B^{3+}$ compared with $Ga^{3+}$ and $In^{3+}$. In addition, we present the fresh cross-section microstructures of the samples with different dopings in Figure 5a–d (Figure 5d will be discussed later). It shows relatively large grain sizes ~10 $\mu$m made by hand milling. Compared with ball-milled Al-doped PbSe,[27] the overall lattice thermal conductivity is higher, which further confirms the beneficial effect of ball milling.

Together with Al-doped PbSe (filled triangles),[27] we plot a room-temperature Seebeck coefficient as a function of Hall carrier concentration for B- (half open circles), Ga- (open


dx.doi.org/10.1021/ja307910u | J. Am. Chem. Soc. 2012, 134, 17731–17738

circles), and In-doped PbSe (solid circles) in Figure 6 to clearly show the band information. With the decreasing difference in

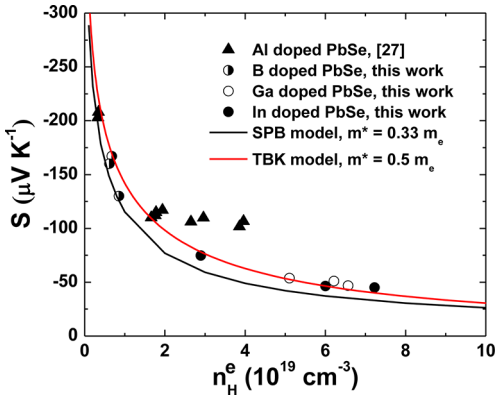


**Figure 6.** Room-temperature Pisarenko plots for $PbSeB_x$ ($x$ = 0.01, 0.02, and 0.03, half open circles), $PbSeGa_x$ ($x$ = 0.003, 0.005, and 0.007, open circles), and $PbSeIn_x$ ($x$ = 0.003, 0.005, and 0.007, solid circles) in comparison with reported data on Al-doped PbSe by Zhang et al.[27] (solid triangles). Black curve is based on SPB model with the electron effective mass of PbSe $m^*/m_e$ = 0.33. Red curve is based on nonparabolic TBK model with the electron effective mass of PbSe $m^*/m_e$ = 0.5.

ionic radius between dopants and Pb, the optimized carrier concentration increases. It is difficult to further increase the carrier concentration of B-doped PbSe because of the small ionic radius of B. High carrier concentration $\sim 7 \times 10^{19}$ cm$^{-3}$ is obtained in both Ga- and In-doped PbSe. The Seebeck coefficients of all the samples decrease with increasing carrier concentration. The measured Seebeck coefficient values are compared with calculated results from two models: In both models, the deformation potential scattering by acoustic phonons was taken to be the dominant carrier scattering mechanism consistent with previous work.[4,13,40] In the first model, a single parabolic band (SPB) is used with effective mass $m^*/m_e$ = 0.33 (black curve). Note that this curve deviates slightly from the data in spite of consideration of the Hall factor.[7,25] In the second model, the nonparabolicity of conduction band of PbSe is included using a two-band Kane (TBK) model,[8,40] which describes the conduction and light hole valence bands about the L-point. The TBK model fits the data well using a much larger effective mass $m^*/m_e$ = 0.5 (red curve), which is close to the optical measurement results.[25] It is clear that no matter which model we use, Al-doped PbSe does not fit the curve. This could be due to resonant scattering.[27]

There are neither resonant states to explain the high Seebeck coefficient nor strong phonon scattering to produce low lattice thermal conductivity demonstrated in these materials. However, the highest $ZT$ values (Figure 7) reach ~1.2 in 0.5 at % Ga- or In-doped PbSe at about 873 K, which is attributed to the high-concentration doping. In Table 2, comparison of room-temperature electrical properties of the optimally doped PbSe using different dopants is presented. Lower carrier concentration and reduced Hall mobility by resonant doping restrict further improvement of Al-doped PbSe. We tried to codope PbSe with Al and Ga or Al and In, but this strategy did not lead to a $ZT$ enhancement. With a low power factor and high lattice thermal conductivity at high temperature, the highest $ZT$ value for B-doped PbSe is only ~0.8 at about 773 K. This $ZT$ value is still comparable with Ga- and In-doped PbSe measured directly

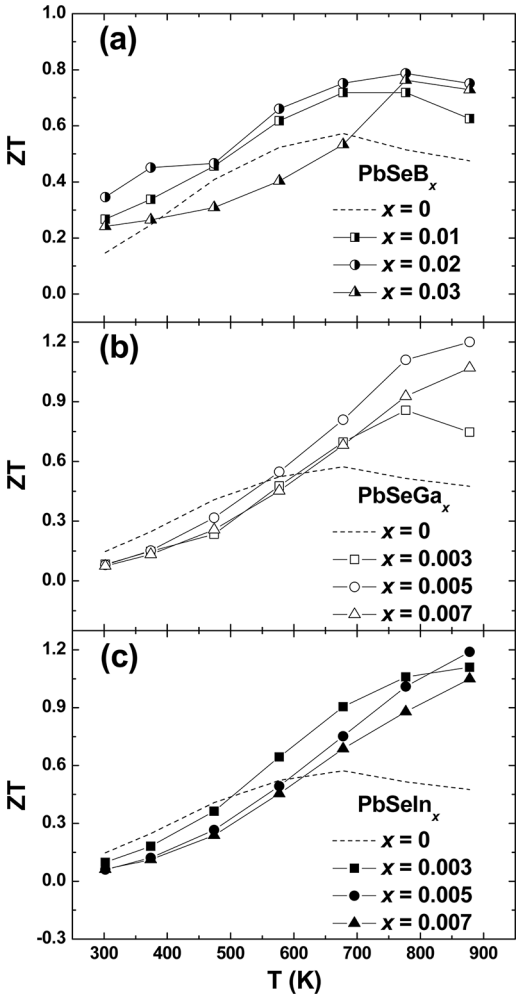


**Figure 7.** Temperature dependence of $ZT$ for (a) $PbSeB_x$ ($x$ = 0, 0.01, 0.02, and 0.03), (b) $PbSeGa_x$ ($x$ = 0, 0.003, 0.005, and 0.007), and (c) $PbSeIn_x$ ($x$ = 0, 0.003, 0.005, and 0.007).

from the ingot specimens by melting.[25] Despite the lower peak $ZT$ of B-doped PbSe, the temperature-averaged $ZT$ is comparable with the Ga- and In-doped PbSe obtained in this work.

It is also worth noting that at all but the highest temperatures measured, the lattice thermal conductivity is the predominant component of the thermal conductivity. For example, in Figure 1 (boron doping) the lattice component at 500 K is approximately 1.2 W m$^{-1}$ K$^{-1}$, while the electronic portion is roughly 0.3 W m$^{-1}$ K$^{-1}$. The figure of merit $ZT$ can be rewritten as

$$ZT = S^2\sigma T/\kappa = S^2 r/L \quad (1)$$

with $S$ the thermopower, $\sigma$ the electrical conductivity, $\kappa$ the thermal conductivity, $r$ the ratio of electronic and total (i.e., lattice + electronic) thermal conductivity, and $L$ the Lorenz number, in the Wiedemann–Franz relation, nominally $L$ = 2.45 × 10$^{-8}$ V$^2$ K$^{-2}$. With $r$ in this case at 0.2 combined with the Seebeck coefficient of approximately −225 μV K$^{-1}$, one finds, as in the experiment, a relatively low $ZT$ of ~0.4 at 500 K. However, if it were possible to reduce the lattice thermal conductivity without comparably affecting the charge carrier mobility, the ratio $r$ would increase and substantial increases in $ZT$ at this temperature, and in fact in the whole temperature


dx.doi.org/10.1021/ja307910u | J. Am. Chem. Soc. 2012, 134, 17731−17738

Table 2. Comparison of Room-Temperature Electrical Properties for Optimally Doped PbSe by B or Al,[27] Ga, In, and Tl

| | B | Al | Ga | In | Tl |
|---|---|---|---|---|---|
| composition | $PbSeB_{0.02}$ | $PbSeAl_{0.01}$ | $PbSeGa_{0.005}$ | $PbSeIn_{0.005}$ | $PbSeTl_{0.01}$ |
| $\sigma$ ($10^4$ S m$^{-1}$) | 8.72 | 12.9 | 38.5 | 35.4 | 3.97 |
| S ($\mu$V K$^{-1}$) | −167 | −117 | −51 | −46.4 | 82.8 |
| $n_H$ ($10^{19}$ cm$^{-3}$) | 0.677 | 1.94 | 6.215 | 6 | 4.475 |
| $\mu_H$ (cm$^2$ V$^{-1}$ s$^{-1}$) | 827 | 416 | 465 | 433 | 39 |

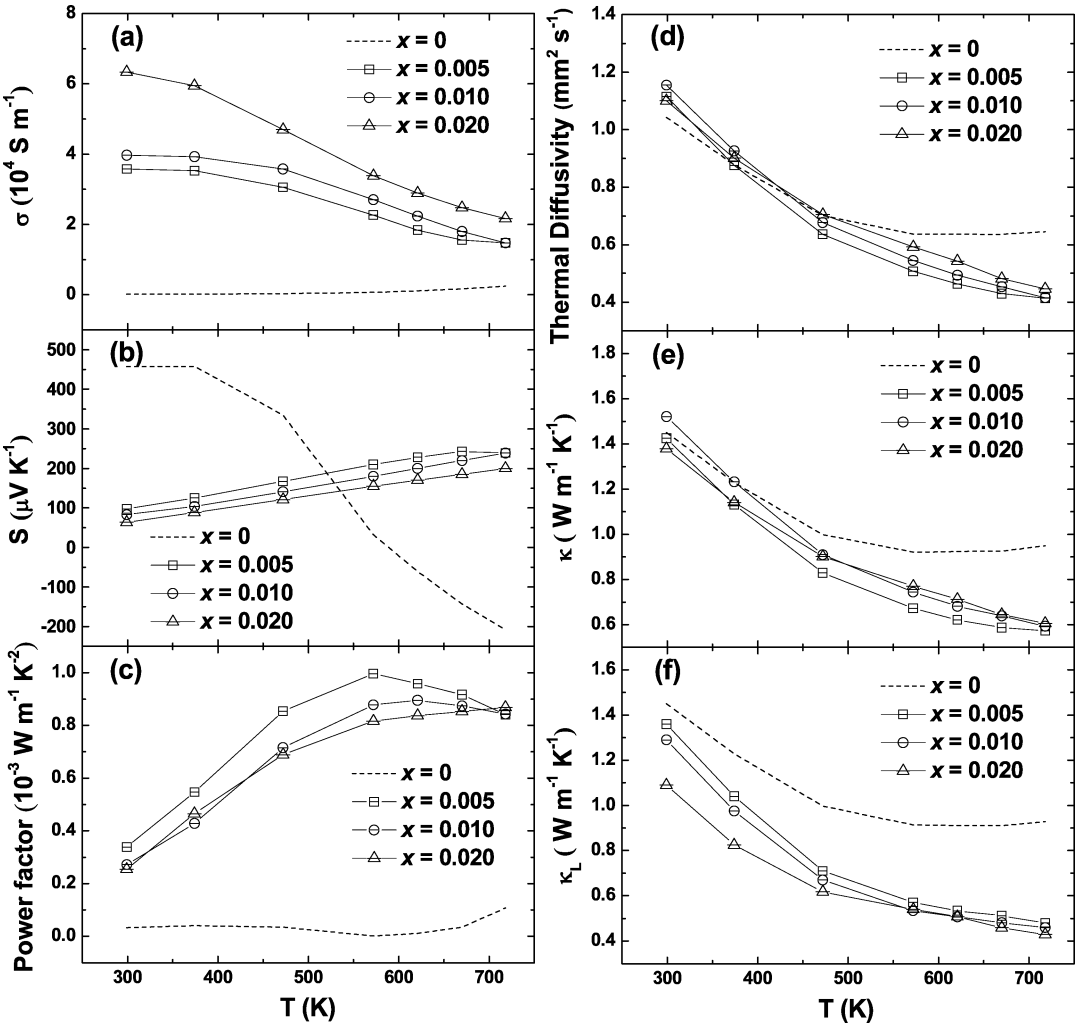


Figure 8. Temperature dependence of (a) electrical conductivity, (b) Seebeck coefficient, (c) power factor, (d) thermal diffusivity, (e) total thermal conductivity, and (f) lattice thermal conductivity for $PbSeTl_x$ ($x$ = 0, 0.005, 0.01, and 0.02).

range from 300 to 700 K would be possible. Such a lattice thermal conductivity reduction has already been shown possible in ref 41, where a $ZT$ of 1.4 for $Bi_2Te_3$ was found, significantly higher than the "optimized" value of 1.0 in bulk, which itself includes alloying optimization, which was not performed here and could itself have a beneficial impact if applied here.

Such an optimization would generally require, in the lowest temperature range from 300 to 500 K, lower doping levels than the best values here, with optimal doping ranges increasing with temperature. Reducing the temperature where $ZT$ is maximum in PbSe is of interest for solar thermal and waste heat recovery applications.

Like Tl doping in PbTe,[11] Tl in PbSe also acts as acceptor, different from other group IIIA elements. The electrical conductivity, Seebeck coefficient, power factor, thermal diffusivity, total thermal conductivity, and lattice thermal conductivity for $PbSeTl_x$ ($x$ = 0, 0.005, 0.01, and 0.02) are shown in Figure 8. It should be noted that all the properties presented for Tl-doped samples are on material that was prepared by ball milling directly. We also tried Tl-doped PbSe by melting and hand milling, as we did for B-, Ga-, and In-doped PbSe, but the properties are quite poor because Tl could not be doped into the lattice during melting process. This situation is similar for Al-doped PbSe and requires further studies. With increasing content of Tl, the electrical conductivity increases, but the Seebeck coefficient and the power factor decrease. The maximum power factor is only ~1.0 × $10^{-3}$ W m$^{-1}$ K$^{-2}$ at 300 °C for 0.5 at % Tl-doped PbSe, much lower than that of B- or Al-,[27] Ga-, and In-doped PbSe. However, the lattice thermal conductivity is as low as ~0.43 W


dx.doi.org/10.1021/ja307910u | J. Am. Chem. Soc. 2012, 134, 17731−17738

$m^{-1}$ $K^{-1}$ at about 720 K, lower than other dopings in all the measured temperature range. It is the result of stronger phonon scattering by heavier $Tl^{3+}$ ion as well as the increased mid-to-long wavelength phonon scattering by increased boundary scattering, corresponding to the grain structure shown in Figure 5d. The grain size is only ~200−500 nm, even smaller than ball-milled Al-doped PbSe.[27] However it is puzzling why the thermal conductivity of the pure PbSe is so much higher for a similar grain size. We did not further study this due to the very low *ZT* for the pure PbSe.

The room-temperature Pisarenko plot for Tl-doped PbSe (open circles) is shown in Figure 9 to elucidate the electrical transport. For comparison, we also presented other reported p-type PbSe doped with Na (open squares)[24] and K (open triangles)[9] and also p-type PbTe doped with Tl (solid circles),[11] Na (solid squares),[16] and K (solid triangles).[9] Similar to PbTe, PbSe has a light hole region at the valence band maximum and a heavier band behavior ~0.35−0.4 eV below this.[13] To fit the data, the two-band Kane model described before is combined with an additional parabolic heavy hole portion of the valence band. We refer this as the valence band model (VBM). Again, scattering of holes is assumed to be by acoustic phonons through the deformation potential interaction. Further details of the VBM can be found elsewhere.[9] Due to the contribution from the heavy hole portion in PbTe, the Seebeck coefficient remains unchanged when heavily doped. Especially when Tl is doped, the Seebeck coefficient is as high as ~130 $\mu$V $K^{-1}$.[11] This Tl-doped PbTe is an excellent thermoelectric material. PbSe has qualitatively similar valence band features, in particular light holes at the valence band edge and a crossover to heavier behavior at high doping levels.[9,13,24] However, the heavy hole region only contributes at high temperatures, with almost the same trend like having one band at room temperature. The Seebeck coefficient decreases

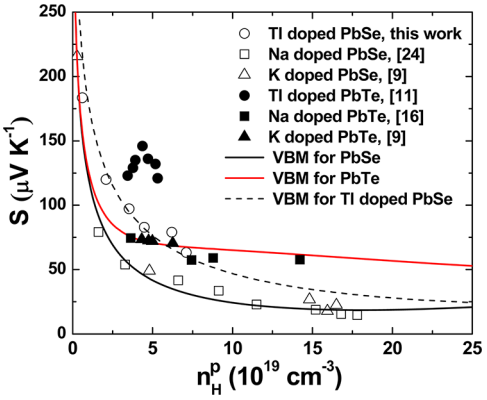


**Figure 9.** Room-temperature Pisarenko plots for $PbSeTl_x$ ($x$ = 0.00125, 0.0025, 0.005, 0.01, 0.015, and 0.02, open circles) in comparison with the reported data on K-doped PbTe (solid triangles),[9] K-doped PbSe (open triangles),[5] Na-doped PbTe by Pei et al.[16] (solid squares), Na-doped PbSe by Wang et al.[24] (open squares), and Tl-doped PbTe by Heremans et al.[11] (solid circles). The solid black curve is based on a VBM for PbSe, and the solid red curve is based on a VBM for PbTe.[9] The dashed black curve is based on a VBM for Tl-doped PbSe. For PbTe, we use heavy hole effective mass $m^*_{hh}/m_e$ = 2 and a separation between light hole portion and heavy hole portion of 0.12 eV. For PbSe, we use heavy hole effective mass $m^*_{hh}/m_e$ = 2.5 and a separation between light and heavy hole portions of 0.26 eV. The light hole effective mass $m^*_{lh}/m_e$ = 0.4 for Na-doped PbSe and $m^*_{lh}/m_e$ = 0.7 for Tl-doped PbSe.

all the way with increasing carrier concentration in Na- and K-doped PbSe and falls well on the line calculated using the VBM, which is also not much different from the TBK model at room temperature.[9] Interestingly, we found the same trend happens in Tl-doped PbSe with increased Seebeck coefficient ~50 $\mu$V $K^{-1}$ for each corresponding carrier concentration, which can be fitted by VBM using light hole effective mass $m^*_{lh}/m_e$ = 0.7 (dashed black line), much higher than for Na-doped PbSe $m^*_{lh}/m_e$ = 0.4 (solid black line). In previous *ab initio* calculations, it was found that there is local increase of DOS in Tl-doped PbSe, however, the impurity states reside in the band gap, which degrades the increase of Seebeck coefficient and makes it even lower than Na-doped PbSe.[36] Our data shown in Figure 9 have a small abnormality at $n_H^p = 6 \times 10^{19}$ $cm^{-3}$ in qualitative agreement with the first-principles calculations of ref 36, Figure 12b. It shows an increase in the Seebeck coefficient, which is possibly due to some band modifications by Tl doping near Fermi level. In Table 1, the low Hall mobility of Tl-doped PbSe may be the result of increased scattering by modulated effective mass, which lowers the electrical conductivity as well as power factor.

The highest *ZT* value of Tl-doped PbSe is ~1.0 at about 723 K, shown in Figure 10. It is lower than that of Tl-doped PbTe.[17] With increasing temperature, the *ZT* value increases, showing no sign of decreasing for 1 at % and 2 at % Tl-doped PbSe. However, the highest mechanically stable temperature for all the ball-milled Tl-doped samples is ~750 K, which is consistent with ball-milled Tl-doped PbTe.[10,21] It seems that with increasing ionic radius of dopants, the stable temperature decreases for ball-milled IIIA-doped PbSe samples. As in the case of PbTe, it is also possible to include silicon and sodium together in Tl-doped PbSe. It may be possible to use this to produce stable samples at higher temperature and enhance *ZT*.[10]

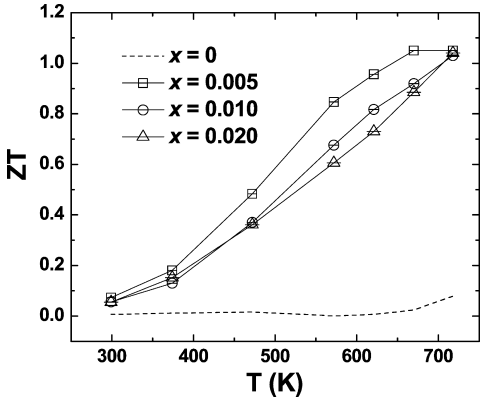


**Figure 10.** Temperature dependence of *ZT* for $PbSeTl_x$ ($x$ = 0, 0.005, 0.01, and 0.02).

## CONCLUSIONS

The detailed effect of B or Ga, In, and Tl doping on the thermoelectric properties of PbSe has been studied. There is no evidence for resonant states in B-, Ga-, or In-doped PbSe, but it seems that there may be band structure modification by Tl doping around the Fermi level. Relatively high Seebeck coefficients are obtained in B-doped n-type PbSe, even though the maximum obtainable carrier concentration is limited, and Tl-doped p-type PbSe with high DOS effective mass but low


dx.doi.org/10.1021/ja307910u | J. Am. Chem. Soc. 2012, 134, 17731−17738

Hall carrier mobility. The highest $ZT$ value obtained is ~1.2 in 0.5 at % Ga- or In-doped n-type PbSe at about 873 K. Due to the large reduction in lattice thermal conductivity by ball milling, Tl-doped PbSe has a maximum $ZT$ of ~1.0 at about 723 K.

## AUTHOR INFORMATION


### Corresponding Author

gchen2@mit.edu; renzh@bc.edu


### Notes

The authors declare no competing financial interest.

## ACKNOWLEDGMENTS

This work is supported by "Solid State Solar Thermal Energy Conversion Center ($S^3$TEC)", an Energy Frontier Research Center funded by the U.S. Department of Energy, Office of Science, Office of Basic Energy Science under award number DE-SC0001299 (D.B., G.C., C.O., D.P., D.J.S., and Z.F.R.).

## REFERENCES


(1) Majumdar, A. *Science* **2004**, *303*, 777.
(2) Rowe, D. M. *CRC Handbook of Thermoelectrics, Macro to Nano*; CRC Press, Taylor & Francis Group: Boca Raton, FL, 2006.
(3) Kraemer, D.; Poudel, B.; Feng, H. P.; Cavlor, J. C.; Yu, B.; Yan, X.; Ma, Y.; Wang, X. W.; Wang, D. Z.; Muto, A.; McEnaney, K.; Chiesa, M.; Ren, Z. F.; Chen, G. *Nat. Mater.* **2011**, *10*, 532.
(4) Pei, Y. Z.; Shi, X. Y.; LaLonde, A.; Wang, H.; Chen, L. D.; Snyder, G. J. *Nature* **2011**, *473*, 66.
(5) Pei, Y. Z.; LaLonde, A. D.; Heinz, N. A.; Shi, X. Y.; Lwanaga, S.; Wang, H.; Chen, L. D.; Snyder, G. J. *Adv. Mater.* **2011**, *23*, 5674.
(6) Biswas, K.; He, J. Q.; Zhang, Q. C.; Wang, G. Y.; Uher, C.; Dravid, V. P.; Kanatzidis, M. G. *Nat. Chem.* **2011**, *3*, 160.
(7) Pei, Y. Z.; Lensch-Falk, J.; Toberer, E. S.; Medlin, D. L.; Snyder, G. J. *Adv. Funct. Mater.* **2011**, *21*, 241.
(8) LaLonde, A. D.; Pei, Y. Z.; Snyder, G. J. *Energy Environ. Sci.* **2011**, *4*, 2090.
(9) Zhang, Q.; Cao, F.; Liu, W. S.; Lukas, K.; Yu, B.; Chen, S.; Opeil, C.; Chen, G.; Ren, Z. F. *J. Am. Chem. Soc.* **2012**, *134*, 10031.
(10) Zhang, Q. Y.; Wang, H. Z.; Zhang, Q.; Liu, W. S.; Yu, B.; Wang, H.; Wang, D. Z.; Ni, G.; Chen, G.; Ren, Z. F. *Nano Lett.* **2012**, *12*, 2324.
(11) Heremans, J. P.; Jovovic, V.; Toberer, E. S.; Saramat, A.; Kurosaki, K.; Charoenphakdee, A.; Yamanaka, S.; Snyder, G. J. *Science* **2008**, *321*, 554.
(12) Zhang, Q.; Sun, T.; Cao, F.; Li, M.; Hong, M. H.; Yuan, J. K.; Yan, Q. Y.; Hng, H. H.; Wu, N. Q.; Liu, X. G. *Nanoscale* **2012**, *2*, 1256.
(13) Singh, D. J. *Phys. Rev. B* **2010**, *81*, 195217.
(14) König, J. D.; Nielsen, M. D.; Gao, Y. B.; Winkler, M.; Jacquot, A.; Böttner, H.; Heremans, J. P. *Phys. Rev. B* **2011**, *84*, 205126.
(15) Guch, M.; Sankar, C. R.; Salvador, J.; Meisner, G.; Klernke, H. *Sci. Adv. Mater.* **2011**, *3*, 615.
(16) Pei, Y. Z.; LaLonde, A.; Iwanaga, S.; Snyder, G. J. *Energy Environ. Sci.* **2011**, *4*, 2085.
(17) Nielsen, M. D.; Levin, E. M.; Jaworski, C. M.; Schmidt-Rohr, K.; Heremans, J. P. *Phys. Rev. B* **2012**, *85*, 045210.
(18) Volkov, B. A.; Ryabova, L. I.; Khokhlov, D. R. *Phys. Usp.* **2002**, *45*, 819.
(19) Jovovic, V.; Thiagarajan, S. J.; Heremans, J. P.; Komissarova, T.; Khokhlov, D.; Nicorici, A. *J. Appl. Phys.* **2008**, *103*, 053710.
(20) Xiong, K.; Lee, G.; Gupta, R. P.; Wang, W.; Gnade, B. E.; Cho, K. *J. Phys. D: Appl. Phys.* **2010**, *43*, 405403 (8pp).
(21) Yu, B.; Zhang, Q. Y.; Wang, H.; Wang, X. W.; Wang, H. Z.; Wang, D. Z.; Snyder, G. J.; Chen, G.; Ren, Z. F. *J. Appl. Phys.* **2010**, *108*, 016104.
(22) Jaworski, C. M.; Heremans, J. P. *Phys. Rev. B* **2012**, *85*, 033204.
(23) Parker, D.; Singh, D. J. *Phys. Rev. B* **2010**, *82*, 035204.
(24) Wang, H.; Pei, Y. Z.; LaLonde, A. D.; Snyder, G. J. *Adv. Mater.* **2011**, *23*, 1366.
(25) Androulakis, J.; Lee, Y.; Todorov, I.; Chung, D. Y.; Kanatzidis, M. *Phys. Rev. B* **2011**, *83*, 195209.
(26) Androulakis, J.; Chung, D. Y.; Su, X.; Zhang, L.; Uher, C.; Kanatzidis, M. G. *Phys. Rev. B* **2011**, *84*, 155207.
(27) Zhang, Q. Y.; Wang, H.; Liu, W. S.; Wang, H. Z.; Yu, B.; Zhang, Q.; Tian, Z. T.; Ni, G.; Lee, S.; Esfarjani, K.; Chen, G.; Ren, Z. F. *Energy Environ. Sci.* **2012**, *5*, 5246.
(28) Wang, S. Y.; Zheng, G.; Luo, T. T.; She, X. Y.; Li, H.; Tang, X. F. *J. Phys. D: Appl. Phys.* **2011**, *44*, 475304.
(29) Alekseeva, G. T.; Gurieva, E. A.; Konstantinov, P. P.; Prokof'eva, L. V.; Fedorov, M. I. *Semiconductors* **1996**, *30*, 1125.
(30) Nemov, S. A.; Gurieva, T. A.; Konstantinov, P. P.; Prokof'eva, L. V.; Proshin, M. I. *Semiconductors* **1998**, *32*, 689.
(31) Jovovic, V.; Thiagarajan, S. J.; West, J.; Heremans, J. P.; Story, T.; Golacki, Z.; Paszkowicz, W.; Osinniy, V. *J. Appl. Phys.* **2007**, *102*, 043707.
(32) Schlichting, U.; Gobrecht, K. H. *J. Phys. Chem. Solids* **1973**, *34*, 753.
(33) Kaĭdanov, V. I.; Mel'nik, R. B.; Germanas, N. V. *Sov. Phys. Semicond.* **1972**, *6*, 627.
(34) Prokof' eva, L. V.; Gurieva, E. A.; Zhumaksanov, Sh. M.; Konstantinov, P. P.; Maĭlina, Kh. R.; Ravich, Yu. I.; Stil'bans, L. S. *Sov. Phys. Semicond.* **1987**, *21*, 1078.
(35) Kaĭdanov, V. I.; Nemov, S. A.; Ravich, Yu. I. *Sov. Phys. Semicond.* **1992**, *26*, 113.
(36) Peng, H. W.; Song, J. H.; Kanatzidis, M. G.; Freeman, A. J. *Phys. Rev. B* **2011**, *84*, 125207.
(37) Heremans, J. P.; Wiendlocha, B.; Chamoire, A. M. *Energy Environ. Sci.* **2012**, *5*, 5510.
(38) Jaworski, C. M.; Wiendlocha, B.; Jovovic, V.; Heremans, J. P. *Energy Environ. Sci.* **2011**, *4*, 4155.
(39) Yan, X.; Poudel, B.; Ma, Y.; Liu, W. S.; Joshi, G.; Wang, H.; Lan, Y. C.; Wang, D. Z.; Chen, G.; Ren, Z. F. *Nano Lett.* **2010**, *10*, 3373.
(40) Ravich, Y. I.; Efimova, B. A.; Smirnov, I. A. *Semiconducting Lead Chalcogenides*; Plenum Press: New York, 1970.
(41) Poudel, B.; Hao, Q.; Ma, Y.; Lan, Y.; Minnich, A.; Yu, B.; Yan, X.; Wang, D.; Muto, A.; Vashaee, D.; Chen, X.; Liu, J.; Dresselhaus, M. S.; Chen, G.; Ren, Z. F. *Science* **2008**, *320*, 634.

# Classroom

**In this section of *Resonance,* we invite readers to pose questions likely to be raised in a classroom situation. We may suggest strategies for dealing with them, or invite responses, or both. "Classroom" is equally a forum for raising broader issues and sharing personal experiences and viewpoints on matters related to teaching and learning science.**

## Differential Scanning Calorimetry: Fundamental Overview

Kevin Lukas and Peter K LeMaire
Department of Physics, Central Connecticut State University, New Britain, CT 06050.
Email: lemaire@ccsu.edu

**This paper discusses the fundamentals of Differential Scanning Calorimetry (DSC) including functions and outputs of a Differential Scanning Calorimeter along with common uses in academia and industry.**

### Introduction

A solid material can be amorphous, crystalline, or a combination of the two. An amorphous material is one with no discernable orientation for its atoms or molecules; they are arranged in a random fashion. Crystals on the other hand are arranged in a specific pattern, which is repeatable and predictable. A material may also be a combination of amorphous and crystal structure; this material could be crystalline in one area, and amorphous in another, or islands of crystalline arrangements which are randomly distributed in an amorphous system. The thermodynamic state affects the structure of a material which in turn affects its properties. Variations in the thermodynamic state of a material thus lead to variations in its properties. Using Differential Scanning Calorimetry (DSC), one can better understand phase transitions and reactions in materials, and how they contribute to the properties and characteristics of the material.

**Keywords**
Heat flow, phase transitions, latent heat.

## DSC

DSC is a method of thermal analysis that is widely used to study thermal transitions, i.e., solid-solid transitions as well as solid-liquid and various other transitions and reactions. A solid-solid phase transition would be if the material had its structure altered, but not gain enough energy to become a liquid. Using thermal analysis, it is possible to understand what is happening in a material, even if there is no visual evidence that a change has occurred. For instance, it is easy to see when an ice cube melts into water and when water boils into steam; these are visible changes. There are however several different phase changes within water in a solid state. Ice at colder and colder temperatures can have several different crystal structures and undergo many solid-solid phase transitions, and in each of these phases, the ice has different properties ranging from brittleness to conductivity. By understanding the technique and instrumentation of DSC, it is possible to understand what the materials go through during energy gain or loss. Earlier versions of the DSC were known as Differential Thermal Analyzers (DTA).

## Instrumentation Basics

In a DSC, there are two pans isolated from the ambient environment in a chamber. One pan contains the sample to be analyzed, and the other pan is empty and is used as a reference pan. Both pans have heaters underneath them that are used to raise or lower the temperature. Each pan also has a sensor that indicates what the temperatures of the pans are at any given moment. Using computer controlled sensors and logic, the heaters are set to heat the pans at a constant rate ($\Delta T/\Delta t$), that is the rate of temperature change is the same, for example 5 degrees celsius per minute. The instrumentation is also designed to ensure that the pans heat at the same rate as each other. Having the pans heat at a constant rate, but also the same rate as each other might seem repetitious; however the *heat flow*, which is the rate at which thermal energy ($\Delta Q/\Delta t$) is supplied to the pans, does differ, due to the fact that there is material in one of the pans, and nothing in the other pan. Consider, for example, two pots, one with water and one empty, and both pots start out at the same initial temperature and are then placed on stoves. If each pot is heated at the same rate (both stove settings are placed on low, for example) the pot with the water in it will heat up slower, that is the rate of temperature change will be smaller than the pot with nothing. This is because heat capacity is different for water than it is for air. The same thing happens in the pans of our instrument, the pan with the material/sample in it will heat up slower than the reference pan which contains nothing. Going back to our example of the two pots, the computer would control the stoves and set the pots to be heated at a constant 5 degrees per minute, and also monitor the temperature of each pot and ensure that the two heat at the same rate. Since the pot with the water in it will heat up slower than the empty pot, the computer will have to supply a higher *heat flow* to the pot containing water in order to force the pots to heat at the same rate.

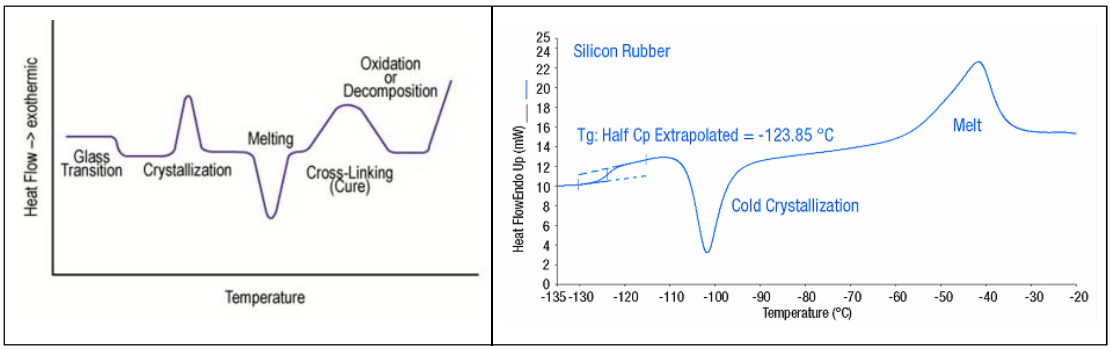


***Figure 1 (left). DSC profile. In this profile, exothermic heat flow is measured versus temperature.***
Courtesy: TA Instruments, Inc.
***Figure 2 (right). DSC profile. Here the endothermic heat flow is measured versus temperature.***
© 2006-2008, PerkinElmer, Inc. All rights reserved. Printed with permission

The computer keeps track of the starting temperature, heating rate, and heat flow, and records the difference in *heat flow* between the reference pan and the sample pan (water pot in our example), which is the *heat flow* for the sample, and plots it against temperature as shown in *Figures* 1 and 2.

As seen from *Figures* 1 and 2, the heat flow may be measured as exothermic, or endothermic and plotted against temperature. The slope of the curve is the rate of change of heat capacity, $\Delta C_p/\Delta t$. As previously stated, the heating rate ($\Delta T/\Delta t$) is set, and the heat flow ($\Delta Q/\Delta t$) is measured. The heat flow may be divided by the heating rate to obtain a value for heat capacity, i.e., $(\Delta Q/\Delta t)\ /(\Delta T/\Delta t) = \Delta Q/\Delta T = C_p$. Knowing the mass ($m$) of the sample, the specific heat capacity ($c_p = C_p/m$), as a function of temperature may be obtained, thus yielding information on the variations in the physical properties of the material.

## Phase Transitions

Every solid state material when continuously heated will come to a point where it changes phase. For example ice, when heated, at standard atmospheric pressure, will undergo a phase change from solid to liquid (melt) at a transition temperature (melting point) of 0 °C, and when the resulting water is heated, it will eventually undergo another phase transition from liquid to gas (vaporize) at a transition temperature (boiling point) of 100 °C. We are also relatively familiar with solid to gas transitions in solids such as dry ice. As a material is heated, the atoms and/or molecules gain more energy. At the solid to liquid transition temperature, the atoms/ molecules have enough energy to break away from their rigid structure to a less restricted state which is the liquid state. The energy supplied simply goes into converting the solid to liquid, that is, the energy is spent in breaking down the rigid solid structure into the much less rigid liquid

state, leading to gain in energy of the material (an endothermic transition). The energy per unit mass used in bringing about such a phase change is known as the latent heat. Transitions that have latent heats associated with them are said to be first order transitions. The energy supplied does not lead to a temperature change until the phase transformation is complete. A similar process takes place during the phase transformation from liquid to gas.

As discussed earlier a DSC measures the heat absorbed or released by a material as a function of temperature or time (isothermally). This then allows the determination of important thermal characteristics such as transition temperatures, for example, melting and boiling points as well as other transition temperatures such as glass transition temperature ($T_G$), and crystallization temperature ($T_c$), which will be discussed later in this article. It also allows for the determination of quantitative measurements such as the specific heat capacity, heat of fusion, heat of vaporization, heat of polymerization, heat of crystallization, and heat of reaction. Practically all DSC instruments allow such measurements to be done under various atmospheres.

## Glass Transitions

Glass transitions can only take place in an amorphous material. A glass transition has no latent heat associated with it, and such transitions are referred to as second order transitions. The heat flow vs. temperature for a glass transition is as shown in *Figure* 3.

In this case, the heat capacity has increased and the molecules have become more mobile, and so the material is now in a state where its atoms/molecules have more energy. In order to keep the heat rate constant, the sample pan heater needed to increase heat flow. The material is still amorphous but has undergone a transition from a lower energy state to a higher energy state. The temperature at which the material undergoes a glass transition is known as the glass transition temperature ($T_G$), and as seen in *Figure* 3, the $T_G$ is assigned to the mid point temperature of the range of temperature during the transition. A simple example of a glass

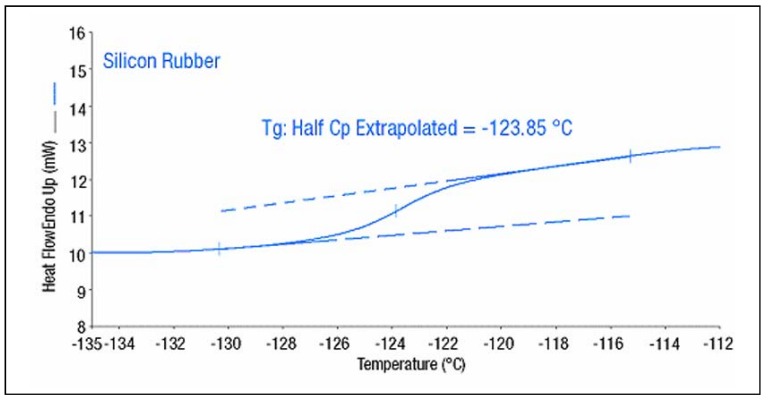


***Figure 3. Glass transition temperature ($T_g$) of Silicon Rubber.***

©2006–2008, PerkinElmer, Inc. All rights reserved. Printed with permission.

transition can be seen in plastics. When a plastic or rubber material is placed in a freezer, it becomes very brittle and can easily be shattered, the plastic or rubber is then in a 'glass' state. When it is warmed the plastic or rigid rubber becomes very pliable, or goes into a 'rubbery' state. The glass transition temperature of Polyethylene Terephthalate (PET), the plastic material that various beverage containers are made of, has a $T_G$ of about 70 $^oC$, and the $T_G$ for glass used as containers is about 550 $^oC$. A word of caution as to the glass transition temperatures: they can vary significantly depending on the rate at which the material is heated or cooled. However, under continuous heating, the next step for an amorphous material will be for the material to become crystalline.

## Crystallization

When a material is crystallized, it becomes ordered. Crystallization is a first order transition, and thus a latent heat is associated with the transition. As shown in *Figure* 2, the process is exothermic, that is, thermal energy is released and the sample gets hotter, and so during crystallization, the sample heater supplies less energy than the reference heater to maintain the constant set heat rate. As can be seen from the shape of the crystallization profile in *Figure* 2, it takes a while for all the material to go from the amorphous state to the crystalline state, and so the presence of mixed phases during the crystallization process. The shape is also affected by constraints of current technology.

The crystallization temperature ($T_c$) is at the peak of the depression in the graph. The area of the depression can be obtained and using the heating rate and the mass of the sample, the latent heat of crystallization may be calculated. At or near the crystallization temperature, the material has gained enough energy so that its atoms/molecules could re-arrange into a more stable and ordered state. By nature, materials tend toward the lowest energy state, and the lowest energy state possible is one of order. A crystalline material can undergo solid-solid phase transitions. For example Cesium Nitrate, undergoes a solid-solid phase transition at 154 $^oC$ [1,2].

## Melting

When a material melts, it becomes disordered in the form of a liquid. In materials that are made up of either several different phases or different components, a DSC may show multiple melting transitions. There are various theories as to what causes a material to melt and what is actually happening on the molecular level as it melts. General observations about melting include three major components. The first is that melting always occurs with an increase in disorder. Second, there is always a change in volume (positive or negative). Third, there is always a change in heat capacity. A simple theory of melting backed by experiments, is that of Lindemann (1910) [3,4,5]. He theorized that melting is caused by instability in the crystal lattice structure due to

vibrations. As the temperature increases, the vibrational amplitudes increase, finally reaching a critical fraction of the lattice distance that renders the crystal unstable [5]. A material cannot melt unless it is a crystal. Therefore, any material that melts must first crystallize. An example of the heat flow vs. temperature graph during melting can be seen in *Figures* 1 and 2, showing melting as an endothermic process.

Similar to when the material gave off heat/energy as it became a crystal, at the melting point ($T_m$), it must now absorb energy to go to higher energy state. In this case the sample heater supplies more energy per unit time as compared to the reference heater, and the temperature of the material at the melting point will stay constant until the material goes from the solid phase to the liquid phase as discussed earlier. Once the solid has become a liquid, the liquid can then proceed to heat up. So in the graph of the heat flow vs. temperature, the heat flow to the sample must increase dramatically in order for the sample to melt and still keep the same heating rate as the reference pan. The peak of the curve is the melting temperature ($T_m$) and the area under the curve may be used to find the latent heat of fusion (melting).

*Figure* 1 shows the range of transitions. An amorphous material will first undergo a glass transition where its heat capacity is increased, but no latent heat is present. The material will then crystallize and release energy. The material can undergo solid-solid phase transitions by re-crystallizing into different arrangements; this is known as polymorphism, followed eventually by melting and may undergo additional phase changes in the liquid phase. Inherently crystalline materials thus may only undergo solid to solid transitions and then melt. As mentioned earlier, depending on the thermodynamic state of the material it may undergo a solid to gas transition in a process known as sublimation, and the latent heat of sublimation may be measured.

**Thermogravimetric Analysis (TGA)**

A thermogravimetric analyzer (TGA) is used to complement a DSC, and measures mass changes of a sample as a function of temperature or time. The measurements also can be done under various atmospheres just like the DSC. The TGA thus allows, among others, the determination of thermal and oxidative stability, and optimum processing conditions. The TGA can be used as a stand alone instrument, but it is often used in conjunction with other thermal equipment such as the DSC. For example, if one sees an endothermic or exothermic reaction using a DSC, the TGA measurements will help determine whether the change is physical or chemical in nature. The reaction is chemical in nature if a mass change is associated with it and physical if no mass change occurs. An example of a physical change is melting of a solid to liquid, and iron rusting in air is an example of a chemical change.

*Figure* 4 shows a simultaneous DSC and TGA thermal profile of Barium Yttrium Oxides,

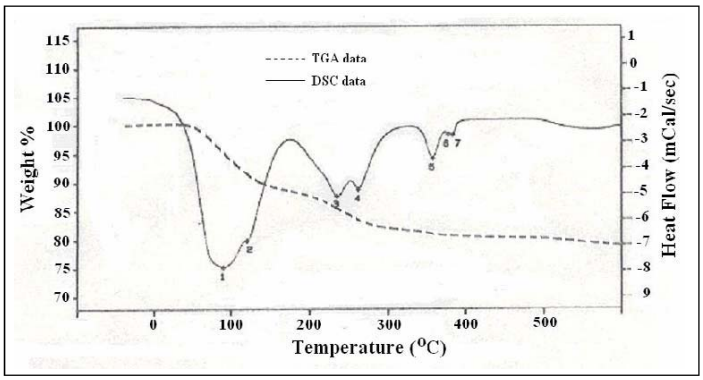


***Figure 4. Thermal profile of Barium Yttrium Oxide showing TGA (weight changes) and DSC (heat flow).***

showing loss of adhered and hydrated water in the sample followed by decomposition into component crystalline and amorphous materials. The latter was confirmed by X-ray Diffraction measurements [6].

**Applications of DSC**

In addition to materials research applications, Thermal Analysis (DSC and TGA) have found uses in a large number of industries, such as tools manufacturing, semiconductor technology, battery safety, food technology, explosives manufacturing, metallurgy, cosmetics, textiles, energy companies – petroleum and coal. Others include applications in quality control, testing and catalysis, for example, for the screening of catalysts for CO oxidation in the automotive industry. For explosives development, a DSC may be used to measure safely, the energy released by a small amount of a sample without any catastrophic consequences.

DSC is used for many industrial applications which include finding polymorphic transitions, melting points/profiles, glass transition (softening point), thermal history/processing conditions, crystallization temperature, percent crystallinity, thermal safety/stability, effect of additives (plasticizers, etc.), polymer blends, degree of cure, and protein denaturation.

In the study of Copper Iodide (CuI) nanocrystals, crystallographic phase transitions from "zincblende ($\gamma$-phase) to distorted wurtzite ($\beta$-phase) to disordered zincblende ($\alpha$-phase)" were investigated using DSC, obtaining transition temperatures, enthalpies and other thermodynamic information to help explain the process for the formation of these nanocrystals [7]. In materials research DSCs and TGAs are often used to verify and/or corroborate results from other research methods. In the case of the mixed conductor $Ag_{3.0}CS_2$ [8], an amorphous material that conducts both electrons and ions, electrical conductivity data showed an abrupt change at about 178 $^oC$. DSC showed what seems to be a crystallization transition at that temperature in support of the conductivity results.

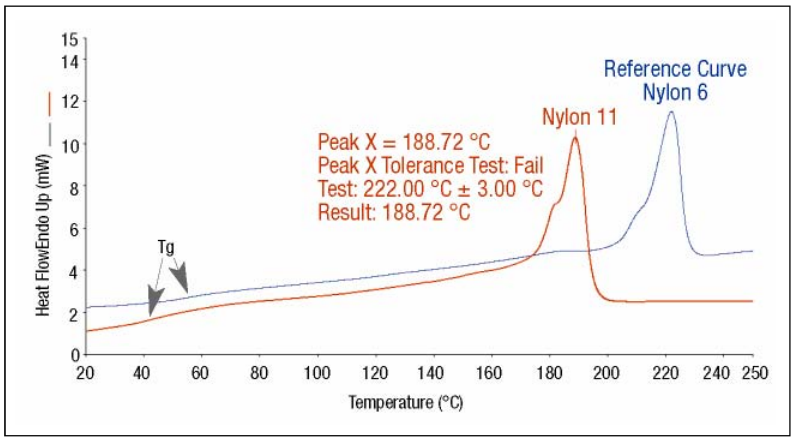


***Figure 5. Industrial raw material inspection.***
© 2006–2008, PerkinElmer, Inc. All rights reserved. Printed with permission.

One major purpose of DSC is to identify a material. Similar DSC profiles may suggest similar materials. For example, by running samples and finding the value for $T_g$ and $T_m$, the material can be identified and qualified by running a sample of an unknown content and comparing the DSC profile to that of a known material. In the example in *Figure* 5, DSC is used in quality assurance and control, where "incoming Nylon's melting point is compared to the quality standard for melting temperature". In this case it turns out that the incoming nylon turns out to be Nylon 11 instead of the required Nylon 6 which has a higher melting point.

There are many practical applications for DSC during the fabrication of a component or material. No matter how much planning goes into design and fabrication there may still be problems that may need to be addressed: a material may melt when it should not break when it should not or not act as it was designed, etc. Every time that a component fails or does not act as expected, an investigative analysis is run called 'failure analysis'. During failure analysis, DSC is a powerful tool that can be used to see if there is something going on in the material that may not be visible to the naked eye, under a microscope, or during other tests.

*Figure* 6 shows another example of the use of DSC in industry and research. In this case the effect of additives on the oxidative stability of polyethylene is studied by measuring the Oxidative Induction Time (OIT). As seen in the figure, the "failed polyethylene sample lasted less than 5 minutes in an oxidative atmosphere before decomposing".

With improvements in DSC technology more information can be obtained using DSC. In *Figure* 7, Perkin Elmer's Jade DSC is used to study liquid crystal phase transitions by running a cooling and heating cycle between 30 °C and 155 °C. The high resolution and sensitivity of the instrument allows otherwise barely visible transitions to be observed. Advancements in cooling accessories have also improved the application of DSCs at sub-ambient temperatures, usually

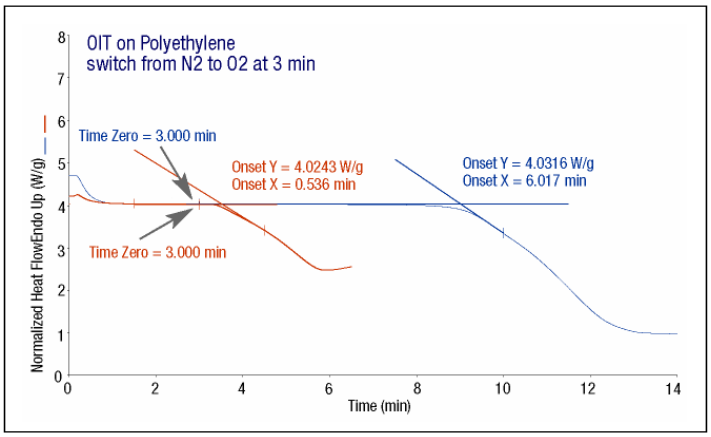


***Figure 6. Oxidative Induction Time measurements on polyethylene.***
©2006–2008, PerkinElmer, Inc. All rights reserved. Printed with permission.

down to liquid nitrogen temperatures. For example, the "CryoFill" automated liquid nitrogen cooling DSC accessory, allows easier determination of transitions, such as $T_G$, even at extremely low temperatures. As indicated earlier, the shape of thermal profiles measured by DSC is affected by the state of current technology. In *Figure* 8, Advanced Tzero$^{TM}$ technology is shown to improve the profile of the melting peak of Indium to be closer to the true shape, which is supposed to be a well-defined sharp peak.

Employee health and safety issues are high priority, especially in today's work place. DSC is used to analyze samples for potential health issues. For example, long-term overexposure to respirable crystalline silica and other particulates may cause silicosis and other respiratory diseases [9]. Worker safety regulatory agencies such as the Occupational Safety and Health Agency (OSHA) of the United States Department of Labor has ruled that "an employee's exposure to particulates, not otherwise regulated, should not exceed 5 mg/m$^3$ (respirable dust),

***Figure 7. Liquid crystal phase transitions.***
© 2006-2008, PerkinElmer, Inc. All rights reserved. Printed with permission.

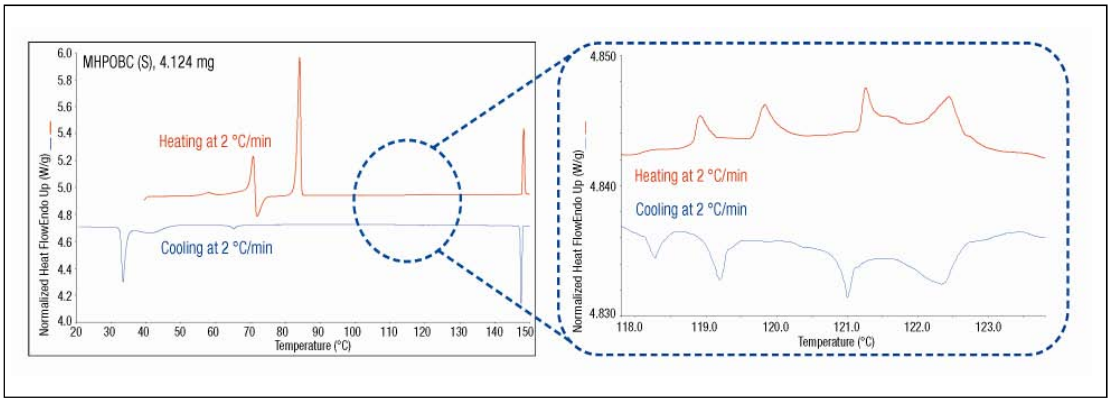

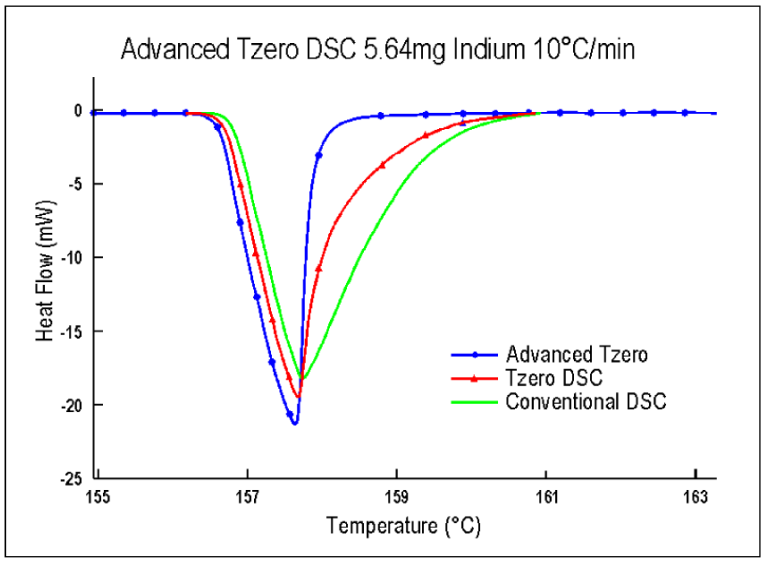


***Figure 8. Melting of Indium showing Tzero™ technology.***
Courtesy: TA Instruments, Inc.

15 mg/m$^3$ (total dust), 8-hr time weighted average" [9]. By properly identifying the percentage of toxic material, the safety and well being of all employees can be ensured.

DSC plays a critical role in the study of explosive material. In a search for "more powerful, safer and environmentally friendly explosives" DSC was used to study the solid-solid phase transition kinetics of 1,1-diamino-2,2-dinitroethene (FOX-7) and to measure the enthalpies associated with the transitions [10].

As a material 'ages', its thermal profile changes. In pharmaceutical industry, DSC is used to study 'aging' and shelf life of pharmaceuticals, as well as other basic research and development [11,12]. An example is in the study of the two polymorhs of the drug 'carbamazepine' and to accurately determine associated enthalpy [12].

In the Food Industry, DSC has numerous applications to monitor thermal events discussed earlier such as melting, crystallization, etc, as well as decomposition, denaturation, dehydration, polymorphism, oxidation, etc [13,14,15,16,17]. For example "the effect of storage temperature on phase transitions of the lipid components" in apple and capsicum cuticles was studied using DSC, and it was found that at "low temperatures, the cuticular membrane underwent a change in structure and the melting enthalpy of the waxes present decreased" [13].

DSC finds use in both industry and academia. It has a range of practical applications, and its fundamental principles are important in understanding material structure.

## Acknowledgements

The authors are indebted to Prof. Sadanand Nanjundiah for his encouragement in getting this article prepared, and to TA Instruments Inc., and Perkin Elmer Inc., for providing high quality thermograms and figures.

## Suggested Reading

[1] W Dodakian and P K LeMaire, *Bull. Am. Phys. Soc. Trans*. A, Vol.4, No.4, p.1472, 1997.
[2] E Charrier, E L Charsley, P G Laye, H M Markham, B Berger, and T Griffiths, *Thermochimica Acta*, Vol. 445, No.1, p.36, 2006.
[3] F A Lindemann, Über die Berechnung Molecularer Eigenfrequenzen, *Phys. Z*., Vol.11, pp.609–612, 1910.
[4] Edith A Turi, *Thermal Characterization of Polymeric Materials,* Academic Press, Inc. New York, 1981.
[5] C J Martin and D A O'Connor, An experimental test of Lindemann's melting law, *J. Phys. C: Solid State Phys.,* Vol.10, pp.3521–3526, 1977.
[6] P LeMaire (unpublished data)
[7] P S Kumar, Y L Saraswathi, *Mater. Phys. Mech*., Vol.4, pp.71–74, 2001.
[8] P K LeMaire, R Speel, R Ruotolo, *Journal of the Electrochemical Society*, Vol.148, No.5, 2001.
[9] DuPont Starblast: Blasting Abrasive, *Material Spec. Sheet*, 2006.
[10] A K Burnham, R K Weese, R Wang, Q S M Kwok, and D E G Jones, Solid - Solid Phase Transition Kinetics of FOX-7, University of California, Lawrence Livermore National Laboratory, 2005 NATAS Annual Conference Universal City, CA, United States.
[11] A F Barnes, M J Hardy and T J Lever, *Journal of Thermal Analysis and Calorimetry,* Vol.40, No.2, 1993.
[12] C McGregor, M H Saunders, G Buckton and R D Saklatvaia, *Thermochimica Acta,* Vol. 417, No 2, 2004.
[13] P Aggarwal, *Thermochimica Acta,* Vols.367–368, 9–13, 2001.
[14] www.-unix.oit.umass.edu/~mcclemen/581Thermal.html
[15] Semih Otles, Serkan Otles, *Electronic Journal of Polish Agricultural Universities (EJPAU),* Vol.8, No. 4, 2005. or www.ejpau.media.pl/volume8/issue4/art-69.html
[16] http://www.setaram.com/files/documents/Characterization-Food-products.pdf
[17] Rachit Suwapanich and Methinee Haewsungcharern, Effect of Storage Temperature on Thermal Properties of mango cv. Nam Dok Mai Si Thong, Conference on International Agricultural Research for Development, Tropentag 2005, Stuttgart Hohenheim, October 11–13, 2005.
[18] H K D H Bhadeshia, *Differential Scanning Calorimetry*, University of Cambridge, Materials Science & Metallurgy, www.msm.cam.ac.uk/phasetrans/2002/Thermal2.pdf
[19] *Differential Scanning Calorimetry*, *Glass Transition*, Department of Polymer Science, University of Southern Mississippi, http://pslc.ws/macrog/dsc.htm, http://pslc.ws/macrog/tg.htm